

INQUIRIES INTO THE CONSEQUENCES OF
PLANETARY-SCALE IMPACTS AND THE IMPLICATIONS OF
CARBONATES IN THE HYPER-ARID CORE OF THE SAHARA

Thesis by

Margarita M. Marinova

In Partial Fulfillment of the Requirements
for the Degree of
Doctor of Philosophy



CALIFORNIA INSTITUTE OF TECHNOLOGY

Pasadena, California

2010

Defended May 11, 2010

© 2010

Margarita M. Marinova

All Rights Reserved

ACKNOWLEDGEMENTS

Starting graduate school is the easy part – it's the long and winding path through classes and research and late nights and life and thoughts of careers and futures that are the hard part. And I have been incredibly lucky to have had a wonderfully winding path, surrounded by amazing people who made the journey both enjoyable – and doable.

My sincere thanks to everyone who has helped me grow as a scientist. Thanks to my advisor, Oded Aharonson, for suggesting the Mars dichotomy problem (I do enjoy making Mars on my desk, and flinging large objects at it!). Thanks to the amazing faculty here and the many fascinating discussions with you: Andy Ingersoll, Dave Stevenson, Paul Asimow, Mike Brown, George Rossman, Jess Adkins, John Grotzinger. An important part of my scientific growth and learning during my grad school years has been field work with collaborators outside of Caltech: Chris McKay, Darlene Lim, Bernard Laval, Jen Heldmann, Bekah Shephard, Donnie Reid, Dale Andersen, Wayne Pollard. Thanks for believing in me, and giving me the freedom and experience to grow. The guidance that I received from all of you is what has made me into the scientist that I am today!

During my winding and sometimes rocky path of grad school, I always had the support of my amazing friends and family! Thanks to my office crew – Darin Ragozzine, Alejandro Soto, Kaveh Pahlevan, Aaron Wolf – for all the crazy, fun, and heartfelt times we've had: whether it was long discussions on whether Saturn really could float in a bathtub, late night coffee runs, or just musing on life. You guys are incredible, and the hardest part about leaving Caltech will be not sharing an office with you every day! Thanks to my best friends since high school Megan Tam and Candice Lee, my roommates Ashley

Jones and Amy Hofmann, and Nele Meckler and Irma Black for your incredible friendship and love and support and frozen yoghurt. I am endlessly grateful to have you in my life! To all of you, my deepest gratitude for always having my back! Thanks also to the many other people who have made my time here rewarding and fun: Colette Salyk, Jenny Meyer, Kristin Bergmann, Alex Hayes, Emily Schaller, and Jack Wisdom, to name a few.

And perhaps most importantly, I could have never gotten through the past 6 years without the constant shipments of Swiss chocolate from my parents, my brother whisking me away to amazing places, my family in Bulgaria always asking when I would visit next, and all of their endless support and willingness to help. Who knew, mom and dad, that when you were telling me stories of meeting Yuri Gagarin I'd end up aiming for the stars myself? ☺

I dedicate this thesis to my grandmother. Through her example, she gave me the strength to deal with life head-on, taught me to always be true to myself and stand up for what's right, and showed me what it meant to have a constant fire inside of you. Thank you for supporting and believing in this rambunctious kid! Обичам те, бабо!

ABSTRACT

This thesis focuses on the geophysical and morphological consequences of planetary-scale impacts – the last remnants of planetary accretion. In this size regime, the impact crater size is a significant fraction of the size of the planet, and the finite size of the target is important: its surface curvature, radial gravity, and large relative size of the impactor with respect to the target. A fully three-dimensional hydrodynamics model is used to simulate the events, thus capturing these finite-size effects. Simulated are a range of impact energies ($0.02\text{--}5.89 \times 10^{29}$ J), velocities (6–50 km/s), and angles ($0^\circ\text{--}75^\circ$) into a Mars-like planet. In addition, the variation in results with impactor type, for both single-material and differentiated impactors, is also examined. For this range of impact conditions, the crater size can span up to $\sim 60\%$ of the planetary circumference, and the ellipticity of the crater can be significant even for intermediate angle impacts. This is consistent with the observed large craters, which are commonly elliptical. Despite the large melt volumes produced, the planetary surface is preserved in most cases, as much of the melt is placed in the mantle. Antipodal crustal removal is common for the more energetic cases. For impacts with more than about three times the mutual impactor-target escape velocity, the impact has a net erosive effect, with more mass being removed than deposited. These large impacts are sufficiently massive that they can give an initially stationary Mars a rotation period of less than a day. The simulation results suggest that the Mars hemispheric dichotomy may have formed by a single, planetary-scale impact; the required impact conditions are consistent with accretion models.

The last chapter of this thesis examines the paleoclimate implications of reef-like carbonate structures in the currently hyper-arid core of the Sahara (southwestern Egypt). The carbonates suggest a wetter epoch about 9,000–10,000 years ago, and the presence of long-term, standing water. Despite the higher precipitation, the chemical composition of the carbonates suggests that the vegetation cover was sparse.

CONTENTS

Acknowledgements	iii
Abstract	v
Table of Contents	vii
List of Figures	ix
List of Tables	ix
Chapter 1	1
Chapter 2 Mega-impact formation of the Mars hemispheric dichotomy	9
2.1 Abstract	10
2.2 Introduction	11
2.3 Results	12
2.4 Conclusions	19
2.5 Methods	20
2.6 Bibliography	21
2.7 Acknowledgements	24
2.8 Supplementary information	25
Chapter 3 Geophysical consequences of planetary-scale impacts into a Mars-like planet ..	27
3.1 Abstract	28
3.2 Introduction	29
3.3 Modeling	31
3.3.1 SPH modifications and improvements	32
3.3.2 Equation of state	33
3.3.3 Initial conditions	36
3.3.4 Impact parameter space	39
3.3.5 Characteristics of the impact	41
3.4 Results	43
3.4.1 Morphology of planetary-scale craters	44
3.4.1.1 Crater size	45
3.4.1.2 Crater ellipticity	51
3.4.1.3 Crustal thickness and redistribution	53
3.4.1.4 Mantle melt	59
3.4.2 Global consequences of planetary-scale impacts	63
3.4.2.1 Depth of transient crater cavity	63
3.4.2.2 Melt production and the maximum retainable crater size	68
3.4.2.3 Antipodal disruption	82
3.4.2.4 Orbiting and escaping material	87
3.4.2.5 Post-impact rotational period	93
3.5 Resolution effects	96
3.6 Conclusions	100
3.7 Acknowledgements	104
3.8 Bibliography	105

Chapter 4 The importance of impactor composition on the geophysical consequences of planetary-scale impacts into a Mars-like planet	113
4.1 Abstract	113
4.2 Introduction	114
4.3 Modeling	116
4.3.1 SPH model setup	116
4.3.2 Initial conditions	118
4.3.3 Impact parameter space	119
4.3.4 Characteristics of the impact	121
4.4 Mechanics of the impact process	124
4.5 Results	130
4.5.1 Crustal thickness and redistribution	131
4.5.2 Crater size	133
4.5.3 Ellipticity	144
4.5.4 Depth of penetration	146
4.5.5 Melt production	154
4.5.6 Melt distribution	162
4.5.7 Comparison of scaling relations	168
4.5.8 Planetary deformation	173
4.5.9 Mantle melt	176
4.5.10 Material mixing	178
4.5.11 Escaping and orbiting material	181
4.5.12 Antipodal disruption	190
4.5.13 Post-impact rotational period	190
4.6 Resolution effects	192
4.7 Conclusions	195
4.8 Appendix A. Details of the impact events	200
4.9 References	208
Chapter 5 Holocene carbonate reef structures in the hyper-arid Gebel Uweinat region of the Sahara Desert (southwestern Egypt)	213
5.1 Abstract	214
5.2 Introduction	214
5.2.1 Site description	217
5.3 Methods	219
5.4 Results	220
5.5 Discussion	222
5.6 Conclusions	226
5.7 Acknowledgements	226
5.8 References	227

LIST OF FIGURES

2-1 Schematic summary of simulation results	13
2-2 Surface melt distribution	15
2-3 Crater sizes and ellipticities	16
2-4 A favored impact scenario compared to Mars crustal thickness	17
2-A1 Timesteps from the best-fit simulation	25
2-A2 Crater rim around a smaller crater	26
3-1 Hugoniot for forsterite, fayalite, and Fo75.	36
3-2 Crater diameter results	47
3-3 Crater size comparisons	48
3-4 Penetration depth	51
3-5 Ellipticity	52
3-6 Peak pressure contours	53
3-7 Post-impact crustal thickness	57
3-8 Surface material distribution	59
3-9 Mantle melt	61
3-10 Depth of penetration	64
3-11 Penetration depth versus impactor mass	67
3-12 Melt production	70
3-13 Post-impact internal energy and pressure	70
3-14 Melt distribution	73
3-15 Melt partitioning	75
3-16 Melt volume	77
3-17 Melt volume scaling	79
3-18 Surface melt fraction as a function of melt amount	81
3-19 Antipodal cavity size	83
3-20 Antipodal cavity scaling	85
3-21 Antipodal cavity location	87
3-22 Escaping mass	89
3-23 Maximum ejection velocity	91
3-24 Accretionary versus erosive impacts	92
3-25 Angular momentum transfer	94
3-26 Post-impact rotational period	96
3-27 Resolution comparisons	97
3-28 Detailed resolution errors	99
4-1 Head-on impact by a differentiated impactor	126
4-2 Oblique impact by a differentiated impactor	128
4-3 Highly oblique impacts	129
4-4 Crustal thickness maps	133
4-5 Crater size comparison	134
4-6 Crater size results	136

	x
4-7 Crater size fitting results	138
4-8 Crater diameter relations	142
4-9 Crater ellipticity	146
4-10 Penetration depth	148
4-11 Penetration depth scaling.....	150
4-12 Depth of penetration relations	154
4-13 Melt production.....	156
4-14 Energy deposition in the planet	159
4-15 Melt scaling.....	161
4-16 Surface melt cover maps	163
4-17 Surface melt cover results.....	164
4-18 Surface melt cover versus total melt mass	165
4-19 Melt reservoirs	168
4-20 Planetary deformation versus surface melt cover	174
4-21 Mantle melt	178
4-22 Radial and circumferential mantle mixing.....	180
4-23 Escaping mass.....	182
4-24 Maximum ejection velocities	184
4-25 Orbiting mass	185
4-26 Composition of escaping material.....	186
4-27 Composition of orbiting material	187
4-28 Accretional and erosional regimes	189
4-29 Antipodal cavity size	190
4-30 Angular momentum transfer and post-impact rotational period	192
4-31 Resolution effects summary	195
4-A1 Head-on, slow impacts.....	200
4-A2 Head-on, slow, iron impactors.....	201
4-A3 Head-on impacts, different energies.....	202
4-A4 Slow, oblique impacts.....	203
4-A5 Slow, oblique, iron impactors.....	204
4-A6 Oblique differentiated impactors	205
4-A7 Highly oblique impacts.....	206
4-A8 Fast impacts.....	207
5-1 Contextual map of the eastern Sahara	216
5-2 Calcite structures at the study sites.....	219
5-3 Calcite matrix composition.....	221

LIST OF TABLES

3-1 Tillotson equation of state properties	35
3-2 Simulated impact conditions	40
3-3 Resolution comparisons summary	97
4-1 Summary of simulated impact conditions	121
4-2 Crater size scaling for shallow impacts	143
4-3 Summary of scaling relations	172
4-4 Resolution effects summary	193

CHAPTER 1

INTRODUCTION

A single look at Mars, and the sizeable scars of its past are evident: the planet had a violent infancy.

The Solar System started out as a cloud of gas, but with time the gas became dust, then dust bunnies, then kilometer-sized objects and larger. In the final stages, the planetesimals – objects a few thousand kilometers across – completed the accretional dance by coalescing with each other into the planets we observe today. These last, violent stages of planet formation left behind planetary-sized scars: impact craters thousands and tens of thousands of kilometers across. Such craters are observed on most Solar System objects with a solid surface: Mercury with its Caloris Basin, South Pole–Aitken Basin on the Moon, Hellas Basin on Mars, and Herschel Crater on Saturn’s moon Mimas, to name a few. The geophysical consequences of these impacts determine the features we see today. And understanding these impact processes provides insight into their thermal and geochemical consequences for the young planet.

This thesis focuses on the geophysical and morphological consequences of planetary-scale impacts into Mars. We ask: How do planetary-scale impacts differ from small impacts? What remnant surface features are expected to form? Is the planet resurfaced? How much melt is produced and is a magma ocean present? Can we determine the impact conditions required to form an observed crater and what are its implications for the evolution of the planetary surface?

We approach the study of planetary-scale impacts through numerical, three-dimensional simulations using a smoothed particle hydrodynamics (SPH) model. Simulating the entire planet captures the finite-size effects of this size regime: the surface curvature of the target, the radial gravity, and the large relative size of the impactor to the target. In the SPH model, material is represented by particles, allowing us to track the fate of impactor and target material by recording their locations and physical properties. We explore impact energies over two orders of magnitude (1.98×10^{27} to 5.89×10^{29} J), impact velocities of 6 to 50 km/s, impact angles from 0° (head-on) to the highly-oblique 75° (Chapter 3, 4), and a range of single-composition and differentiated impactors (Chapter 4). In all cases the impacts penetrate through, and remove, the surrounding crust, forming a crater cavity. The resulting crater cavities are about 2,000 to 13,000 km across, equivalent to 9% to more than half (61%) of Mars' circumference.

We find that for the lowest impact energies simulated here, the resulting crater features are generally similar to what would be expected for small impacts: a rim is formed around the crater cavity, little of the surface is covered by melt, and the crater ellipticity is low even for the most oblique impacts simulated. In addition, the impactor does not penetrate deeply into the mantle, and the total amount of material ejected to space is small.

For higher impact energies, the crater morphology changes. A rim-like structure is no longer formed, but instead the excavated material is distributed more evenly over the entire planetary surface. This is aided by the curvature of the planet, which effectively increases the flight distance with respect to a flat surface.

With increasing impact energy, the amount of melt produced also increases, as expected. However, the highly heterogeneous distribution of that melt – partitioned between

the mantle, the planetary surface, and ejected to space – is dependent on the impact conditions. Thus even though energetic impacts produce melt amounts equivalent to up to a 200 km thick layer over the Martian surface, in most cases less than 50% of the surface is covered by the melt. Of all simulated impacts, only the highest energy, head-on, and most massive (slow) impacts result in sufficiently widespread surface melt cover to suggest complete surface resetting by a global magma ocean and no preservation of the impact feature. From our simulations it appears that at least some of the planetary surface is preserved, even when the impact produces very large melt amounts.

The simulated impactors penetrate deeply into the planet: the largest and denser impactors can penetrate into the core. However, no mixing with the core material is observed. The deep penetration into the planet suggests that much of the impact energy is released deep in the planet. The impact induces significant planetary oscillations, of order tens to a few hundred kilometers, further modifying the crust.

In addition to the main crater cavity that is excavated around the impact location, energetic ($> 10^{29}$ J), fast (> 6 km/s), and low angle ($\leq 45^\circ$) impacts initiate shockwaves of sufficient strength to excavate crustal material at the planetary antipode of the impact point. The excavation of the crust is accompanied by melting of the local material. For the range of simulated conditions, antipodal cavities up to 4,800 km in diameter are formed.

The most massive impactors in our simulations (impactor to planet mass ratio of $\sim 5\%$) can contribute sufficient angular momentum to set Mars' rotational period to less than a day (0.6 days). The transfer of angular momentum is most efficient for denser impactors, striking the target at low velocities and at intermediate angles ($\sim 45^\circ$). These impact velocities and angles are the impact conditions expected at the end of accretion,

suggesting that late accretionary impacts are likely to have significantly altered the rotational state of the planets.

We find that most impacts in our simulated range result in orbiting and escaping material, where the latter is commonly about 10 times larger. Both quantities increase with impact energy. The placement of material into orbit suggests that moons generated through large impacts should be common. In examining the net effect of the impact on the mass of the planet, we find that for slow impacts much of the impactor accretes onto the planet, resulting in a net accretionary event. However, for impact velocities higher than about 3 times the mutual planet-impactor escape velocity (~ 18 km/s), the mass ejected to space is greater than the impactor mass, thus resulting in a net erosional event. Taking these effects into account may be important for improving the fidelity of planetary accretion models.

Looking at the surface of Mars, the largest confirmed planetary-scale crater is Hellas Basin, in the southern hemisphere. However, the most notable possible planetary-scale feature is the Mars hemispheric dichotomy. The dichotomy is the difference in crustal thickness (~ 30 km), elevation (~ 4 km), and surface age between the Northern Lowlands and Southern Highlands: the thin-crusted and lower-lying Lowlands that may be the remnants of a planetary-scale impact basin. But could a $\sim 10,000$ km, elliptical, rimless impact basin be produced and retained?

Covering the large parameter space noted above, we are able to explore whether a single impact could produce the observed Lowland features on Mars (Chapter 2). We find that the dichotomy can be formed by a single impact. The required impactor size and its orbital characteristics are similar to the objects expected to have been in Mars' vicinity at the end of accretion. In addition, the target's post-impact rotational period is about a day

(depending on the impactor composition), similar to Mars' current 1.03 day period. We find that the required impact conditions are an impact energy of about 3×10^{29} J, an impact velocity of 6–10 km/s, and an impact angle of 30–60°. Varying the impactor composition and characteristics does not significantly change the range of impact conditions required to reproduce the observed Lowlands basin characteristics.

In short, planetary-scale impacts have a traumatizing effect on the planet; however, in most cases at least part of the surface is preserved to attest to the occurrence of the impact.

While our work focuses on impacts into a Mars-like planet, this thesis represents an initial study into the implications of planetary-scale impacts. Further work into the importance of target properties will significantly contribute to our understanding of the toddler years of the terrestrial planets.

The last chapter of this thesis addresses the climate implications of reef-like carbonate structures that were discovered in the hyper-arid core of the Sahara, in southwestern Egypt (Chapter 5). The Sahara is currently the second largest desert on Earth, after Antarctica, but extensive rock art in the area depicts scenes of abundant animals, as well as putative images of swimmers; studies of the rock art have assumed that the animals and scenes depicted on the walls represent real activities in the lives of the painters. Geochemical evidence in the area indicates a wetter climate about 10,500 to 5,000 years ago. But how much wetter was it? Was the precipitation sufficient to support grasslands, human habitation, and the herds of cattle portrayed in the ubiquitous petroglyphs?

Carbonates can be used as climate indicators to address these questions, as their formation requires the presence of liquid water.

The discovery of reef-like carbonate deposits in a valley in the mountainous Gebel Uweinat region of the Sahara, near the triple border of Egypt, Sudan, and Libya (N22°, E25°), has provided insight into the area's paleoclimate. In addition to requiring water to form, their reef-like – or “bathtub ring” – structure along the valley wall requires the presence of long-term standing water. This in turn suggests a climate with increased and persistent precipitation, rather than rare torrential rain events.

Despite the formation of the carbonates in standing water, the dense incorporation of sand into their structure implies that the surroundings were not densely vegetated but instead that windblown sand was ubiquitous. This has important implications for the interpretation of the numerous local cow petroglyphs, which have been interpreted as a close link between past human habitation and cattle herding. However, if grasslands were not widespread, the petroglyphs could instead suggest that cows were revered as rare commodities.

Interestingly, the reef-like structures at Gebel Uweinat are morphologically similar to carbonates found on the other side of the Earth: in Pavilion Lake, British Columbia, Canada. If these Pavilion Lake structures, which appear to still be actively forming, can be used as a proxy, then the valley at Gebel Uweinat would have contained water for thousands of years.

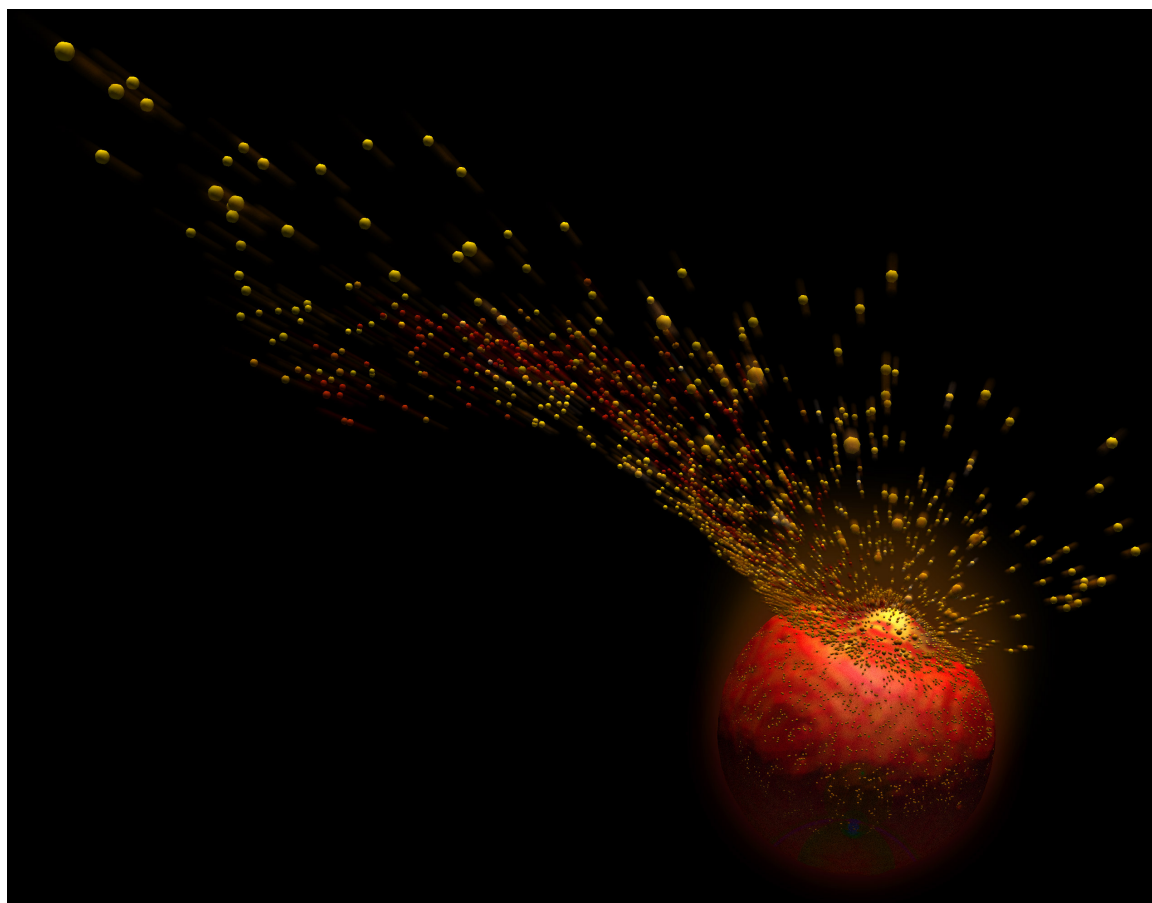
The presence of persistent pools of water relates to drawings in the Cave of the Swimmers made popular by the movie *The English Patient*. Questions have been raised as to whether the drawings represent people who are swimming or in a trance state. The

proximity of the Cave and the putative pools of water at Gebel Uweinat suggests that these drawings may in fact represent swimming.

The discovered carbonate structures have implications for understanding the Sahara's past, and through their study we may advance our ability to use carbonates as paleoclimate indicators both on Earth and possibly on other planets.

CHAPTER 2

MEGA-IMPACT FORMATION OF THE MARS HEMISPHERIC DICHOTOMY



This chapter has been published in its entirety under the same title by authors M.M. Marinova, O. Aharonson, and E. Asphaug (2008) in *Nature* 453, 1216–1219.

2.1 *Abstract*

The Mars hemispheric dichotomy is expressed as a dramatic difference in elevation, crustal thickness and crater density between the southern highlands and northern lowlands (which cover 42% of the surface)^{1,2}. Despite the prominence of the dichotomy, its origin has remained enigmatic and models for its formation largely untested^{3–5}. Endogenic degree-1 convection models with north–south asymmetry are incomplete in that they are restricted to simulating only mantle dynamics and they neglect crustal evolution, whereas exogenic multiple impact events are statistically unlikely to concentrate in one hemisphere⁶. A single mega-impact of the requisite size has not previously been modelled. However, it has been hypothesized that such an event could obliterate the evidence of its occurrence by completely covering the surface with melt⁷ or catastrophically disrupting the planet^{3,8}. Here we present a set of single-impact initial conditions by which a large impactor can produce features consistent with the observed dichotomy’s crustal structure and persistence. Using three-dimensional hydrodynamic simulations, large variations are predicted in post-impact states depending on impact energy, velocity and, importantly, impact angle, with trends more pronounced or unseen in commonly studied smaller impacts⁹. For impact energies of $\sim(3–6) \times 10^{29}$ J, at low impact velocities ($6–10 \text{ km s}^{-1}$) and oblique impact angles ($30–60^\circ$), the resulting crustal removal boundary is similar in size and ellipticity to the observed characteristics of the lowlands basin. Under these conditions, the melt distribution is largely contained within the area of impact and thus does not erase the evidence of the impact’s occurrence. The antiquity of the dichotomy¹⁰ is consistent with the contemporaneous presence of

impactors of diameter 1,600–2,700 km in Mars-crossing orbits³, and the impact angle is consistent with the expected distribution¹¹.

2.2 Introduction

The martian dichotomy may be defined by topographical, morphological and structural characteristics. Isostatic modelling combining gravity and topography have provided a description of global crustal thickness in which the northern lowlands are distinguished from the southern highlands by a reduction in crustal thickness of ~30 km (ref. 1). By accounting for lithospheric stresses, it is possible to compute the effects of overlying loads, in particular of the largest load represented by the Tharsis province. When the loads are separated, the lowlands are remarkably well described by an ellipse with dimensions ~10,650 km x ~8,520 km (ellipticity ,1.25) (ref. 2). The boundary is expressed as steep scarps in some longitudes and as gentle slopes in others^{3,12,13}; significant crustal thickening is not observed at the boundary. Geochemical evidence and surface-crater densities show that the dichotomy formed within the first 50 Myr of Solar System formation, with little mantle-crust remixing since^{1,10,14}. Subsequent events, such as known impact-basin formation, have modified the dichotomy boundary.

The mega-impact formation hypothesis is supported by geologic evidence including massifs and narrow plateaux concentric to the dichotomy boundary³, steep scarps at the boundary, and by the similarity of the lowlands to other large impact basins such as South Pole–Aitken basin on the Moon, Caloris basin on Mercury and Hellas basin on Mars. The impact hypothesis has previously been challenged by several arguments. First, by the expectation that at the relevant energy, the impact would disrupt

the planet sufficiently to effectively erase evidence of the event³. Second, by the circularity of craters for all but the most oblique angles for smaller impacts¹⁵. Third, by the lack of crustal thickening in an annulus around the basin, typical for smaller impacts. However, craters resulting from planetary-scale impacts have until now not been accurately modelled. This class of impacts is distinguished from the more thoroughly studied smaller impacts, which effectively form in a half-space target, in part because of the importance of surface curvature in the larger size regime and the larger fractional size of the projectile relative to the target.

2.3 Results

Single, planetary-scale impact events are simulated using a three-dimensional self-gravitating smoothed particle hydrodynamics (SPH) code^{16–18}. Our simulations sample a large parameter space, with impact energies of $(0.1–5.9) \times 10^{29}$ J, which is representative of, according to traditional scaling laws^{3,9}, nominal impact crater diameters of 4,000–12,000 km. For comparison, the energy of the Moon-forming impact¹⁸ was $\sim 10^{31}$ J. For each impact energy, we consider impact velocities of 6–50 km s⁻¹, ranging from near escape velocity to twice Mars’s orbital velocity, and impact angles of 0 (head-on), 15, 30, 45, 60 and 75° for each velocity (Supplementary Information). For this parameter space, impactor diameters range from 400 to 2,700 km. Figure 2-1 schematically shows a summary of the results and the ‘sweet spot’ simulations that produce a crustal excavation feature remarkably similar to the lowlands.

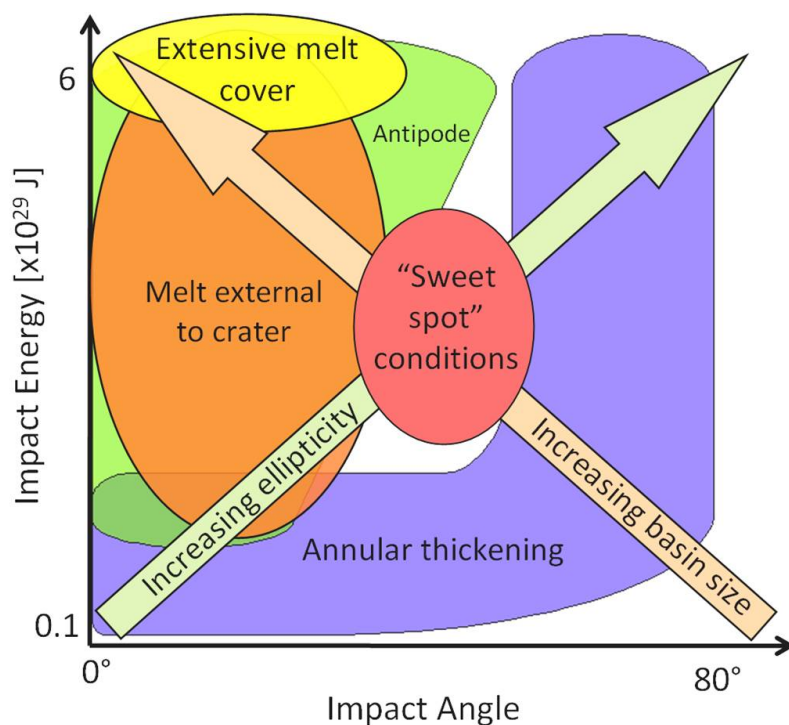


Figure 2-1 Schematic summary of simulation results. Shown are the impact characteristics resulting in extensive surface melt cover (> 25% of the surface), significant melt outside the crustal excavation boundary, presence of antipodal crustal disruption, presence of a thickened annulus of crust around the crustal excavation boundary, and the directions of increase in ellipticity and basin size. The results at a given energy are averaged over impact velocity. A ‘sweet spot’ of impact conditions emerges for which the resulting simulation characteristics closely match the observed Mars dichotomy features². A compatible hypothesis is found at an impact energy of $\sim 3 \times 10^{29}$ J, velocity ~ 6 km s⁻¹ and, importantly, an impact angle of $\sim 45^\circ$. These parameters represent probable impact conditions in the early Solar System^{3,11}.

The pre-impact resolution (particle size or smoothing length) is 118 km for $N = 200,000$ particles. The model uses the semi-empirical Tillotson equation of state¹⁹ (EOS). We derived EOS parameters to approximate the behaviour of olivine, to match the planet’s pressure-density profile. The olivine EOS results in a realistic early Mars internal energy–pressure profile, allowing calculation of post-impact melt using the pressure-dependent forsterite liquidus curve as an internal energy melting threshold²⁰. The pre-impact planet has no initial spin: Mars’s current rotational period is long compared with the timescale of the impact process. The crust is defined as the planet’s pre-impact

outermost particle layer, resulting in a crustal thickness of ~ 140 km, compared with recent estimates of 5–90 km (ref. 1). Because of the large particle size, the simulations cannot directly resolve the crustal thickness. However, the region of complete crustal removal may be mapped and the boundary of the crustal anomaly is expressed over a lateral distance of only several resolution elements. Thus the computed crustal excavation boundary size is a robust result. In addition to this boundary, we consider the integrated amount and spatial distribution of melt, crustal thickening and the extent of antipodal disruption.

The distribution of crust and surface melt are calculated as a fraction of the material within the top 150 km. An ellipse is fitted to the crustal excavation boundary (the contour of 50% crustal fraction) in polar coordinates, with the origin centred on the excavated region. Our analysis of the impact melt and its distribution shows that previous assumptions about melting during planetary-scale cratering events have been oversimplified.

In contrast to smaller, half-space craters, whose size and melt production dominantly scale with the impact energy²¹, for planetary-scale impacts we find that impact velocity and impact angle fundamentally affect the crustal excavation boundary, its ellipticity, and the amount and distribution of melt. In particular, we identify possible impacts that are consistent with the crustal distribution of Mars.

Planetary-scale impacts penetrate into the mantle. The resulting rarefaction wave completely removes the surrounding crust, which re-impacts elsewhere on the planet or is ejected to space. The size of the crustal excavation boundary is representative of the size of the crustal thickness dichotomy that is likely to remain, neglecting later geologic crater

modification. Simulation results show that the crustal excavation boundary size increases with increasing impact energy. For a given impact energy, the boundary size decreases with increasing velocity and with increasingly oblique impacts (Figures 2-2 and 2-3a). For smaller, half-space impact craters, a deviation in circularity is only present for highly oblique impacts^{9,15} ($> 80^\circ$). In contrast, our planetary-scale impact simulations show that with increasing impact energy, the removed crustal region becomes significantly elongated at relatively shallow angles (Figure 2-3b).

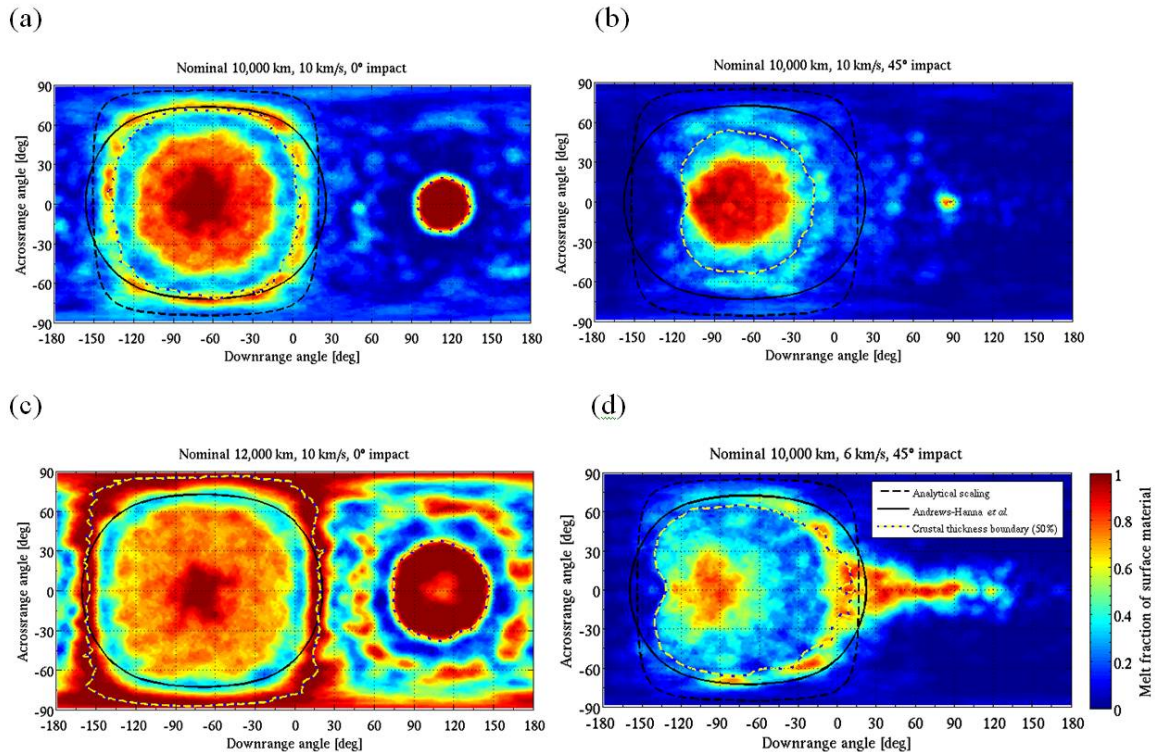


Figure 2-2 Surface melt distribution. Change in melt distribution and crustal removal boundary with impact characteristics. Crustal excavation boundary, nominal crater size, and a fit by Andrews-Hanna *et al.*² to the dichotomy boundary are overlaid. The melt distribution is computed at a 2° resolution and smoothed over a 10° diameter cap area. The surface melt cover fraction is 25%, 8%, 71%, and 12% respectively. Note the changes in features with impact energy (nominal crater size), velocity, and angle. The planet has been rotated to center the excavation boundary at about -60° downrange angle.

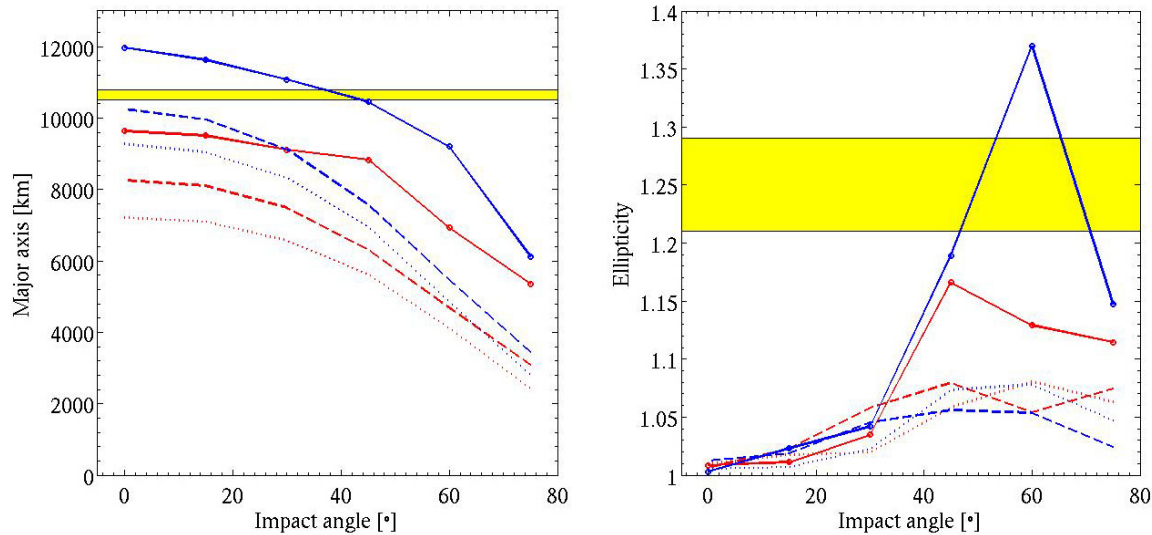


Figure 2-3 Crater sizes and ellipticities. Major axis (a) and ellipticity (b) for impact energies of 3.1 and 5.9×10^{29} J (red and blue, respectively). Shown are impact velocities of 6 km/s (solid line), 10 km/s (dashed line), and 50 km/s (dotted line). The filled region is the acceptable range of values according to the observed crustal geometry². A “sweet spot” emerges for these impact energies and at impact velocities of 6–10 km/s and impact angles of 30–60°.

The pattern of crustal redistribution depends upon impact angle. Although angles above $\sim 60^\circ$ result in a distinct rim-like feature, less oblique impacts ($< 45^\circ$) produce widespread crustal thickening but no short length-scale variations, in agreement with dichotomy characteristics (Figure 2-4; contrast with Supplementary Information). In cases with high ejection velocity, the flight path of ejected material is of the order of the radius of the planet; thus the ejected material is distributed globally.

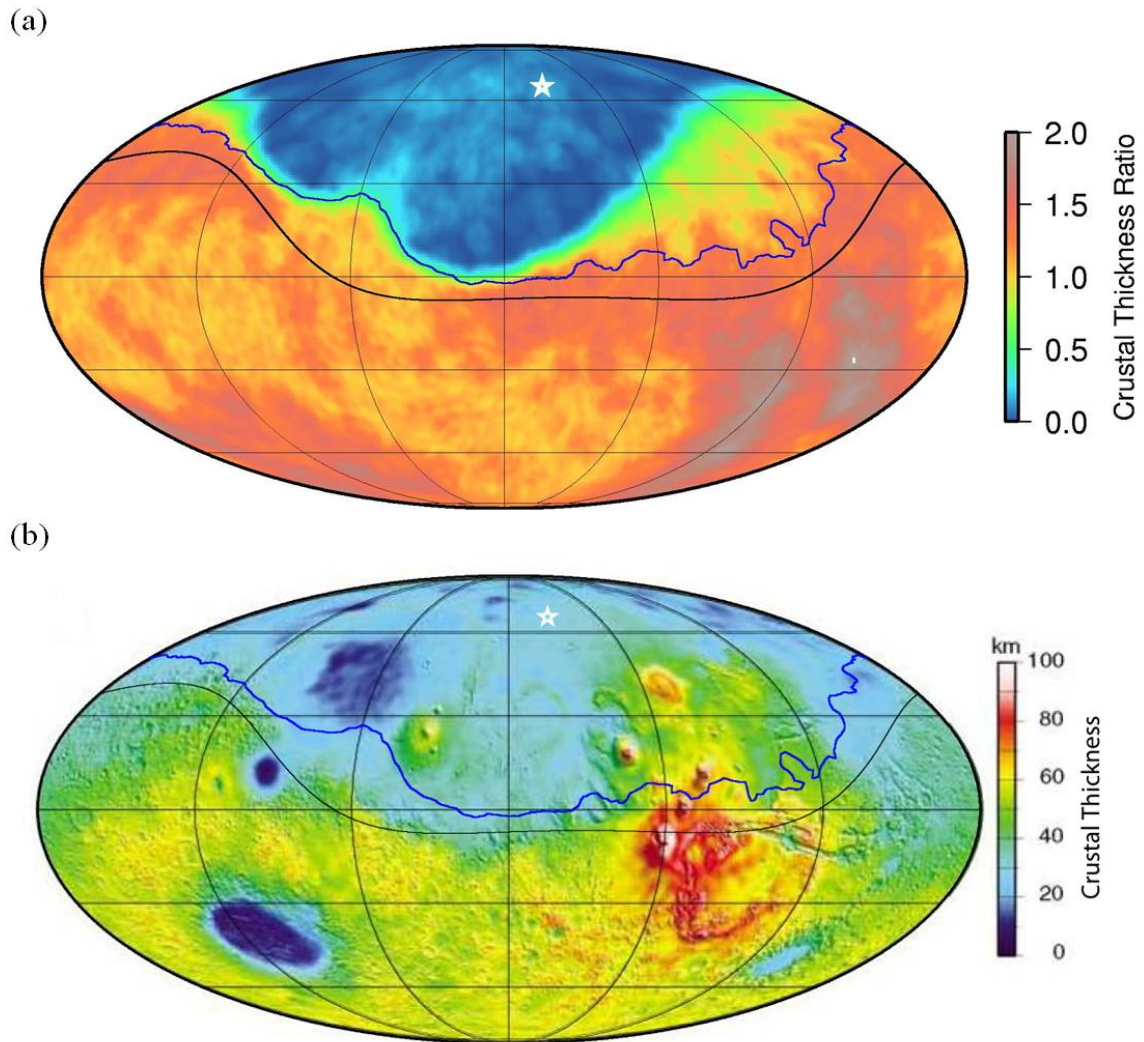


Figure 2-4 A favored impact scenario compared to Mars' crustal thickness. Post- to pre-impact simulation crustal thickness ratio (a), and model thicknesses (based on gravity and topography¹⁰, revised by Neumann *et al.*, in prep.) (b). Superimposed are the Andrews-Hanna *et al.* dichotomy boundary² (black line) and the crustal excavation boundary from the simulation results (blue line). Impact simulation characteristics: 3.1×10^{29} J (nominal 10,000 km crater), 6 km/s, 45° , impactor diameter 2,230 km. Crustal excavation boundary center² (star) shown at 66°N , 206°E . In (a) the crustal thickness is computed at a 2° resolution and smoothed over a 10° diameter cap area.

Melt production and distribution are also strongly dependent on impact energy, velocity and angle. The total amount of melt increases with increasing impact energy, and at constant energy and low impact angles exhibits a weak maximum at intermediate velocities ($10\text{--}20 \text{ km s}^{-1}$). Melt significantly decreases with increasing impact angle. As

an example, for a nominal 10,000-km crater, head-on (0°) impacts produce a Mars global equivalent layer (GEL) melt depth of 60–80 km (depending on impact velocity), whereas 75° impacts produce a GEL melt depth of only 6–20 km. The vaporized mass is less than 1% of the molten mass.

Global melt depths of tens of kilometres have been argued to be sufficient to erase the signature of the dichotomy⁷; however, GEL depths do not represent the highly heterogeneous distribution of melt. The distribution varies with impact characteristics. For all but the highest energies (nominal crater size $\leq 10,000$ km), melt is largely contained within the crustal excavation boundary and extends to depth (Figures 2-1, 2-2). Depending on impact angle, 50–70% of the melt resides inside the excavation boundary, 25–30% is deposited outside the boundary and the remainder is ejected from the planet. Most redeposited material is of crustal composition and results in a thickening of up to ~60% compared with the original crustal thickness.

In areas where crust is removed and the mantle melts, fresh crust that crystallizes is likely to leave a difference in crustal thickness. The amount of mantle melt, and hence the thickness of the new crustal layer, is dependent on impact conditions.

For highly energetic and fast impacts, the shock wave produced is sufficiently strong to induce antipodal effects including crustal removal and melting. These are inconsistent with the lack of observed topographic, gravitational or magnetic anomalies antipodal to the proposed impact location. Thus we only consider viable simulations that produce antipodal features smaller than 10° in diameter.

We consider the effect of numerical resolution on the simulation results. The resolution and fidelity of post-impact crustal features in these simulations is higher than

that of previous three-dimensional SPH studies. For simulations with a particle smoothing length of 150 km, the basin major axis, ellipticity, antipode size and melt cover differ from the nominal 118-km resolution simulations by an average of -8% , -1% , -28% and -16% , respectively, for nominal 10,000- and 12,000-km craters. Thus the qualitative conclusions are robust.

2.4 Conclusions

Combining the crust and melt distribution results, we find a ‘sweet spot’ in parameter space, where the simulations show striking similarity to the observed Mars dichotomy features (Figures 2-1, 2-3 and 2-4). Importantly, this range represents impact conditions that are probable in light of the age of the dichotomy¹⁰ and probability distribution of the impact angle^{11,22}. This parameter space ‘sweet spot’ is at impact energies of $\sim(3-6) \times 10^{29}$ J, impact angles of $30-60^\circ$ and impact velocities of $6-10 \text{ km s}^{-1}$, which imply impactor diameters of 1,600–2,700 km. These favoured simulation conditions encompass the range of uncertainty in the geometry of the observed crustal anomaly. The early age of the dichotomy is consistent with the expected timing of the influx of large impactors. These objects are also expected to have similar orbital velocities²³, resulting in impacts at or slightly above Mars’s escape velocity ($\geq 5 \text{ km s}^{-1}$). The most likely impact angle¹¹ is 45° .

Results from the large parameter space explored by the simulations provide new insights pertinent to global-scale impact processes thought to prevail in the early Solar System. Our simulations provide quantitative constraints for the previously only hypothesized extent of surface melting, planetary disruption and crustal removal as a

function of impact energy and geometric characteristics. The predicted melt distribution over the surface may provide a heterogeneous geochemical signature observable by future Mars missions.

2.5 *Methods*

SPH is a lagrangian method in which matter is represented by point masses smoothed over a particle radius (smoothing length), with density and internal energy computed according to kernel-weighted summation and by the conservation of mass, momentum and energy¹⁶. Pressure, as a function of internal energy and density, is computed with the Tillotson EOS, and pressure gradients and self-gravitating forces accelerate the particles. Our simulations conserve energy and angular momentum to better than 1 part in 2,000. Simulations are run for 26 h of model time, after which the r.m.s. particle velocity does not appreciably oscillate. We assume an olivine composition of Fo₇₅Fa₂₅ (ref. 24). Density ($\rho_0 = 3,500 \text{ kg m}^{-3}$) (ref. 25), bulk modulus ($K = 131 \text{ GPa}$) (ref. 26), heat capacity²⁶ and heat of vaporization ($H_{vap} = 10.013 \text{ MJ kg}^{-1}$) (ref. 27) are measured material values; the nonlinear Tillotson compressive term (B) and two of the Tillotson EOS fitting parameters (b , U_0) are set to the average of those published for basalt, granite, anorthosite low- and high-pressure phases, and andesite ($B = 49 \text{ GPa}$, $b = 1.4$, $U_0 = 550 \text{ MJ kg}^{-1}$); b varies by only 8%. The remaining Tillotson EOS fitting parameters are identical for all given rocky materials ($a = 0.5$, $\alpha = 5$, $\beta = 5$). The olivine Hugoniot internal energy curve is on average 15% lower and 11% higher than the experimentally determined pure forsterite and fayalite curves, respectively, for 0–200 GPa. Using a forsterite EOS with Tillotson parameters fitted to the experimental curve

results, on average, in 8% more melt (impacts of 8,000–12,000 km) and similar melt distribution. Both the mantle and crust are composed of olivine because a single-particle basalt layer would be numerically unresolved. The core is composed of iron and the impactor of basalt. The SPH code was modified to initialize with randomly distributed particles of prescribed composition, internal energy, pressure and mass as a function of radial position. Transient oscillations are damped during a relaxation period run. The initial internal energy-pressure profile is set to that of hydrostatic equilibrium, whereas the surface and core-mantle boundary temperatures are set to those of parameterized convection models of Mars²⁸. The internal energy–pressure–density profile is computed assuming adiabatic compression into the planet (core radius 1,600 km, central pressure 50 GPa, compatible with models^{29,30}). The crustal excavation boundary size is a robust result: for a nominal 10,000-km crater, fitting the 20% and 80% crustal-fraction contours changes the boundary size by 29% and 12%, respectively.

2.6 Bibliography

1. Zuber, M. T. The crust and mantle of Mars. *Nature* 412, 220–227 (2001).
2. Andrews-Hanna, J. C., Zuber, M. T. & Banerdt, W. B. The Borealis basin and the origin of the martian crustal dichotomy. *Nature* doi:10.1038/nature07011 (this issue).
3. Wilhelms, D. E. & Squyres, S. W. The martian hemispheric dichotomy may be due to a giant impact. *Nature* 309, 138–140 (1984).
4. Zhong, S. J. & Zuber, M. T. Degree-1 mantle convection and the crustal dichotomy on Mars. *Earth Planet. Sci. Lett.* 189, 75–84 (2001).

5. Frey, H. & Schultz, R. A. Large impact basins and the mega-impact origin for the crustal dichotomy on Mars. *Geophys. Res. Lett.* 15, 229–232 (1988).
6. McGill, G. E. & Squyres, S. W. Origin of the martian crustal dichotomy – evaluating hypotheses. *Icarus* 93, 386–393 (1991).
7. Hart, S. H., Nimmo, F., Korycansky, D. & Agnor, C. Probing the giant impact hypothesis of the martian crustal dichotomy. *Proc. 7th Int. Conf. Mars* abstr. 3332 (2007).
8. Nimmo, F. & Tanaka, K. Early crustal evolution of Mars. *Annu. Rev. Earth Planet. Sci.* 33, 133–161 (2005).
9. Melosh, H. J. *Impact Cratering: A Geologic Process* (Oxford Univ. Press, New York, 1989).
10. Solomon, S. C. et al. New perspectives on ancient Mars. *Science* 307, 1214–1220 (2005).
11. Shoemaker, E. M. in *Physics and Astronomy of the Moon* (ed. Kopal, Z.) 283–359 (Academic Press, New York, 1962).
12. Smith, D. E. et al. The global topography of Mars and implications for surface evolution. *Science* 284, 1495–1503 (1999).
13. Aharonson, O., Zuber, M. T. & Rothman, D. H. Statistics of Mars' topography from the Mars Orbiter Laser Altimeter: slopes, correlations, and physical models. *J. Geophys. Res.* 106 (E10), 23723–23735 (2001).
14. Frey, H. V. et al. Ancient lowlands on Mars. *Geophys. Res. Lett.* 29, doi:10.1029/2001GL013832 (2002).

15. Gault, D. E. & Wedekind, J. A. Experimental impact craters formed in water –gravity scaling realized. *Trans. Am. Geophys. Union* 59, 1121 (1978).
16. Benz, W. in Proc. *NATO Adv. Res. Worksh. Numer. Modell. Nonlin. Stellar Puls.* (ed. Buchler, J. R.) 1–54 (Kluwer Academic, Boston, 1990).
17. Benz, W., Slattery, W. L. & Cameron, A. G. W. The origin of the Moon and the single-impact hypothesis. 1. *Icarus* 66, 515–535 (1986).
18. Canup, R. M. & Asphaug, E. Origin of the Moon in a giant impact near the end of the Earth's formation. *Nature* 412, 708–712 (2001).
19. Tillotson, J. H. *Metallic Equations of State for Hypervelocity Impact*. Report No. GA-3216, July 18 (General Atomic, San Diego, California, 1962).
20. Asimow, P. D. Magmatism and the evolution of the Earth's interior, in *Goldschmidt Conference Abstracts*, A40 (<http://www.goldschmidt2007.org>) (2007).
21. Cintala, M. J. & Grieve, R. A. Scaling impact melting and crater dimensions: implications for the lunar cratering record. *Meteorit. Planet. Sci.* 33, 889–912 (1998).
22. Gilbert, G. K. The Moon's face, a study of the origin of its features. *Bull. Phil. Soc. Wash.* 12, 241–292 (1893).
23. Canup, R. M. & Agnor, C. B. in *Origin of the Earth and Moon* (eds. Canup, R. M. & Righter, K.) 113–129 (Univ. Arizona Press, Tucson, Arizona, 2000).
24. Sanloup, C., Jambon, A. & Gillet, P. A simple chondritic model of Mars. *Phys. Earth Planet. Inter.* 112, 43–54 (1999).
25. Klein, C. *The Manual of Mineral Science* 22nd edn, 491–495 (Wiley, New York, 2002).

26. Anderson, D. L. & Isaak, D. G. in *Mineral Physics and Crystallography: A Handbook of Physical Constants* (ed. Ahrens, T. J.) 64–97 (American Geophysical Union, Washington DC, 1995).
27. Hashimoto, A. Evaporation metamorphism in the early solar nebula – evaporation experiments on the melt FeO-MgO-SiO₂-CaO-Al₂O₃ and chemical fractionations of primitive materials. *Geochem. J.* 17, 111–145 (1983).
28. Hauck, S. A. & Phillips, R. J. Thermal and crustal evolution of Mars. *J. Geophys. Res.* 107 (E7), doi:10.1029/2001JE001801 (2002).
29. Yoder, C. F. et al. Fluid core size of Mars from detection of the solar tide. *Science* 300, 299–303 (2003).
30. Bertka, C. M. & Fei, Y. W. Density profile of an SNC model martian interior and the moment-of-inertia factor of Mars. *Earth Planet. Sci. Lett.* 157, 79–88 (1998).

2.7 Acknowledgements

We thank Francis Nimmo, Maria Zuber, Jeffrey Andrews-Hanna and Robin Canup for discussions, Jay Melosh and an anonymous reviewer for their comments, and Steve Squyres for suggesting the problem and the approach more than a decade ago. This work was supported by the Henshaw Fellowship, NSERC, and CSA.

Author Information Reprints and permissions information is available at npg.nature.com/reprintsandpermissions. Correspondence and requests for materials should be addressed to M.M.M (mmm@caltech.edu).

2.8 Supplementary information

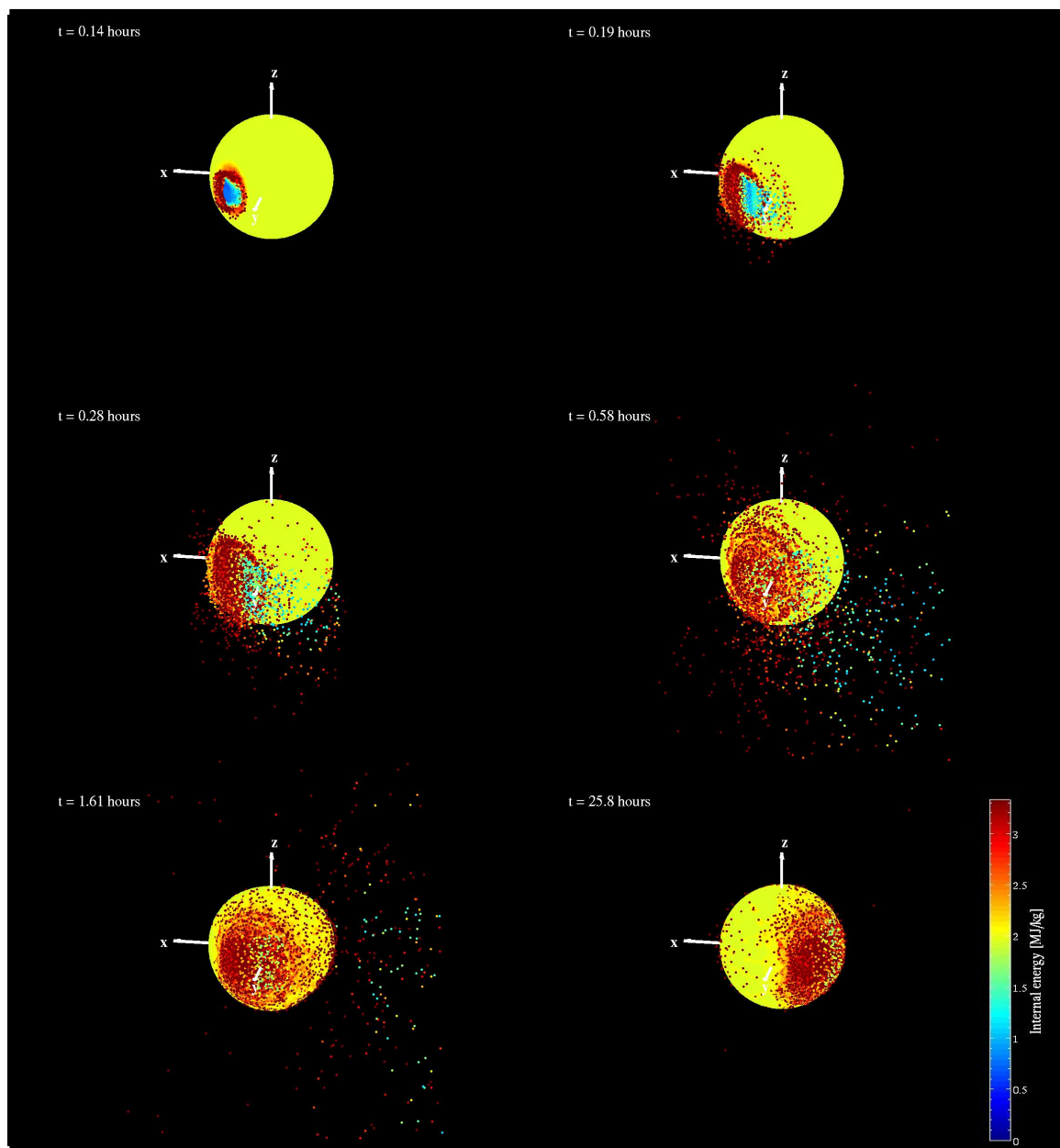


Figure 2-A1. Six simulation timesteps for a 1.45×10^{29} J impact (nominal 8,000 km crater), at 10 km/s and 45° angle. Color represents internal energy of particles. The rotation of the planet is due to the angular momentum imparted by the impactor. The stress wave from the impact requires about 0.06 hrs to travel through the impactor itself, resulting in the unheated impactor material seen in early timesteps. Note the geographical concentration of molten material at the impact site.

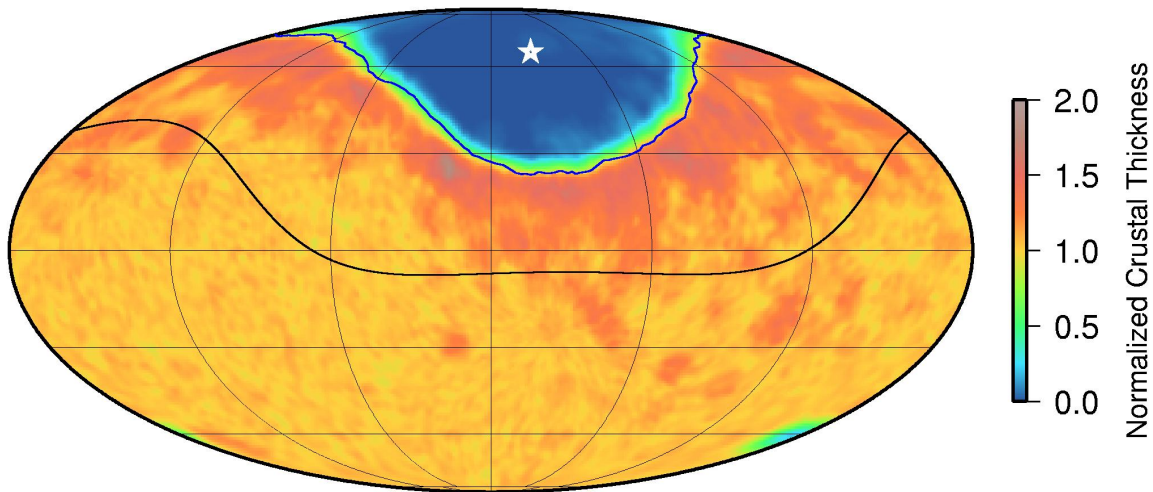


Figure 2-A2. Impact conditions resulting in a rim-like concentration of crustal material surrounding the crustal excavation boundary: 12,000 km nominal crater size, 20 km/s, 60° impact. The presence of a distinct rim-like feature for these impact conditions is in contrast to the more uniform crustal thickening resulting from similarly energetic, but slower, less oblique impacts, and is in contrast to the absence of a rim-like feature in Mars' crustal thickness (Neumann *et al.* manuscript in preparation, model available at <ftp://ltpftp.gsfc.nasa.gov/projects/tharsis/marscrust3/>).

CHAPTER 3

**GEOPHYSICAL CONSEQUENCES OF PLANETARY-SCALE
IMPACTS INTO A MARS-LIKE PLANET**

This chapter has been submitted in its entirety to *Icarus* under the same title by authors M.M. Marinova, O. Aharonson, and E. Apshaug.

3.1 Abstract

All planetary bodies with old surfaces exhibit planetary-scale impact craters: vast scars caused by the large impacts at the end of Solar System accretion or the late heavy bombardment. Here we investigate the geophysical consequences of planetary-scale impacts into a Mars-like planet, by simulating the events using a smoothed particle hydrodynamics (SPH) model. Our simulations probe impact energies over two orders of magnitude (2×10^{27} to 6×10^{29} J), impact velocities from the planet's escape velocity to twice Mars' orbital velocity (6 to 50 km/s), and impact angles from head-on to highly oblique (0° to 75°). The simulation results confirm that for planetary-scale impacts, surface curvature, radial gravity, the large relative size of the impactor to the planet, and the greater penetration of the impactor, contribute to significant differences in the geophysical expression compared to small craters, which can be effectively treated as acting in a half-space. The results show that the excavated crust cavity size and the total melt production scale similarly for both size regimes is a function of impact energy. However, in planetary-scale impacts a significant fraction of the melt is sequestered at depth and thus does not contribute to resetting the planetary surface; complete surface resetting is likely only in the most energetic (6×10^{29} J), slow, and head-on impacts simulated. A crater rim is not present for planetary-scale impacts with energies $> 10^{29}$ J and angles $\leq 45^\circ$, but rather the ejecta is more uniformly distributed over the planetary surface. Antipodal crustal removal and melting is present for energetic ($> 10^{29}$ J), fast (> 6 km/s), and low angle ($\leq 45^\circ$) impacts. The most massive impactors (with both high impact energy and low velocity) contribute sufficient angular momentum to increase the rotation rate of the Mars-sized target to about once per day. Impact velocities of > 20 km/s result in net mass erosion from the target, for all simulated energies and angles. The

hypothesized impact origin of planetary structures may be tested by the presence and distribution of the geochemically-distinct impactor material.

3.2 Introduction

Planetary-scale impacts are characterized by impact structures for which the crater diameter is of order the planetary circumference. In contrast, for small impacts the crater is sufficiently small that the planetary curvature can be ignored and the surface can be approximated as a flat plane. The planetary-scale size regime differs from small impacts due to the planetary surface curvature on the scale of the impact event, the radial gravity, and the relative large size of the impactor with respect to the target. The size transition from small impacts to planetary-scale impacts is not well understood. As a result of these differences, the characteristics and scaling relationships derived from small impacts, which have been extensively studied in-situ (e.g., Gault et al., 1975; Lana et al., 2003; Pike, 1980), experimentally (e.g., Colwell and Taylor, 1999; Gault and Wedekind, 1978; Hartmann, 1985; Hörz and Cintala, 1997), and numerically (e.g., Artemieva et al., 2004; Collins and Melosh, 2002; Pierazzo and Melosh, 2000b), may not be applicable in the planetary-scale size regime. The differences in geometry and thus the relative importance of physical processes for planetary-scale impacts are expected to change the resulting impact cavity characteristics. The planetary-scale size regime differs from the even larger mega-impact events – such as the Moon-forming event and protoplanet impacts – since mega impacts are sufficiently energetic to remove evidence of their occurrence by catastrophically disrupting the impacted planet or forming a global magma ocean, which resets the surface (e.g., Asphaug et al., 2006; Canup, 2004). The energy scale relevant for

the planetary-scale impacts is between half-space craters such as the much smaller K-T impact with a formation energy of $\sim 10^{23}$ J (Morgan et al., 1997), and the much more energetic impacts such as the Moon-forming impact with an impact energy of $\sim 10^{31}$ J (Canup and Asphaug, 2001) or impacts between similarly-sized bodies (Asphaug, 2010).

Planetary-scale impacts significantly affect the impacted body due to the large amount of energy and angular momentum (depending on impact angle) that is deposited, and the large-scale redistribution of material on the surface. The global effects of the impact require that the thermodynamic state of the planet be considered, in contrast to half-space impacts where crustal properties dominate. In planetary-scale impacts the impactor penetrates into the mantle and may reach the core, thus shockwave propagation and melting calculations require proper thermal and density profiles for the planetary interior. Planetary-scale impacts are expected to have primarily occurred at the end of accretion and during the late heavy bombardment, when large objects in planet-crossing orbits were ubiquitous (e.g., Agnor et al., 1999; Neukum et al., 2001; Wetherill, 1985). Accordingly, large craters are observed on most planetary bodies with old surfaces. Studying this cratering size regime will result in better understanding of early Solar System processes. Examples of planetary-scale craters in the inner Solar System include: Caloris Basin on Mercury (1,550 km diameter, 10% of planet's circumference; Murchie et al., 2008); South Pole–Aitken Basin on the Moon (2,500 km diameter, 23% of circumference; Spudis et al., 1994); Hellas Basin on Mars (2,000 km diameter, 9% of circumference; Wilhelms, 1973); and possibly the Northern Lowlands on Mars (10,600 by 8,500 km, $\sim 42\%$ of circumference; Andrews-Hanna et al., 2008; Marinova et al., 2008; Nimmo et al., 2008). Examples of this cratering size regime in the outer Solar

System include Herschel Crater on Mimas (135 km diameter, 11% of circumference; Moore et al., 1974), and Odysseus on Tethys (400 km diameter, 12% of circumference; Moore et al., 1974). While the planetary and impact characteristics of these bodies vary, they all represent large impacts where the surface curvature and radial gravity were important to the impact process.

Here we present results on the morphology and global consequences of planetary-scale impact simulations into a Mars-like planet. We compare how these impact results differ from the characteristics of small impacts. The simulations cover a large range of impact energies, angles, and velocities.

3.3 Modeling

We use a fully three-dimensional smoothed particle hydrodynamics (SPH) model to simulate planetary-scale impacts (Benz, 1990). SPH is a Lagrangian method in which matter is represented by point masses smoothed over a particle diameter (smoothing length), with density and internal energy computed according to kernel-weighted summation and by the conservation of mass, momentum, and energy. The kernel-weighted (bell-shaped) description of the particles in the simulations gives each particle a finite size while allowing for the particles to interact by overlapping. This results in smoothly varying density and pressure fields. Pressure gradients and self-gravitating forces accelerate the particles in our simulations. All simulated impacts are strictly in the gravity regime, with crater diameters two to three orders of magnitude larger than the transition from strength- to gravity- dominated processes; material strength in this regime is of minor importance and is therefore not simulated. This SPH gravity code has been

extensively used for simulating the Moon-forming impact (Canup and Asphaug, 2001) and other mega impacts (e.g., Asphaug et al., 2006). Our simulations typically use 200,000 particles. The pre-impact effective particle size, set by the smoothing length assigned to each particle, is uniform with a mean of $118 \text{ km} \pm 6 \text{ km}$. A consistent particle size at the beginning of the simulation is required for numerical stability and physically realistic interactions between the particles. Impactors are composed of basalt (mean particle mass = $2.7 \times 10^{18} \text{ kg}$), the planet's mantle is olivine (mean particle mass = $3.1 \times 10^{18} \text{ kg}$), and its core is iron (mean particle mass = $7.6 \times 10^{18} \text{ kg}$); the differences in particle masses are due to the constant particle size, but material-dependent density. Particle sizes change during the simulation in response to forces, adjusting the particle density to be suitable for the local pressure, internal energy, and equation of state. In all impacts the total energy is conserved to better than a part in 10^3 .

3.3.1 SPH modifications and improvements

We use the SPH model most recently implemented by Canup and Asphaug (2001) and Asphaug et al. (2006). We have modified the initial setup to decrease computational time and increase versatility of planet formation. Traditionally, objects in SPH are formed by placing particles with an assigned energy in a hexagonal close packing configuration followed by damped relaxation to the lowest energy state (e.g., Canup, 2004). To form a differentiated object, the proto-core and proto-mantle are formed, relaxed separately, and are then slowly impacted and again allowed to relax (“hot starts” in Canup, 2004). We have modified this setup by placing particles randomly within a sphere and assigning a pre-determined profile of internal energy and material composition with radius inside the

planet; the object is then relaxed to a lowest energy configuration. The assignment of material and internal energy properties is similar to the “warm starts” used by Canup (2004). This allows the formation of an intact planet with directly specified internal structure and pressure-density-internal energy profiles, thus increasing the versatility of the planet formation process. In addition, the computational time is greatly reduced. The damped relaxation proceeds for ~ 21 hrs of simulation time; at the end of the relaxation period, the planet’s root mean square particle velocity has remained less than 2 m/s for over 8 hrs. The final internal energy, density, and pressure profiles show good agreement with the calculated and desired profiles. The relaxed planet is used in all subsequent simulations.

Small objects are formed by placing particles in an equidistant configuration for numerical stability. Thus impactors are formed using the hexagonal close packing setup and their two halves are impacted at slow velocity and relaxed for ~ 20 hrs of simulation time. Impactors are given an initial energy of 0.1 MJ/kg, representing an uncompressed object heated to a temperature of ~ 120 K. This internal energy estimate is valid for smaller impactors which will rapidly cool to space, but may underestimate the internal energy of larger impactors. The same set of prepared impactors are used for all impact angles.

3.3.2 Equation of State

We use the semi-empirical Tillotson (1962) Equation of State (EOS), which has been employed extensively in SPH (e.g., Benz et al., 1986; 1987; 1989; Canup and Asphaug, 2001). Proper implementation of the initial conditions requires choosing

appropriate core and mantle materials. We chose iron for the core, as the available material in the Tillotson EOS library; neglecting the core's minor sulfur component is not expected to appreciably affect the results. The Tillotson EOS library did not include an olivine-like material; thus to match mantle density we derived parameters for an olivine EOS – $\text{Fo}_{75}\text{Fa}_{25}$ – which is representative of the Mars mantle composition (Sanloup et al., 1999). The equation of state parameters for $\text{Fo}_{75}\text{Fa}_{25}$ are determined by linear interpolation between forsterite and fayalite values, in the Tillotson EOS formulation. Values for density (Klein, 2002), bulk modulus (Anderson and Isaak, 1995), temperature-dependent heat capacity (Anderson and Isaak, 1995), heat of fusion (Navrotsky, 1995), and heat of vaporization (Hashimoto, 1983) were obtained from the literature; the non-linear Tillotson compressive term (B) and two of the Tillotson EOS fitting parameters (b , U_0) are set to the average of the values published for basalt, granite, anorthosite low-pressure phase and high-pressure phase, and andesite ($B = 49$ GPa, $b = 1.4$, $U_0 = 550$ MJ/kg); b varies by only 8% for all given rocky materials. The remaining Tillotson EOS fitting parameters are identical for all given rocky materials ($a = 0.5$, $\alpha = 5$, $\beta = 5$). Table 3-1 shows the parameters used for our olivine EOS, and the values for basalt, granite, and iron for comparison.

The temperature-averaged heat capacities for iron and basalt are used: 449 J/kg K (Lide, 1995) and 840 J/kg K (Navrotsky, 1995), respectively. The heat of fusion of iron is 247 kJ/kg (Lide, 1995) and for olivine is 718 kJ/kg (Navrotsky, 1995).

Table 3-1 Tillotson equation of state properties. Tillotson EOS values for granite, basalt, olivine, and iron. ρ_0 is the material density at zero pressure; K is the bulk modulus; B is the non-linear Tillotson compressive term; a , b , α , β , and U_0 are Tillotson EOS fitting parameters; E_s is the incipient vaporization energy; and E_{sp} is the energy of total vaporization.

	Granite¹	Basalt²	Olivine³	Iron⁴
ρ_0 (kg/m ³)	2680	2700	3500	7860
K (GPa)	18	26.7	131	128
B (GPa)	18	26.7	49	105
a	0.5	0.5	0.5	0.5
b	1.3	1.5	1.4	1.5
α	5	5	5	5
β	5	5	5	5
U_0 (MJ/kg)	16	487	550	9.5
E_s (MJ/kg)	3.5	4.72	4.5	1.42
E_{sp} (MJ/kg)	18	18.2	14.5	8.45

¹ Allen (1967)

² Benz and Asphaug (1999)

³ this study

⁴ Tillotson (1962)

The generated olivine Hugoniot internal energy curve was compared to experimental results for forsterite and fayalite (Chen et al., 2002; Mosenfelder et al., 2007; Syono et al., 1981). For the relevant pressure range (0–200 GPa), the olivine Hugoniot curve is on average 15% lower and 11% higher than the experimentally determined pure forsterite and fayalite curves, respectively (Figure 3-1). This is appropriate for our target olivine composition of Fo₇₅. To test the robustness of the melt calculations, some simulations were reproduced using a forsterite EOS with Tillotson parameters fitted to the experimental Hugoniot curve (mean absolute error of 5%). For the cases compared, with impact energies of 1.45, 3.14, and 5.89x10²⁹ J, the simulations produced similar melt distributions, and on average 8% more melt; a few times more sublimed material was produced, still totaling only a few percent of the melt mass.

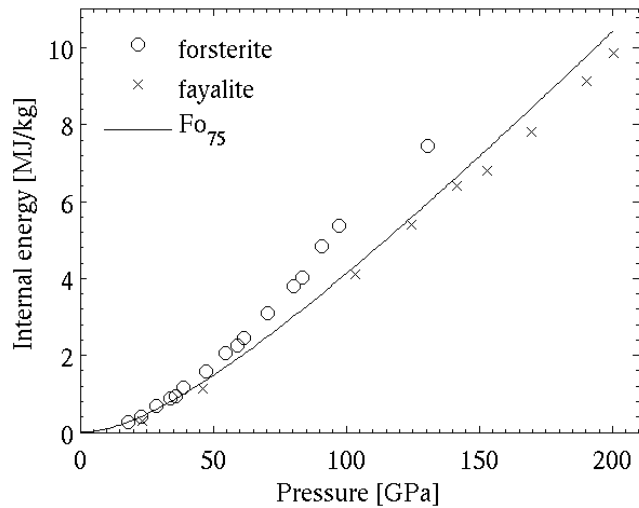


Figure 3-1 Comparison of our developed Hugoniot curve for Fo_{75} (solid line) and experimental results for forsterite (circles; Mosenfelder et al., 2007; Syono et al., 1981) and fayalite (crosses; Chen et al., 2002).

3.3.3 Initial Conditions

For planetary-scale impacts, the preservation of the impact structure is dependent on melt production. Accordingly, care must be taken to implement the appropriate initial thermal state, pressure profile, and structure (e.g., core size) of the planet, as well as to use suitable materials. We use an olivine EOS as the mantle material of the planet, which allows for Mars-like pressure and density profiles to be simultaneously matched. Since most planetary-scale impacts occurred during the last stages of planetary accretion, the initial thermal conditions of the simulated planet are based on the modeled thermal conditions of a young Mars, that has not yet lost its accretional heat. For impacts which occurred later, such as during the late heavy bombardment, the target would have cooled and less melt would be produced by the impact event; the greatest difference in melt is expected for slow impacts where a small amount of energy is added to a large volume of material (see *Melt production* section).

The Tillotson EOS is an explicit function of internal energy, pressure, and density, but not of temperature, making it difficult to calculate and verify the internal profiles of the planet. We calculate the pressure and thermal profiles of Mars by assuming hydrostatic equilibrium and an adiabatic profile, which are likely for an early Mars with a convecting mantle. The surface boundary condition is the average temperature of the top 100 km of Mars at the end of planetary formation as modeled by Hauck and Phillips (2002), $T = 1725$ K. The internal energy (U) of the surface material, which is at zero pressure ($P = 0$), is solely a function of the temperature (T) and heat capacity (C_p) of the material ($U_{P=0} = \int C_p dT$) and has no work component. The mantle internal energy-pressure-density profiles are calculated by discretizing and integrating the equations of material compressibility and hydrostatic equilibrium in the direction of increasing pressure:

$$K = -V(dP/dV)_S$$

$$dU = P dV$$

where K is bulk modulus, V is volume, P is pressure, and S is entropy. The boundary conditions for the core are given by the core-mantle boundary (CMB) pressure, as calculated in the mantle profile, and the CMB temperature (Hauck and Phillips, 2002). The planetary radius and mass are set initial conditions, while the central pressure and core radius are calculation results and are verified against standard values. Using the olivine EOS parameters developed here, we obtain a reasonable interior structure for Mars, supporting this EOS as an appropriate approximation.

The resulting density profile is similar to models by Bertka and Fei (1998). The calculated Mars core radius of 1,600 km and central pressure of 50 GPa are in good

agreement with the modeled core radius of 1,520–1,840 km (Yoder et al., 2003) and modeled central pressure of ~40 GPa (Bertka and Fei, 1998).

Both the mantle and crust are composed of olivine in the model, since a compositionally-distinct single particle layer cannot be numerically resolved and may cause numerical instabilities. The outermost layer of particles in the planet is labeled as the crust, giving an initial, mean crustal thickness of ~140 km. This material is tracked throughout the simulation and is assumed to retain its crustal properties. The thickness of Mars' crust at the end of accretion, after the last resurfacing impact and when the surface had cooled, is not known. The initial crust can be modified by volcanic events (such as the Tharsis bulge), and redistributed by planetary-scale impacts: the former mechanisms would thicken the crust while the latter generally does not affect the mean crustal thickness. Thus the initial crust is expected to be similar to or thinner than the current average crustal thickness of ~50 km (Zuber, 2001). While our crustal thickness is an overestimate, our simulations show that the studied impact features, including crater excavation, are mostly insensitive to the choice of particle size, and thus crustal thickness, that is used (see *Resolution effects*). Our crater size results, which track complete crustal removal, are necessarily similar to or smaller than the crater size, which would result with a thinner crust, since a thinner crust would necessarily be removed in areas where our thicker crust is excavated. The relative crustal thickness and qualitative distribution of crust after the impact are also consistent for the range of simulated crustal thicknesses (particle sizes), since the excavation process is largely unaffected by the crustal properties. These conclusions are supported by the similarity in results for the

three simulated particle sizes, which resulted in effective crustal thicknesses of 140 km (nominal resolution), 160 km, and 200 km (see also section *Resolution effects*).

Neither the planet nor the impactor have initial spin in our simulations. This is likely to be appropriate to Mars, whose rotational period is not expected to have changed significantly after the last accretionary impact and whose current rotational period (24.6 hrs) is long compared to the impact processes timescales. Changes in planetary spin rate due to the impact are considered below in the section *Post-impact rotational period*.

3.3.4 *Impact parameter space*

To guide our choice of impact energies, as well as allow a comparison of our results to those for small craters, we use the gravity regime, small crater scaling relation of Wilhelms and Squyres (1984) as an estimate of the nominal crater size resulting from a given impact energy:

$$D = k E_k^j g^u \quad (3-1)$$

where D is the impact crater diameter (m), E_k is the kinetic energy of the impactor (J), and g is the acceleration due to gravity (m/s^2). When D , E_k , and g are in mks units, the constants k , j , and u are taken to be 0.0348 m, 0.29, and $-1/6$, respectively, following Housen et al. (1979). The dependence on gravity, g , follows the relationship found by Gault and Wedekind (1977).

We simulate impacts with velocities from 6 to 50 km/s, impact angles of 0° (vertical, head-on impact), 15° , 30° , 45° , 60° , and 75° , and impact energies sufficient to form nominal 2,300 to 12,000 km craters according to Eq. 1 ($E_k = 1.98 \times 10^{27}$ to 5.89×10^{29} J). For Mars, ~ 6 km/s is the mutual planet-impactor escape velocity for planetary-scale

impacts, and 50 km/s is twice the orbital velocity. The impact angle is defined as the angle between the velocity vector and the line connecting the centers of the planet and impactor at the time of initial contact. Table 3–2 shows the simulated impact energies, the nominal basin size, the nominal basin size to planetary circumference ratio, and the approximate impactor size. The maximum impactor to planet mass ratio is 0.05.

Solar System accretion models provide a range for the most likely impact characteristics at the end of accretion. Dynamical friction equalizes the velocity of large objects at the end of accretion, resulting in encounter velocities similar to the mutual escape velocity of the objects (Canup and Agnor, 2000). The three largest bodies in Mars-like orbits at the end of accretion are modeled to be hundreds to a few thousand kilometers in diameter (e.g., Hartmann and Davis, 1975; Weidenschilling, 2008; Raymond et al., 2009). Gilbert (1893) and Shoemaker (1962) showed that the most likely impact angle is 45°.

Table 3-2 Simulated impact energies and velocities, and the resulting impactor diameter. The nominal crater diameter (using the half-space scaling of Wilhelms and Squyres, 1984) and the crater diameter as a fraction of the circumference of Mars are also shown. The grayed-out boxes represent conditions that could not be simulated due to the small impactor size and resulting numerical instability from too few particles.

Nominal crater diameter (km)	Crater diam. / planet circumf.	Impact energy (J)	Impact velocity (km/s)							
			6	10	15	20	25	30	40	50
			Impactor diameter (km)							
2,300	0.11	1.98×10^{27}	250							
4,000	0.19	1.33×10^{28}	750	520	280					
6,000	0.28	5.39×10^{28}	1230	870	640	520	400	280		
8,000	0.37	1.45×10^{29}	1740	1220	920	750	650	550	400	280
10,000	0.47	3.14×10^{29}	2270	1600	1210	980	850	740	600	520
12,000	0.56	5.89×10^{29}	2830	1980	1500	1230	1050	920	750	650

In these simulations, we have not varied the properties of the impactor (density, bulk modulus, degree of differentiation, etc.). Although these properties are relatively unimportant in small impacts, they may be important in planetary-scale impacts, because the impactor interacts with the target in more complicated ways. For instance, the impactor properties may affect the penetration depth and thus the ambient pressures (and associated sound speeds) that it will encounter; pressure and sound speed changes are insignificant for small impacts. The composition – and size – of the impactor also affects how it interacts with the curvature of the target at oblique angles. For these reasons, we should not expect the results quoted here for basalt impactors to hold to the same precision for impactors with different properties. An associated change to the best fit parameters for the scaling relations is also present. Future work explores the importance of impactor composition and structure (Marinova et al., *in prep.*).

3.3.5 Characteristics of the impact

We characterize the impact event by determining the crater size and ellipticity, crustal thickness and redistribution, geochemical signatures of the impact, mantle melting, depth of the transient cavity, melt production and distribution, antipodal effects, orbiting and escaping mass, and angular momentum transfer. The depth of the transient cavity is evaluated as the impact progresses; all other results are determined at the end of the simulated time, at 25.8 hrs, when the velocity of oscillations is minimal and orbiting and ejected material is near steady-state.

Material distributions are calculated as a fraction of total material in the surface layer of the planet (top ~150 km). The planetary surface is sampled at 2° intervals, and

the data is averaged over overlapping 10° diameter caps. The crater is defined as the area of excavation where the surface crustal thickness is 50% of the pre-impact crustal thickness (the 50% contour boundary). Antipodal crustal removal is determined using the 80% contour of post- to pre-impact crustal thickness. The molten region is defined as the area with a melt fraction larger than 50%. The qualitative aspects of the surface distribution of material are robust and do not vary on the timescale of the simulation, nor with the choices of sampling or averaging criteria.

The amount of melt produced is determined using a pressure-dependent internal energy melting criterion for forsterite (Asimow, 2007). The melting criterion is fitted by

$$E_{melt} = 39.7 P + 2885$$

where E_{melt} is the complete melting internal energy (kJ/kg) and P is the static pressure (GPa). The absolute error of the fit is less than 0.4% for pressures less than 120 GPa, which encompasses the pressure range for the interior of a Mars-like planet. Using the pressure-dependent melting criterion allows us to determine the amount of melt in the mantle underlying the crater. Knowing the mantle melt amount allows for a zeroth order estimate of the thickness of the new crust that will form in the crater as the melted mantle cools. The forsterite melting criterion describes the essential dependence of melting on pressure, despite its difference in composition from the mantle material (Fo₇₅). For comparison, at zero pressure, complete melting in forsterite occurs at ~ 2.89 MJ/kg, and for Fo₇₅ at ~ 2.96 MJ/kg; the Fo₇₅ melting energy is equivalent to the melting energy of forsterite at ~ 2 GPa.

The depth of the transient impact cavity is calculated using the maximum depth of penetration of the impactor material. Since using the results from a single particle can

give a spurious result, we average the 10% of the impactor mass that penetrates the deepest. The depth varies by less than 9% when the averaged mass considered is halved and doubled.

In calculating the orbiting and escaping material masses we use the following criteria. A particle is orbiting if its velocity is higher than the circular orbital velocity, but lower than the escape velocity, for its location with respect to the target center. In addition, to ensure that the particle does not re-impact the planet, its angular momentum must be higher than that of a particle orbiting at the planet's radius. For a particle to be escaping, it must have more than escape velocity, given its location with respect to the target center.

Confidence intervals for the reported fits are determined using the bootstrap Monte Carlo method; 95% confidence intervals for the fitting parameters are reported. All comparisons to small crater scaling relations are for gravity regime impacts.

In subsequent sections the presented results are for $N = 200,000$ particles and initial particle size of 118 km, except where resolution effects are considered.

3.4 Results

The results of the impact processes for small and planetary-scale impacts necessarily differ to some extent due to surface curvature, unidirectional versus radial gravity, and relative size of the impactor to the target. In understanding the implications of planetary-scale impacts by basalt impactors, we consider: the degree of similarity in morphology between small and planetary-scale craters; the largest impact structure that can be retained when taking into account the production and distribution of melt;

antipodal effects; the net mass accretion or erosion as a result of the impact; and the post-impact rotational state of the planet. By better understanding the consequences of planetary-scale impacts, we can assess the likely impactors that formed the currently observed planetary-scale craters on the planets and compare these to the predicted size distribution of co-orbital bodies at the end of accretion.

3.4.1 Morphology of planetary-scale craters

The morphology of small impact craters in the gravity regime has been well documented. The smallest impacts excavate a bowl-shaped cavity, while with increasing impact energy the shape becomes increasingly more complex and a central peak and multiple rings form (e.g., Melosh, 1989). For planetary-scale impacts, the transient cavity is far from hydrostatic equilibrium and cannot be supported by the surrounding material. It thus rebounds to equilibrium on the timescale of the gravity wave period (Melosh, 1989); the equilibrium structure is expected to have a shape and depth to diameter ratio different from those of smaller impacts. During planetary-scale impact events, the entire thickness of the crust around the site of impact is removed and a remnant impact structure results from the thickness difference between any new crust that forms in the excavated area and the primordial crust beyond the excavation boundary. The thickness of the new crust depends on the composition, post-impact thermal state, and evolution of the underlying mantle (Debaille et al., 2007; Elkins-Tanton et al., 2005; Elkins-Tanton et al., 2003).

3.4.1.1 Crater size

For small impacts, the crater size is primarily a function of impact energy, and is modified by impact velocity, impactor diameter, the density difference between the impactor and target material, gravity, and impact angle (e.g., Gault and Wedekind, 1977; Holsapple, 1993; Melosh, 1989; O'Keefe and Ahrens, 1993; Pierazzo and Melosh, 2000c). In planetary-scale impacts, the relative importance of these impact characteristics on the crater size is modified by the large relative size of the impactor to the planet, the curvature of the impacted surface, and the radial gravity direction. The definition of the crater size also changes between the two size regimes: small impact craters are defined as the rim-to-rim diameter of the impact structure, while for planetary-scale events we define the crater as the area where at least 50% of the pre-impact crust is excavated by the impact.

Comparing our results for planetary-scale impacts by basalt impactors to those of small impacts, we find that the impact energy is important in setting the crater size in both size regimes. However, at constant energy, the crater size is more strongly modified by impact velocity and angle for planetary-scale impacts. The importance of velocity scaling in the two size regimes is shown by the empirical fit of the small crater population without the explicit dependence on velocity (e.g., Eq. 3-1) versus the significant improvement in the crater size fit for planetary-scale impacts with the inclusion of the velocity parameter (see Eq. 3-2 below). For impact angles, small crater scaling relations commonly include the dependence of $\cos^{1/3}\gamma$ (e.g., Gault, 1974), while for planetary-scale impacts the best fit is obtained with an exponent value of ~ 0.67 (see Eq. 3-2 below).

For small impacts, gravity and target-impactor density differences also play a role, as is exemplified in the crater diameter scaling $D_{at} = 1.8 \rho_p^{0.11} \rho_t^{-1/3} g^{-0.22} L^{0.13} E_k^{0.22} \cos^{1/3} \gamma$, where D_{at} is the apparent diameter of the transient crater, ρ_p is the density of the projectile, ρ_t is the density of the target, g is gravity, L is the projectile diameter, E_k is the impact energy, γ is the impact angle, and all units are in the mks system (Gault, 1974; Melosh, 1989). The gravity and target-impactor density parameters were not varied in our simulations. For planetary-scale impacts, gravity is expected to have a similarly important effect on material excavation, and density differences and heterogeneities in the target are likely to be less important due to the large interaction volume effectively averaging the material properties. While near-surface material heterogeneities may not strongly affect planetary-scale impacts, the core size relative to the planet size is expected to be important, due to the change in shockwave propagation and impactor penetration caused by the mantle-core density difference. The crater size for the range of impact energies, velocities, and angles we have simulated is shown in Figure 3-2. The size of the crater is determined by fitting an ellipse to the crater boundary in coordinates centered on the excavated region. As described earlier in *Characteristics of the impact*, the crater boundary follows the 50% contour of the post-impact to pre-impact crustal thickness ratio. The crater size is a robust feature since after the impact, the lateral transition from a surface with no crust to a surface with a crust thicker than the pre-impact crustal thickness occurs over only a few resolution elements (~300 km). For a nominal 10,000 km crater, fitting the 20% and 80% contours changes the boundary size by -9% and +12% with respect to the 50% contour, respectively. For smaller impacts, the condition of complete crustal removal is less robust: for a nominal 2,300 km crater, fitting the 20%

and 80% contours results in an average boundary size change of -25% and $+33\%$, respectively. The crustal excavation boundary size does not capture post-impact, material-specific processes in the crater modification stage, such as wall slumping and mass-wasting. For small impacts the modification stage changes the size of the impact structure significantly; however, for planetary-scale impacts these processes are expected to result in minor relative changes.

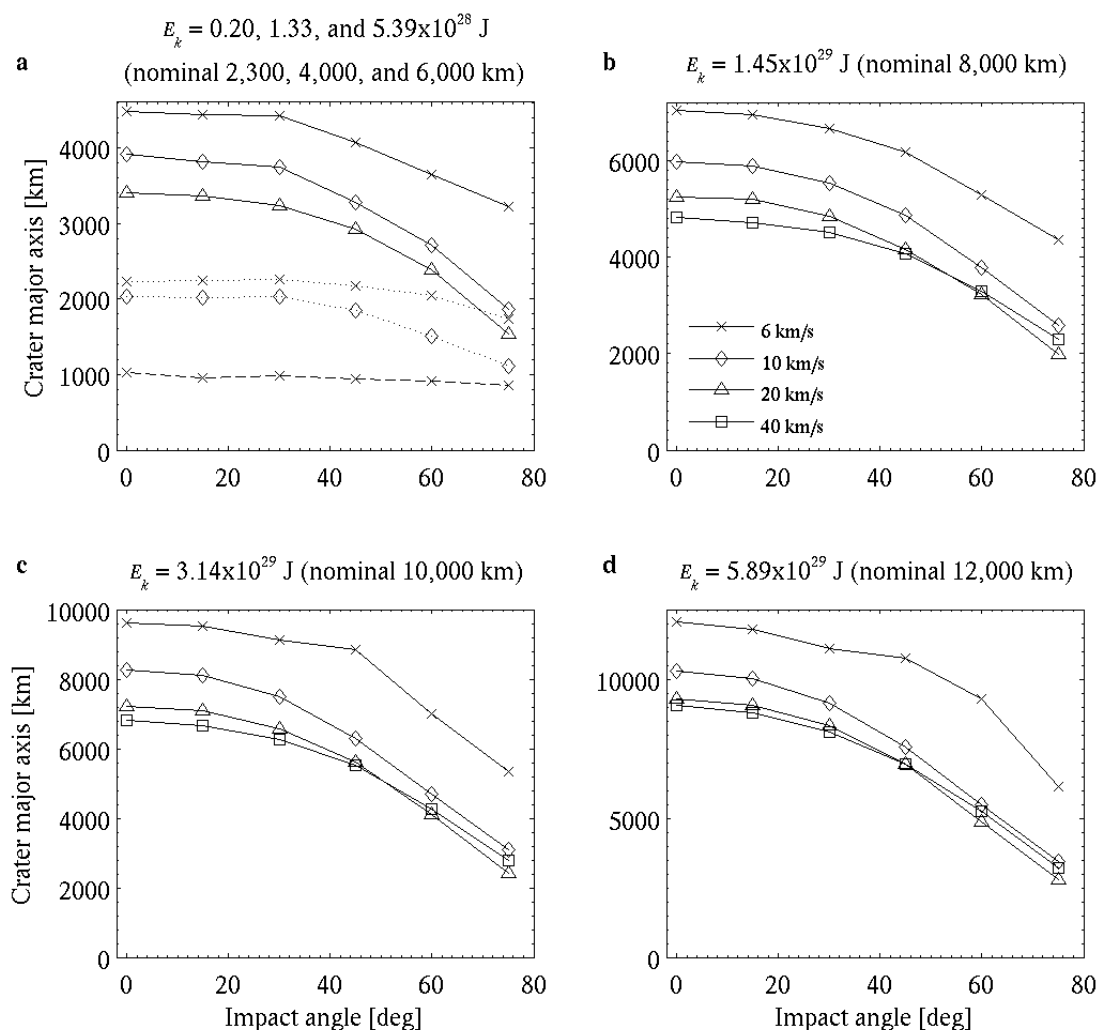


Figure 3-2 Crater diameter results. Panel (a) shows the results for impact energies of $E_k = 1.98 \times 10^{27} \text{ J}$ (dashed), $1.33 \times 10^{28} \text{ J}$ (dotted), and $5.39 \times 10^{28} \text{ J}$ (solid). The nominal crater size refers to the prediction from small crater relations (Eq. 3-1), which are 2,300 km, 4,000 km, and 6,000 km, respectively, for panel (a). Panels (b–d) show the results for impact energies of $E_k = 1.45, 3.14, \text{ and } 5.89 \times 10^{29} \text{ J}$. Impacts with velocities of 6, 10, 20, and 40 km/s are shown, or a subset thereof if the condition was not simulated (as per Table 3-2).

For a given impact energy, the largest crater is formed by head-on, slow impacts. Increasing either impact velocity or angle results in a smaller crater size. None of the simulated impacts shatter or catastrophically disrupt the planet.

We compare our crater size results for head-on impacts with four published gravity regime scaling relations for small impacts (Figure 3-3), to assess the applicability of small crater scaling relationships to the planetary-scale size regime. Our results are encompassed within the variation in crustal excavation sizes predicted by these four scaling laws. However, for the modeled energy range, our trend shows a steeper growth of crater size with impact energy than the small crater scaling laws. Self-consistent modeling of small to large impacts is needed to understand the transition from the small to planetary-scale size regime; this is currently unattainable with our technique.

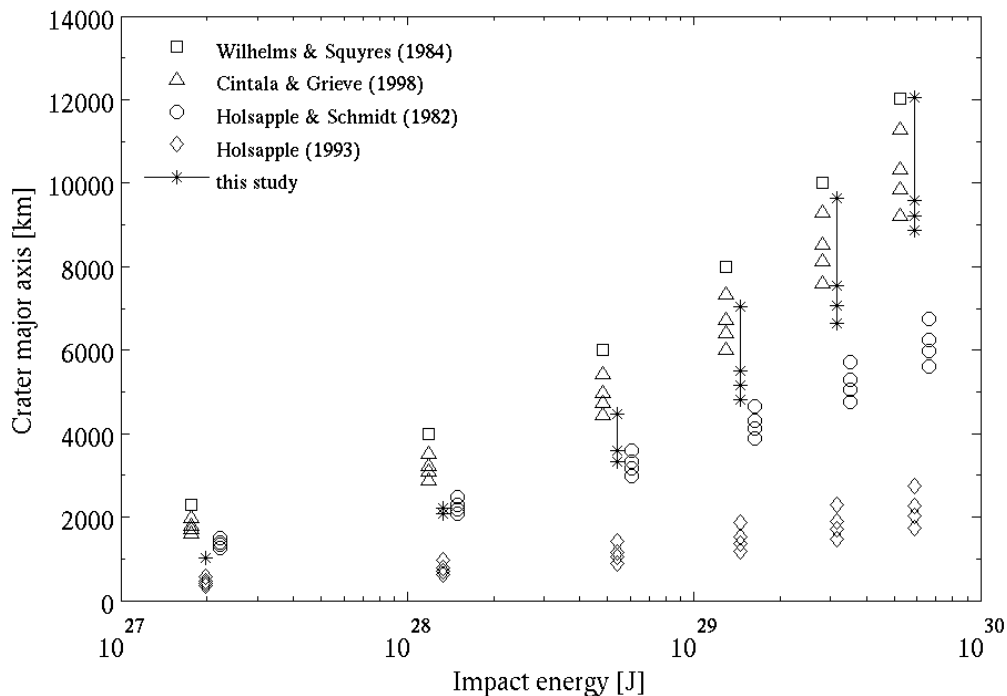


Figure 3-3 Crater size comparisons: simulation results versus scaling relations for head-on, small impacts. Plotted are the same impact energies as in our simulations, and impact velocities of 6, 15, 25, and 50 km/s. Symbols are slightly offset horizontally for clarity. At each energy, for each scaling relation and our model results, the crater size is largest for the slowest impact velocity, and decreases with increasing velocity.

In analogy to the scaling relationship by Wilhelms and Squyres (1984) and Housen et al. (1979), and including a dependence on velocity and impact angle, we fit a scaling to the relationship between impact energy, velocity, and angle and the resulting crater cavity size for planetary-scale impacts:

$$D' = q(E'_k)^r (v'_{imp})^s \cos^t \gamma \quad (3-2)$$

where D' is the crater major axis normalized by the planetary radius ($r_0 = 3,313$ km); E'_k is the impact energy normalized by the binding energy of the target ($E_0 = 5.22 \times 10^{30}$ J); v'_{imp} is the impact velocity normalized by the planetary escape velocity ($v_0 = 5.085$ km/s); γ is the impact angle; and q , r , s and t are constants. Fitting all impact energies, velocities, and angles for these basalt impactors, we find that the best fit (and 95% confidence interval) is given by $q = 8.70 \pm 0.053$, $r = 0.392 \pm 0.014$, $s = -0.185 \pm 0.027$, and $t = 0.672 \pm 0.061$. The uncertainties in the fitting parameters are not independent: the correlation of q with r , s , and t is 0.29, 0.73, and 0.33, respectively. For head-on (0°) impacts, the mean absolute fitting error is 6%, with the largest error ($\sim 20\%$) occurring for the slowest and least energetic impacts. For impact energies of 0.02, 0.13, 0.54, 1.45, 3.14, and 5.89×10^{29} J (all velocities and angles) the mean absolute fitting errors are 22%, 13%, 8%, 7%, 7%, and 10%, respectively. The constant q effectively contains the dependence on gravity and impactor properties, which was not explored in our simulations. The larger magnitude of t relative to s shows the stronger dependence on impact angle compared to impact velocity. The negative exponent assigned to the velocity, as well as the cosine angle scaling, underscores the inverse relationship of crater size with impact velocity (at constant energy) and angle. If we look at crater size for constant momentum and head-on impacts, we find that the largest crater results from the

slowest impact. Further work examines the effect of impactor properties on the results and best fit parameters (Marinova et al., *in prep*).

We consider the relationship between depth of penetration, as previously defined, and the excavated crust boundary major axis (Figure 3-4). We find the following relation to represent the dependence of the diameter, D (km):

$$D' = m (E'_k)^n (h')^p$$

where h' is the depth of penetration of the impactor normalized by the planetary radius, and m , n , and p are constants. Simulations that resulted in a penetration depth less than one resolution element ($h < 118$ km, 19 of 204 simulations) were considered uncertain and were not used when determining the fit or for the reported fit errors. The best fit values for the constants (and 95% confidence intervals) for these basalt impactors are $m = 8.38^{+0.58}_{-0.51}$, $n = 0.336 \pm 0.015$, $p = 0.378 \pm 0.033$; the uncertainties in the fitting parameters are not independent: the correlation of m with n and p is 0.31 and 0.65, respectively. The mean absolute errors are 4 to 7% for each of the six simulated energies. The fit parameterization is supported by the physical consideration that no crater should form when there is no impact energy and no penetration into the planet. The residuals of the fit have a standard deviation of 470 km (four particle diameters), suggesting that the fit complexity is appropriate given the confidence in the results (see *Resolution effects* and the error for crater sizes reported therein). The fitting error increases significantly for simpler fits: when the power law dependence on E_k is removed (i.e., setting $n = 1$), the simulation results cannot be fit adequately; and removing the power law dependence on h (i.e., setting $p = 1$) does not allow the functional form of the data to be matched. Note that

impactor composition and structure affects the penetration depth and associated best fit parameters (Marinova et al., *in prep.*).

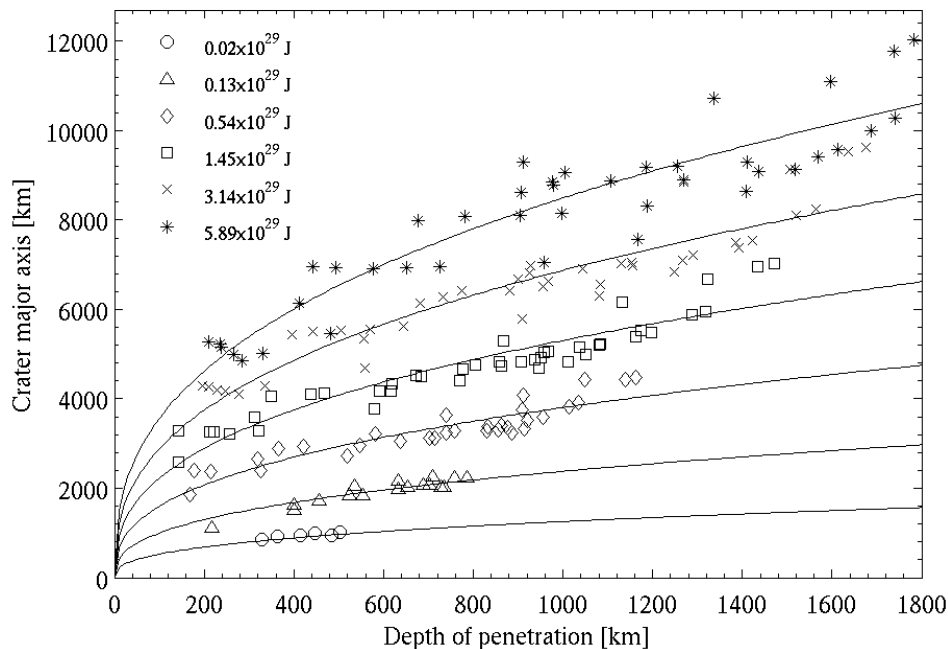


Figure 3-4 Depth of penetration versus crater major axis and the obtained fit. Impacts resulting in a penetration depth of less than a resolution element are not plotted.

3.4.1.2 Crater ellipticity

For small craters, the ellipticity resulting from oblique impacts is substantial only for angles higher than $\sim 75^\circ$ from the vertical (Gault and Wedekind, 1978). In contrast, our results show that for planetary-scale events, with increasing energy, slow impacts produce elliptical basins at smaller angles (Figure 3-5). This change in excavation mechanics is interpreted to be due to the increased penetration depth of energetic impacts: the impact cannot be well approximated as a point source explosion, but acts over a volume elongated in the direction of downrange motion, as noted by previous authors (e.g., Pierazzo and Melosh, 2000b). This downrange elongation of the pressure

streamlines also results in elongation in the streamlines of constant velocity, thus excavating an elliptical cavity.

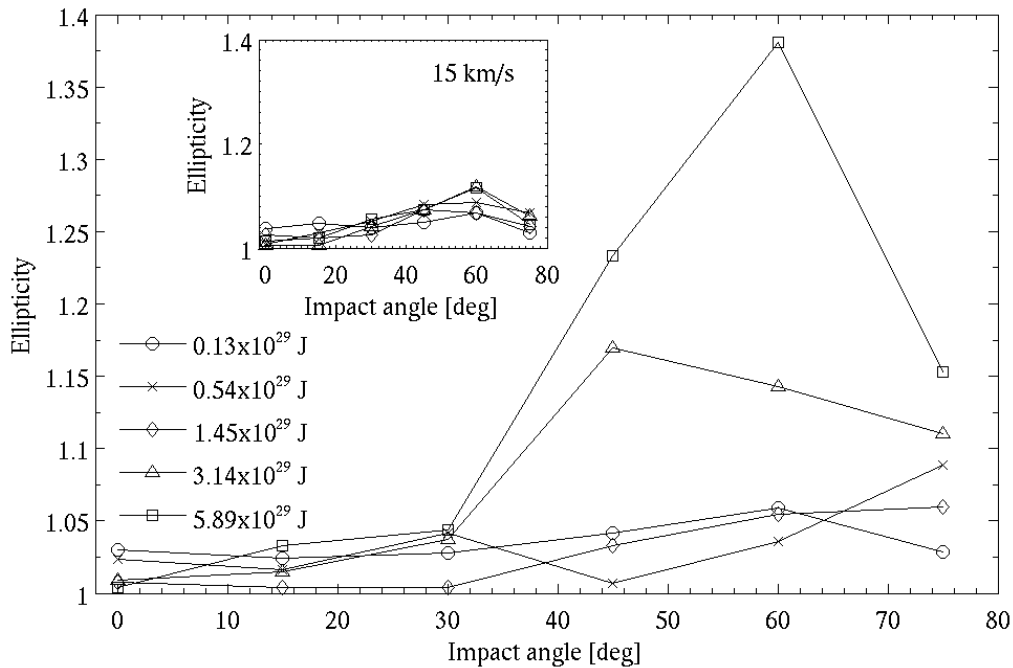


Figure 3-5 Ellipticity as a function of impact energy and angle. For high impact energies at low impact velocity (6 km/s, main figure), the ellipticity becomes significant at intermediate angles. The ellipticity at higher impact velocities is minimal: the inset shows the crater ellipticity for 15 km/s impacts.

Pierazzo and Melosh (2000b) performed calculations demonstrating the downrange elongation of the peak pressure contours by oblique impacts; the contours appear to be similar to those produced in planetary-scale impacts (Figure 3-6). The variation of peak pressure with impact angle for planetary-scale impacts is proportional to the sine of the impact angle, as was also found by Pierazzo and Melosh (2000a). A more precise comparison between the two sets of simulations is difficult due to differences in the utilized models: Pierazzo and Melosh used the Eulerian model CTH with the SESAME equation of state and about three times more particles per impactor radius. Nevertheless, the contours are generally similar and some inferences can be made about

the consequences of the curvature of the surface on the resulting crater shape. The elongation of the crater cavity in planetary-scale impacts for relatively low impact angles may be explained by the geometric relationship between the surface and the peak pressure contours. The high pressure region is spatially extensive compared to the diameter of the planet, resulting in the high pressure contours intersecting the surface. This shallowness of the downrange high pressure contours makes the excavation of the downrange material possible, resulting in increasing crater ellipticity at relatively low impact angles ($\sim 45^\circ$). Conversely, for small impacts the significant depth of material overlying the high pressure zone may not be excavated, given the same pressure and material velocities, resulting in a mostly circular crater.

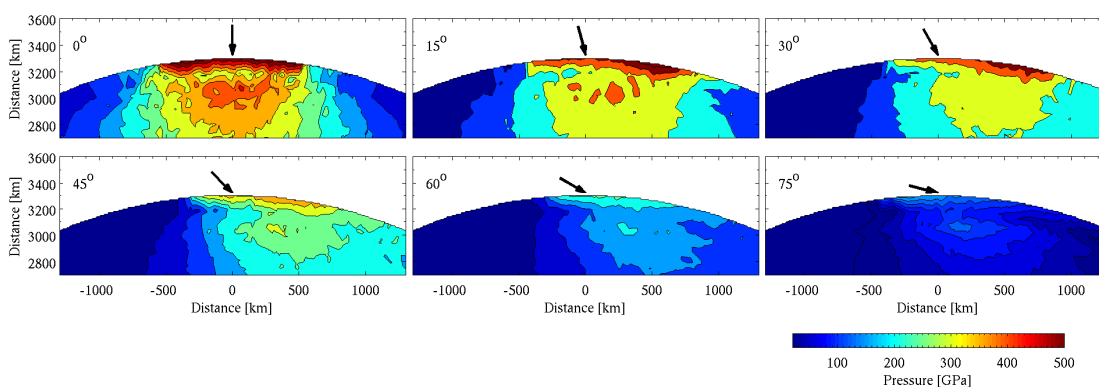


Figure 3-6 Peak pressures achieved by 5.89×10^{29} J, 20 km/s impacts for the range of simulated impact angles. Compare to Fig. 3 of Pierazzo and Melosh (2000b). Arrows indicate impact point and direction.

3.4.1.3 Crustal thickness and redistribution

The material excavated by the impact is redistributed over the surrounding area. In the case of small impacts, the ejecta is redeposited in an annulus around the excavated region, forming a crater rim that encircles the crater cavity and beyond that the more expansive ejecta blanket. For these half-space impacts, the ejecta blanket thickness has

been found to decrease as a power law with distance from the crater (e.g., Melosh, 1989). In addition, the ejecta distribution around small craters scales self-similarly, since the ejection velocity is proportional to the crater radius (Melosh, 1989). However, for planetary-scale impacts we do not find a self-similar character to the ejecta distribution. Instead, for a given crater size, the maximum ejection velocity is not constant, but increases with impact velocity, all other parameters held constant. For small, head-on impacts, combining the ejection velocity relationship of Melosh (1989) and the impact scaling relation of Wilhelms and Squyres (1984) suggests a relationship of $v_{ej} \propto v_{imp}^{0.58}$, where v_{ej} is the maximum ejection velocity. In hypervelocity experiments of aluminum spheres into quartz sand, Gault and Wedekind (1978) find that the maximum ejection velocity is comparable to the impact velocity, for impact velocities of ~ 6 km/s. A more precise relationship between impact and ejection velocities could not be determined due to limitations in the experimental equipment. For planetary-scale impacts, we find that the ratio of maximum ejection velocity to impact velocity is 0.4 to 2.2 for the range of simulated conditions. Both the absolute and normalized maximum ejection velocities increase with increasing impact angle, despite the associated decrease in peak pressure of the impact. This may be attributed to the change in the location of the highly shocked material with impact angle. In all cases the most shocked material is located at the initial contact point between the planet and the impactor; however, with increasing impact angle, the majority of the highly compressed material is closer to the planetary surface and buried beneath less impactor material. This increase in ejection velocity with impact angle, as well as the location of this highly compressed material, appears analogous to the process of “jetting” that has been described for small impacts (e.g., Melosh, 1989). In

addition, for head-on impacts the highly pressurized material is accelerated towards the center of the planet during the initial stages of the impact event, and its ejection requires first overcoming this radially inward component of the velocity. For oblique impacts, the highly pressurized material is close to the surface and does not experience acceleration radially into the planet.

The ejecta distribution pattern in planetary-scale impacts is additionally complicated by the large ejection distances, which are of order the radius of the planet. An increase in ejection velocity in planetary-scale impacts results in a larger increase in ejection distance than for a flat surface, due to the combination of planetary curvature and radial gravity. As a comparison, an ejection distance of 1,000 km on a flat surface would be 15% greater on Mars due to the planetary curvature, assuming a 45° ejection angle and using the intersection between the ballistic trajectory and the curved planetary surface (Melosh, 1989). A 3,200 km flat surface ejection distance is 50% greater on the curved Martian surface. The available area for ejecta deposition with distance from the impact basin also changes non-linearly, in contrast with the simple quadratic dependence for a flat surface.

In our simulations, post-impact crustal thickness is determined by tracking the redistribution of the crustal particles. We define the rim as contiguous crustal thickening for more than half the circumference of the crater cavity, where the thickening is more than 1.3 times the initial crustal thickness; 1.3 times is the average crustal thickening within half a crater radius from the boundary of the excavation cavity. Conversely, a more uniform redistribution is characterized by thickening over a large lateral distance.

The simulations show that for energies $E_k \leq 5.39 \times 10^{28}$ J (nominal crater size $\leq 6,000$ km; crater diameter versus planet circumference $\leq 21\%$), a rim is present (Figure 3–7a, b). For head-on impacts, the continuous crustal thickening extends two to three radii from the center of the excavation, similar to ejecta blanket scaling relations for small craters (Moore et al., 1974).

Above an impact energy of $\sim 10^{29}$ J and for impact angles $\leq 45^\circ$, the crustal redistribution pattern transitions to a more uniform thickening over the planet and a rim-like annular thickening is not present (Figure 3–7c, d, e). For these impact events, the ejection velocity is higher and the ejecta flight path is significantly increased by the curvature of the planet compared to a flat surface. This combined increase in ejection distance results in a more uniform crustal redistribution on the planetary surface and no apparent crater rim.

For $E_k > 10^{29}$ J and impact angles above 45° , rim-like crustal thickening still occurs, however, the thickening does not commonly encompass the entire crater cavity (Figure 3–7f). This is the result of the preferential ejecta emplacement downrange of the impact point.

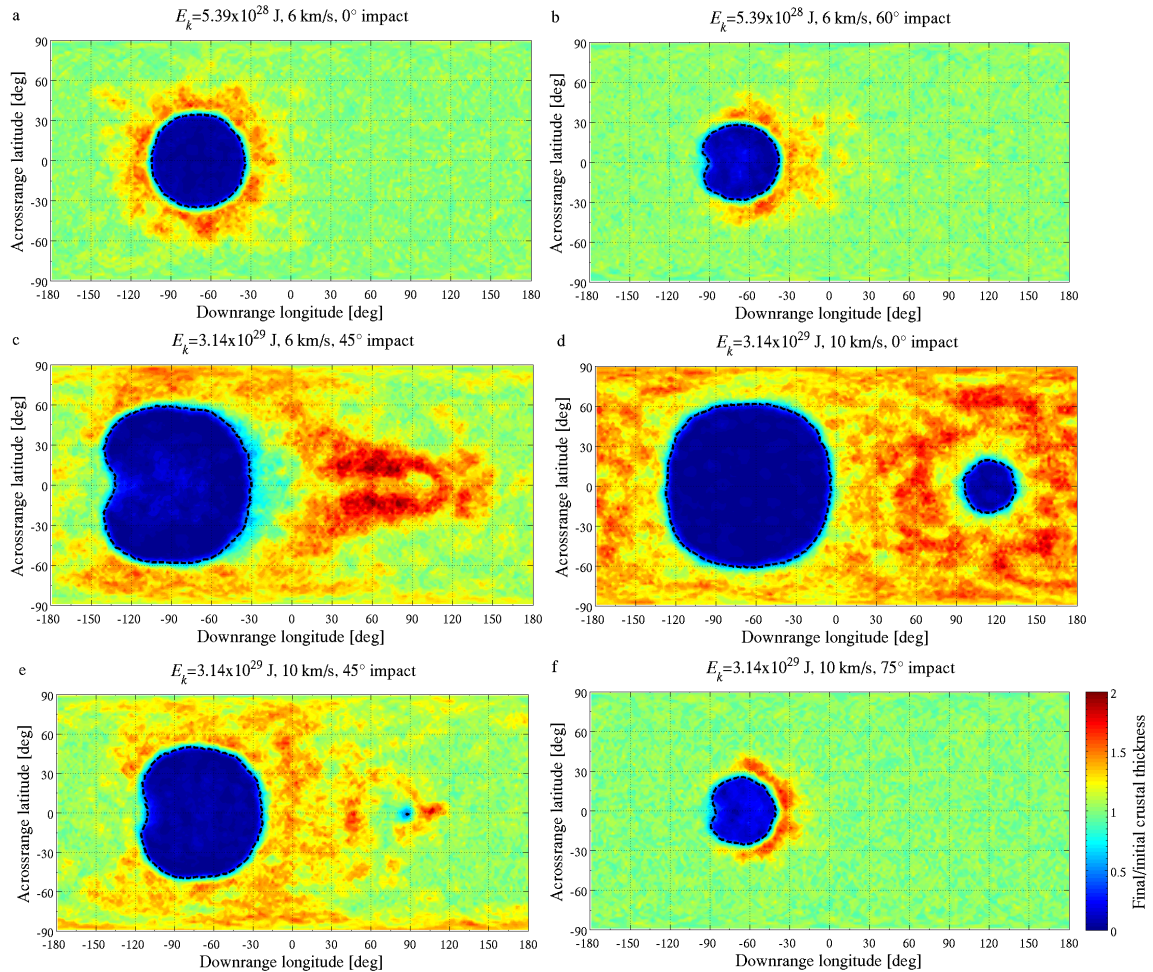


Figure 3-7 Post-impact crustal thickness normalized to initial (pre-impact) crustal thickness. Annular crustal thickening is evident in (a), demonstrating that the resolution of the simulations is sufficient to capture crustal effects. The crater boundary is overlaid (dashed line). The distribution of crustal thickening changes from a contiguous annular thickening (similar to a rim) at low impact energies, to a more uniform and expansive thickening at higher impact energies, and a partial rim at high energy, high impact angles.

Planetary-scale impact simulations enable testable predictions regarding the distribution of primordial crust, mantle, and impactor material, and each of these components is expected to be chemically and isotopically distinct (e.g., Chambers, 2004). Due to the occurrence of planetary-scale impacts exclusively in the early Solar System, the commonly observed impact signatures such as impact breccia and hydrothermal activity are likely to have been significantly modified and obscured during the

intervening 4.5 Gyr or be difficult to uniquely associate with a specific event. However, while surface material may be modified or buried, the geochemically-distinct signature of the reservoirs is likely to be preserved through geologic time. Through geochemistry surveys of the planet, it may be possible to verify the occurrence of planetary-scale impacts. This is especially pertinent in cases such as the possible impact formation of the Mars Northern Lowlands, where an alternate, endogenic formation scenario is also plausible (e.g., Marinova et al., 2008; *cf.* Zhong and Zuber, 2001).

The distribution of geochemically-distinct material could also be used to establish impact and impactor characteristics for a given crater, together with numerical model predictions. The distribution of the material provides an additional set of indicators, which may help reduce the ambiguity in using a crater size and shape to determine the impact velocity, angle, and energy. The ability to determine impact angle and velocity based on the impactor material distribution is demonstrated in Figure 3-8, where all shown simulation results have a crater major axis of about 7,000 km, but the distribution of impactor material varies significantly. Specifically, the distribution of impactor material varies significantly with impact velocity and angle (Figure 3-8), and thus can be used in deconvolving the effects of impact energy, velocity, and angle on the crater size. Simulations show that with increasing impact angle, impactor material accumulation shifts in the downrange direction of the excavated cavity and is also deposited downrange outside of the cavity (Figure 3-8c). With increasing velocity, for constant energy, the extent of the impactor material cover decreases as the impactor mass decreases (Figure 3-8b, d *cf.* c). Given the impact angle and velocity, the impact energy can be determined using the scaling relations developed in section *Crater Size* and elsewhere in this paper.

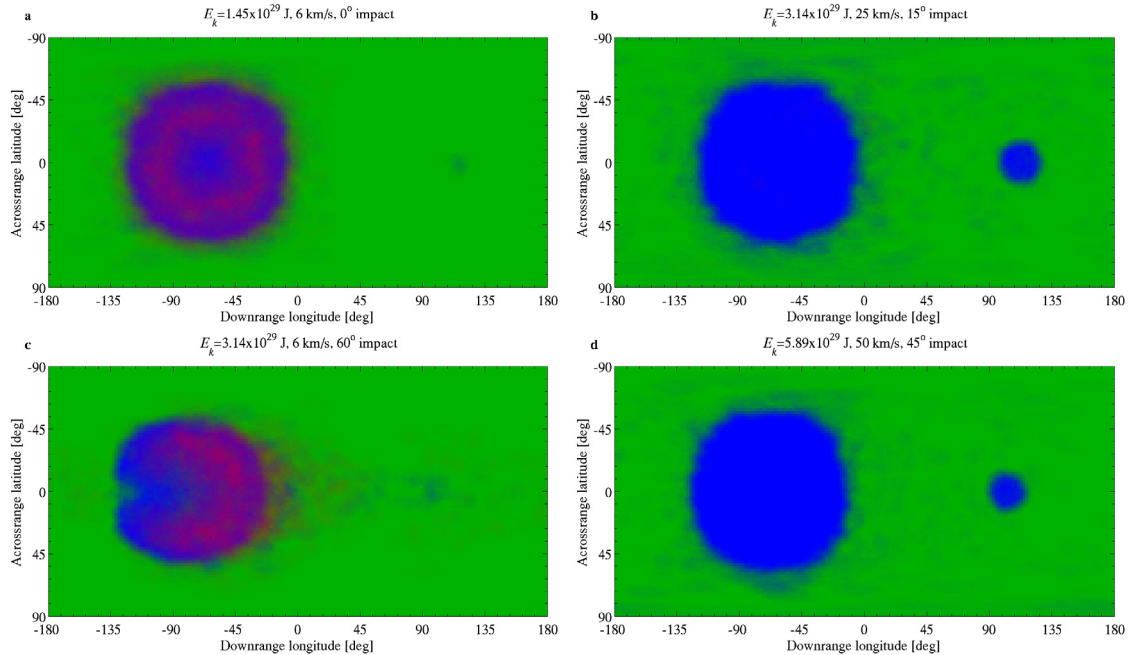


Figure 3-8 False color composites of material distribution on the surface. Impactor, crust, and mantle material are assigned the red, green, and blue channels, respectively. In all cases the major axis of the crater is $\sim 7,000$ km, however, the impact energy, velocity and angle – and the resulting impactor distribution – are significantly different. Disruption that is antipodal to the impact site can be seen in (b) and (d).

3.4.1.4 Mantle melt

The crustal excavation boundary represents the potential size of the impact structure that may remain. However, the characteristics of the new crust that forms inside the boundary determine the observable structure over geologic time. The thickness of the new crust is a function of the underlying column amount of mantle melt, and its post-impact cooling and differentiation history. We quantitatively determine the post-impact mantle melt and its thermal state, enabled by the realistic internal energy-pressure-density profile of the planet in our simulations, and the pressure-dependent internal energy melting criterion (Figure 3-9). We find a general trend of greater maximum depth of melt with increasing crater diameter (Figure 3-9b *cf.* c, d), consistent with the trend found by Grieve and Cintala (1992). The maximum depth of melting decreases with increasing

impact angle. At constant energy, impact velocity has little effect on the maximum melt thickness; however, it affects the mantle melt thickness distribution radially away from the center of the crater cavity (Figure 3-9b *cf.* e). With increasing impact energy the depth of mantle melt increases, consistent with the availability of more energy for melting and the deeper impactor penetration depositing more energy at depth. Increasing the impact angle results in less melt at depth, attributable to two effects. First, the depth of penetration of the impactor decreases. Second, large impactors incident on a curved surface may in part miss the planet and fail to impart their kinetic energy. Impact energy partitioning confirms that in head-on impacts more of the impact energy is converted to thermal energy, and for increasingly oblique impacts more remains as kinetic energy carried by material travelling away from the planet. The details of the results are affected by the impactor composition, as the impactor size, depth of penetration, and its geometric interaction with the planet change with varying impactor composition and structure (Marinova et al., *in prep.*).

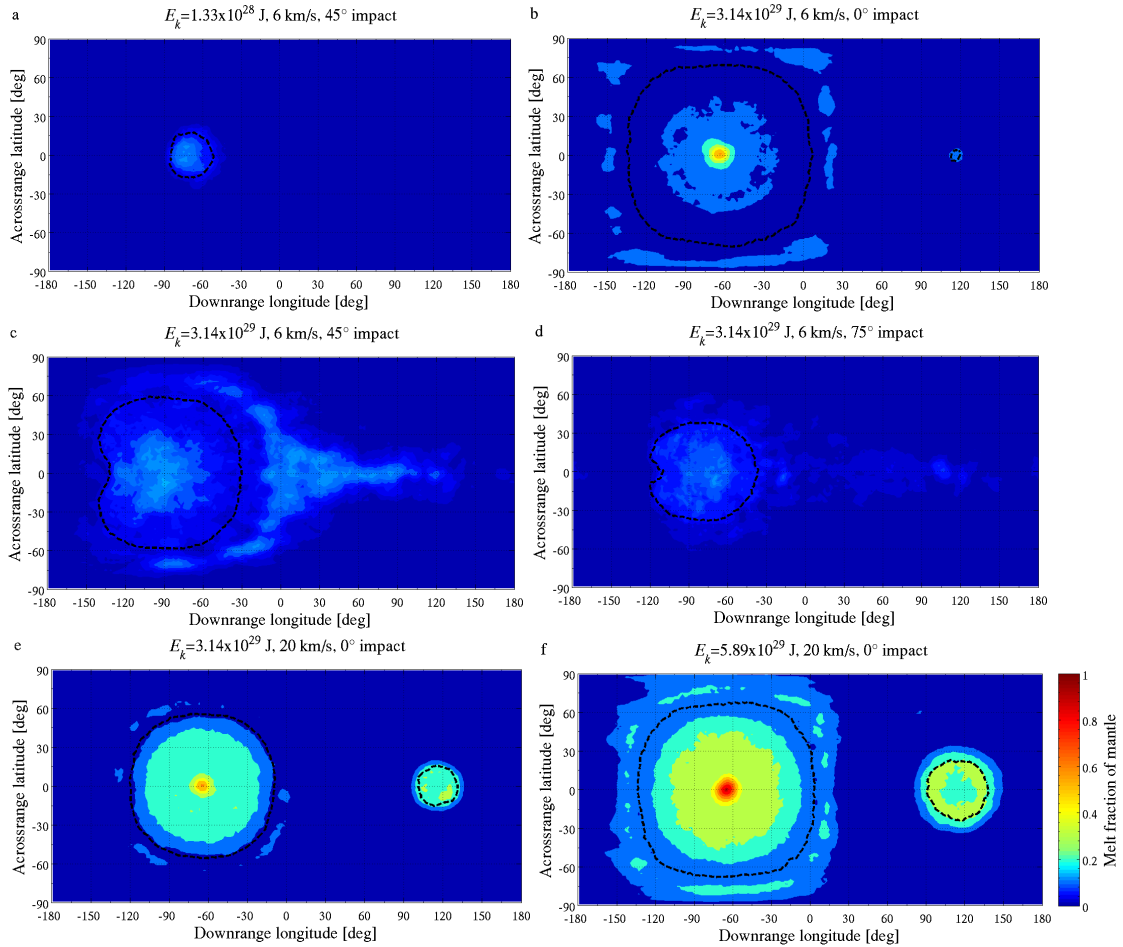


Figure 3-9 Molten material fraction in the mantle and crust. The crater boundary is overlaid (dashed line).

The primordial Martian crust is thought to have differentiated from a mostly molten, low viscosity mantle undergoing whole mantle convection at the end of accretion (Elkins-Tanton et al., 2005; Hauck and Phillips, 2002; Schubert and Spohn, 1990). Subsequent impact-induced melting that is less than the full thickness of the mantle is expected therefore to form a thinner-than-primordial crust. In our simulations only the most energetic and head-on impacts melt a significant fraction of the mantle thickness at the sub-impact point, and even then, the molten thickness fraction decreases quickly away from the sub-impact point. The deep, buoyant melt is likely to rise on a timescale

shorter than the cooling time, providing an approximately constant depth – but relatively shallow – melt pool as a source for the formation of new crust.

An observable characteristic of planetary-scale impacts is the difference in crustal thickness between the impact site and the surrounding crust. Quantifying the depth of mantle melt as a function of impact conditions provides information about the expected thickness of the crust formed at the site of impact and therefore the prominence of the preserved structure. For small impacts the depth to diameter ratio of the crater remains about constant with impact energy (e.g., Melosh, 1989), and therefore with increasing energy, the crater depth increases accordingly, and the impact structure becomes more prominent. However, for planetary-scale events, increasing impact energy results in more mantle melting and therefore a proportionally thicker post-impact crust. The primordial crustal thickness, and the thickness of crust that result from melting the residual mantle during a large impact, both depend on the composition and cooling history of the mantle. Hence the ratio of post-impact to primordial crustal thickness depends not only on the parameters of the crater formation event, but also on the formation process, timing, and extent of recycling of the primordial crust (Debaille et al., 2007; Elkins-Tanton et al., 2005; Elkins-Tanton et al., 2003). Nonetheless, larger impacts, which melt a larger fraction of the mantle, will likely result in the formation of thicker crust and thus a smaller contrast between pre- to post-impact crustal thickness. This trend could account for example for the crustal thickness difference of ~60 km between Hellas Basin and its surroundings versus the difference of ~30 km between the much larger, proposed Northern Lowlands impact basin and its surroundings.

3.4.2 Global consequences of planetary-scale impacts

3.4.2.1 Depth of transient crater cavity

The penetration distance of the impactor into the planet sets the depth of the transient crater cavity and the maximum depth from which material is excavated. The depth of penetration also correlates with the strength of the gravity waves initiated in the planet, and thus the degree of planetary surface disruption. Since the impactor properties affect the peak pressure at the impact site, as well as the relative density with respect to the mantle, the depth of penetration is also varies with the impactor composition, for a given set of impact conditions (Marinova et al., *in prep.*).

We calculate the depth of penetration as the closest approach of the impactor to the center of the planet (Figure 3-10). The impactor reaches the core only for the most energetic (5.9×10^{29} J) and head-on impact, and mixing of the core and impactor is not observed for any conditions.

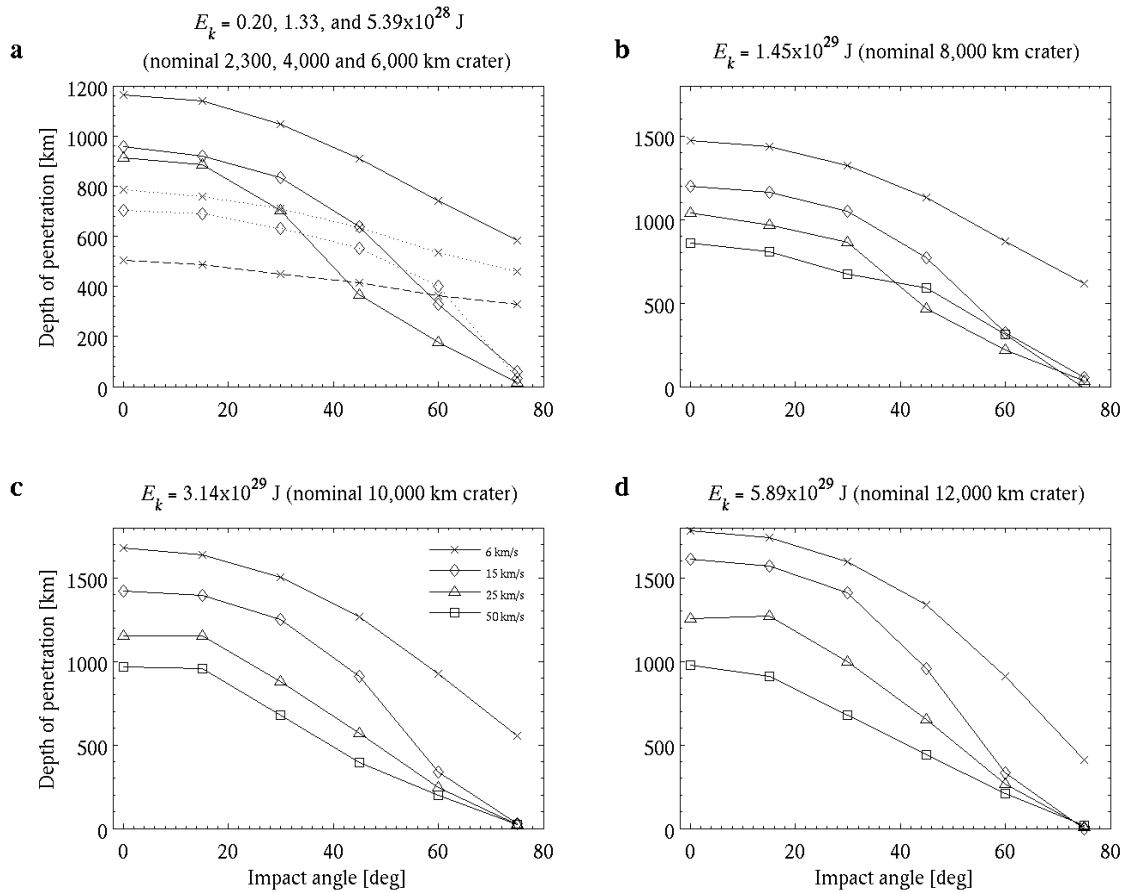


Figure 3-10 Depth of penetration of the deepest 10% of impactor mass. Shown are the results for all simulated energies, and a sampling of impact velocities. The legend in (c) applies to all panels. Panel (a) shows the results for three impact energies: $E_k = 1.98 \times 10^{27} \text{ J}$ (dashed line) with only $v_{imp} = 6 \text{ km/s}$ shown, $E_k = 1.33 \times 10^{28} \text{ J}$ (dotted line) with only $v_{imp} = 6 \text{ and } 15 \text{ km/s}$ shown, and $E_k = 5.39 \times 10^{28} \text{ J}$ (solid line) with only $v_{imp} = 6, 15, \text{ and } 25 \text{ km/s}$ shown; the reduced range of plotted velocities is as per Table 3–1. The full range of velocities is shown in (b–d). The core-mantle boundary is at a depth of 1,800 km.

We find that the depth of penetration is chiefly a function of the impactor’s mass and impact angle (Figure 3–11), and is modulated by impact velocity. Since the results reported here are only for one impactor type, we cannot deconvolve the importance of impactor mass and size. Given the observed logarithmic relationship between impactor mass and penetration depth, we find the scaling relationship

$$h' = c (M'_{imp})^d \cos \gamma$$

where h' is the depth of penetration normalized by the planetary radius, M'_{imp} is the impactor mass normalized by the planetary mass ($M_0 = 6.41 \times 10^{23}$ kg), γ is the impact angle, and c and d are constants. The best fit (and 95% confidence intervals) for these basalt impactors is obtained with $c = 1.00^{+0.08}_{-0.06}$ and $d = 0.179^{+0.014}_{-0.011}$ for impact angles of 0 to 60°. For $\gamma = 0^\circ, 15^\circ, 30^\circ,$ and 45° , the mean absolute errors (all velocities) are 11%, 11%, 8%, and 20%, respectively; for 60° impacts the fitting error increases to 68%. Impacts with a 75° impact angle have penetration depths generally less than a resolution element (120 km), resulting in a high uncertainty of the results; these results are not included in determining the fit. The large error associated with the 60° impacts also likely reflects the uncertainty in the associated shallow depth of penetration ($\langle h \rangle = 380 \pm 210$ km). The fit parameterization is supported by the physically-realistic zero penetration for an infinitesimal impactor mass, and the significant increase in fitting error when the fit is simplified by removing the power law dependence on the impactor mass: setting $d = 1$ results in a non-viable fit. The fit residuals have a standard deviation of ~ 140 km (1.2 particle diameters), suggesting that the fit complexity is appropriate given the uncertainty in the results (see *Resolution effects*).

The error of the fit can be reduced modestly by the addition of a power law dependence on the impact angle, which is commonly assumed (e.g., Pierazzo and Melosh, 2000a; Pierazzo and Melosh, 2000b), and is supported by the change in slope with impact angle seen in the results (Figure 3-11):

$$h' = c \left(M'_{imp} \right)^d \cos^e \gamma$$

The best fit (and 95% confidence intervals) for these basalt impactors is obtained with $c = 1.05^{+0.13}_{-0.08}$, $d = 0.176^{+0.018}_{-0.013}$, and $e = 1.48 \pm 0.15$ for impact angles of 0 to 60°. The

uncertainties in the fitting parameters are not independent: the correlation of c with d and e is -1 and 0.022 , respectively. The fit residuals have a standard deviation of ~ 115 km (one particle diameter), suggesting that this fit complexity is also appropriate given the uncertainty in the results (see *Resolution effects*). For $\gamma = 0^\circ, 15^\circ, 30^\circ$, and 45° , the mean absolute errors (all velocities and energies) are 9%, 9%, 8%, and 17%, respectively. For 60° impacts the mean absolute error of the fit increases to 44%. Impacts with a 75° impact angle are not included in determining the fit. Both penetration depth scaling relationships suggest that for head-on impacts, penetration of the crust ($h = 50$ km) requires an impactor mass of $\sim 2 \times 10^{13}$ kg (~ 5 km diameter impactor), which is of order the calculated 10–14 km diameter of the Chicxulub impactor (Morgan et al., 1997). Detailed simulations of the Chicxulub impact using the 3D hydrocode CTH and a dunite impactor have shown a depth of penetration of 15–25 km, depending on impact angle, for a 10 km diameter impactor (Pierazzo and Melosh, 1999), in general agreement with our fitting results.

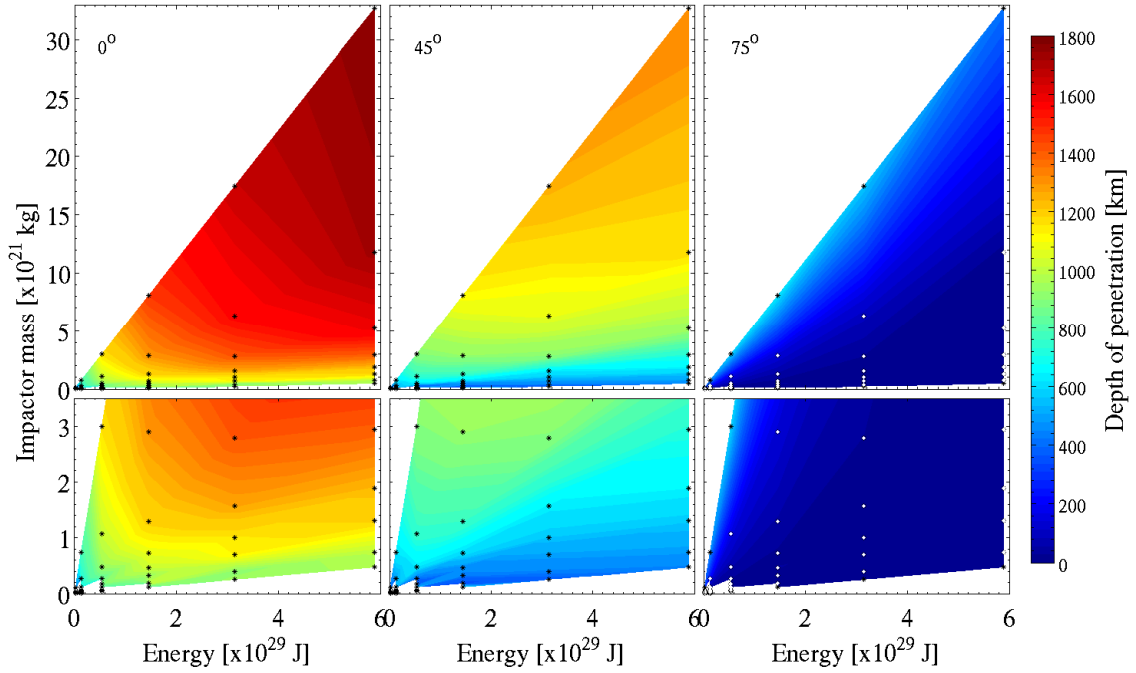


Figure 3-11 Depth of penetration as a function of impactor mass and energy for the range of simulated impact angles. The bottom row of panels is a blow-up of lowest range of impactor mass (y-axis). The conditions of the simulated impacts (black stars) are overlaid. The contour lines are generally horizontal, especially for the head-on impacts, suggesting that the depth of penetration is chiefly a function of the impactor mass.

We compare our simulation results for head-on impacts to those of O’Keefe and Ahrens (1993), who developed a scaling relation based on numerical models of impacts into a half-space, single material configuration. O’Keefe and Ahrens (1993) give the scaling relationship $h = 1.2 r_{imp}^{0.78} g^{-0.22} v_{imp}^{0.44}$, where h is the depth of penetration (m), r_{imp} is the impactor diameter (m), g is the acceleration due to gravity (m/s), and v_{imp} is the impact velocity (m/s). Using the mass of the impactor instead of the impactor’s radius, the relationship is $h \propto M_{imp}^{0.26}$, similar to, but steeper than, the dependence found from our results for head-on impacts ($h \propto M_{imp}^{0.176}$). The O’Keefe and Ahrens (1993) scaling gives a penetration depth about 15% to 50% greater than found in our simulations, for the range of simulated impactor masses. By O’Keefe and Ahrens’ scaling into a single-

material target, impact energies above $\sim 2 \times 10^{29}$ J (impactor mass $> 10^{21}$ kg) give penetration depths greater than 1,800 km, which would result in core penetration for a Mars-like planet; no core penetration is present in any of our simulations. The difference in results is not surprising given the model differences, and highlights the importance of both geometry of the impacted surface and the presence of a substantial density discontinuity on the penetration depth.

3.4.2.2 Melt production and the maximum retainable crater size

In planetary-scale impacts, the amount, and especially the distribution, of melt determine the preservation of the impact structure (not taking into account later geological modification). Our simulations show that the amount of melt is primarily a function of impact energy and angle (Figure 3-12). The amount of melt increases with increasing impact energy, as would be expected since more energy is available to be deposited into the planet, and decreases for more oblique impacts, since more material is ejected into space and thus more of the impact energy is carried away as kinetic energy. For a given impact energy and angle, the melt production is a weak function of impact velocity, as can be seen in Figure 3-12. For head-on impacts, the figure also shows a consistent trend in melt production with impact velocity: the most melt is produced by 15 km/s impacts (dashed line), with less melt produced by the slower 6 km/s (solid line) and the faster 50 km/s (dotted line) impacts. For head-on impacts, the trend can be understood as follows. At constant energy, slower projectiles produce only a compression wave, with little or no shocks, and deposit little energy in the material per unit volume. However, the large impactor effectively initiates a plane compression wave, as it encounters the planet

before it is slowed by the backward-travelling compression wave. The plane compression wave deposits little energy per unit mass into the compressed material; however, this occurs over a large area and therefore a large volume. Since the planet is already near its melting point this added energy is sufficient to cause melting. As the velocity increases, the shockwave strength increases as well, and thus a larger volume of material is compressed and heated beyond its melting point. However, as impactor velocity increases further at the same impact energy, the impactor size decreases such that the shockwave initiation region more closely approximates a point source. The higher impact velocity results in higher shock pressures at the source, and thus more energy deposited per unit mass; however, due to the point source and radial shock strength decrease, the total volume of material that is compressed to the melting limit decreases. This effect is illustrated by the cumulative planetary material above a given internal energy after the impact (Figure 3-13a): at constant impact energy, the total mass that exceeds the melting criterion is lowest for the slowest, 6 km/s impact; increases to a maximum for the intermediate velocity, 15 km/s impact; and as the velocity increases further the melted mass decreases. The magnitude of the effect is consistent with the observed variation in impact melt with impact velocity, holding impact energy and angle constant. The figure also illustrates the increase in energy deposited per unit mass with increasing velocity: the fastest impact produces the highest internal energy per unit mass, and the slowest impact the lowest specific internal energy.

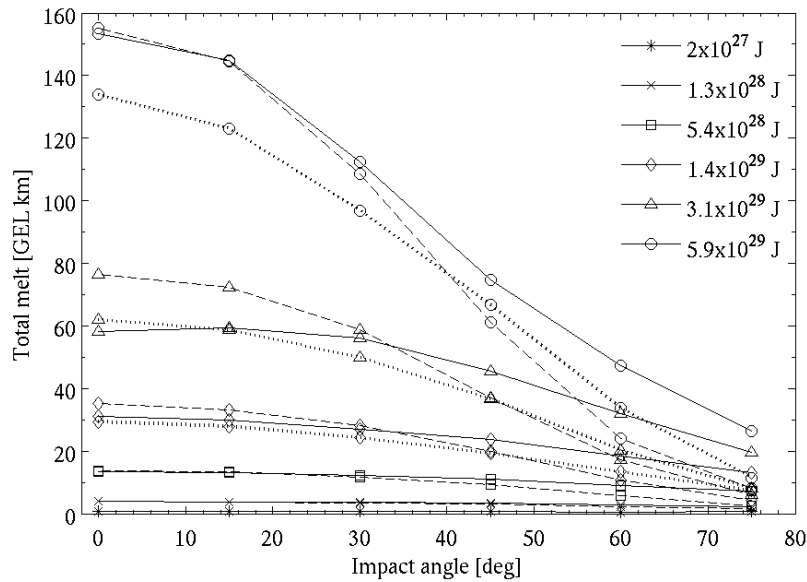


Figure 3-12 Amount of melt produced by 6 km/s (solid line), 15 km/s (dashed line), and 50 km/s impacts (dotted line), for all simulated energies (symbols), in terms of global equivalent layer (GEL) depth on Mars (1 km GEL = 5.1×10^{20} kg melt). GEL depths are illustrative of the total melt amount, but are not representative of the actual melt distribution on the surface.

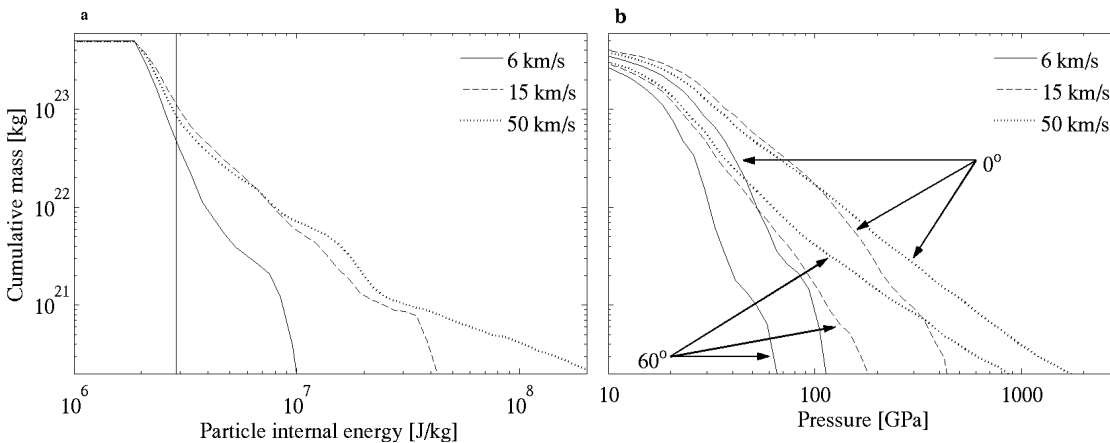


Figure 3-13 Post-impact internal energy and pressure. Cumulative distribution function of planetary mass as a function of the maximum achieved (a) specific internal energy and (b) pressure during the impact event, for an impact energy of $E_k = 3.14 \times 10^{29}$ J. In panel (a), the vertical solid line represents the olivine melting criterion at zero pressure, showing the approximate mass that is molten for the given velocity impact. Note that the slowest, 6 km/s impact produces the least melt, the melt amount reaches a maximum for the intermediate velocity, 15 km/s impact, and then decreases slightly as the impact velocity increases further, similar to the results shown in Figure 3–12. In panel (b), the pressure profiles show a similar behavior, with the notable low maximum pressures achieved by the slowest impacts. Note that the total planetary mantle mass is 4.9×10^{23} kg.

The amount of material that is compressed during the impact event provides insight into phase changes and petrographic signatures that may be left in the shocked material. The maximum pressure produced by the impact increases from the slowest to the fastest impact velocities, as would be expected and as discussed above (Figure 3-13b). Maximum pressures of about 4,200, 4,700, and 5,300 GPa are achieved by impacts with energies of 1.45, 3.14, and 5.89×10^{29} J, in each case by the 50 km/s impacts. Using the planar impact approximation, with the Tillotson parameters, the maximum expected impact pressure is 3,800 GPa. For a given impact velocity and energy, the highest pressures occur for intermediate impact angles. The variation of maximum pressure with impact angle and velocity is similar for all simulated energies. The compression of material up to 200 GPa is of particular interest for geologic materials since petrographic shock indicators are sensitive to this range and most materials will be molten or vaporized when decompressing from higher shock pressures. We find that for head-on collisions, faster impacts (> 15 km/s) compress similar amounts of material for the range of 0–150 GPa. However, faster impacts compress about an order of magnitude more material than the slowest (6 km/s) impacts for impact angles of 0–60° (Figure 3-13b). For the most oblique impacts simulated here (75°), the cumulative mass achieving a given pressure falls off more steeply than for shallower angles. The decreasing total pressurized mass with increasing impact angle is explained by the decrease in energy deposited in the target, as a larger fraction of the impact energy is carried away by ejected material.

In the energy range simulated here, the melt volume is equivalent to tens of kilometers' depth if distributed evenly as a global equivalent layer (GEL) over the

planetary surface (Figure 3-12). While such large melt amounts may suggest a global magma ocean, the actual melt distribution is highly heterogeneous (Figure 3-14); only for the most energetic impacts is the melt cover sufficiently widespread that complete surface resetting would be expected. The impact energy above which the surface is reset signifies the upper limit for planetary-scale crater retention. Impact energies less than 1.45×10^{29} J ($\leq 8,000$ km nominal crater size) result in less than 9% surface melt cover, and only for the most energetic impacts ($E_k = 5.89 \times 10^{29}$ J) is more than 25% of the surface covered by melt. The maximum melt cover for any of the performed simulations is 71%, resulting from a 5.89×10^{29} J, head-on impact at 10 km/s.

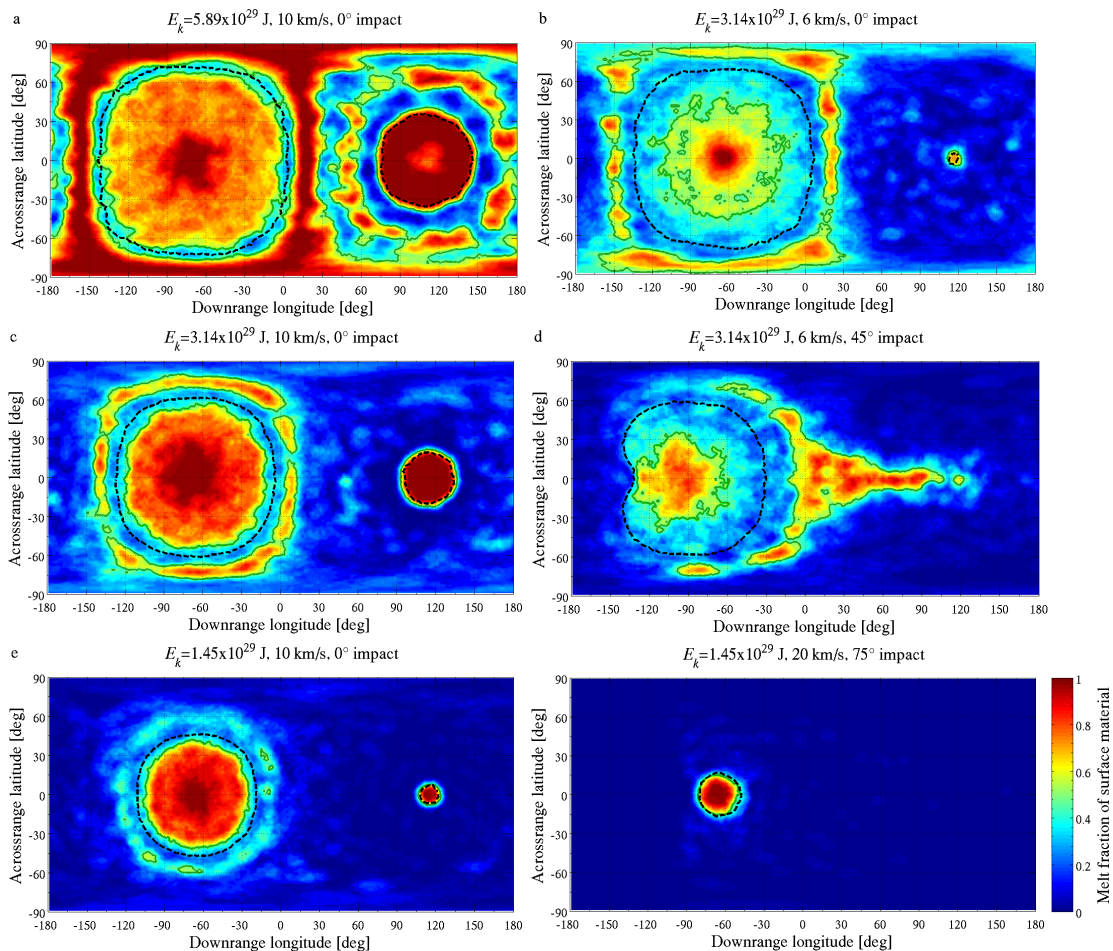


Figure 3-14 Melt distribution with varying impact conditions. Most of the melt is contained within the crater (dashed line) and extends to depth (Figure 3–9). Melt pools (more than 50% surface melt fraction) are outlined (green), as is the antipodal cavity (antipodal area with > 20% crustal excavation; see *Antipodal disruption*). In oblique impacts, some melt is deposited downrange of the impact but also more melt is ejected.

The partitioning of melt between the surface, subsurface, and ejected to space is a function of the impact characteristics (Figure 3-14, Figure 3–15). Specifically, not only is the amount of melt on the surface of the planet – and particularly on the surface outside the crustal excavation boundary – a function of the impact angle and velocity, but the relative distribution of melt also changes with impact energy (Figure 3-15). With increasing energy, an increasing fraction of molten material is deposited in the mantle and ejected from the planet. Consequently, a smaller melt fraction is deposited on the

planetary surface, both outside and inside the crustal excavation boundary; the only exception is the increasing fraction of molten material inside the cavity for the highest simulated impact angle (75°). For the lowest energy impacts, 45–60% of the melt is on the surface outside the crustal excavation boundary, while for the highest energy impacts, 18–30% of the melt is outside the boundary. This change in melt distribution is due to more energetic impacts also containing more momentum and penetrating deeper into the mantle. This results in the impact energy being deposited deeper in the mantle, producing both absolutely and relatively more mantle melt and relatively less molten material on the planet's surface. Additionally, the fraction of melt that is ejected increases with impact energy, further reducing the surface melt cover. Because of the heterogeneity in melt distribution, as well as the changing partitioning of melt between locations as a function of impact energy, the energetic limit for retaining a signature of the impact event is higher than would be expected from total melt amount considerations.

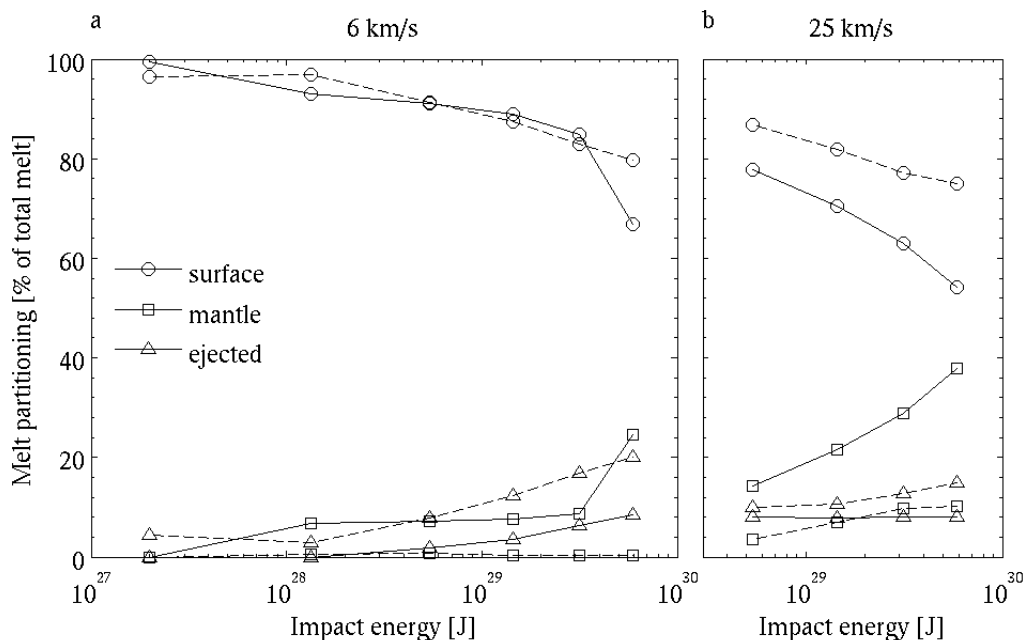


Figure 3-15 Partitioning of melt: in the surface layer (inside and outside the crater), in the mantle, and ejected to space. Results shown are for 0° (solid line) and 75° (dashed line) impact angles, and impact velocities of (a) 6 km/s and (b) 25 km/s; an impact velocity of 25 km/s could not be simulated for impact energies of 0.20 and 1.33×10^{28} J (Table 3-2). The trends are similar for all impact velocities. Note that with increasing impact energy the fraction of melt distributed on the surface decreases, while a higher fraction of melt is ejected to space or sequestered at depth.

Impact angle affects the distribution of melt more significantly than velocity, for a given impact energy in the simulated range of parameter space. For constant energy and impact angle, the melt inside the crustal excavation boundary and ejected melt remain about constant with impact velocity. The fraction of melt outside the excavation boundary decreases by about 10% with increasing impact velocity (from 6 to 50 km/s), and mantle melt generally increases by about 15% from 6 to 20 km/s and then remains constant for higher velocities (compare to Figure 3-15).

Our melt production results show a constant melt to impactor volume ratio for head-on impacts of a given velocity (Figure 3-16), in agreement with the calculations by O'Keefe and Ahrens (1977) for impacts into a planar target. This relationship is a

statement that melt production is proportional to impact energy, as is also seen in our findings and exemplified by the good fit of the quadratic relationship $V_{melt}/V_{imp} = \delta v_{imp}^2$ to our data (Figure 3-16), where V_{melt} is the melt volume, V_{imp} is the impactor volume, and δ is a constant. In fitting our data, the best fit (and 95% confidence interval) is obtained with $\delta = 0.0421^{+0.0028}_{-0.0019}$ s²/m², giving a mean absolute error of 12%. The fit can be modestly improved by also fitting the power dependence of velocity, which then gives an exponent value of $1.84^{+0.12}_{-0.09}$ and $\delta = 0.075^{+0.028}_{-0.025}$; the resulting mean absolute error is 9%. Applying the same quadratic fit to the four data points given in O'Keefe and Ahrens (1977), the best fit (and 95% confidence interval) is $\delta = 0.0497^{+0.0006}_{-0.0034}$, with a mean absolute error of 25%, where the absolute error of 75% for the slowest velocity data point significantly biases the overall mean error. Fitting a power law relationship to the O'Keefe and Ahrens data gives a best fit (and 95% confidence intervals) for an exponent of $2.18^{+0.39}_{-0.96}$ and $\delta = 0.025^{+0.004}_{-0.016}$, with a mean absolute error of 7%.

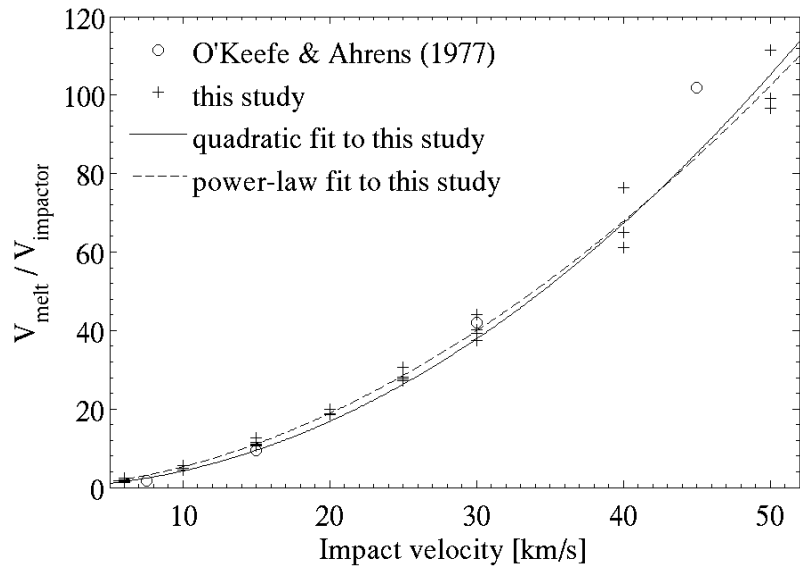


Figure 3-16 Melt to impactor volume ratio as a function of impact velocity for head-on impacts. Our results (crosses) are very close to the small, half-space impact simulation results of O'Keefe and Ahrens (1977; circles) for a gabbroic anorthosite impactor and target. The results show that the melt amount scales with impact energy, as exemplified by the good fit of a v_{imp}^2 scaling (solid line, fit to results of this study). Our multiple results for a given impact velocity represent the range of impact energies we simulated; no consistent trend is present for V_{melt}/V_{imp} versus impact energy for all impact velocities.

Dence (1965) showed that field observations of melt produced in impact events on Earth can be described by a power law relationship:

$$M'_{melt} = \varepsilon(D')^\xi,$$

where M'_{melt} is the melt mass normalized by the planetary mass ($M_0 = 6.41 \times 10^{23}$ kg for Mars, $M_0 = 5.97 \times 10^{24}$ kg for Earth), D' is the crater diameter normalized by the planetary radius ($R_0 = 3,313$ km for Mars, and $R_0 = 6,370$ km for Earth), and ε and ξ are fitting constants. Here we use the melt mass rather than melt volume, to avoid ambiguities about the density of the material given its internal energy and pressure state.

Using this functional form we fit Earth field observations of craters ranging from 4.5 km to 200 km in diameter as listed in Table 1 of Grieve and Cintala (1992), excluding Ries

and Logoisk craters because of their abnormally low melt masses, and Brent crater as the only crater below the simple-to-complex size transition. We obtain fitting values (and 95% confidence intervals) of $\varepsilon = (1.69^{+2.71}_{-1.00}) \times 10^{-4}$ and $\xi = 2.99 \pm 0.18$, giving a mean absolute error of 34%. Using the same functional form to fit our simulation results, we find that fast impacts (≥ 15 km/s; all impact energies and angles) are well fitted (and 1σ confidence intervals) by $\varepsilon = (0.937 \pm 0.018) \times 10^{-2}$ and $\xi = 2.33 \pm 0.04$; mean absolute error of 6% (Figure 3-17). Slower impacts (6 km/s and 10 km/s) significantly deviate from a simple power law, producing less than half as much melt for a given crater diameter than would be expected from the power scaling. This deviation is consistent with the decrease in melt production seen in our simulations for a given impact energy at low impact velocities. The effect is likely due to these slower impacts producing a shock pressure that is comparable to the melting pressure of the mantle material, thus pressure melting does not significantly contribute to the total melt amount. On Earth, where the escape velocity, and hence, the minimum impact velocity is ~ 11 km/s, this deviation is not expected to occur since the shock pressures would be significantly higher.

Thus, comparing the scaling for small Earth impacts to the planetary-scale impacts results, we find that for small craters the melt volume is directly proportional to the excavated volume ($V_{melt} \propto D^3$), while for planetary-scale impacts, melt increases with a smaller exponent ($V_{melt} \propto D^{2.3}$). It should be noted that the excavated volume scaling is not appropriate for the planetary-scale size regime, since it is strictly only applicable for an infinite half-space. The empirical fit of the melt volume versus crater diameter is about 20 times larger for planetary-scale impacts than for small impacts. This significant difference may be the result of several factors including an underestimation of melt

volume from field observations of craters on Earth, as has been noted to be the case for at least some craters (Grieve and Cintala, 1992); and the difference in the thermal state of the effectively cold, crustal target in small impacts versus the close-to-melting mantle target in planetary-scale impacts.

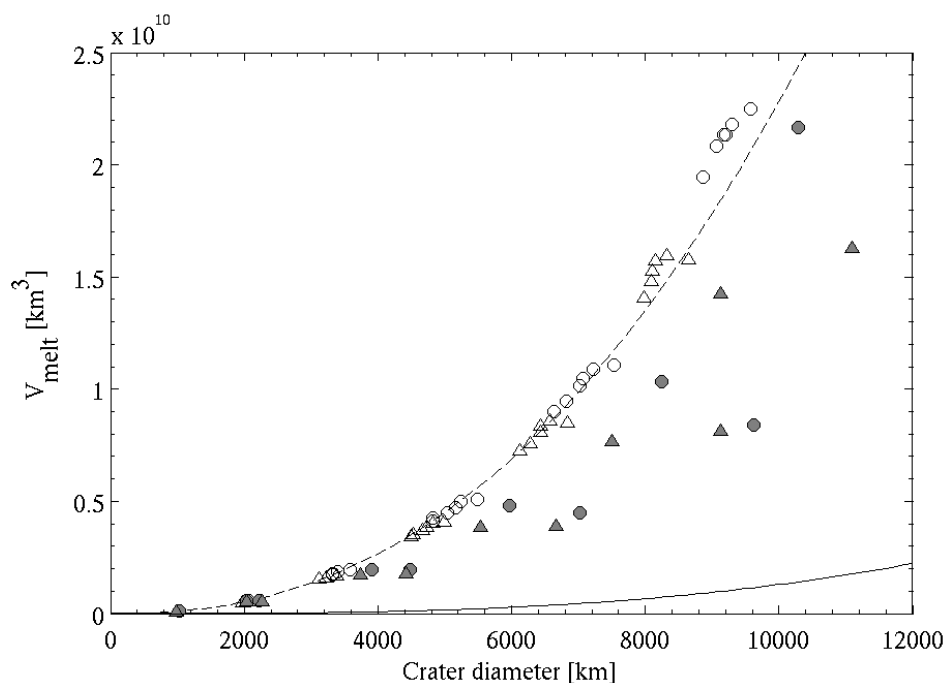


Figure 3-17 Melt volume scaling comparison: our head-on and 30° impacts results (open circles and open triangles, respectively) and fit (dashed line) versus a fit to Earth field observations (solid line) as reported by Grieve and Cintala (1992). The planetary-scale impacts results follow a trend similar to the Earth scaling, except for a significant deviation from the trend for our simulated impact velocities of 6 and 10 km/s (shaded symbols). The deviation likely results because these slower impacts cannot initiate a strong shockwave in the target material. A mean density of 3,500 kg/m³ was assumed for the melt.

Combining the scaling relationships between melt volume and impactor diameter discussed above, with the scaling between impactor diameter and impact energy developed earlier, supports the exceptional similarity in the scaling of melt amount with impact energy between small and planetary-scale impacts (Figure 3-16). For small impacts in the gravity regime, the scaling relationships between melt, excavated cavity

size, and energy are $V_{melt} \propto D^3$ and $D \propto E_k^{0.29}$, giving $V_{melt} \propto E_k^{0.87}$. For planetary-scale impacts, the scaling relationships are $V_{melt} \propto D^{2.3}$ and $D \propto E_k^{0.39}$, giving $V_{melt} \propto E_k^{0.90}$: the power law dependence of melt volume on impact energy is very similar for small and planetary-scale impacts. The comparable melt to energy scaling relationships suggest that the impact energy is partitioned similarly into thermal and kinetic energy in both size regimes. For planetary-scale impacts, this trend is apparent in the consistent ejection mass normalized by impactor mass trends for all simulated energies. While for small impacts in the gravity regime material is not necessarily ejected from the planet, the excavation of material carries kinetic energy away from the impact site.

Tonks and Melosh (1993) modeled melting caused by planetary-scale impacts, taking into account the sphericity of the planet. They calculate the strength of the shockwave with distance from the impact site and compared this to the pressure melting criterion for the impacted material (dunite with a composition of Fo₈₈). For a 15 km/s impact with a 0.01 impactor/planet mass ratio, similar to our $E_k = 5.89 \times 10^{29}$ J (nominal 12,000 km crater), 15 km/s impact simulation, Tonks and Melosh (1993) give an upper bound result of ~8% melting of the planet (for an initial planetary temperature of 1,490 K) compared to our computed melt fraction of 12% of the planet (15% of the mantle); melting of the impactor is not included. The discrepancy in the results may be explained by our higher initial mantle temperature compared to that used in the Tonks and Melosh model. Additionally, the Tonks and Melosh model simulates impacts into an undifferentiated, dunite planet. An impact with such high energy penetrates about 1,600 km into the planet and deposits some of its energy directly at depth, affecting the total melt production.

Relating the surface melt cover fraction to the total melt amount seen in our results, we use a *sigmoid* function:

$$f_{melt} = \frac{-1}{e^{-\Psi}} + \frac{1 + e^{-\Psi}}{e^{-\Psi}(1 + e^{-\Gamma M_{melt}'' - \Psi})}$$

where f_{melt} is the fraction of the planet covered by melt, M_{melt}'' is the mass of melt normalized by the mass of the surface layer ($M_{surf} = 7.09 \times 10^{22}$ kg), and Γ and Ψ are fitting constants. The best fit values (and 95% confidence intervals) for these basalt impactor simulations are obtained with $\Gamma = -1.74 \pm 0.29$ and $\Psi = 2.00^{+0.34}_{-0.29}$ (Figure 3–18). The mean absolute error, for fitting all simulations simultaneously, is 11%. Note that the melt fraction does not distinguish between melt inside and outside the crustal excavation boundary, and at the antipode. It is also noteworthy that the surface melt cover fraction remains proportional to the total melt amount, despite the change in the fraction of the total melt in each of the four reservoirs (melt on the surface inside and outside the excavation cavity, in the mantle, and ejected to space).

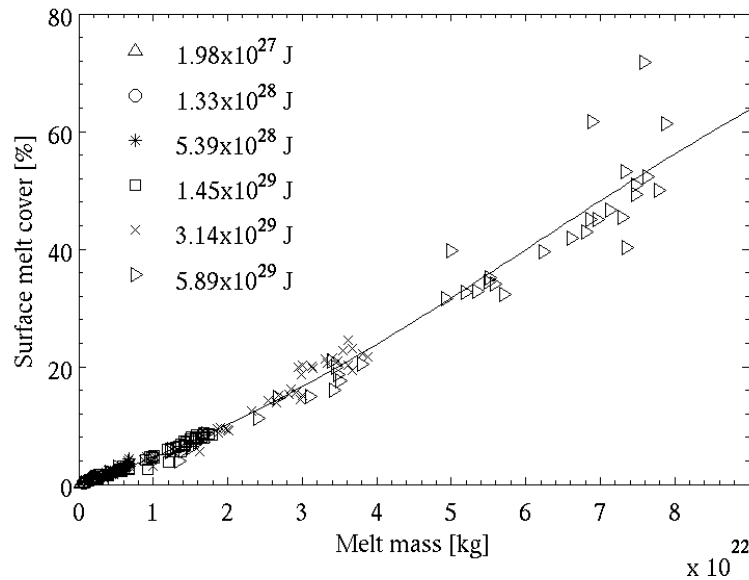


Figure 3-18 Surface melt fraction as a function of melt amount. The symbols represent the range of simulated energies, while the solid line is the fitted relationship.

3.4.2.3 *Antipodal disruption*

The shockwave initiated by an impact travels through the planet and converges at the antipodal free surface boundary. Antipodal stresses larger than the material tensile strength will cause fracturing (Schultz and Gault, 1975), and stronger shocks can accelerate antipodal material sufficiently to remove it. Our simulations show antipodal disruption – here defined as at least 20% crustal removal with respect to the pre-impact crustal thickness – for impact energies above 10^{29} J and for a variety of impact velocities and angles (Figure 3-19). A molten region of the same size as the excavated crust area occurs concurrently. The smallest identified antipodal cavity is ~160 km. While smaller antipodal cavities likely occur, we are unable to distinguish them, due to the model resolution (~120 km) and the grid averaging applied when examining the crustal thickness. Antipodal disruption (crust removal) first becomes apparent for the 1.45×10^{29} J impacts; however, the range of sufficient velocities and angles are limited (Figure 3-19a). With increasing impact energy, antipodal effects occur for a larger range of impact velocities and increasingly oblique impacts, because a stronger shockwave is initiated. No antipodal disruption is present for any of the simulated 75° impacts. Smaller-scale disruption, including crustal fracturing and weakening, is expected to occur at lower energies, but cannot be characterized by our model.

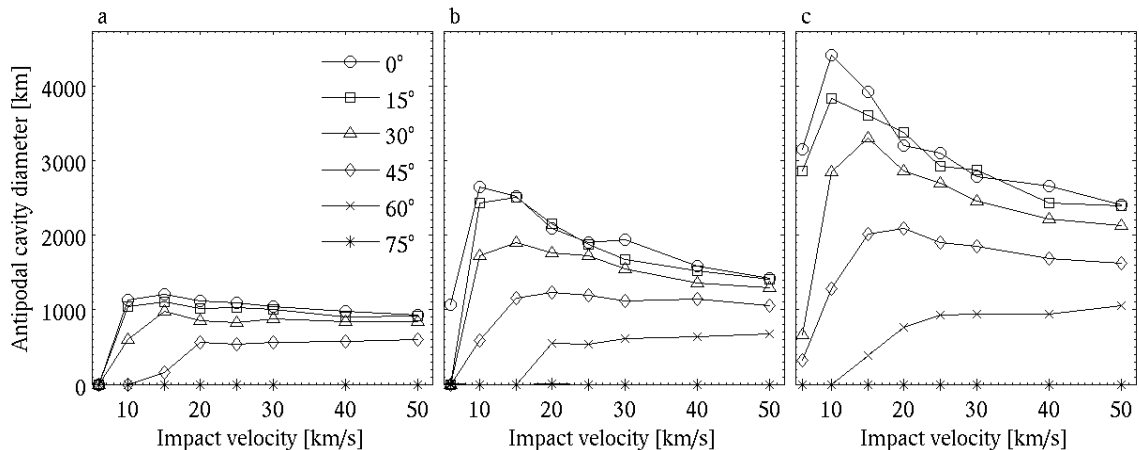


Figure 3-19 Antipodal cavity size for impact energies of (a) 1.45×10^{29} J, (b) 3.14×10^{29} J, and (c) 5.89×10^{29} J for the simulated basalt impactors. Antipodal crust removal is not present for lower energies. Note that the error in this measurement is estimated at $\sim 5^\circ$ (see Table 3–3), thus while the smallest plotted antipodal disruptions do represent significant antipodal stresses, it is uncertain if these stresses result in complete crustal removal.

Previous studies have used numerical modeling to assess whether antipodal features are expected on Mars and correlated their predictions with photogeological observations. For a Hellas-forming impact ($\sim 3.4 \times 10^{27}$ J), Williams and Greeley (1994) found maximum antipodal pressures of 0.99–1.2 GPa for a head-on impact at 6 km/s. They argue that the stress caused by this compressive wave would exceed the tensile strength of the material and cause fracturing, which is now associated with Alba Patera. Our results for a slightly less energetic impact ($E_k = 1.98 \times 10^{27}$ J) show a maximum antipodal pressure of ~ 1.2 GPa, similar to Williams and Greeley (1994) despite their use of a different model (simplified arbitrary Lagrangian Eulerian finite element code), mantle composition (low pressure anorthosite), and a factor of two decrease in resolution (~ 226 km resolution). Our results are consistent with their argument for antipodal fracturing caused by the Hellas impact, and do not show antipodal crustal blowoff or melting for this impact case.

We find a correlation between the antipodal excavated area and the main crater size. Our results show that impacts resulting in a crater larger than $\sim 4,000$ km generate a sufficiently strong shockwave for antipodal crustal excavation, however, other considerations such as the velocity and angle of the impact are also of importance. For example, antipodal surface disruptions are not present for impact simulations of 6 km/s and 5.4×10^{28} J, which produced a crater $> 4,000$ km in diameter. Thus while no antipodal disruption is present for impact energies less than 10^{29} J, a higher impact energy is not a sufficient condition for the presence of antipodal crustal removal.

The general trend between the sizes of the antipodal and primary craters can be described well quadratically:

$$D_{ant} = z \left(\frac{D}{D_{Mars}} \right)^2,$$

where D_{ant} is the antipodal excavated area diameter (km), D is the crustal excavation boundary major axis (km), D_{Mars} is the diameter of Mars (6780 km), and z is a constant. Significant deviations from the trend occur for the slowest antipode-producing impacts for each energy (Figure 3-20). When the 6 km/s impacts are excluded, the best fit (and 1σ confidence intervals) for these basalt impactors is obtained by $z = 1,700 \pm 30$ km, with mean absolute error of 17%; when all results are included, the best fit is obtained by $z = 1,440 \pm 100$ km, with a mean absolute error of 38%. Note that a 6 km/s impact does not initiate a strong shockwave in the planet.

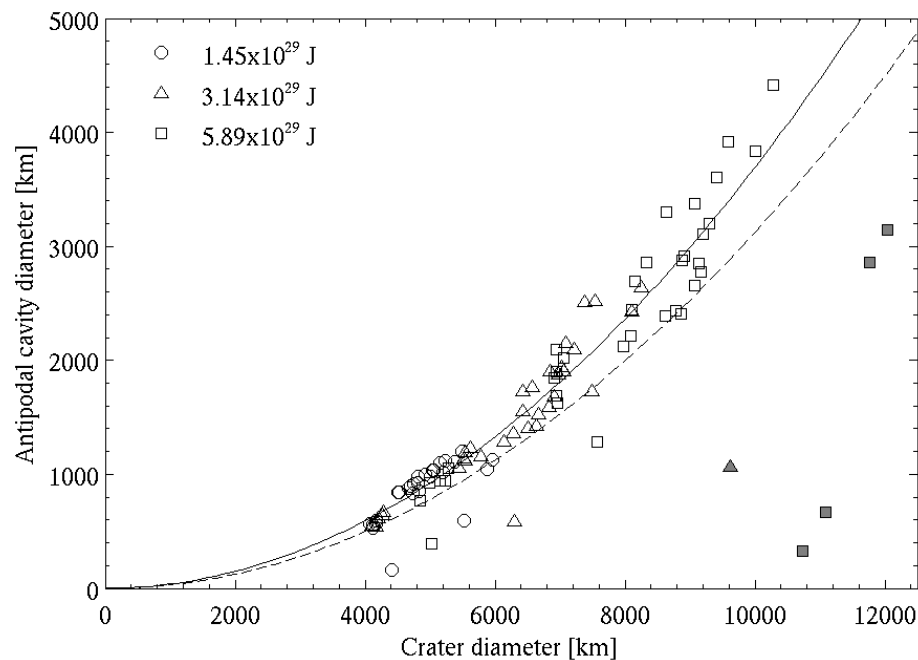


Figure 3-20 Relationship between antipodal and primary crater diameters. A general trend is present, however, notable exceptions to the trend occur for slow velocity impacts (6 km/s impacts are shaded symbols). The fits to all results (dashed line) and only to simulations with an impact velocity greater than 6 km/s (solid line) are shown.

For head-on impacts, the center of the antipodal excavation is diametrically opposite the center of the primary crustal excavation area. With increasing impact angle, as a general trend, the relative location of the antipodal disruption shifts, with a maximum offset of 25° (Figure 3-21a); the offset varies appreciably with impact angle, velocity, and energy. The antipodal disruption is 180° from the location where the energy of the impact is deposited and the shockwave is initiated. The shift in antipode location may be the result of the significant penetration of oblique impacts in the downrange direction before the impactor is stopped. The penetration distance is of order the size of the impactor, thus shifting the effective point of energy release significantly in this size regime. In the case of highly energetic, oblique impacts, this penetration results in a significantly shifted location of the initiation of the shockwave, thus resulting in antipodal crustal excavation

that is not 180° from the center of the primary excavation cavity. To determine the effective location of shockwave initiation in the impact process, we examined the angular distance between the antipodal disruption and: the point of impact, defined as the location of first contact between the planet and the impactor; the stopping point of the impactor, defined as the location of deepest penetration of the impactor; and the point of maximum pressure. All of these locations are better predictors of the antipode location than the center of the primary crater cavity, but no clear trend of impact angle with separation angle is seen. Of the three criteria, the point of maximum pressure most consistently results in a 180° separation from the antipodal disruption (Figure 3-21b); however, a few notable exceptions are present for the slow (6 and 10 km/s) and most energetic ($E_k = 5.89 \times 10^{29}$ J) impacts. Of the three comparisons, the deviation from 180° is greatest for the angle between the impact point and the antipodal cavity. Both the stopping point and maximum pressure point show smaller deviations; however, neither is consistently smaller. This is likely the result of the stopping point not being well defined in the planetary-scale size regime: the impactor material spreads over much of the planet, and for oblique impacts much of the impactor is ejected and not effectively stopped by the planet. This explanation is consistent with the notable deviations from the observed trend occurring particularly for the most massive impactors: the most energetic ($E_k = 5.89 \times 10^{29}$ J) and slowest (6–10 km/s) impacts.

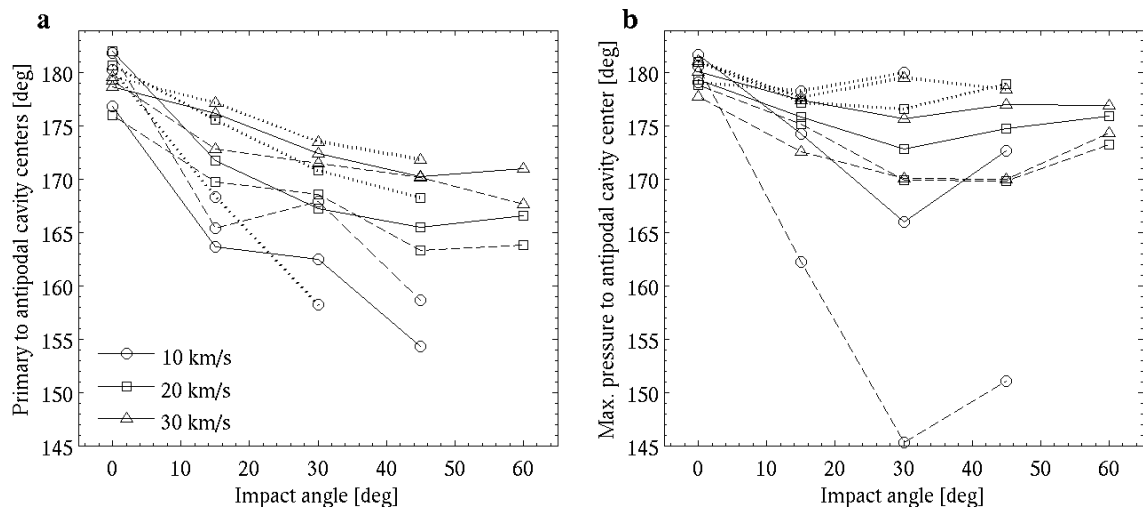


Figure 3-21 Antipodal cavity location. Angular distance between the centers of the antipodal cavity with (a) the primary crater and (b) the point of maximum pressure. Shown are results for impact energies of 1.45×10^{29} J (dotted line), 3.14×10^{29} J (solid line), and 5.89×10^{29} J (dashed line), and impact velocities of 10 km/s (circles), 20 km/s (squares), and 30 km/s (triangles). Deviations from the main trend are limited to the slow (6–10 km/s), most energetic ($E_k = 5.89 \times 10^{29}$ J) impacts, likely due to the massive impactor, and therefore ambiguity in determining the point of maximum pressure and stopping point. For all comparisons the maximum deviation from the trend is for the 30° and 45° impacts.

This sensitivity of the antipodal disruption on the impact conditions, as well as the shift in location of the antipode with impact angle, can provide additional constraints when determining the characteristics of the impactor responsible for a planetary-scale crater.

3.4.2.4 Orbiting and escaping material

During the impact event material is accelerated and can reach orbital or ejection velocities. Orbiting material may accrete to form a moon (Canup and Agnor, 2000), while ejected material greater than the impactor's mass results in net erosion of the target (Asphaug et al., 2006). Orbiting and escaping masses are determined ~25 hrs after the impact, when the distribution of material and particle velocities have reached steady-

state. A particle is orbiting if its velocity is between the circular orbital and escape velocities at its distance from the planet, and its angular momentum is higher than for a circular orbit at the planet's radius). An escaping particle is defined by its velocity exceeding the escape velocity at its location. In our simulations, we find that for impact energies $> 10^{29}$ J, the amount of orbiting material is of order 0.01% of the planet's mass and of order 1% of the impactor's mass (Figure 3-22a). At maximum, the orbiting mass is equivalent to 0.06% of the planet's mass and 15% of the impactor's mass. For a given impact energy, slow and intermediate angle impacts result in the most orbiting material (Figure 3-22a). For the simulated impact energies of 0.54, 1.45, 3.14, and 5.89×10^{29} J, the maximum orbiting masses are 0.46, 1.2, 2.2, and 3.6×10^{20} kg, respectively. For the two lowest simulated energies, the amount of orbiting material is less than the numerical uncertainty of our results, which is of order a few particles (a few percent of the impactor mass; see *Resolution effects*). Longer simulations with more particles are necessary to assess whether the orbiting material accretes to form a satellite.

The largest escaping mass, holding impact energy constant, is for massive (low velocity) and high angle impacts. Pierazzo and Melosh (2000c) similarly found that both the amount of ejected material and its ejection velocity increase with increasing impact angle. We find that for the entire range of simulated impact energies and velocities, and impact angles $< 45^\circ$, 3 to 100 times more mass escapes than is placed in orbit; higher impact angles result in up to 1,000 times more material escaping than orbiting (Figure 3-22). For the simulated impact energies of 0.13, 0.54, 1.45, 3.14, and 5.89×10^{29} J, the maximum escaping masses are 2.5×10^{20} kg, 1.3×10^{21} kg, 4.7×10^{21} kg, 1.3×10^{22} kg, and 2.7×10^{22} kg, respectively (Figure 3-22b). The escaping mass is about a linear function of

impact energy for head-on impacts; the slope of the relationship changes with impact velocity. For the lowest simulated energy, the amount of escaping material is less than the numerical uncertainty (see *Resolution effects*).

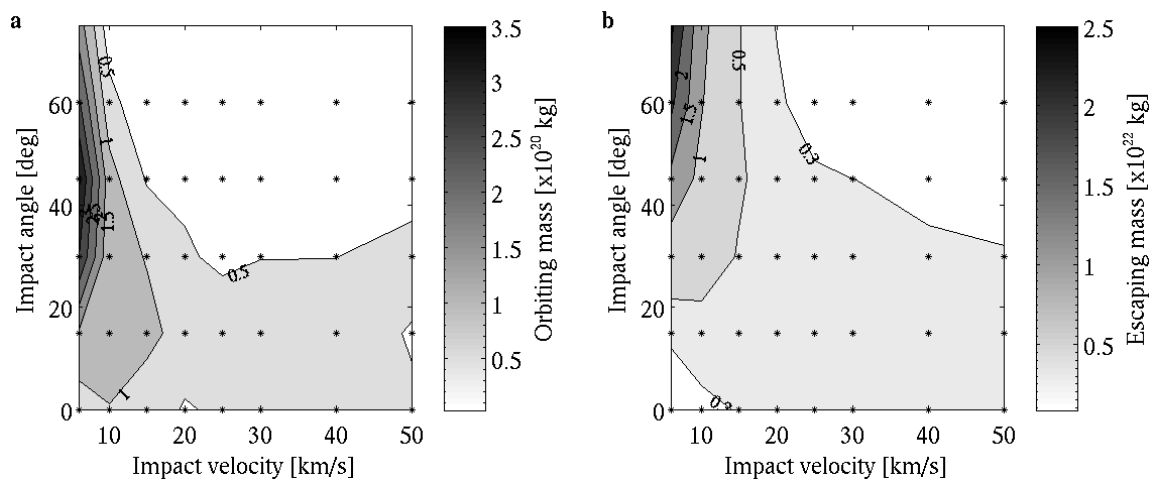


Figure 3-22 Total, post-impact orbiting (a) and escaping (b) masses for the most energetic impact ($E_k = 5.89 \times 10^{29}$ J). The total orbiting mass is significant only for the slowest, oblique, and most energetic impacts. The most material is ejected by slow, highly oblique impacts. The impact angle-velocity trend of orbiting and escaping mass are very similar for all impact energies. Simulated conditions are overlaid (stars).

For small impacts, where peak ejection velocity scales with the crater diameter and ejection velocity decreases radially from the impact point, the ejected and orbiting masses increase monotonically with crater size (Melosh, 1989). However, we find that for planetary-scale impacts, the amount of orbiting and escaping material is not simply a function of the crater size. Instead, we find that for a given crater size, more material is removed by each of larger (slower) impacts, more oblique impacts, and more energetic impacts, holding the other two parameters constant. In the case of constant energy but varying impact velocity (and mass), slower, larger impactors interact with a larger volume of material. The larger interaction volume results in more material being compressed and accelerated upon decompression.

The maximum ejection velocity increases with impact angle and velocity, and increases less significantly with increasing impact energy over the simulated range (Figure 3-23). The change in ejection velocity with impact angle becomes more pronounced at higher impact velocities. For impact energies of 1.45 to 5.89×10^{29} J and an impact velocity of 6 km/s, the maximum ejection velocities are about 11 km/s for all impact angles. However, significantly higher ejection velocities result from the highest impact velocity (50 km/s) and most oblique (75°) impacts: maximum ejection velocities of 64 km/s, 77 km/s, and 79 km/s for the $E_k = 1.45$, 3.14, and 5.89×10^{29} J impacts, respectively. The particles that attain the highest ejection velocities are located on the downrange side of the collision point. Higher maximum ejection velocities are also correlated with maximum achieved pressure, for a given impact angle, as the highly pressurized material expands to high velocities. The ejection velocity increases with impact angle due to the corresponding shallower burial of highly pressurized material and its decreasing radially-inward velocity vector at the end of the compression stage, as discussed in *Crustal thickness and redistribution*. Similar to small impacts, planetary-scale head-on impacts result in a material ejection angle of $\sim 45^\circ$ through the penetration stage. The ejection angle appears to increase slightly with increasing impact angle.

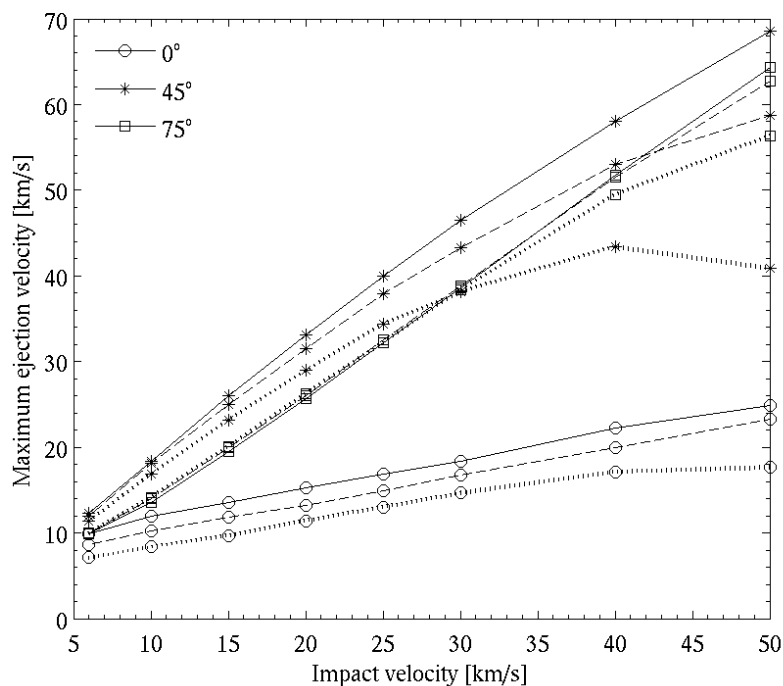


Figure 3-23 Maximum ejection velocities for simulations with impact energies of $E_k = 1.45 \times 10^{29}$ J (dotted), 3.14×10^{29} J (dashed), and 5.89×10^{29} J (solid). For a given impact angle and velocity, the maximum ejection velocity changes by up to a few km/s for this range of impact energies. Variation in either impact angle or velocity can cause a change in the maximum ejection velocity of up to 50 km/s, holding impact energy constant.

Impact events where the sum of the orbiting and ejected material exceeds the mass of the impactor result in net removal of mass from the planet; that is, the impact is erosive rather than accretionary. We analyzed the simulations for orbiting and escaping material as a fraction of the impactor mass to determine the parameters for which a collision transitions from being accretionary to erosive. The maximum orbiting and escaping mass are equivalent to 0.1 and 7.7 times the impactor's mass, respectively, and in both cases are the result of fast, head-on ($<45^\circ$) impacts. The results for orbiting and escaping material normalized by impactor mass, as a function of impact angle and velocity, are very similar for all simulated energies; only a partial comparison could be made for the lower impact energies since the full range of impact velocities could not be

simulated (Table 3–2). The results show that for all energies in the simulated range, net erosion occurs for impact velocities higher than ~ 18 km/s, or ~ 3 times the mutual escape velocity, for all simulated impact angles (Figure 3-24). An impact velocity of ~ 2 times the mutual escape velocity, results in $\sim 50\%$ accretion. Planetesimal accretion simulations generally assume that all collisions are inelastic, merging the impactors into a single object (e.g., Agnor et al., 1999; Chambers, 2001). Planet formation simulations show that in the first million years impact velocities are comparable to the mutual escape velocity, implying complete accretion according to our results. However, later impacts are at higher velocities, up to six times the mutual escape velocity (Agnor et al., 1999), suggesting that the use of more realistic accretion efficiencies may be important in simulating and understanding these later stages.

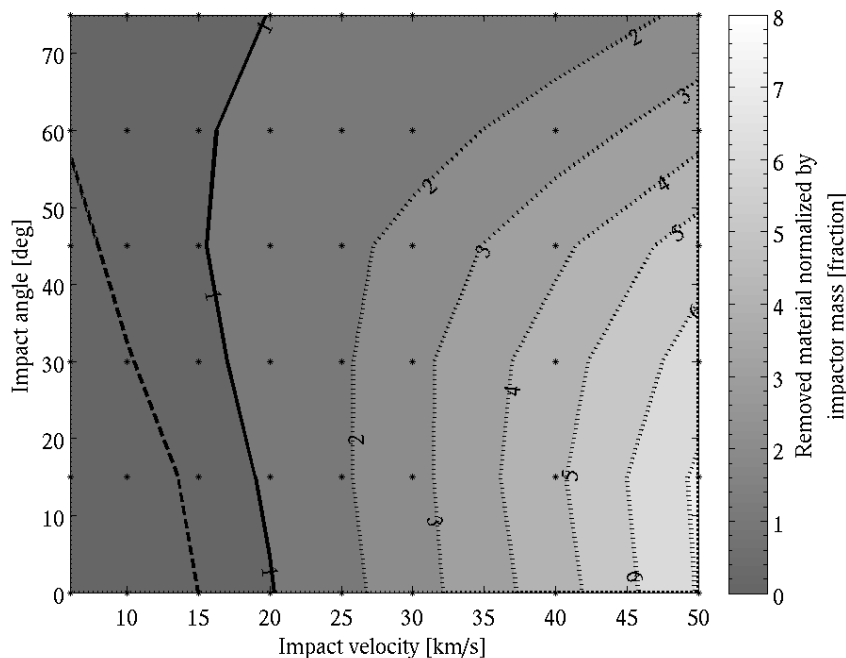


Figure 3-24 Accretionary versus erosive impacts. Removed material (escaping and orbiting) normalized by impactor mass for an impact energy of 3.14×10^{29} J; the results for all other impact energies are very similar. The contours where the equivalent of half of the impactor mass (dashed line) and no net material (solid line) are removed are overlaid. Net mass erosion occurs for velocities above ~ 18 km/s, which is ~ 3 times the two-body escape velocity. The majority of removed mass ($> 98\%$) escapes. Simulated conditions are overlaid (stars).

3.4.2.5 *Post-impact rotational period*

Off-axis impactors transfer angular momentum to both the planet and to orbiting and escaping ejecta. The efficiency of angular momentum transfer to the target can be determined in our simulations by examining the post-impact rotational rate of the planet (Figure 3-25); in our simulations the planet is stationary prior to the impact event. For a given impact energy, the angular momentum carried by the impactor increases with increasing impact angle and increasing mass (decreasing velocity).

Angular momentum transfer efficiencies to the planet are highest for low angle (close to head-on) and low velocity (massive) impacts (Figure 3-25). This is due to both the low amount of ejected material and its low ejection velocity. As the impact angle increases, holding impact energy and velocity constant, the momentum transfer efficiency decreases. For impact velocities < 20 km/s this is the result of both the ejected mass and the ejection velocity increasing; for impact velocities > 20 km/s, the ejected mass decreases but the increase in ejection velocity dominates, still resulting in lower momentum transfer efficiency to the planet. This pattern is similar for all impact energies; however, over the simulated two-orders-of-magnitude energy range, the overall angular momentum transfer efficiency decreases by $\sim 15\%$ with increasing impact energy. This efficiency decrease is due to more momentum being carried away as the material ejection velocity increases with increasing impact energy, holding impact angle and velocity constant.

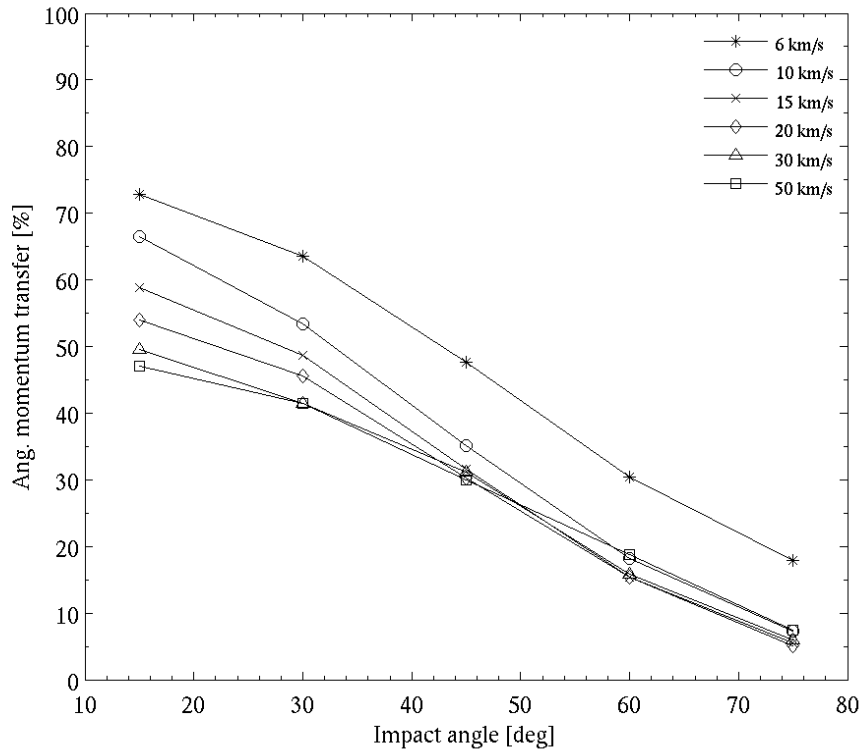


Figure 3-25 Efficiency of angular momentum transfer to the planet: post-impact angular momentum of the planet as a fraction of the angular momentum carried by the impactor. $E_k = 3.14 \times 10^{29}$ J.

The angular momentum carried by oblique impactors with impact energies more than 10^{29} J exceeds the angular momentum of a Mars-size planet with a rotation period of order 10 days, for our simulated range of parameters. Our simulated impactors in this energy range are also consistent with the expected size of planetesimals in Mars-like orbits at the end of accretion (e.g., Chambers, 2001; Wilhelms and Squyres, 1984). Hence, it has been proposed that the last large impact into a planet may be responsible for the final direction and rate of planetary rotation (Canup and Agnor, 2000; Lissauer et al., 2000). Planet formation simulations by Agnor et al. (1999) suggest that in fact it is the last few collisions that are important in determining the final angular momentum of the

planet, and not simply the single largest impact; however, their simulations assumed complete angular momentum transfer.

Examining the post-impact planet rotational period we find that for a given impact energy, slow, therefore massive, 30–45° impacts result in the fastest spin rates (Figure 3-26). The rotational period is a product of the angular momentum carried by the impactor and the momentum transfer efficiency. For the $E_k = 0.2$ to 5.39×10^{28} J impacts, the final rotational period is 6–100 days. However, for the $E_k = 3.14$ and 5.89×10^{29} J impacts, for impact velocities below 15 km/s, the rotational periods are generally less than 5 days, and as short as 0.8 days; Mars' current rotational period is 1.03 days. These results suggest that the last (few) large impacts to occur on Mars could have caused a rotational period similar to that observed today. Note that the most likely impact angle of the impacting population (45°) also results in the largest rotational period change, making it more likely that large impacts significantly change the rotational rate of a planet.

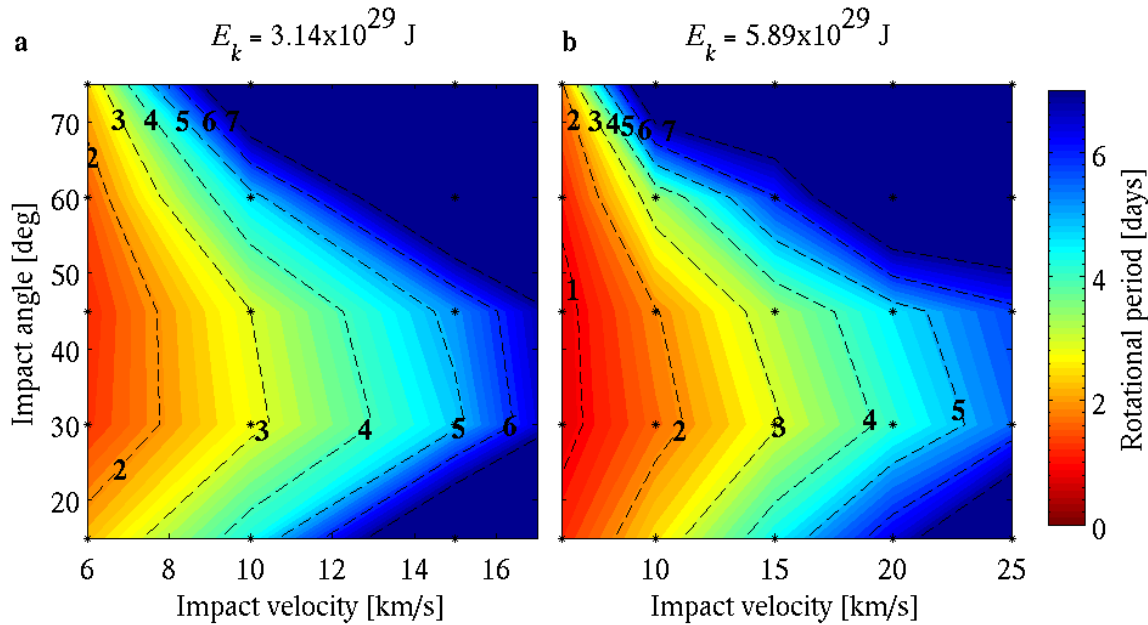


Figure 3-26 Post-impact rotational period for (a) $E_k = 3.14 \times 10^{29}$ J (nominal 10,000 km) impact and (b) $E_k = 5.89 \times 10^{29}$ J (nominal 12,000 km) impact. Stars represent simulated impact conditions. The highest simulated impact energies at low impact velocity produce rotational periods of order a day.

3.5 Resolution effects

To understand the applicability and limitations of the model results, we performed tests to assess the errors associated with the numerical resolution and parameter sensitivity. A key numerical parameter is the particle size, and the associated number of particles in the simulation. We have duplicated our simulations over a range of particle sizes: 118 km ($N = 200,000$), 150 km ($N = 100,000$), and 180 km ($N = 50,000$), to determine which model results vary with particle size and which are insensitive to this parameter. Table 3–3 shows the variation in the main impact results expressed with respect to the nominal case (118 km particle size). A general conclusion from this comparison is that model predictions for features and processes that are much larger in scale than the particle size vary only slightly over the range of particle sizes that was

considered, while features that are comparable to the particle size vary considerably. Hence large features, such as most crater cavities, the depth of penetration, mass of melt and escaping material, and angular momentum transfer, are not significantly affected by the particle size used in the simulations (less than few percent mean absolute difference, Figure 3-27). Smaller features, such as orbiting mass and some antipodal cavity sizes, are more susceptible to resolution effects, with changes of order 10% over the range of the particle sizes considered. The presence of features, such as antipode formation and orbiting material, and the spatial distribution of material (melt, crustal thickening, etc.) are invariant over the range of particle sizes tested.

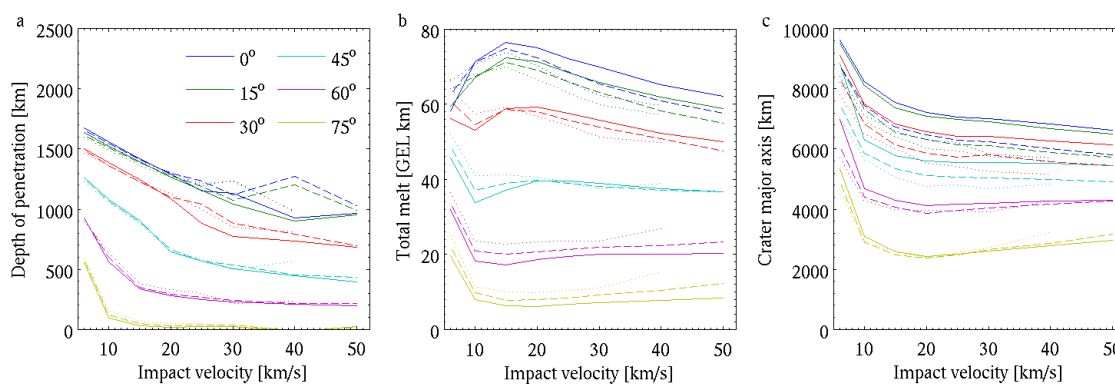


Figure 3-27 Resolution comparisons. Depth of impactor penetration (a), melt amount (b), and crater major axis (c) for simulations with resolutions of 118 km (solid), 150 km (dashed), and 180 km (dotted). $E_k = 3.14 \times 10^{29}$ J (nominal 10,000 km crater).

Table 3-3 Summary of resolution comparisons. Shown are the mean absolute differences for $E_k = 1.45, 3.14,$ and 5.89×10^{29} J (nominal 8,000, 10,000, and 12,000 km craters), with respect to the nominal 118 km resolution ($N = 200,000$ particles) simulations. Primary and antipodal cavity size: normalized by the circumference of the planet; maximum penetration depth: normalized by the radius of the planet (3400 km); ellipticity and rotation period: normalized by the nominal simulation results; melt cover: normalized by the planetary surface area; melt mass: normalized by the mantle mass; and escaping mass: normalized by the impactor mass.

Resolution	Crater size	Antipode size	Max. depth	Ellipticity	Rotation period	Melt cover	Melted mass	Escaping mass
150 vs. 118 km	2.0%	1.4%	0.8%	2%	7%	2.2%	0.2%	8%
180 vs. 118 km	2.7%	2.5%	1.3%	6%	10%	2.8%	0.4%	11%

To assess the presence of any systematic bias in the results due to particle resolution, we examine the distribution of the differences between the two lower resolution simulations (150 and 180 km particles) compared to the nominal simulations with 118 km particles (Figure 3-28). Pronounced trending in the scatter of the differences between simulations can indicate a bias in the results. For most of our simulations, there is only a few percent variation between the results, and only in a few cases is the range more than 10%. Details on how simulation differences were normalized for each parameter are described in Figure 3-28. For the planetary rotational frequency and the escaping mass (Figure 3-28e, h), a significant variation in results is seen for the smallest values. When the escaping mass is small, simulations with larger particles overestimate the total escaping mass. This is because overestimation of the escaping mass results in an overestimation of the rotational frequency (underestimation of the rotational period), as more momentum is carried away by the escaping material. Ellipticity, melted mass, and depth of penetration have small mean differences: 0.6, -0.1, and 0.6%, respectively, suggesting that for all three resolutions the particle size is sufficient to capture the essential effects. The difference distribution for the crater size and melt cover (Figure 3-28a, f), and to a lesser extent the antipodal cavity size and melted mass (Figure 3-28b, g), show that lower resolutions (larger particle sizes) increasingly underestimate the results compared to the nominal, 118 km particle size. The excavation boundary size (Figure 3-28a) prominently shows this trend. The underestimation in these results is due to the finite size of the particles, which average the energy and velocity gradients set by the passing shockwave over their smoothing length. Compared to large particles, smaller particles effectively sample more points along the gradient to determine whether the

material at that point meets the excavation or melting criterion. Importantly, for all difference comparisons, the results of the 150 km particle size simulations versus the nominal resolution simulations have a smaller mean difference, smaller mean absolute difference, and smaller standard deviation as compared to the 180 km particle size comparisons, suggesting convergence in the results as the particle size decreases.

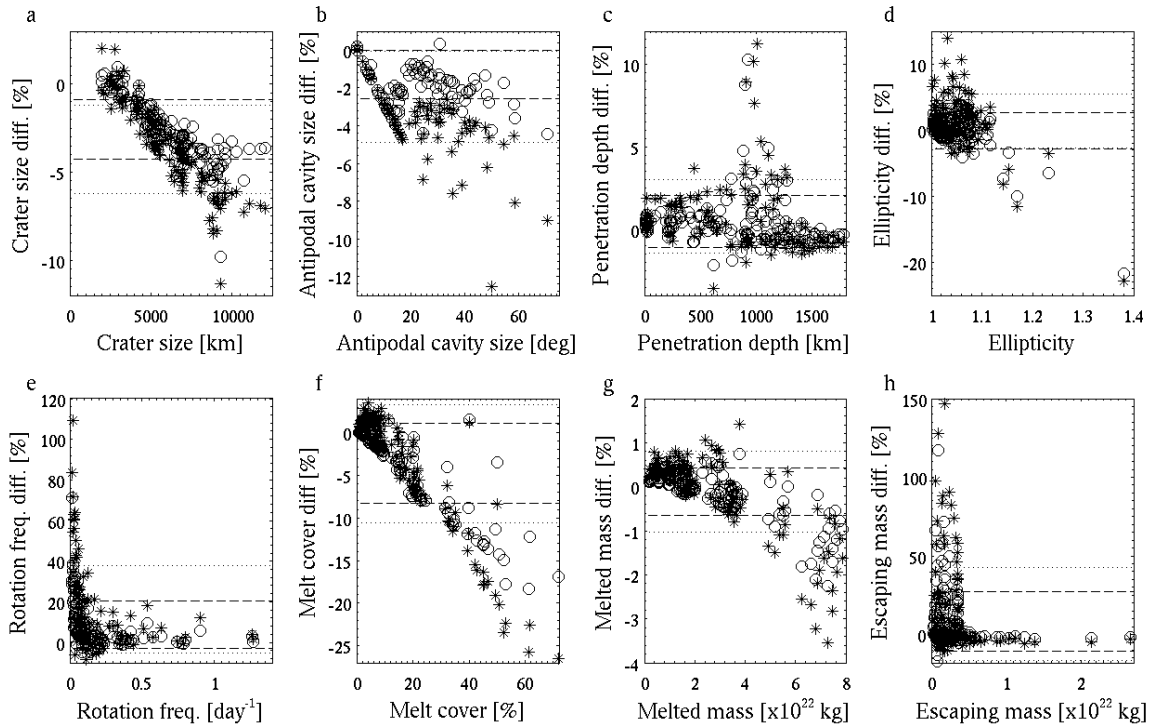


Figure 3-28 Resolution comparisons summary. Distribution of differences for simulations with resolutions of 150 km (circles) and 180 km (stars) with respect to the nominal simulations with a resolution of 118 km. The associated one standard deviation ranges are overlaid (dashed and dotted lines, respectively). Shown are all simulations for impact energies of $E_k = 1.45, 3.14,$ and 5.89×10^{29} J. In calculating the percent error, the parameters are normalized as in Table 3–3: crater and antipode size: normalized by the planet circumference; maximum penetration depth: by the radius of the planet (3400 km); ellipticity and rotation frequency: by the 118 km resolution results; melt cover: by the planetary surface area; melt mass: by the mantle mass; and escaping mass: by the impactor mass. The linear feature in (b) is composed of data points where an antipode was identified at the nominal resolution, but not at the lower resolution simulations.

3.6 Conclusions

The presented planetary-scale impact simulations provide insight into the morphology, global consequences, and comparison to half-space craters for this size regime over a wide range of impact conditions: 0.02 to 5.9×10^{29} J (nominal 2,300 to 12,000 km craters), 6 to 50 km/s, and 0° to 75° (from vertical). The observed divergence in results from half-space impacts can be explained by the surface curvature, radial gravity, large relative size of the impactor to the planet, and greater penetration of the impactor resulting in a change in the location of energy deposition and shock initiation.

We find that small crater scaling relations for crater size and the melt to impactor volumes are consistent with the results from our planetary-scale impacts simulations. Notable differences between small and planetary-scale impacts are the total melt volume production with respect to crater size and the depth of penetration of the impactor. Up to the most energetic modeled impacts, the resulting ejecta and melt distributions generally suggest that evidence of the impact event will be retained.

For the simulated impact energy range, the impacts are sufficiently energetic to penetrate and remove the surrounding crust. The area of excavated crust is the largest-scale impact feature, and is thus expected to be the global-scale observable characteristic most likely to be preserved over geological time. The resulting crustal excavation area is within the size range predicted by the different empirical, half-space scaling relations we examined. However, the distribution of ejecta for these energetic impacts differs from half-space impacts: for impact energies above $\sim 10^{29}$ J and impact angles $\leq 45^\circ$, the ejecta does not form a distinct annular crustal thickening similar to a crater rim but is instead

more uniformly distributed over the planetary surface. This is a result of the increased ejection distance due to surface curvature.

Impactors are expected to have a geochemically-distinct composition (Chambers, 2001); thus the presence of extra-planetary material on the planetary surface can confirm the impact origin of a feature via global geochemistry surveys. The distribution of the geochemically unique impactor material, exposed mantle, primordial crust, and newly formed crust could be used to establish the impact characteristics.

The depth of penetration of the impactor determines the effective depth of energy deposition and shockwave initiation. We find that the depth of penetration scales with impactor mass and impact angle: for a given impact energy, slower and therefore larger impactors penetrate further. Deeper shockwave initiation produces a larger crater, increased mantle melting, and larger resulting surface oscillations. The largest impactors reach the core, however no mixing with the core material is observed within the simulated range of parameters. Our analysis does not consider the long-term consequences of the planetary oscillations produced by the impacts, such as planet-wide surface modification and enhancement of volcanism due to deep fracturing of the crust (Williams and Greeley, 1994).

We find that antipodal crustal removal and melting is present for energetic ($> 10^{29}$ J), fast (> 6 km/s), and low angle ($\leq 45^\circ$) impacts. The simulated conditions produced antipodal cavities up to 4,140 km in diameter. For oblique impacts, the center of the antipodal disruption moves with respect to the diametrical point of the center of the primary crater, with a maximum deviation of 25° . However, for most impact conditions, the antipodal cavity center is $180 \pm 10^\circ$ from the point of maximum pressure.

The preservation of the geophysical expression of the impact event over geological time requires that a significant fraction of the pre-impact crust remain unaltered. We find that the total melt mass is comparable to the crustal mass: tens to 150 km global equivalent layer (GEL) depth for the range of simulated impact conditions. However, the highly heterogeneous distribution of melt, and particularly a large melt fraction residing in the mantle for the most energetic impacts, results in the preservation of much of the pre-impact surface and crust outside of the crater cavity. This in turn suggests the preservation of the global-scale geophysical signature of the impact event due to a resulting dichotomy in crustal thickness and surface expression between the pre- and post-impact crust. Of all simulated impacts, only the head-on, most massive and slow impact with $E_k \approx 6 \times 10^{29}$ J resulted in sufficiently widespread surface melt cover to suggest complete surface resetting by a global magma ocean and no preservation of the impact feature. Planetary oscillations may further contribute to the resetting of the surface through frictional melting and fracturing of the crust, promoting volcanism. Conventionally, large oscillations caused by impact shockwaves have been considered only with respect to antipodal effects (e.g., Schultz and Gault, 1975; Watts et al., 1991; Williams and Greeley, 1994); however, for our simulated highly energetic impacts, the resulting planetary oscillations of order tens to a few hundred kilometers may be sufficient to cause global fracturing of the crust for the most energetic impacts.

The most massive impactors in our simulations (impactor to planet mass ratio of $\sim 5\%$) can contribute sufficient angular momentum to increase Mars' rotation rate to one rotation per day. The impact velocity and angle that contribute the most angular momentum to the planet are consistent with the encounter velocities at the end of

accretion of several to tens of km/s (e.g., Raymond et al., 2009) and the most likely impact angle of 45° (Shoemaker, 1962), suggesting that late accretionary impacts significantly altered the rotational state of the impacted planets.

Most simulated impacts result in orbiting material, with the orbiting mass increasing with impact energy. In the least energetic impacts, our simulations show no orbiting material; however, this is likely an artifact of the simulation resolution. Thus, for the simulated energy range, impacts generally produce orbiting material and impact-formed satellites should be common. The combined orbiting and ejected mass exceeds the impactor mass for impact velocities > 18 km/s for all simulated impact energies and angles; 18 km/s is about three times the mutual planet-impactor escape velocity. At maximum, the ejected material reaches net mass removal up to eight times the impactor mass. Consequently, impacts at velocities below ~ 18 km/s have a net accretionary effect, while faster impacts have a net erosional effect, for our range of simulated conditions.

In using the results from the presented simulations, it is important to keep in mind that these represent only one impactor type and the details of the results change for different impactor properties. Future work explores the importance of impactor composition and structure on the resulting planetary-scale impact features and the best fit parameters for the associated scaling relations (Marinova et al., *in prep.*).

Exploring the presented planetary-scale impact results allows for the critical assessment of whether Mars' Northern Lowlands may be the result of a single large impact 4.5 Gyr ago (e.g., Solomon et al., 2005; Wilhelms and Squyres, 1984). Review of the consequences of impacts over the large range of impact conditions that were simulated, have shown that a $\sim 3 \times 10^{29}$ J impact at ~ 6 km/s and at a $\sim 45^\circ$ angle produces

features similar to the Northern Lowland characteristics (Marinova et al., 2008). These impact conditions – impactor size, angle, and velocity – are the most likely values for the epoch in which the event occurred, and the impact event gives an initially stationary Mars a post-impact rotational period of 1.3 days, similar to Mars' current 1.03 day rotational period.

The results from the presented simulations can be further used to understand the provenance of planetary-scale impact structures on other Mars-sized objects, and provide general understanding of the differences between small and planetary-scale impact events and the resulting impact structures.

3.7 Acknowledgements

We thank Robin Canup, Paul Asimow, Andy Ingersoll, and Dave Stevenson for insightful discussions. This work was supported by a Henshaw Fellowship, an NSERC post-graduate fellowship, and a Canadian Space Agency supplement.

3.8 Bibliography

- Agnor, C. B. et al., 1999. On the character and consequences of large impacts in the late stage of terrestrial planet formation. *Icarus*. 142, 219–237.
- Allen, R. T., Equations of state of rocks and minerals. Interim report to DASA under Contract DA 49–146–XZ–462. In: G. D. R. G. MD–7834, (Ed.), 1967.
- Anderson, D. L., Isaak, D. G., Elastic constants of mantle minerals at high temperature. In: T. J. Ahrens, (Ed.), *Mineral Physics and Crystallography: A Handbook of Physical Constants*. Am. Geophys. Union, 1995, 64–97.
- Andrews-Hanna, J. C. et al., 2008. The Borealis Basin and the Martian crustal dichotomy. *Nature*. 453, 1212–1215.
- Artemieva, N. et al., 2004. Investigating the Lake Bosumtwi impact structure: Insight from numerical modeling. *Geochemistry, Geophysics, Geosystems*. 5, Q11016.
- Asimow, P. D., 2007. Magmatism and the evolution of the Earth's interior. *Goldschmidt Conference Abstracts*.
- Asphaug, E., 2010. Similar-sized collisions and the diversity of planets. *Chemie der Erde*. (submitted).
- Asphaug, E. et al., 2006. Hit-and-run planetary collisions. *Nature*. 439, 155–160.
- Benz, W. Numerical modeling of non-radial stellar pulsation: Problems and prospects. NATO ASI series C. Kluwer, Dordrecht, 1990, 269.
- Benz, W., Asphaug, E., 1999. Catastrophic disruptions revisited. *Icarus*. 152, 5–20.
- Benz, W. et al., 1989. The origin of the Moon and the single impact hypothesis III. *Icarus*. 81, 113–131.

- Benz, W. et al., 1986. The origin of the Moon and the single-impact hypothesis I. *Icarus*. 66, 515–535.
- Benz, W. et al., 1987. The origin of the Moon and the single impact hypothesis II. *Icarus*. 71, 30–45.
- Bertka, C. M., Fei, Y. W., 1998. Density profile of an SNC model Martian interior and the moment-of-inertia factor of Mars. *Earth and Planetary Science Letters*. 157, 79–88.
- Canup, R. M., 2004. Simulations of a late lunar-forming impact. *Icarus*. 168, 433–456.
- Canup, R. M., Agnor, C. B., Accretion of the terrestrial planets and the Earth-Moon system. In: R. M. Canup, K. Righter, Eds.), *Origin of the Earth and Moon*. University of Arizona Press, Tucson, Arizona, 2000, 113–129.
- Canup, R. M., Asphaug, E., 2001. Origin of the Moon in a giant impact near the end of the Earth's formation. *Nature*. 412, 708–712.
- Chambers, J. E., 2001. Making more terrestrial planets. *Icarus*. 152, 205–224.
- Chambers, J. E., 2004. Planetary accretion in the inner Solar System. *Earth and Planetary Science Letters*. 223, 241–252.
- Chen, G. Q. et al., 2002. Shock-wave equation of state of molten and solid fayalite. *Physics of the Earth and Planetary Interiors*. 134, 35–52.
- Cintala, M. J., Grieve, R. A., 1998. Scaling impact melting and crater dimensions: Implications for the lunar cratering record. *Meteoritics & Planetary Science*. 33, 889–912.
- Collins, G. S., Melosh, H. J., 2002. Hydrocode simulations of Chicxulub Crater collapse and peak-ring formation. *Icarus*. 157, 24–33.

- Colwell, J. E., Taylor, M., 1999. Low-velocity microgravity impact experiments into simulated regolith. *Icarus*. 138, 241–248.
- Debaille, V. et al., 2007. Coupled ^{142}Nd - ^{143}Nd evidence for a protracted magma ocean in Mars. *Nature*. 450, 525–528.
- Dence, M. R., 1965. The extraterrestrial origin of Canadian craters. *Annals of the New York Academy of Sciences*. 123, 941–969.
- Elkins-Tanton, L. T. et al., 2005. Possible formation of ancient crust on Mars through magma ocean processes. *Journal of Geophysical Research*. 110, E12S01.
- Elkins-Tanton, L. T. et al., 2003. Magma ocean fractional crystallization and cumulate overturn in terrestrial planets: Implications for Mars. *Meteoritics & Planetary Science*. 38, 1753–1771.
- Gault, D. E., Impact cratering. In: R. Greeley, P. H. Schultz, Eds., *A primer in lunar geology*. NASA Ames, Moffett Field, 1974, 137–175.
- Gault, D. E. et al., 1975. Some comparisons of impact craters on Mercury and the Moon. *Journal of Geophysical Research*. 80, 2444–2460.
- Gault, D. E., Wedekind, J. A., Experimental hypervelocity impact into quartz sand II, Effects of gravitational acceleration. In: D. J. Roddy et al., Eds.), *Impact and explosive cratering*. Pergamon, New York, 1977, 1231–1244.
- Gault, D. E., Wedekind, J. A., 1978. Experimental studies of oblique impact. *Proceedings of the Lunar and Planetary Science Conference 9th*. 3843–3875.
- Gilbert, G. K., 1893. The moon's face, a study of the origin of its features. *Bull. Philos. Soc. Wash. (D.C.)*. 12, 241–292.

- Grieve, R. A. F., Cintala, M. J., 1992. An analysis of differential impact melt-crater scaling and implications for the terrestrial impact record. *Meteoritics*. 27, 526–538.
- Hartmann, W. K., 1985. Impact experiments: 1. Ejecta velocity distributions and related results from regolith targets. *Icarus*. 63, 69–98.
- Hartmann, W. K., Davis, D. R., 1975. Satellite-sized planetesimals and lunar origin. *Icarus*. 24, 504–515.
- Hashimoto, A., 1983. Evaporation metamorphism in the early Solar Nebula – evaporation experiments on the melt FeO-MgO-SiO₂-CaO-Al₂O₃ and chemical fractionations of primitive materials. *Geochemical Journal*. 17, 111–145.
- Hauck, S. A., Phillips, R. J., 2002. Thermal and crustal evolution of Mars. *Journal of Geophysical Research – Planets*. 107, 5052.
- Holsapple, K. A., 1993. The scaling of impact processes in planetary sciences. *Annual Reviews of Earth and Planetary Science*. 21, 333–373.
- Holsapple, K. A., Schmidt, R. M., 1982. On the Scaling of Crater Dimensions: 2. Impact Processes. *Journal of Geophysical Research*. 87, 1849–1870.
- Hörz, F., Cintala, M., 1997. Impact experiments related to the evolution of planetary regoliths. *Meteoritics & Planetary Science*. 32, 179–209.
- Housen, K. R. et al., 1979. Asteroidal regoliths. *Icarus*. 39, 317–351.
- Klein, C., 2002. *The Manual of Mineral Science*. John Wiley & Sons, Inc., New York.
- Lana, C. et al., 2003. Impact tectonics in the core of the Vredefort dome, South Africa: Implications for central uplift formation in very large impact structures. *Meteoritics & Planetary Science*. 38, 1093–1107.

- Lide, D. R. (Ed.) 1995. CRC Handbook of Chemistry and Physics. CRC Press, Inc., USA.
- Lissauer, J. J. et al., Origin and evolution of terrestrial planet rotation. In: R. M. Canup, K. Righter (Eds.), Origin of the Earth and Moon. University of Arizona, Tucson, 2000.
- Marinova, M. M. et al., *in preparation*. The importance of impactor composition on the geophysical consequences of planetary-scale impacts into a Mars-like planet.
- Marinova, M. M. et al., 2008. Mega-impact formation of the Mars hemispheric dichotomy. *Nature*. 453, 1216–1219.
- Melosh, H. J., 1989. Impact cratering: A geologic process. Oxford University Press, New York.
- Moore, H. J. et al., 1974. Multi-ringed basins – Illustrated by Orientale and associated features. Proceedings of the Lunar and Planetary Science Conference 5th. 71–100.
- Morgan, J. et al., 1997. Size and morphology of the Chicxulub impact crater. *Nature*. 390, 472–476.
- Mosenfelder, J. L. et al., 2007. Thermodynamic properties of Mg_2SiO_4 liquid at ultra-high pressures and shock measurements to 200 GPa of forsterite and wadsleyite. *Journal of Geophysical Research*. 112, B06208.
- Murchie, S. L. et al., 2008. Geology of the Caloris Basin, Mercury: A view from MESSENGER. *Science*. 321, 73–76.
- Navrotsky, A., Thermodynamic properties of minerals. In: T. J. Ahrens (Ed.), *Mineral Physics and Crystallography*. American Geophysical Union, 1995, 18–28.

- Neukum, G. et al., 2001. Cratering records in the inner Solar System in relation to the lunar reference system. *Space Science Reviews*. 96, 55–86.
- Nimmo, F. et al., 2008. Implications of an impact origin of the martian hemispheric dichotomy. *Nature*. 453, 1220–1223.
- O'Keefe, J. D., Ahrens, T. J., Impact-induced energy partitioning, melting, and vaporization on terrestrial planets. *Lunar Science Conference, 8th, Houston, TX, 1977, 3357–3374.*
- O'Keefe, J. D., Ahrens, T. J., 1993. Planetary cratering mechanics. *Journal of Geophysical Research*. 98, 17011–17028.
- Pierazzo, E., Melosh, H. J., 1999. Hydrocode modeling of Chicxulub as an oblique impact event. *Earth and Planetary Science Letters*. 165, 163–176.
- Pierazzo, E., Melosh, H. J., 2000a. Hydrocode modeling of oblique impacts: The fate of the projectile. *Meteoritics & Planetary Science*. 35, 117–130.
- Pierazzo, E., Melosh, H. J., 2000b. Melt production in oblique impacts. *Icarus*. 145, 252–261.
- Pierazzo, E., Melosh, H. J., 2000c. Understanding oblique impacts from experiments, observations, and modeling. *Annual Reviews of Earth and Planetary Science*. 28, 141–167.
- Pike, R. J., Control of crater morphology by gravity and target type: Mars, Earth, Moon. *Lunar and Planetary Science Conference, 11th, Vol. 3. Pergamon Press, Houston, TX, 1980, 2159–2189.*
- Raymond, S. N., O'Brien, D. P., Morbidelli, A., Kaib, N. A., Building the terrestrial planets: Constrained accretion in the inner Solar System. *Icarus*. 203, 644–664.

- Sanloup, C. et al., 1999. A simple chondritic model of Mars. *Physics of the Earth and Planetary Interiors*. 112, 43–54.
- Schubert, G., Spohn, T., 1990. Thermal history of Mars and sulfur content of its core. *Journal of Geophysical Research*. 95, 14095–14104.
- Schultz, P. H., Gault, D. E., 1975. Seismic effects from major basin formations on the Moon and Mercury. *The Moon*. 12, 159–177.
- Shoemaker, E. M., Interpretation of Lunar Craters. In: Z. Kopal (Ed.), *Physics and Astronomy of the Moon*. Academic Press, New York, 1962, 283–359.
- Solomon, S. C. et al., 2005. New perspectives on ancient Mars. *Science*. 307, 1214–1220.
- Spudis, P. D. et al., 1994. Ancient multiring basins on the Moon revealed by Clementine laser altimetry. *Science*. 266, 1848–1851.
- Syono, Y. et al., 1981. Shock compression measurements of single-crystal forsterite in the pressure range 15–93 GPa. *Journal of Geophysical Research*. 86, 6181–6186.
- Tillotson, J. H., *Metallic equations of state for hypervelocity impact*. GA-3216, General Atomic, San Diego, California, 1962.
- Tonks, W. B., Melosh, H. J., 1993. Magma ocean formation due to giant impacts. *Journal of Geophysical Research*. 98, 5319–5333.
- Watts, A. W. et al., 1991. The formation of terrains antipodal to major impacts. *Icarus*. 93, 159–168.
- Weidenschilling, S. J., 2008. Accretion of planetary embryos in the inner and outer solar system. *Physica Scripta*. T130, 014021.
- Wetherill, G. W., 1985. Occurrence of giant impacts during the growth of the terrestrial planets. *Science*. 228, 877–879.

- Wilhelms, D. E., 1973. Comparison of Martian and Lunar multiringed circular basins. *Journal of Geophysical Research*. 78, 4084–4095.
- Wilhelms, D. E., Squyres, S. W., 1984. The Martian hemispheric dichotomy may be due to a giant impact. *Nature*. 309, 138–140.
- Williams, D. A., Greeley, R., 1994. Assessment of antipodal-impact terrains on Mars. *Icarus*. 110, 196–202.
- Yoder, C. F. et al., 2003. Fluid core size of Mars from detection of the solar tide. *Science*. 300, 299–303.
- Zhong, S. J., Zuber, M. T., 2001. Degree-1 mantle convection and the crustal dichotomy on Mars. *Earth and Planetary Science Letters*. 189, 75–84.
- Zuber, M. T., 2001. The crust and mantle of Mars. *Nature*. 412, 220–227.

CHAPTER 4

THE IMPORTANCE OF IMPACTOR COMPOSITION ON THE GEOPHYSICAL CONSEQUENCES OF PLANETARY- SCALE IMPACTS INTO A MARS-LIKE PLANET

4.1 Abstract

The surfaces of the terrestrial planets are pockmarked with craters, ranging in size from microscopic to planetary-scale. Here we examine the geophysical and morphological effects of planetary-scale impacts, and in particular the importance of impactor composition and internal structure on the resulting impact features. A fully three-dimensional smoothed particle hydrodynamics (SPH) model is used to simulate the impacts into a Mars-like planet, for impactors with an encompassing range of densities, from basalt to iron, as well as a differentiated olivine-iron projectile. The simulated impact conditions range in energy from $0.1\text{--}5.9 \times 10^{29}$ J (0.2–11% of Mars' total binding energy), in velocity from 6–50 km/s (escape to twice Mars' orbital velocity), and angle from 0° (head-on) to 75° . Over the simulated range, we find that the resulting crater cavity sizes are not very sensitive to the impactor density or composition, however, the shape of the cavity is especially sensitive to the presence of a coherent iron component in the impactor. With increasing impactor density, the crater cavity is elliptical for a large range of impact conditions, consistent with the commonly elliptical planetary-scale impact basins that are observed on the planets (e.g., South Pole–Aitken basin on the Moon, Hellas Basin on Mars, Caloris Basin on Mercury). As with the crater size, the antipodal cavity size is also not affected by the impactor composition. In examining the

melt production, we find that the total melt amount produced is very sensitive to the impactor type, as is the partitioning of the melt between the mantle, surface, and ejecta reservoirs. Interestingly, the net effect is that the total melt production to surface melt cover relationship is similar for all impactor types. The amount of ejected and orbiting material for all impactor types is similar, however, the composition does vary. In all cases the impactor material in the ejecta increases with increasing impact angle. When examining the net accretion or erosion by the impacts, that is, whether the impactor mass is larger than the ejected mass, the distribution with impact velocity and angle are a function of the impactor density and type. The differences in accretional efficiency with impact angle are of special interest compared to the impact angle probability, which is symmetric about 45° . The impactor density is also important for the angular momentum transfer efficiency, where denser impactors impart a faster rotation rate on the target. In light of these new results for an encompassing range of impactor compositions, we find that the Mars hemispheric dichotomy can be formed by a realistic range of impact conditions, which are similar to those found by Marinova et al. (2008).

4.2 Introduction

In the planetary-scale impact regime, the crater cavity is a large fraction of the planetary circumference. Due to its size, the curvature of the planet, the radial gravity, and the large relative size of the impactor to the target are important, unlike for small, effectively half-space, impacts. The impactors in the planetary-scale size regime commonly fall in the category of planetesimals. As such, these bodies are likely differentiated due to their size and significant accretional heating: the impactors are

comparable to, or bigger than, differentiated asteroids such as Ceres (940 km diameter; Thomas et al., 2005) and Vesta (520 km diameter; McCord et al., 1970; Thomas et al., 1997). Here we explore the geophysical consequences of a range of impactor compositions, particularly differentiated impactors (olivine and iron), and single-composition olivine ($\rho_0 = 3,500 \text{ kg/m}^3$), undifferentiated ($\rho_0 = 4,570 \text{ kg/m}^3$), and iron ($\rho_0 = 7,800 \text{ kg/m}^3$) impactors, and how these compare to the previously-studied basalt impactors ($2,700 \text{ kg/m}^3$; Marinova et al., submitted). These end-member compositions encompass the range of impactor densities and interim structures that would have comprised the planetary-scale impactors. Variations in the impactor composition, and thus density, changes the impactor size for a given impact energy and velocity, and affects the relative buoyancy of the impactor with respect to the planetary mantle. In the case of differentiated impactors, where a significant density difference is present between the impactor mantle and core, we consider how their interaction with the planet compares to that of single-composition olivine and iron impactors, as well as the undifferentiated impactor. The undifferentiated impactor is simulated by a single material with a density equivalent to a well-mixed, undifferentiated impactor.

The exact timing of the differentiation of planetesimals and the planets is uncertain; however, the differentiation process is expected to have been mostly complete by the end of accretion (Lee and Halliday, 1996). The planetesimal-sized impactors that we simulate – up to a few thousand kilometers across – are likely to have differentiation timescales similar to those of a Mars-like planet. We therefore also simulate the effects of a differentiated impactor, and compare those results to the single-composition impactors.

Here we study the effect of impactor composition on the geophysical and morphological results of the impact. This new broad range of impactor types allows a comprehensive characterization of consequences of planetary-scale impacts, and their expected expression on planetary surface. These results promote better interpretation of the formation mechanism of large impact structures observed on other planets.

4.3 Modeling

We use a fully three-dimensional smoothed particle hydrodynamics (SPH) model to simulate the impacts (e.g., Benz, 1990; Canup, 2004; Marinova et al., submitted). SPH is a Lagrangian model, where objects are represented by a collection of particles. Each particle extends over a given smoothing length (particle diameter). The particle retains its individual mass while its internal energy, pressure, and density respond to outside forces; the particle's mass, and the total momentum and energy are conserved. This SPH model has been previously used to simulate planetary-scale impacts (Marinova et al., submitted), as well as the more energetic mega-impacts (e.g., Asphaug et al., 2006; Canup, 2004). Planetary-scale impacts are in the gravity regime, with the impact energy orders of magnitude above the strength- to gravity-dominated cratering transition; the utilized SPH model does not take material strength into account.

4.3.1 SPH model setup

The details of our approach have been previously published (Marinova et al., submitted) and are only briefly summarized here. Novel or differing aspects, such as the formation of the impactors, are described in greater detail below.

The simulations use 200,000 particles, with a mean particle diameter (smoothing length) of 118 ± 6 km. Both the planet and differentiated impactors are composed of an olivine (Fo75) mantle and an iron core. The single-composition impactors are each composed of only olivine, iron, or “undifferentiated” material. The “undifferentiated” impactor is simulated by creating a single material with a bulk density equivalent to that of a differentiated, olivine-iron impactor ($\rho_0 = 4,570 \text{ kg/m}^3$), but with all other equation of state parameters identical to that of olivine. This “undifferentiated” impactor is used to overall simulate the impact effects of well-mixed, still undifferentiated impactors, since olivine and iron particles cannot be directly mixed in SPH due to possible numerical instabilities. For all impacts, the total energy in the simulation is conserved to better than a part in a thousand.

The target planet is formed by randomly placing particles in a sphere. The particles are then assigned a material type, pressure, density, and internal energy that is appropriate for their radial position, matching the internal structure and thermodynamic properties of Mars shortly after accretion (Hauck and Phillips, 2002; Sanloup et al., 1999). We use the Tillotson (1962) equation of state formulation, with material properties for olivine and iron given by Marinova et al. (2008) and Tillotson (1962), respectively. The planetary formation procedure is described in detail in Marinova et al. (submitted).

The differentiated impactors are formed by the same procedure as the planet. The core is set to span half the impactor radius and thus contains about 24% of the impactor mass. The total internal energy of the impactor is set equal to its gravitational binding energy, assuming a constant density object and no compression. Both of these assumptions result in an underestimate of the accretional energy as they do not take into

account heating due to differentiation, as well as the lower potential energy of the smaller, compressed object. Conversely, we do not consider radiative cooling during the accretion process, thus overestimating the energy retained by the impactor. In net, the assumed internal energy should broadly approximate the internal energy of planetesimals at the end of accretion. All particles are assigned the same specific internal energy, as thermal equilibration is assumed. The impactor is then relaxed, with artificial damping, for 21.5 hrs until the mean particle motion is negligible.

For olivine, undifferentiated, and iron impactors we use the same procedure as Marinova et al. (submitted). The impactors are formed as two halves, with a uniform internal energy of 0.1 MJ/kg; the halves are slowly impacted and equilibrated.

4.3.2 *Initial conditions*

Due to the global consequences of planetary-scale impacts, the thermodynamic and structural initial conditions of the target and impactor are important in determining the outcome of the impact event. Planetary-scale impacts occurred predominantly at the end of accretion, and therefore the target and impactor properties are matched to our understanding of the planetary conditions at this early stage of Solar System history. The properties of the target, a Mars-like planet, are matched to those modeled for a young, post-accretional Mars (Bertka and Fei, 1998; Hauck and Phillips, 2002). More details are given in Marinova et al. (submitted).

The crustal composition of the planet is not distinct from that of the mantle, since a compositionally-distinct single particle layer cannot be numerically resolved and may produce numerical instabilities. To track the fate of the surface material, we label the

outermost layer of olivine particles on the planet, mean thickness of ~ 140 km, as “crust” and track them during the simulations.

The target has no pre-impact spin, similar to Marinova et al. (submitted). This scenario is appropriate for Mars as its current rotational period of ~ 25 hrs is long compared to the timescale of the impact event, and Mars’ rotation rate is not expected to have changed significantly since the end of accretion.

4.3.3 *Impact parameter space*

To guide the choice of impact energy required to nominally produce a desired crater size, we use the half-space, small crater scaling law of Wilhelms and Squyres (1984):

$$D = k E_k^n g^u \quad (4-1)$$

where D is the impact crater diameter, E_k is the kinetic energy of the impactor, and g is the acceleration due to gravity. When D , E_k , and g are in mks units, the constants k , n , and u are taken to be 0.0348, 0.29, and $-1/6$, respectively, following Housen et al. (1979). The dependence on gravity, g , follows the relationship suggested by Gault and Wedekind (1978).

We simulate impacts with energies of $0.13\text{--}5.89 \times 10^{29}$ J (nominal 4,000 to 12,000 km impact craters), velocities of 6–50 km/s (about Mars escape velocity to twice its orbital velocity), and impact angles of 0° (vertical, head-on impact) to 75° . The impact angle is defined as the angle between the velocity vector and the line connecting the centers of the planet and impactor at the time of initial contact. Small impactors, resulting from low impact energies or fast velocities, could not be simulated due to the minimum number of neighboring particles required for SPH to realistically simulate the behavior of

an object. Table 4-1 shows a summary of the simulated conditions and the corresponding impactor sizes. Based on dynamical and theoretical considerations, the mostly likely impact conditions into Mars are close to the mutual escape velocity of the target-impactor system (~ 6 km/s in this case; Canup and Agnor, 2000); an impact angle of 45° (Gilbert, 1893; Shoemaker, 1962), and an impactor size 400–1,800 km in diameter (Hartmann and Davis, 1975). The simulated maximum impactor to planet mass ratio is 0.09, $\sim 50\%$ smaller than the 0.12–0.25 impactor to Earth mass ratio for the Moon-forming event (Canup, 2008).

Table 4-1 Summary of simulated impact conditions: nominal crater size using the half-space scaling relation of Wilhelms and Squyres (1984) and the nominal crater size as a fraction of the target's circumference; the impact energy; and the impactor diameter for each of the simulated impact velocities and impactor types. Some impact events could not be simulated due to the exceedingly small impactor (--). The presented impactor sizes for each impact condition are in the following order: basalt (Marinova et al., submitted), olivine, undifferentiated, differentiated, and iron. Note that the differentiated impactors are slightly larger than the undifferentiated impactors, due to the higher internal energy of the former and the resulting slightly lower bulk density.

Nominal crater diameter (circumf. fraction)	Impact energy (J)	Impactor type	Impact velocity (km/s)									
			6	7	8.5	10	15	20	25	30	40	50
			Impactor diameter (km)									
4,000 km (0.19)	1.33x10 ²⁸	Basalt	760	--	--	540	380	--	--	--	--	--
		Olivine	690	620	550	490	340	--	--	--	--	--
		Undiff.	630	570	500	450	--	--	--	--	--	--
		Diff.	640	600	530	--	--	--	--	--	--	--
		Iron	520	470	420	350	--	--	--	--	--	--
6,000 km (0.28)	5.39x10 ²⁸	Basalt	1240	--	--	880	660	540	440	380	--	--
		Olivine	1130	1020	890	800	600	490	400	340	--	--
		Undiff.	1030	930	810	720	540	450	360	--	--	--
		Diff.	1080	970	860	760	560	--	--	--	--	--
		Iron	860	770	670	600	460	350	--	--	--	--
8,000 km (0.37)	1.45x10 ²⁹	Basalt	1740	--	--	1220	930	760	660	570	430	380
		Olivine	1590	1440	1250	1120	850	690	590	520	430	330
		Undiff.	1460	1310	1140	1020	770	630	540	480	350	320
		Diff.	1520	1380	1210	1060	830	680	560	--	--	--
		Iron	1200	1080	950	850	630	520	450	410	--	--
10,000 km (0.47)	3.14x10 ²⁹	Basalt	2270	--	--	1610	1210	990	860	750	610	540
		Olivine	2070	1870	1640	1460	1110	910	770	680	560	480
		Undiff.	1890	1700	1490	1340	1010	830	700	620	510	440
		Diff.	2000	1800	1560	1400	1060	860	760	640	530	--
		Iron	1570	1410	1240	1110	830	680	580	510	430	340
12,000 km (0.56)	5.89x10 ²⁹	Basalt	2830	--	--	1980	1500	1230	1060	930	760	660
		Olivine	2560	2310	2020	1820	1370	1130	960	850	690	590
		Undiff.	2330	2100	1850	1660	1250	1030	880	780	630	540
		Diff.	2480	2240	2000	1740	1310	1070	900	810	690	560
		Iron	1950	1750	1530	1370	1040	850	730	640	520	450

4.3.4 Characteristics of the impact

The consequences of the impact that were considered include: the crustal redistribution and crater size, crater ellipticity, melt production and distribution, mantle melting, orbiting and escaping material, and angular momentum transfer. Particular emphasis is placed on comparing if, and how, the impact outcomes differ with impactor composition and internal structure (differentiation).

Material distribution is calculated as a fraction of total material in the surface (top ~150 km) layer of the planet, similar to Marinova et al. (submitted); the provenance of the material is tracked. The planetary surface is sampled at 2° intervals, and the data is averaged over overlapping 10° diameter caps. The crustal excavation boundary is set to represent the 50% contour of the surface crustal thickness with respect to the pre-impact crustal thickness. Thickening of the crust is used to determine the formation of a rim-like structure by the impact. Antipodal crustal removal is determined using the 80% contour of post- to pre-impact crustal thickness. The molten region represents the area with a melt fraction larger than 50%. The qualitative aspects of the surface distribution of material do not vary appreciably on the timescale of the simulation, nor with the choices of simulation parameters such as particle size (see *Resolution effects*). At the end of the simulated time, 25.8 hrs, velocity oscillations are minimal and orbiting and ejected material is in steady-state.

To determine the total amount of olivine melt at the surface and at depth, we use the pressure-dependent forsterite melting criterion (Asimow, 2007; Marinova et al., submitted), given by $E_{melt} = 39.7 P + 2885$, where E_{melt} is the complete melting internal energy (kJ/kg) and P is pressure (GPa). We take into account molten iron only if it is near the surface of the planet or ejected, such that it is at a pressure < 4 GPa (~350 km depth on Mars). This allows for the iron melt to be determined using the zero-pressure melting limit (internal energy > 1.06 MJ/kg). We find that very little iron remains near the surface of the planet and the iron melting criterion is mostly applied to ejected iron material.

The depth of the transient impact cavity is calculated as the maximum depth of penetration during the first 30 min of the impact process, thus excluding any buoyancy

effects, which act over a longer timescale. We average the deepest 10% of the impactor mass, thus minimizing spurious effects from single particles. Penetration depths of more than 1,800 km represent penetration into the planetary core.

The presented results in subsequent sections are for $N = 200,000$ particles and initial particle size of ~ 118 km, except where resolution effects are considered.

When fitting scaling relations to the impact results, we normalize the values as follows: masses by the mass of the target ($M_0 = 6.41 \times 10^{23}$ kg), distances by the radius of the planet ($R_0 = 3,313$ km), energies by the binding energy of the target ($E_0 = 5.22 \times 10^{30}$ J), density by the mean density of the target ($\rho_0 = 4,221$ kg/m³), and velocity by the escape velocity of the planet ($v_0 = 5.085$ km/s). The normalizations do not affect the power law dependence (i.e., the values of the exponents), and only change the magnitude of the multiplication factor.

In calculating the orbiting and escaping material masses we use the following criteria. A particle is classified orbiting if its velocity is higher than the circular orbital velocity, but lower than the escape velocity, for its location with respect to the target center. In addition, to ensure that the particle does not re-impact the planet, its angular momentum must be higher than that of a particle orbiting at the planet's radius. For a particle to be classified as escaping, it must have higher than escape velocity, for its location with respect to the target center.

Care must be taken in interpreting results where few particles are separated from the bulk of the material, or where there is mixing of different materials. The former case applies especially to the interpretation of the evolution and presence of orbiting material. The latter case particularly applies to the mixing of a few impactor particles in the planet,

or a few iron particles being present at the surface or in the mantle of the planet. Due to the kernel-weighted representation of the particles and their overlapping, the properties of isolated particles are not well defined.

4.4 Mechanics of the impact process

Visualizing the impact event can provide insight into the expected outcomes and the variation in results with changing impact conditions. Here we qualitatively describe the essential features of the impact event, the evolution of the transient cavity, and the fate of the impactor and target material for the range of simulated impact conditions and impactor types. Further information and visualization of the impact events is given in *Appendix 4-A*. The distinguishing features between impactor types and parameters are: the final location of the impactor material including the accretion of the impactor core onto the planetary core, the extent of interaction between the impactor and target, and the skimming of the planetary surface by the impactor.

Overall we find that the final location of the impactor material is consistent with the relative densities between the materials; however, when the densities are similar, mixing may or may not occur. Basalt impactors (uncompressed density, $\rho_0 = 2,700 \text{ kg/m}^3$) are positively buoyant with respect to the planetary mantle (olivine, $\rho_0 = 3,500 \text{ kg/m}^3$), and accordingly, in all simulated cases, the impactor material is at the planetary surface at the end of the impact event. For olivine impactors, the impactor and target are of the same density and mixing is possible. Differentiated impactors are composed of an iron core ($\rho_0 = 7,900 \text{ kg/m}^3$) and an olivine mantle, and thus their interaction with the planet is more complex. We find that for all head-on impacts, including the lowest

simulated energy, the core of the impactor merges with the core of the planet during the initial stage of the impact, due to the longer stopping distance for the impactor's iron core (Figure 4-1). Undifferentiated impactors are denser ($\rho_0 = 4570 \text{ kg/m}^3$) than the planetary mantle and accrete onto the core during the impact process. Their higher density also affects the rebounding after the impact, and mixing between the impactor and planetary mantle occurs for a range of impact conditions (Figures 4-A1, 4-A4). Mixing between the impactor and planetary mantle is present for intermediate-angle impacts. For iron impactors, the impactor commonly accretes onto the planetary core: at least 80% of the impactor accretes for impact angles less than 45° , with the impactor often extensively interacting with the planetary mantle as it settles onto the planetary core (see *Escaping and orbiting material* section).

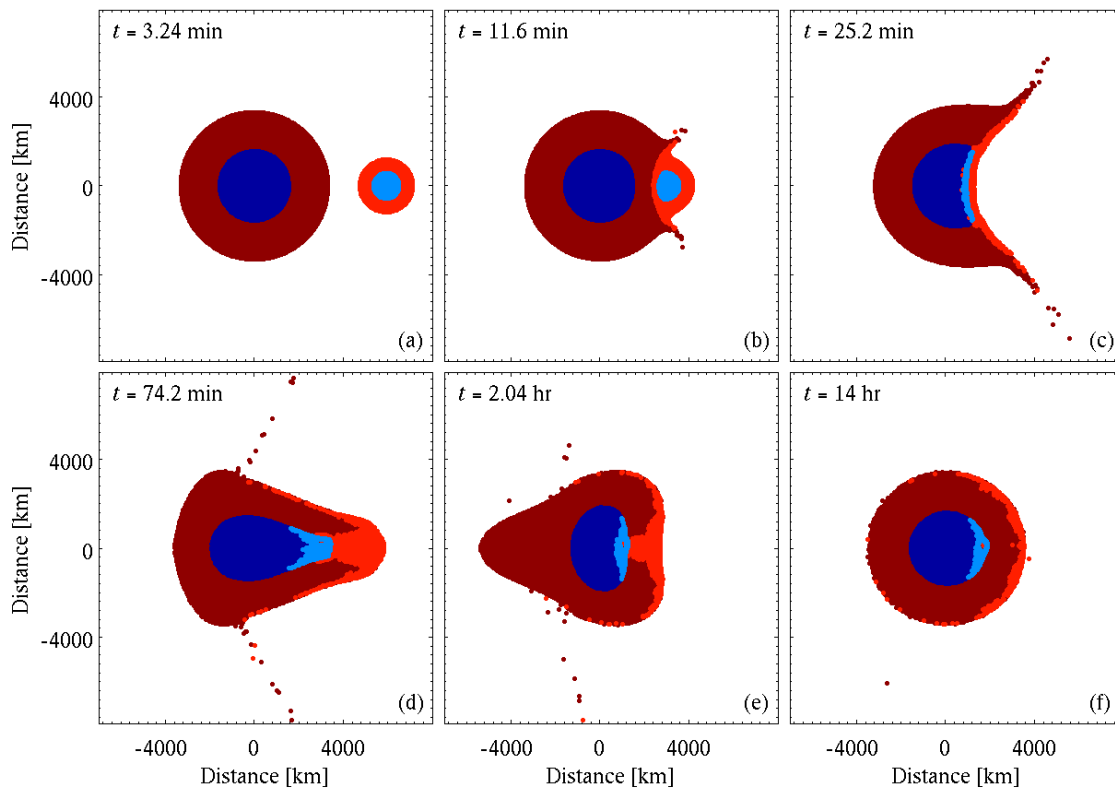


Figure 4-1 Head-on impact by a differentiated impactor. Shown are snapshots in time for a differentiated impactor with $E_k = 5.89 \times 10^{29}$ J, $v_{imp} = 6$ km/s, $\gamma = 0^\circ$. We find that all head-on, differentiated impacts result in the complete accretion of the impactor iron on the planetary core. Iron and olivine are represented by red and blue, respectively, with darker shades representing planetary material. See Figure 4-A1 for snapshots from the other impactor types at a lower energy.

In the case of oblique impacts, the outcome of the interaction between impactors of different densities with the planet is more complex. We see that for basalt and olivine impactors, during the violent impact process the impactors do not mix with the planet, even for significant penetration depths. After the impact, in the case of basalt impactors, the material remains at the surface of the planet, consistent with the low density of basalt. For the olivine impactors, pockets of olivine impactor material may be present in the planet's mantle, depending on the specific impact conditions (e.g., Figure 4-A1). For undifferentiated impactors, the impact process and distribution of material around the planet is similar to that of olivine impactors, however, due to the $\sim 20\%$ higher density of

the impactor material, it begins to sink towards the planetary core as the impact event progresses (Figure 4-A4). Bits of impactor material are distributed throughout the mantle at the end of the simulated ~26 hrs. Compared to the olivine impactor, the undifferentiated impactor penetrates deeper and thus sweeps through the mantle more extensively, however, not as extensively as the iron impactor. For iron and differentiated impactors, in the case of oblique impacts, the impactor is sheared, spread, and effectively sweeps through the mantle of the planet; in the process the iron may become mixed with the mantle of the planet on the timescale of the impact event (Figure 4-2). In general, it appears that impactors that are denser than the mantle – or have a denser component – will interact more extensively with the mantle of the planet than less dense impactors. The obliqueness of the impact angle determines the fate of the iron from the impactor: how much is accreted onto the planetary core, how much resides in the planetary mantle at the end of the simulated ~25 hrs, and how much is ejected to space (see section *Escaping and orbiting material*). For differentiated impactors, the majority of the core accretes for impact angles up to 45°. For the more oblique 60° impacts, part of the impactor core accretes onto the planetary core during the first few hours after the impact, while another fraction of the impactor core is spread over the planetary surface. The surface iron is likely to at least partially mix with other rocky surface material; however, with time, large iron pools that cannot be supported by the lithosphere are expected to descend through the significantly less dense mantle and accrete onto the planet's core. It is only for 75° impacts that the core, together with the majority of the impactor, is ejected to space; in the case of iron impactors, only about 20% of the impactor accretes onto the

planet. Detailed results on the composition of the ejected material for all impactor types are shown in section *Escaping and orbiting material*.

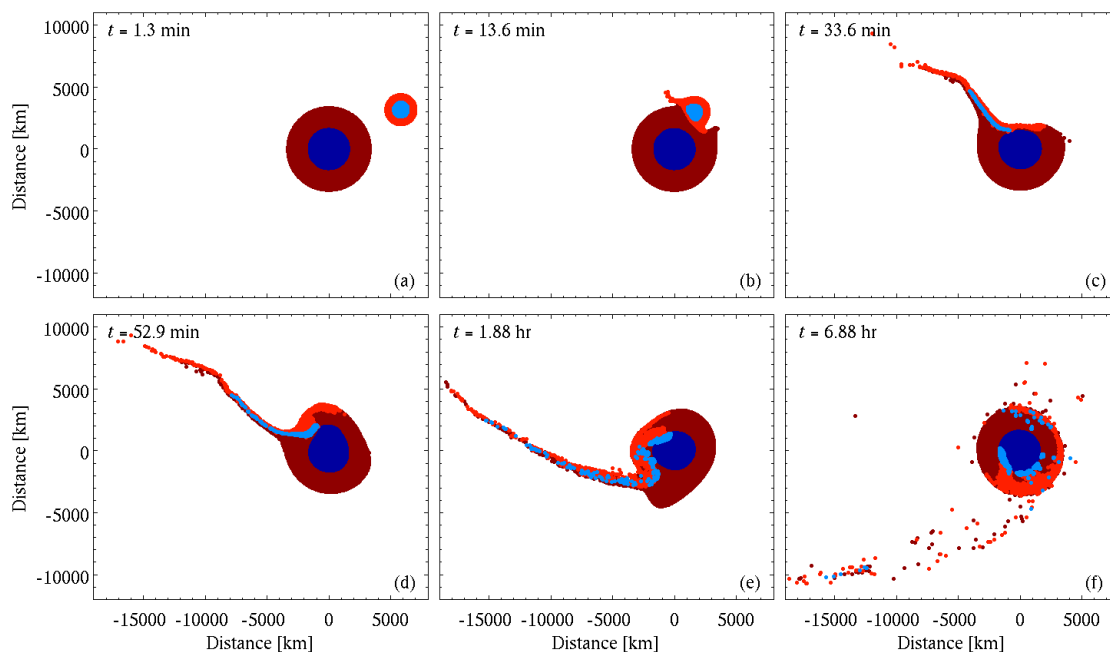


Figure 4-2 Oblique impact by a differentiated impactor. Simulation snapshots showing the sweeping of a differentiated impactor through the mantle of the planet; $E_k = 5.89 \times 10^{29}$ J, $v_{imp} = 6$ km/s, $\gamma = 45^\circ$. Red and blue represent olivine and iron, respectively; darker shades are planetary material. Part of the impactor core accretes (in this case $\sim 90\%$) while the remaining impactor core material is in the “ejecta tail.” The impact progression for other impactor types with these impact conditions are shown in the appendix.

For highly oblique impacts, the impactor skims the target (Figure 4-3). This is a result of the geometry of the impact, and the large size of the impactor relative to the planet: the trajectory of the impactor results in part from the impactor bypassing the planet rather than impacting it (Figure 4-3b). For these skimming impacts, a “tail” is formed between the impactor and the planet: part of this tail, including some impactor material, re-accretes onto the planet, while most of the impactor and the rest of the tail material are ejected (Figure 4-3d–h). Much of the impactor remains intact and continues as an intact object with a velocity much higher than the escape velocity (commonly more

than twice). The ejection velocity for the basalt impactors is fastest, at constant impact conditions, with a decrease of up to $\sim 10\%$ for the iron impactors. For 60° impacts, since more of the impactor collides with the target, the impactor is more effectively sheared and mixed with target material. In none of the simulated cases is any material from the planet's core ejected to space.

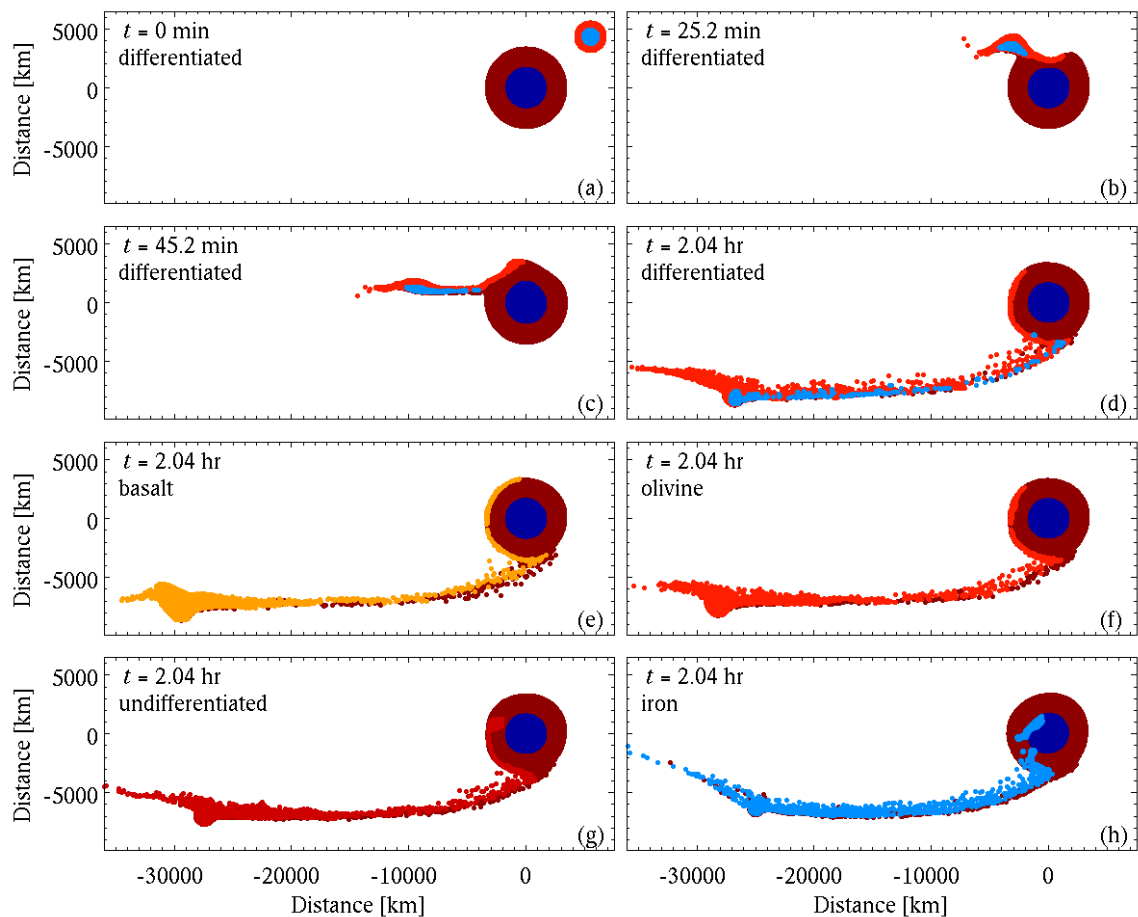


Figure 4-3 Highly oblique impacts skim the surface and remove the crust in their path. While the impactor is sheared, much of it remains intact and escapes to space. Shown are snapshots of impacts with $E_k = 5.89 \times 10^{29}$ J, $v_{imp} = 6$ km/s, $\gamma = 75^\circ$: (a–d) differentiated impactor (lighter red and blue are impactor olivine and iron, respectively); (e) basalt impactor (orange material); (f) olivine impactor (light red material); (g) undifferentiated impactor (rusty red material); and (h) iron impactor (light blue material); dark blue and the darkest red represent iron and olivine in the planet. The skimming nature of the impact is the result of the impact geometry and the large relative size of the impactor with respect to the planet, rather than the impactor composition.

4.5 Results

We present new results for the geophysical consequences for impacts by olivine, undifferentiated, differentiated, and iron impactors with energies of $0.13\text{--}5.89 \times 10^{29}$ J, impact velocities of 6–50 km/s, angles of 0–75°. These results provide information on the importance and effect of impactor characteristics on the resulting impact process and surface features. For the range of impact conditions, we investigate the impact process, the crater size and crustal redistribution, the melt production and distribution, the orbiting and ejected material, and the angular momentum transfer efficiency. Combining our new simulations with results for basalt impactors (Marinova et al., submitted), we can discuss the variation in impact outcomes for a comprehensive range of impactor density and material composition. While the extreme end-member compositions of basalt and iron may not be realistic for all asteroid sizes, these simulated impactor types bracket the possible range of impactor compositions and internal structures expected for planetary-scale impacts in the inner Solar System. Thus we examine the full range of possible outcomes from impacts into a Mars-size target in this impact size regime.

At a given impact energy and velocity, the impactor composition – and density – affect the size of the impactor. A smaller cross-sectional area of the impactor, while carrying the same total momentum and impact energy, can alter the depth of penetration of the impactor, and thus where the majority of the energy of the impact is deposited. The location of deposition of the energy alters the resulting crater size, the location of the produced melt, the location of the antipode, and the crater shape. In addition, for oblique impacts, the large relative size of the impactor with respect to the target can result in only part of the impactor impacting the planet and thus affects the orbiting and escaping

material, momentum transfer, and final rotational period. The relative density of the impactor with respect to the target determines the interaction between these materials as the impact event progresses, whether mixing of the impactor and target can occur, and whether the impactor material will buoyantly rise to the surface. The results show that overall the impactor type affects the depth of penetration, the melt production, the surface melt cover, and the amount of orbiting and escaping material.

4.5.1 Crustal thickness and redistribution

The area of complete crustal removal defines the boundary of the impact crater cavity. We find that the size and shape of the crater, at constant energy, as well as the crustal redistribution, are greatly affected by the impactor type (Figure 4-4). Olivine impactors produce craters similar to those of basalt impactors, while craters from undifferentiated, differentiated, and iron impactors often differ significantly, given the same impact conditions. For head-on and energetic impacts, the basalt, olivine, undifferentiated, and differentiated impactors produce a relatively uniform thickening of the crust outside the crater (Figure 4-4a); iron impactors produce a more local crustal thickening, which resembles a rim (Figure 4-4b). For slow and oblique impacts, iron impactors produce an extremely elongated crater cavity (Figure 4-4d, f), as the impactor penetrates a significant distance downrange of the impact site before being slowed down and thus changes the location of energy deposition (e.g., Figure 4-2, 4-A4 through 4-A8). For basalt and olivine impactors, significant crustal thickening is present downrange of the impact site, about a third to half the planet's circumference (Figure 4-4c). Undifferentiated and differentiated impactors produce an elongated cavity and

downrange crustal deposition (Figure 4-4e), while iron impactors produce crustal thickening on either side of the greatly elongated cavity, especially for intermediate impact angles. At constant energy, as the impact velocity increases and thus the projectile mass and size decrease, the resulting crater shape and crustal redistribution become increasingly similar for the five impactor types. Fast impacts, even at high energies, commonly produce a rim-like structure for all impactor types.

At the highest simulated energy, slow (6 km/s), intermediate angle impacts significantly scour the planetary surface in the downrange direction. Particularly for differentiated and iron impactors the crater cavity becomes greatly elongated (Figure 4-4g, h). Undifferentiated impactors behave similarly to differentiated impactors, but the elongation is not as extreme. Due to the highly irregular shape of the crater cavity for the slow, 45°, highest energy differentiated impact, the major axis of the crater size is set to be the length of the main crater cavity and excludes the narrow downrange crustal excavation zone.

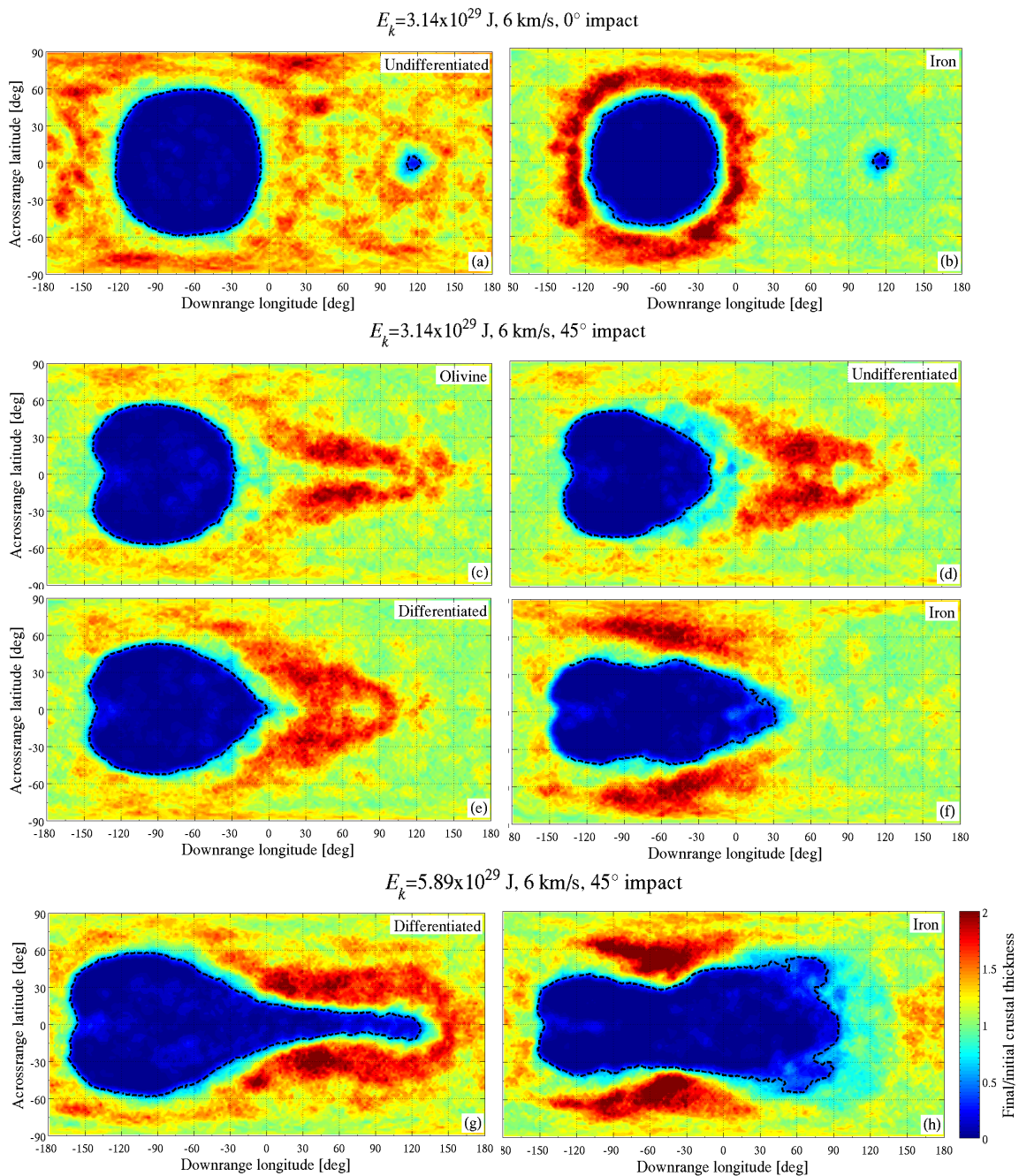


Figure 4-4 Crustal thickness maps. Post-impact crustal thickness normalized by the pre-impact crustal thickness. The crater cavity shape and crustal redistribution are significantly affected by the impactor type, particularly at the highest simulated energy and low impact velocities.

4.5.2 Crater size

We compare the crater sizes resulting from the head-on impacts simulated here with the planetary-scale impact results of Marinova et al. (submitted) and the crater sizes

predicted by the small crater scaling relations of Wilhelms and Squyres (1984), Cintala and Grieve (1998), Holsapple and Schmidt (1982), and Holsapple (1993) in Figure 4-5. While the latter scaling relations were developed for small impacts, we find that our results are encompassed within their variation. This is true for all impactor types. Our results generally seem most compatible with the pi-group scaling of Holsapple and Schmidt (1982), however, in the Holsapple-Schmidt relation the crater size as a function of energy increases less steeply than for the planetary-scale impacts. The crater size results for each impactor simulated here are shown in Figure 4-6.

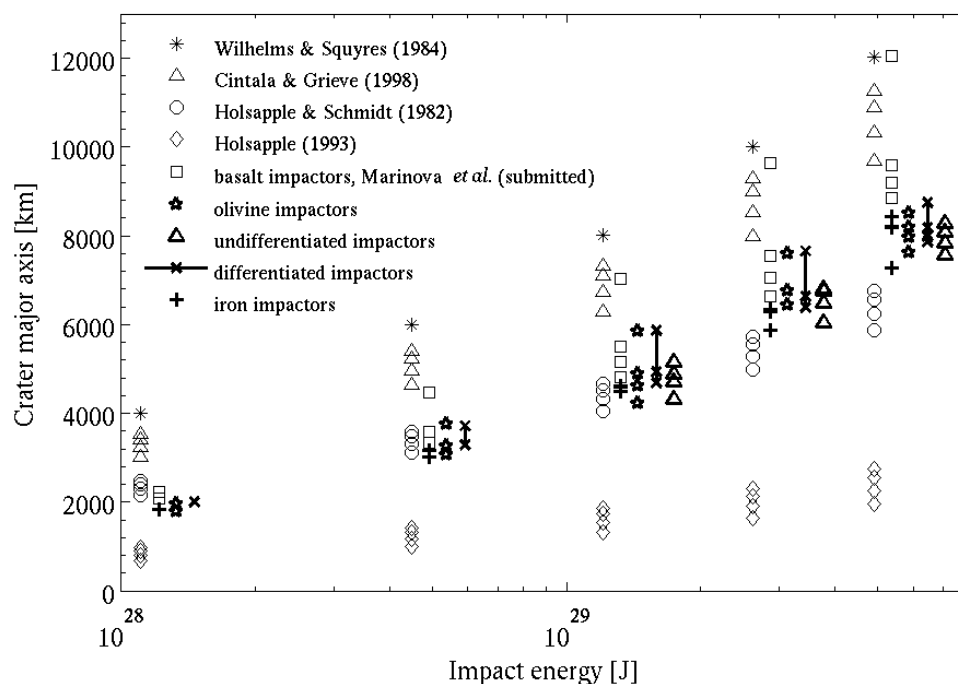


Figure 4-5 Crater sizes from our planetary-scale impact simulations and small, half-space impacts scaling relations, for head-on impacts. Simulation results for basalt (Marinova et al., submitted), olivine, undifferentiated, iron, and differentiated impactors are shown. For each impact energy, impact velocities of 6, 15, 25, and 50 km/s are plotted, if the conditions were simulated (Table 4-1). The olivine results are plotted at the simulated energy; the other symbols are offset horizontally for clarity.

In examining the craters produced for the range of simulated impact conditions, we find that the crater sizes of olivine, undifferentiated, and differentiated impactors are

generally similar with varying velocity and angle. For head-on impacts, the slowest impacts deviate from this trend, such that iron and undifferentiated impactors produce smaller craters than the other impactor types. The basalt and iron impactors bracket the results of the other three impactor types, with the basalt impactor resulting in the larger crater cavities. This trend of decreasing crater size with denser impactor, for a given set of impact conditions, is inversely proportional to the depth of penetration for each of the impactors (see *Depth of penetration*). The depth of penetration correlates with the depth at which the impactor deposits much of its energy and thus the location from where much of the material is accelerated. The initiated flow must penetrate through the surrounding material in order to excavate it. For deeper-penetrating impacts, the strength of the excavation flow may diminish significantly before reaching the surface, and no longer be able to excavate the material. This trend is supported by the results and the corresponding scaling relation of crater diameter as a function of penetration depth found by Marinova et al. (submitted).

For intermediate impact angles, iron and differentiated impactors produce the largest crater cavities, followed by differentiated impactors, due to the significant downrange elongation. Basalt and undifferentiated impactors produce smaller craters, with olivine impactors giving the smallest cavities.

For the most oblique impacts, the basalt, olivine, undifferentiated, and differentiated impactors produce very similarly-sized cavities at all impact velocities; the craters produced by the iron impactors are slightly larger. This results from the skimming nature of these highly oblique impacts; the significant negative buoyancy of the iron

impactors results in their deeper penetration and thus their elongated and larger crater cavities.

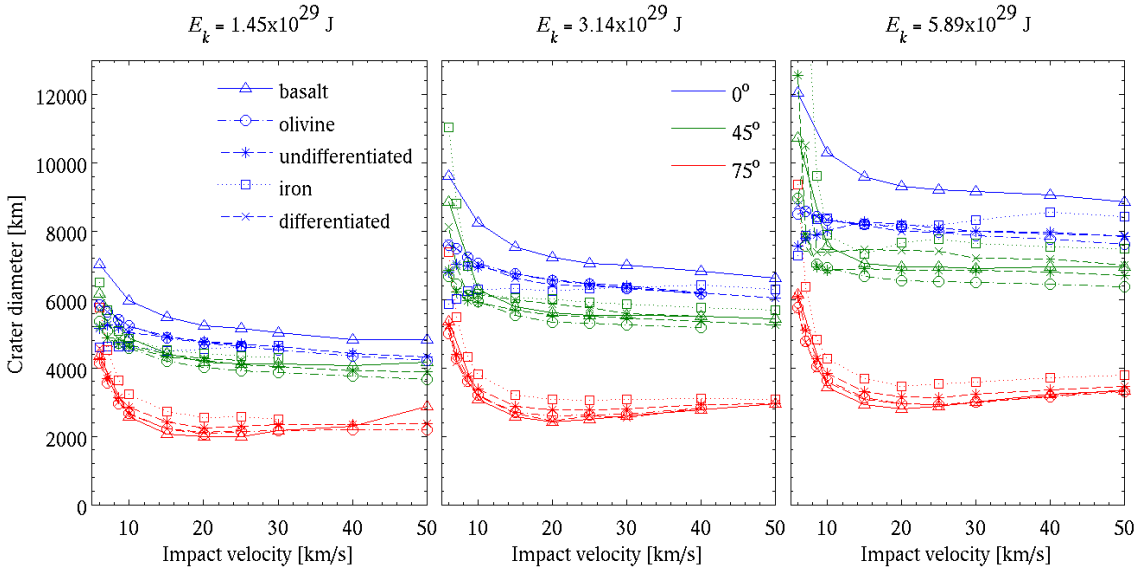


Figure 4-6 Crater size results for the five impactor types (represented by symbols). Shown are simulation results for $E_k = 1.4\text{--}5.9 \times 10^{29}$ J (the three panels), angles of 0° , 45° , and 75° (represented by line colors), and all simulated velocities. The legends in (a) and (b) apply to all panels. For $E_k = 5.9 \times 10^{29}$ J, $v_{imp} = 6$ km/s, $\gamma = 45^\circ$, differentiated impactor, the crater size was manually determined and set to represent the size of the main part of the excavated cavity, excluding the downrange long and narrow area of excavated crust (see *Crustal thickness and redistribution* and Figure 4-4h).

Using the scaling motivated by Wilhelms and Squyres (1984) and Housen et al. (1979), and used by Marinova et al. (submitted), we fit a scaling relation to the crater size results from the simulations:

$$D' = q(E'_k)^r (v'_{imp})^s \cos^t \gamma \quad (4-2)$$

where D' is the crater major axis normalized by the planetary radius ($R_0 = 3,313$ km); E'_k is the impact energy normalized by the binding energy of the target ($E_0 = 5.22 \times 10^{30}$ J); v'_{imp} is the impact velocity normalized by the planetary escape velocity ($v_0 = 5.085$ km/s); γ is the impact angle; and q , r , s and t are fitting parameters. We find that the results from all the impactor types, $E_k = 0.1\text{--}5.9 \times 10^{29}$ J, and all impact velocities and

angles can be fit simultaneously. The best fit (and 95% confidence interval) is then given by $q = 7.01^{+0.60}_{-0.35}$, $r = 0.379^{+0.019}_{-0.010}$, $s = -0.133^{+0.022}_{-0.024}$, and $t = 0.489^{+0.029}_{-0.043}$ (Figure 4-7). The mean absolute errors for basalt, olivine, undifferentiated, iron, and differentiated impactors, respectively, are 11%, 8%, 7%, 13%, and 9%. However, head-on, basalt impactors consistently produce 10–20% larger craters at all impact velocities and the errors are largest for the slowest impacts, $v_{imp} = 6$ km/s. Iron impactors show the largest deviations from the fit (Figure 4-6). Interestingly, the fit is not significantly improved by adding a dependence on density, suggesting that the impactor type does not fundamentally affect the crater size. This is also seen in the summary of crater size results in Figure 4-6. The diminished importance of the impactor type also suggests that the strength of the impact shock is the key feature that sets the size of the crater, and the elongation of the crater cavity due to significant downrange penetration is a secondary effect. The best fit results from fitting each impactor type separately are shown in Table 4-3. Any dependence on gravity and target properties, which were not explored in our simulations, would be contained in the multiplier constant, q .

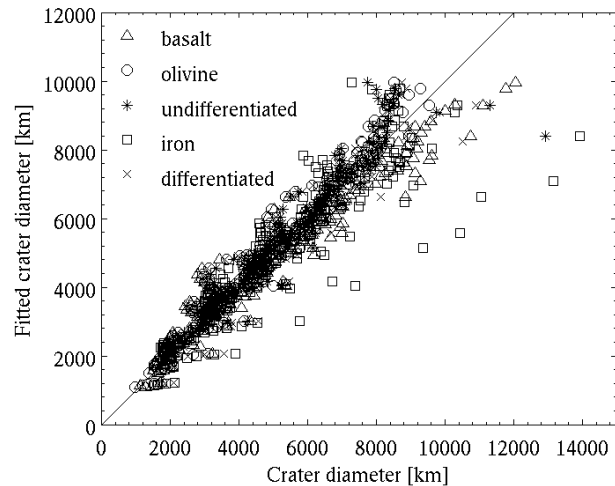


Figure 4-7 Quality of the fit for crater size as a function of impact velocity, energy, and angle. The 1:1 line is also plotted. The symbols represent the different impactor types. The fit is not significantly improved by including a dependence on impactor density. The significant deviations from the trend for the iron impactors result from slow ($v_{imp} = 6$ km/s) and highly oblique impacts.

We compare the obtained best fit exponent parameters (r , s , t) for each of the impactor types, and note that the power law exponents – while very similar – are not identical between the impactor types (Table 4-3). There are a number of possible explanations for this.

Firstly, the scaling relation that is used does not necessarily include all parameters of importance. For example, it is expected that parameters such as the density and size of the target, the bulk modulus and sound speed of the target and impactor, equation of state parameters of the impactor and target, whether the impactor penetrates to the planetary core, and the size of the impactor, all influence the size of the resulting crater cavity. In the case of target properties, which are the same for all simulations, these may be implicitly accounted for in the multiplier. However, aspects such as whether the impactor penetrates into the core are specific to the impactor type and impact characteristics (such as impact energy and velocity) and as such cannot be represented as a constant.

To understand the variation in the parameters between the different impactor types, we reduce some of the complexity of the data by analyzing only the head-on impacts. Following the convention by Gault (1974), if we only take into account the energy and velocity parameters (thus assuming that all other parameters that affect the system, such as target size, density, etc., are constant for all simulations), then the exponents on these two parameters would be related such that $2r + s = 1$, where r and s are as defined in Eq. (4-2). This is required by dimensional analysis: the right hand side must have dimensions of (length)¹. For our fitting results, through dimensional analysis of the data, not taking into account the normalization constants used when doing the fit, we find that for all rocky impactors – that is the basalt, olivine, undifferentiated, and differentiated impactors – result in a net (length)^{0.66±0.02}. This suggests that a property common to these impactor types, with a length scale of (length)^{1-0.66}, is implicitly hidden in the multiplier, q . However, for the iron impactor, we get a net (length)^{0.84}. The difference in the net length scale of the iron impactor, compared to the rocky impactors, suggests that the multiplier does not implicitly include a property that is common to all of them – that is a property of the target – but includes a property of the impactors that is not explicitly included in the fits. In examining all parameters used in the equation of state of the impactor materials, we find that the Tillotson empirical parameter $E_{0,Tillotson}$ is similar for basalt and olivine (and thus also for the undifferentiated impactor which, is simply a dense material with olivine characteristics, and the differentiated impactor for which ~75% of the mass is olivine and iron is thus a minor component) but is different for iron. $E_{0,Tillotson}$ is an empirical fitting parameter that is often close to the vaporization energy of the material and, together with the density ratio, appears as a normalization constant to

the internal energy in the Tillotson EOS. While $E_{0,Tillotson}$ may be important in the fit and may be the missing parameter, we cannot rule out that other parameters are also important and make up for the apparent deficiency in the length-scale dimension.

Secondly, taking into account only head-on impacts, and fitting each impactor type separately (as was done above), we find that even though the length scale for all rocky materials was similar (at 0.66), the fitting coefficients r and s vary significantly. This variation could be due to r and s being a function of the impact or impactor characteristics. The variation in r is not monotonic with the average density of the impactor, and we could not find parameters whose variation could readily explain the variation in r . In the case of s , which represents the dependence on impact velocity, the coefficient is negative for the rocky impactors, and is positive for the iron impactor. This is apparent in the variation of the crater diameter with impact velocity, for a given impact energy (Figure 4-6). Note that both r and s change as we fit other impact angles separately, and the trend in the variation of r and s with impactor type does not stay consistent as the impact angle changes. For example, the exponent s is negative for rocky impactors and positive for the iron impactor for head-on impacts, but for more oblique impacts s is negative for all impactor types. This suggests that the crater diameter dependence on energy and velocity (that is, the fitting coefficients r and s) may themselves be dependent on the impact angle, as well as impactor properties.

Thirdly, in applying scaling relations to the resulting crater size, we make the implicit assumption that the dependence on impact energy, velocity, and angle does not change over the range of simulated conditions. In addition, using a power law relation assumes that the relation has a constant slope in log-log space. Given the large energy

range that is explored here – a factor of 15 between the least and most energetic impacts – this assumption may be violated. For example, as noted earlier, the largest deviation of the fit from the simulation results is for slow and highly energetic impactors. These are the impacts that penetrate the deepest and thus encounter the core of the planet. If the impactor interacts with the core of the planet – a material with significantly different properties than the planet’s mantle – it would be expected for the scaling to change. Scaling relations for small impacts are developed for a single material target and single material impactor. If two materials are affecting the impact process, the assumption of a power-law relationship between crater diameter and the impact characteristics may not apply.

The validity of using a power law to describe the dependence of crater size with impact energy and velocity is apparent in whether the results are described by a constant slope on log-log space (Figure 4-8a–c). It can be seen that in most cases, the relationship between crater size and energy and velocity (varying only one parameter) is not linear in log-log space for all impactor types and the range of simulated conditions. This is not surprising, since the motivation for studying the planetary-scale impacts size regime, and especially for using numerical models, is the expected importance of finite-size effects for both the target and the impactor. Thus we expect the planetary curvature, radial gravity, and the relatively large size of the impactor to the target to affect the impact process in this energy range and to cause a deviation from scalings developed for the small crater regime. Our simulations cover an energy range over which the importance of the finite-size effects changes, which is exhibited as a change in slope of the crater size scaling in log-log space. In the case of crater scaling, the deviation from a power law is

most pronounced for energies and impact conditions for which the impactor directly interacts with the planetary core. However, we cannot rule out other causes for the effect, including planetary curvature.

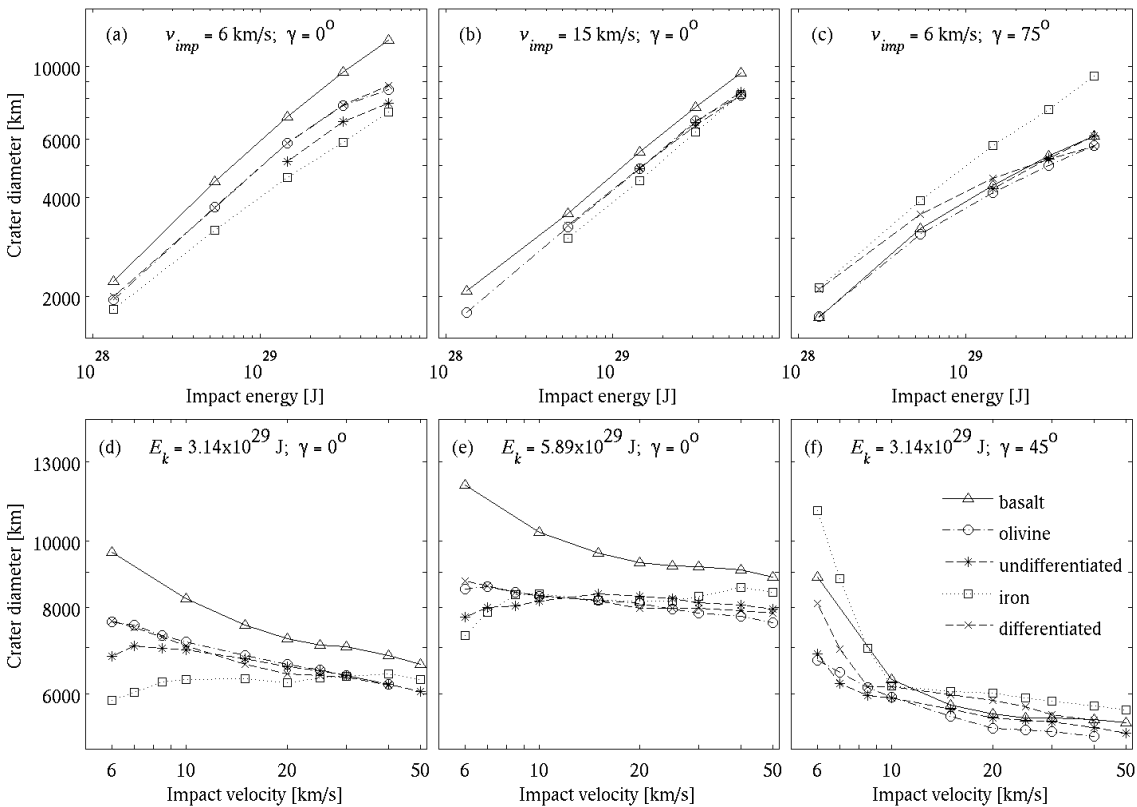


Figure 4-8 Crater diameter variation versus impact energy for a range of impact velocities and angles. For each panel the impact velocity and angle are held constant, at values identified in the panel, and the impact energy is varied. We see that in most cases the relationship is not linear, thus suggesting that either a power-law relationship does not fully describe the relationship, or that the exponent in the power law is itself a function of the impact energy. Note that not only are the impactor types offset, but also the degree of curvature is different between them.

We explore the effect of the core by fitting only head-on impacts which do not penetrate to the core-mantle boundary (1,800 km depth). Interestingly, we find that the dependence on energy is very similar for all impactor types for this restricted subset (Table 4-2). However, there is still significant variation in the dependence on the impact velocity, as may have been expected from the non-linear dependence seen in log-log space (Figure 4-8d-f). Thus the data cannot be fully described by a single power-law

relationship for the entire simulated range, and our scaling is an approximation for the crater size to velocity dependence, rather than a fundamental relation.

Table 4-2 Crater diameter as a function of impact energy and velocity for head-on impacts that only penetrate into the mantle (penetration depth < 1700 km). Note that the dependence on energy, r , is similar for all impactor types. However, the dependence on velocity varies between the impactor types, suggesting that the velocity dependence may be a function of the impactor material. The 95% confidence intervals for each of the fitting parameters are included; the number of points (impact cases) included in the fit, n , is also noted. In all cases the fitting error is only a few percent.

Basalt impactor	Olivine impactor	Undifferentiated impactor	Iron impactor	Differentiated impactor
Crater size scaling: $D' = q(E'_k)^r (v'_{imp})^s$; Only head-on ($\gamma = 0^\circ$), penetration depth < 1700 km				
$q = 9.10 \pm 1.1$	$q = 7.77^{+0.61}_{-0.42}$	$q = 7.50^{+0.26}_{-0.34}$	$q = 6.44^{+1.68}_{-1.47}$	$q = 7.96^{+0.40}_{-1.31}$
$r = 0.420^{+0.021}_{-0.019}$	$r = 0.417^{+0.015}_{-0.011}$	$r = 0.425^{+0.007}_{-0.011}$	$r = 0.422^{+0.033}_{-0.041}$	$r = 0.427^{+0.008}_{-0.027}$
$s = -0.158^{+0.057}_{-0.029}$	$s = -0.140^{+0.018}_{-0.016}$	$s = 0.093^{+0.009}_{-0.008}$	$s = -0.009^{+0.077}_{-0.070}$	$s = -0.123^{+0.052}_{-0.013}$
err: 3% ($n = 31$)	err: 2% ($n = 32$)	err: 1% ($n = 15$)	err: 1% ($n = 11$)	err: 1% ($n = 10$)

When fitting all head-on impacts, regardless of their penetration depth, the power law dependence on energy is no longer constant for all impactor types: $r = 0.419, 0.377, 0.347, 0.403,$ and 0.366 for basalt, olivine, undifferentiated, iron, and differentiated, respectively.

We compare our fitting parameters to those found in previous analyses and modeling. O'Keefe and Ahrens (1993), based on the formalism by Holsapple and Schmidt (1987), use the scaling

$$\frac{D}{a} = K \left(\frac{ga}{v_{imp}^2} \right)^n \quad (4-3)$$

where a is the impactor radius, g is gravity, and K and η are constants. Rearranging the above scaling in order to represent the crater diameter as a function of energy and velocity, as in Eq. 4-2, we obtain:

$$D \propto \left(g^{-0.22} \rho_{imp}^{-0.26} \right) E_k^{0.26} v_{imp}^{-0.08} \quad (4-4)$$

The term in the paranthesis does not vary for a given impactor type and would effectively be included in the multiplier, q , in our fits. The expected exponent values of 0.26 and -0.08 on the energy and velocity, respectively, are quite different from the fitting values we obtain: 0.42 to 0.43 and -0.16 to 0.09 for the respective exponents, for head-on, shallow impacts (discussed below, Table 4-2). The power law dependence on energy and velocity found by Gault (1974) is equivalent to Eq. 4-4.

Despite the difficulties in explicitly showing the fundamental relationship between the crater diameter and the impact characteristics, the fitting results do provide insight into the impact process and provide a scaling relation that summarizes the results and that can be used to understand the observed impact features. In addition, the ability of a single scaling relation, without taking into account any impactor-specific properties, to explain the data with an average deviation of $\sim 10\%$, shows that the impactor properties have a secondary importance compared to the impact characteristics: impact energy, velocity, and angle. The fit to all the impactor results simultaneously gives an R^2 of 0.87, thus the fit explains over 87% of the variation in the results.

4.5.3 Ellipticity

The shape of the crater cavity can be affected by the downrange penetration of the impactor, resulting in increasing ellipticity of the cavity. We find that the shape, and thus

ellipticity, of the crater cavity is greatly affected by the impactor composition. The resulting ellipticities are quite variable between impactor types and impact conditions, pointing to the complex interaction between downrange penetration distance, penetration depth, and crustal excavation. The maximum crater ellipticity for olivine impactors is similar to, but smaller than, that for basalt impactors at low impact velocity (Figure 4-9a, b). For basalt impactors, the two highest simulated energies ($E_k = 3.1\text{--}5.9 \times 10^{29}$ J) produce significant ellipticities (> 1.1) at intermediate impact angles ($\gamma > 30^\circ$). For slow olivine impacts, only the highest impact energy results in ellipticities greater than 1.1, with a maximum ellipticity of about 1.2. Fast basalt and olivine impacts result in similar crater ellipticities. For iron, undifferentiated, and differentiated impactors, ellipticities greater than 1.1 are common and seen for impact angles greater than 15° . This is due to the greater penetration depth by these impactors and thus the greater downrange penetration and crustal excavation by oblique impacts. For slow differentiated impactors, the crater has an ellipticity up to ~ 1.45 , while for slow iron and undifferentiated impactors the ellipticity is up to 2.4 (Figure 4-4g). The iron-containing impactors – especially differentiated impactors – also produce highly elongated craters at higher impact velocities, unlike for basalt and olivine impactors. The significant ellipticity for most off-axis undifferentiated and differentiated impactors – over a range of impact angles and velocities – suggests that elliptical planetary-scale craters should be common. This is the case with the planetary-scale craters observed in the inner Solar System; these craters have ellipticities of: 1.38 for South Pole–Aitken basin on the Moon, 1.33 for Hellas Basin on Mars, 1.25 for Mars’ Northern Lowlands (Andrews-Hanna et al., 2008), and 1.16 for Caloris Basin on Mercury (Fassett et al., 2009).

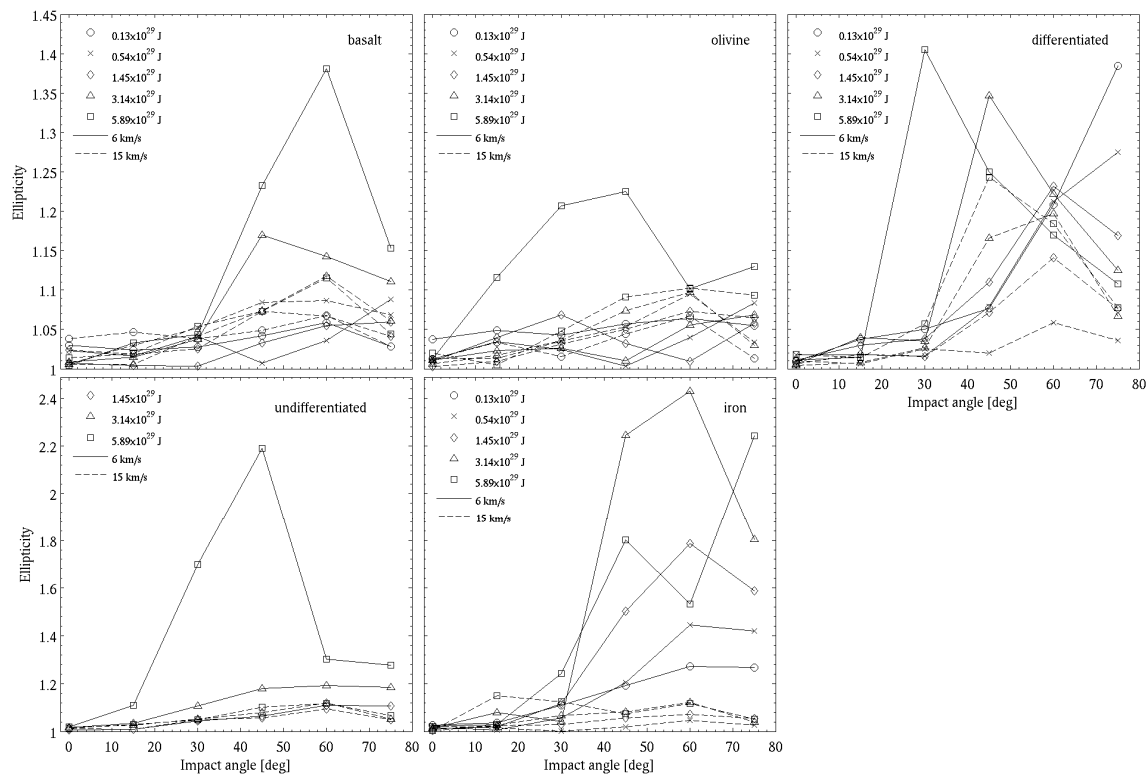


Figure 4-9 Elongation of the crater cavity for slow (6 km/s) and faster (15 km/s) impacts as a function of impact angle, for all simulated impactor types. The largest ellipticities result from slow impacts; however, for differentiated and iron impactors, highly elongated craters are also seen at higher velocities and intermediate impact angles.

4.5.4 Depth of penetration

The depth of penetration of the impactor represents the maximum depth of the transient crater cavity, and the potential depth to which material may be mixed. Our simulation results show that, in general, for a given set of impact conditions, iron impactors penetrate the deepest and the penetration depth decreases with decreasing average impactor density (Figure 4-10). Interestingly, despite the similar bulk densities of undifferentiated and differentiated impactors, they do not penetrate equally: differentiated impactors generally penetrate as deeply as iron impactors, while the penetration depth of undifferentiated impactors is between that of olivine and iron impactors. This is due to the effective decoupling between the mantle and core in differentiated impactors. Thus it

is the densest coherent component in the impactor that determines the maximum penetration depth during the impact, rather than its bulk density or cross-sectional area. As such, in a differentiated impactor the coherent iron core determines the maximum depth of penetration, while in a well-mixed iron and olivine mixture it would be expected for the bulk density to determine the penetration depth. Or more generally, it is the highest density component that sets the penetration depth.

For differentiated and iron impactors, both containing an iron component, penetration into the core is common (depth > 1,800 km). Note that these penetration depths represent the deepest penetration during the initial impact process (the first ~30 min of the impact), and not whether the impactor material sinks due to its negative buoyancy with respect to the planetary mantle. Differentiated impactors combine the features of the olivine and iron impactors, thus while the impactor's mantle material is stopped quickly – similarly to the olivine impactors – the core of the impactor has a much higher momentum per unit volume and continues deeper into the planet. This effect can be distinguished from the effect of the iron's negative buoyancy in the planetary mantle as we examine the penetration depth during the beginning of the impact process.

The impactor iron material accretes onto the planetary core for all head-on impacts, including the least energetic cases simulated. Interestingly, despite the significant deformation and depth of penetration for the more energetic impacts, at the conclusion of most differentiated impactor simulations, the impactor's mantle is not mixed with the planetary mantle but is located at shallow depths. Head-on and low angle impacts by iron impactors also result in the complete accretion of the impactor onto the planetary core. Undifferentiated impactors often result in mixing of the impactor and

planetary mantle during the impact process, unlike all other impactor types. At the conclusion of the simulated time, for mostly head-on impacts, the undifferentiated impactor material is partially accreted onto the planetary core but also forms a continuous mass that extends to the planetary surface (Figure 4-1, 4-A1). For oblique impacts, impactor material initially deposited on the planetary surface is observed to sink through the planetary mantle over the simulated ~ 25 hrs. (Figures 4-A1, 4-A4).

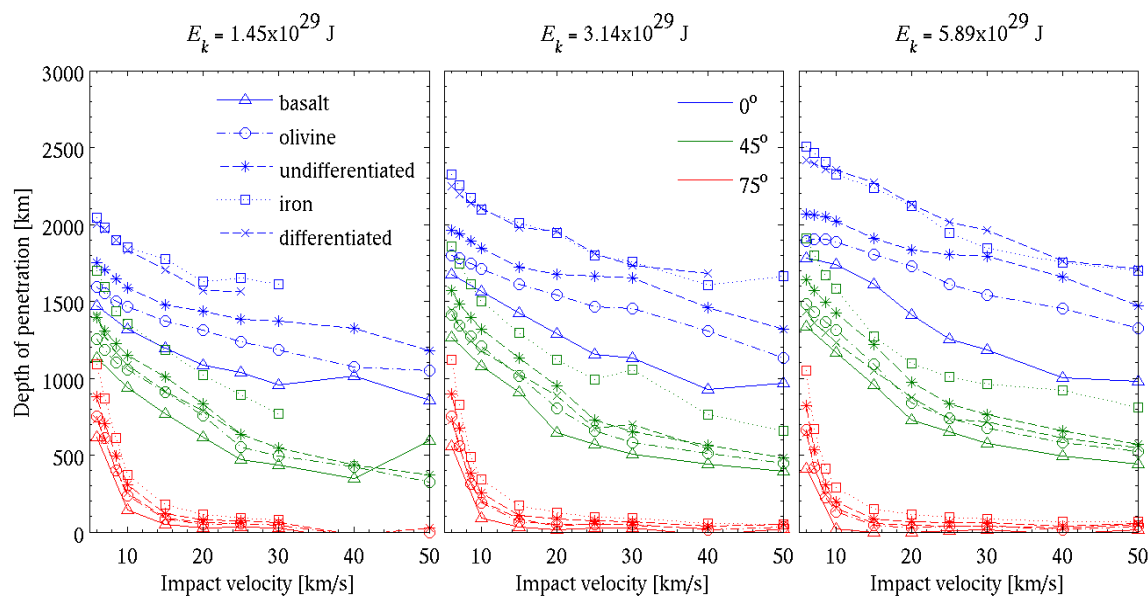


Figure 4-10 Depth of penetration for all simulated impactor types and energies of 1.4 , 3.1 , and 5.9×10^{29} J (for the three panels). The legends apply to all panels: line type and symbol represent impactor type, while line color signifies the impact angle. The penetration depth is measured during the beginning 30 min of the impact process. For a given set of impact conditions, the iron and differentiated impactors penetrate the deepest. For single-material impacts, the depth of penetration decreases as the density decreases. Penetration into the planetary core is common for impactors with an iron component, and olivine and undifferentiated impactors also penetrate the core for head-on, slow, and energetic impacts.

Marinova et al. (submitted) found that the depth of penetration, which defines the depth of the transient cavity, was well described as scaling with impactor mass and impact angle. We find that the same relation can be applied to all impactors simulated here. However, in order to fit the results from all impactors simultaneously, a dependence on density must also be included in the fit:

$$h' = c (\rho')^w (M'_{imp})^d \cos \gamma$$

where h' is the depth of penetration normalized by the target radius (3,313 km); ρ' is the uncompressed average density of the impactor normalized by the average density of the target (4,222 kg/m³); M'_{imp} is the impactor mass normalized by the target mass (6.41x10²³ kg); γ is the impact angle; and c , w , and d are constants. Results from impact angles of 60° and 75° were excluded from the fit as they generally result in shallow penetration of only a few hundred kilometers and thus have a large relative error associated with the result (see *Resolution effects*). When including a density dependence, we fit only the single-material impactors and not the differentiated impactor. By examining how well the fit described the differentiated impactor, we gain insight into whether the bulk density of the impactor is more important than the internal structure. The best fit for fitting all single-material impactor types simultaneously, and corresponding 95% confidence intervals, are $c = 0.981^{+0.031}_{-0.028}$, $w = 0.376 \pm 0.021$, and $d = 0.138 \pm 0.006$ for impact angles of 0–45°, $E_k = 0.1–5.9 \times 10^{29}$ J, and all impact velocities. No upper depth constraint is applied and core-penetrating impacts are included. The mean absolute errors are 13, 14, 13, 9, and 14% for basalt, olivine, undifferentiated, iron, and differentiated impactors, respectively (Figure 4-11a). The best fit when density is not included, and the results from fitting each impactor type separately, are reported in Table 4-3. Note that while the fit captures much of the variation, it tends to overestimate the penetration depth as the impact angle increases. The significant improvement in the fit when density is included suggests that, in addition to the impactor mass, the size of the impactor is also important for the depth of penetration. Note that as defined earlier, the depth of penetration is

measured during the initial impact event; buoyancy effects are expected to act over a longer timescale.

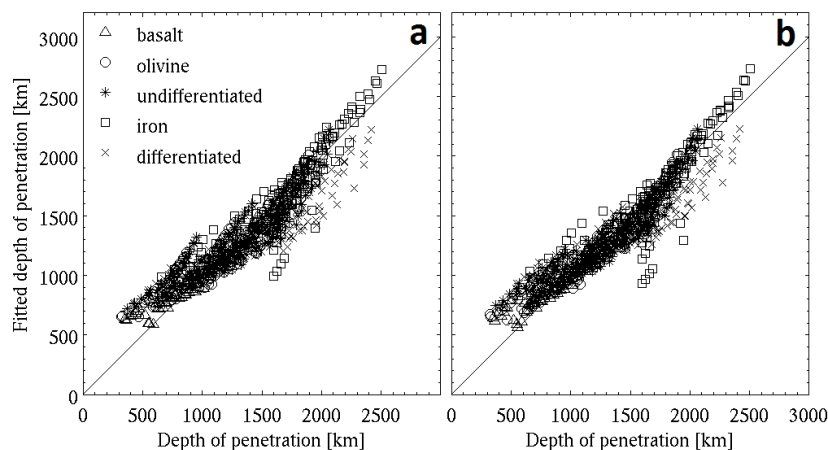


Figure 4-11 Quality of the fit for depth of penetration as a function of (a) average impactor density, mass, and angle, and (b) including a velocity dependence as well (Table 4-3). Symbols represent the different impactor results; the 1:1 line is also shown (solid line). Fitted are impact angles of 0–45°, energies of 0.1–5.9x10²⁹ J, and all velocities; the highly oblique impacts, which generally have shallow penetration depths, were excluded due to the associated large uncertainty in those results. Note that there is some structure to the residuals, suggesting that other parameters may be important. The residual structure was somewhat minimized by the inclusion of a velocity dependence.

In fitting each of the impactors separately, we find that the power law dependence on mass is similar, but not identical, for each of the simulated impactor types. The change in the mass exponent, d , does not appear to follow the bulk or median density of the impactors. We examine head-on and 45° impacts separately to explore the effect of impact angle on the power-law dependence; for head-on impacts $d = 0.152, 0.129, 0.088, 0.110, 0.098$ and for 45° impacts $d = 0.229, 0.230, 0.260, 0.195, 0.169$ for basalt, olivine, undifferentiated, iron, and differentiated impactors, respectively. For each of the impact angles the exponent on mass is not consistent between all the impactor types, and it does not appear to vary consistently with the impactor density, the sound speed of the material, or other equation of state properties. If we fit a line through the relationship of d value

versus impactor density and sound speed, we get $R^2_{\text{density}} = 0.30$ and $R^2_{\text{density}} = 0.22$, for $\gamma = 0^\circ$. For $\gamma = 45^\circ$, the respective best line fits give $R^2_{\text{density}} = 0.39$ and $R^2_{\text{density}} = 0.17$. In both cases it appears that a line does not describe the relationship between the parameters, and no other functional form is apparent. Note that the speed of sound for the basalt, olivine, undifferentiated, and iron materials used here are 3.1, 6.1, 5.4, and 4.0 km/s. However, overall we find that the exponent d is larger for basalt and olivine impactors than for iron impactors, and in all cases the undifferentiated impactor requires lower d values than the basalt, olivine, and iron impactors. The behavior of the differentiated impactor does not seem to follow any consistent trend, possibly an effect of its two-material structure.

We also examine shallow-penetrating impacts separately, to attempt to separate any possible core-related effects. For this limited subset, the power-law dependence on mass is also not compatible among the different impactor types ($d = 0.175, 0.164, 0.158, 0.080, 0.115$ for basalt, olivine, undifferentiated, iron, and differentiated impactors, respectively).

In previous work, through dimensional analysis and modeling, the penetration depth has been found to be a function of the planetary gravity, g , the projectile radius, a , and the impact velocity (e.g., O'Keefe and Ahrens, 1993), as was also noted earlier for the crater size (Eq. 4-3):

$$\frac{h}{a} \propto \left(\frac{ga}{v_{imp}} \right)^{-0.22}$$

We rewrite the relationship on impactor radius to separate the dependences on impactor mass and density, ρ_{imp} :

$$h \propto g^{-0.22} (\rho_{imp})^{-0.26} (M_{imp})^{0.26} (v_{imp})^{0.44} \quad (4-5)$$

This relationship suggests that both the impactor mass and the impactor velocity need to be taken into account for a given planetary gravity and impactor density, and that the stronger dependence is on velocity.

When we use the O’Keefe and Ahrens scaling (Eq. 4-5) for head-on impacts, we find the exponent on mass to be $d = 0.188, 0.198, 0.202, 0.120, 0.118$ and for velocity to be $0.114, 0.233, 0.271, 0.032, 0.080$ for each of the impactor types separately (basalt, olivine, undifferentiated, iron, and differentiated impactors, respectively); the associated fitting errors were 5, 3, 4, 4, and 3%, respectively. These exponents are significantly different from those found by O’Keefe and Ahrens, and the relative magnitude between the mass and velocity exponents is also not preserved. However, interestingly, the exponent on mass is similar for the rocky impactors group (basalt, olivine, undifferentiated), and for the iron-containing impactors group (iron and differentiated), but different between the two groups. The exponent on velocity is not consistent between the impactor types, and does not appear correlated to the impactor size (bulk density). However, the exponent on mass for olivine and undifferentiated impactors – materials that are identical except for their uncompressed density – are very similar.

The non-dimensional analysis applied by O’Keefe and Ahrens (1993), and substantiated by modeling impacts into a half-space, used the non-dimensionalized factor $\mu(ga/v_{imp})^\eta$, where the exponent η is constant for gravity-regime scaling, and only the multiplier μ changes depending on whether the maximum penetration depth or the maximum diameter are fitted. In this context we examine whether the scaling relations we find for crater size and penetration depth are consistent between themselves, despite

their already-mentioned difference from the O'Keefe and Ahrens scaling. The penetration depth and crater scaling, for head-on impacts, relate as follows:

$$h \propto (M_{imp})^d (v_{imp})^e \propto (E_k)^d (v_{imp})^{-2d+e} \propto D$$

where, comparing to Eq. (4-2), $r = d$ and $s = -2d + e$. Using the subset of head-on and shallow ($h < 1,700$ km) impacts, we find that $d = 0.10$ to 0.20 , while $r = 0.42$ to 0.43 . For the velocity exponent, $(2d + e) = -0.26$ to -0.07 , while $s = -0.14$ to 0.16 . Thus our results do not support a similar power law dependence for both penetration depth and crater diameter. This could be explained by the use of a half-space model by O'Keefe and Ahrens to calculate the relations, and the curvature of the planet would likely result in a different – and possibly non-linear – relationship between penetration depth and crater diameter.

In examining the results in log-log space, the depth of penetration is not a linear function of impactor mass, velocity, momentum, or energy, all other parameters being held constant, over the simulated range (Figure 4-12). Thus the use of a power law to describe the results may not fully capture the variations.

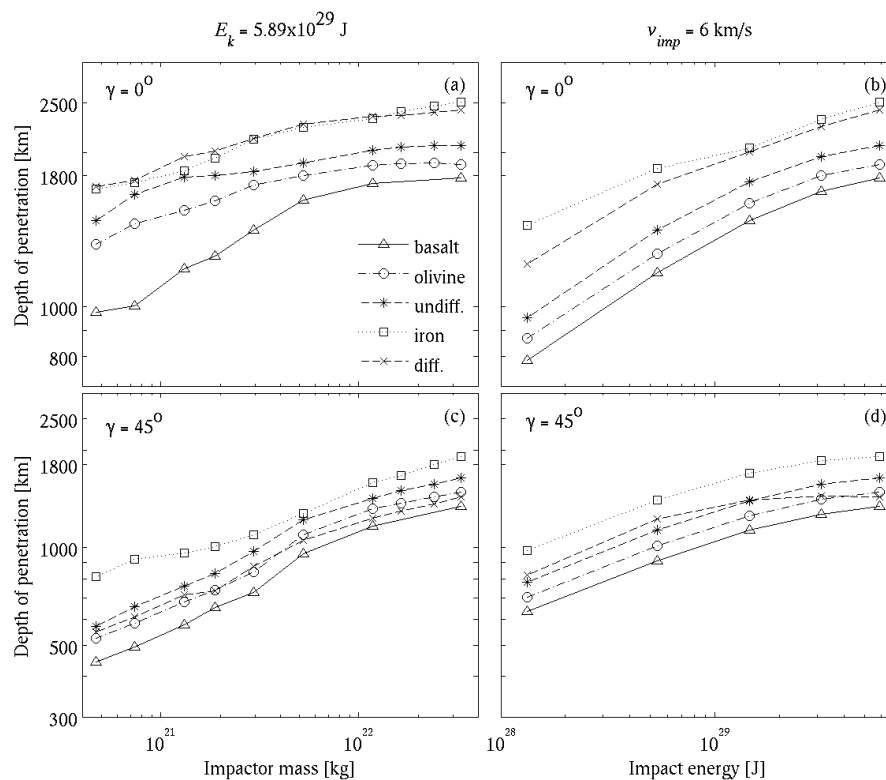


Figure 4-12 Depth of penetration as a function of (a, c) impactor mass ($E_k = 5.89 \times 10^{29}$ J, $\gamma = 0^\circ$, 45°) and (b, c) impact energy ($v_{imp} = 6$ km/s, $\gamma = 0^\circ$, 45°), shown in log-log space. While the relationships are linear for part of the simulated range, a break in slope is apparent for higher impact masses and energies. For example, as the penetration depth of basalt impactors approaches the planetary core (1,800 km), the relationship changes. The legend applies to all panels.

4.5.5 Melt production

For planetary-scale impacts, the production and distribution of melt is important in determining whether the impact structure will be preserved: significant surface melt cover can reset the planetary surface. By examining the amount of melt produced for the range of impactor types simulated here, we can determine for what range of impact conditions a crater cavity is likely to be preserved. Figure 4-13 shows the melt amounts produced by the five types of impactors and the range of simulated impact conditions. Generally, we find that for a given energy, velocity, and impact angle the largest amount of melt is generated by iron impactors, with decreasing amounts of melt produced by the undifferentiated, differentiated, olivine, and basalt impactors. That is, the amount of melt

produced is broadly proportional to the average impactor density. This is supported by the similar melt amounts from the differentiated and undifferentiated impactors. The exception to this trend is for head-on impacts, and especially at slow velocities, for impactors that contain iron (i.e., iron and differentiated impactors): their melt production is low due to the exceedingly large rebound of the planet and associated considerable increase in ejected material, as described in *Mechanics of the impact process* and illustrated in Figure 4-A2.

It is interesting to note that over the convective timescale ($\sim 10^6$ yrs), additional surface melt may be produced as material is adiabatically brought to the surface. For the less energetic impacts, the energy profiles at the end of the simulated time (25 hrs) appear to show that convection has not yet setup adiabatic profiles throughout the mantle. For these impacts highly energetic (hot) material can be buried below less energetic (cold) material. As an example, for differentiated impactors with an energy of $E_k = 3.14 \times 10^{29}$ J, the melt mass can increase by about 10%, for ($\gamma < 50^\circ$), if mantle material is brought to the surface. For highly oblique impacts the melt mass increase is only $\sim 3\%$, as less energy is deposited at depth. For the more energetic $E_k = 5.89 \times 10^{29}$ J differentiated impacts, the simulation appears somewhat different: calculations show that up to $\sim 30\%$ more melt may be produced by decompression melting; however, this value may be an upper limit since for highly energetic impacts much of the mantle appears to be in a convective or stably-stratified (more energetic material over less energetic material) profile radially and circumferentially for most of the planet. However, for less energetic cases, the lateral asymmetry in energy distribution will start convective overturn, and decompression melting may become important.

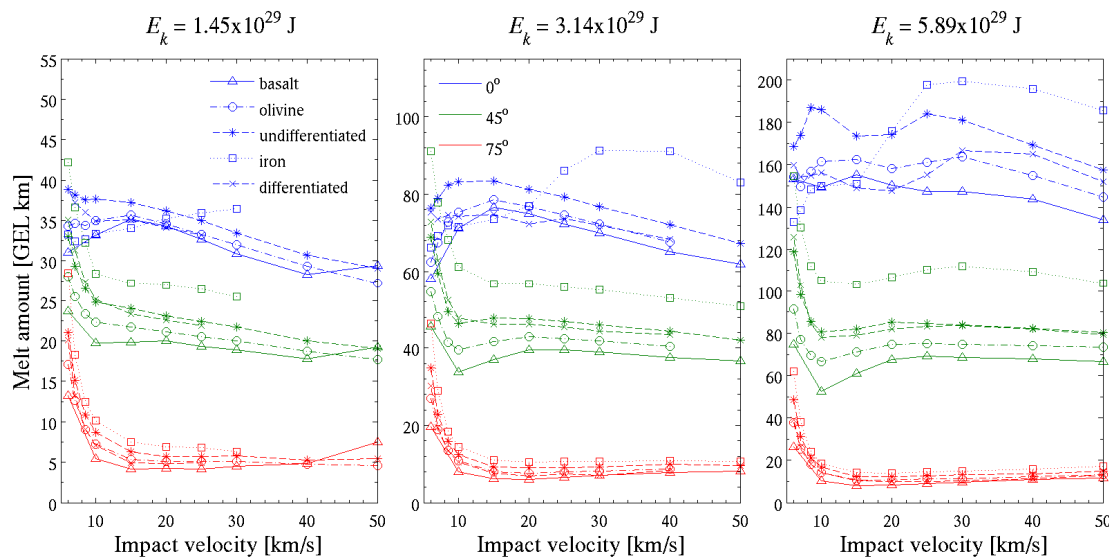


Figure 4-13 Amount of melt produced for the range of simulated impact conditions. The legends apply to all panels. Melt amounts are shown in terms of global equivalent layer (GEL) depths on Mars (1 km GEL = 5.1×10^{20} kg).

The energy of the impact is converted to thermal and kinetic energy, where the former can produce melted mass, while the latter ejects material and increases the rotational rate of the planet. Thus the partitioning between these two energy reservoirs, based on the details of the impact process, provides insight on the amount of melt produced. In our results we find that this trade-off holds, and the amounts of melt and ejecta are consistently inversely related.

For iron and differentiated impactors, additional thermal energy is provided by the accretion of the iron from the impactor onto the planetary core, thus converting gravitational potential into thermal energy. The initial kinetic and total starting energies are held about constant across simulations. The accretion effect is especially important for large (slow) impactors: for the most massive impactor, the difference in potential energy between being placed at the surface of the planet (where basalt impactors remain)

and accretion onto the core-mantle boundary (such as iron impactors), is equivalent to ~35% of the impact energy.

It is important to note that the significantly larger melt production by iron impactors for higher impact velocities ($v_{imp} > 10$ km/s) at head-on to intermediate angles, is due to increased energy availability through a decrease in both the ejected amount as well as the ejection velocity. For highly oblique impacts, the ejection velocities of all impactors become increasingly similar, however the ejection velocity for iron impactors remains slightly slower. These effects are discussed in more detail in *Escaping and orbiting material*.

The melt production results between the five impactor types are most similar for the highly oblique impacts. This is consistent with the qualitative similarity in the simulations for these high impact angles and the general lack of impactor accretion in all cases.

In addition to the melt production, we examine where the impact energy is deposited for the five impactor types. Figure 4-14 shows the change in thermal energy with location in the planet. The change in thermal energy is very similar for the basalt and olivine impactors, with olivine impactors depositing more energy at depth than the basalt impactors. This is consistent with both the greater depth of penetration and the larger melt production (less ejected material) for olivine impactors. For the higher density undifferentiated and differentiated impactors, much of the energy is below the sub-impact point, reaching to the core-mantle boundary; this trend is consistent with these impactors' increased depths of penetration. For iron impactors, the pattern of energy deposition is distinct from that of other impactor types, particularly for slower impacts. This seems to

be a result of the difference in the transient cavity formed by the iron impactors, as described in detail in *Appendix 4-A*. As the impact velocity and angle increase, the energy deposition by iron impactors becomes more similar to that seen for the other impactor types. This correlates with impact conditions for which all impactor types produce qualitatively-similar transient crater cavities and impact events (as described in *Appendix 4-A*). For the undifferentiated and differentiated impactors, the pattern and depth of energy deposition are intermediate between the olivine and iron results. In addition, the energy distribution is more uniform than it is for the iron impactor. The higher total energy deposited in the planet is also apparent. Interestingly, all impactor types produce remarkably similar pattern and magnitude of energy deposition for the fastest (50 km/s) impacts. This supports the idea of a fast, small impact being effectively modeled by a point source explosion, in which the energy of the explosion is most important.

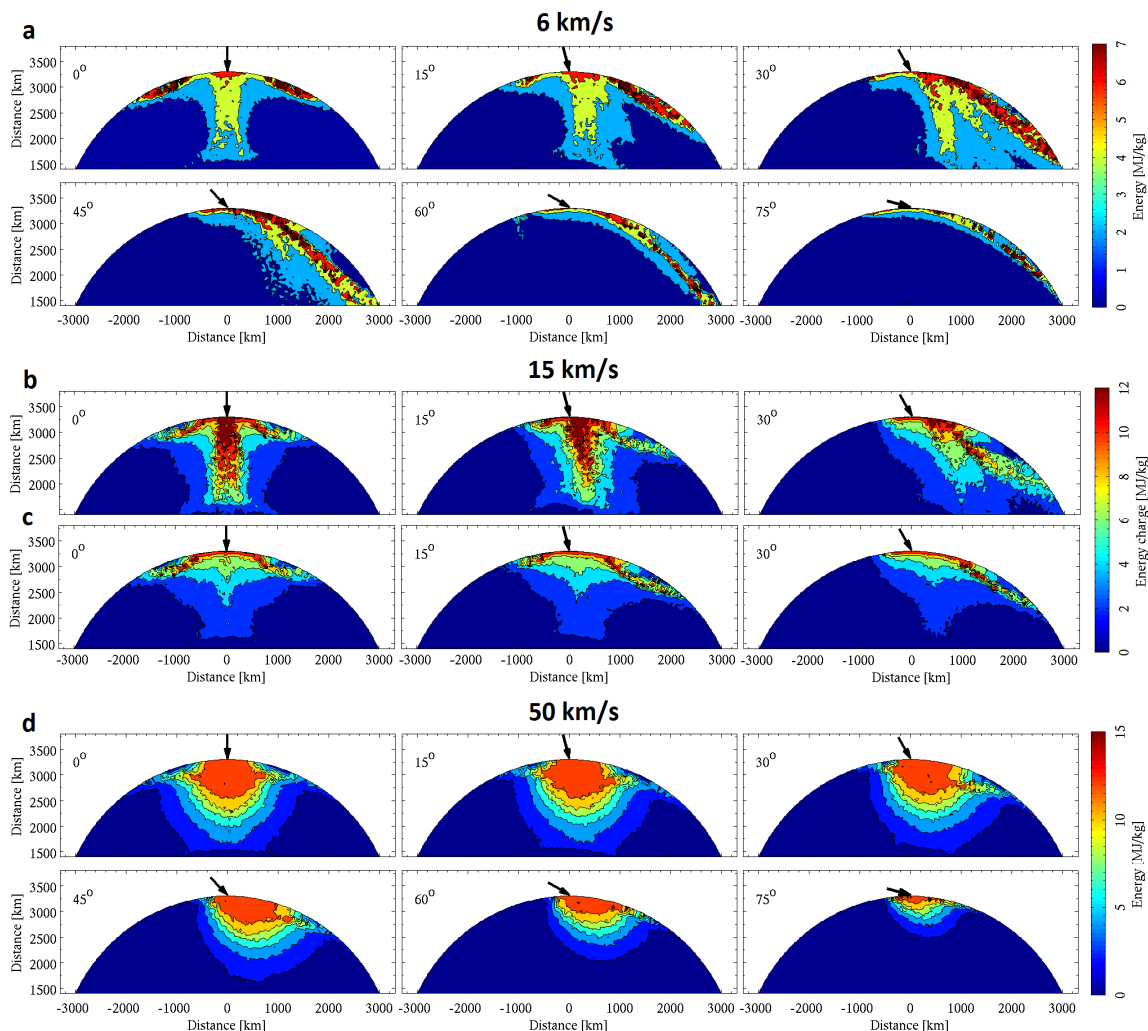


Figure 4-14 Energy deposition in the planet. Energy deposition in the planet by the impact event for $E_k = 5.9 \times 10^{29}$ J and a range of impact conditions and impactor types: (a) differentiated impactor, $v_{imp} = 6$ km/s; (b) differentiated impactor, $v_{imp} = 15$ km/s; (c) basalt impactor, $v_{imp} = 15$ km/s; (d) undifferentiated impactor, $v_{imp} = 50$ km/s. The change in thermal energy of the planetary material is shown. The results are projected onto a slice through the center of the pre-impact planet, before the material is redistributed by the impact.

The total melt mass (M'_{melt}) can be related to the size of the crater (D):

$M'_{melt} = \varepsilon (D')^\xi$, as has also been found empirically for Earth (Dence, 1965; Grieve and Cintala, 1992) and for planetary-scale impacts (Marinova et al., submitted). In this relation M'_{melt} is the melt mass normalized by the mass of the target ($M_{target} = 6.41 \times 10^{23}$ kg) and D' is the size of the crater normalized by the target radius (3,313 km). In the case

of impacts into Mars, Marinova et al. (submitted) found that for basalt impactors, the slow impacts (6 and 10 km/s) deviate from the trend. This is likely because the shock pressure of these slower impacts is about the melting pressure for olivine. Thus pressure melting does not significantly contribute to the melt production for these lower velocities. For olivine, undifferentiated, iron, and differentiated impactors, the melt production by the slow impacts also differs from the overall trend; however, the deviation is largest for basalt and iron impactors. We find that the melt production by the newly simulated four impactor types can also be related to the crater diameter through a power law. However, the quality of the fit when fitting all results simultaneously is greatly improved by including a density dependency. We use the scaling relation

$$M'_{melt} = \varepsilon(\rho')^{\kappa} (D')^{\zeta}$$

where ρ' is the average density of the impactor normalized by the average density of the target (4,222 kg/m³), and ε , κ , and ζ are fitting parameters. Uncompressed densities, ρ_0 , of 2,700, 3,500, 4,570, 7,900, and 4,570 kg/m³ are used for basalt, olivine, undifferentiated, iron, and differentiated impactors. Fitting the results from all single-material impactor types and $v_{imp} \geq 15$ km/s, the best fit is $\varepsilon = (1.07 \pm 0.02) \times 10^{-2}$, $\kappa = 0.180 \pm 0.036$, and $\zeta = 2.48 \pm 0.04$, with mean absolute errors of 12, 10, 9, 14, and 11% for basalt, olivine, undifferentiated, iron, and differentiated impactors, respectively. If results for all velocities are fit simultaneously, again only for the single-material impactors, we obtain a best fit with $\varepsilon = (1.04 \pm 0.01) \times 10^{-2}$, $\kappa = 0.217 \pm 0.052$, and $\zeta = 2.28 \pm 0.04$, with associated mean absolute errors of 22, 15, 14, 27, and 16% for basalt, olivine, undifferentiated, iron, and differentiated impactors, respectively (Figure 4-15). Note that for both the restricted and inclusive sets of velocity, the exponents on the density

dependence, κ , are similar within error bars. For both data sets, even though the differentiated impactor results are not included in computing the best fit parameters, the obtained parameters can be used to fit the differentiated results as well as, or better than, the other impactor types. Table 4-3 shows the full details on the fits both with and without a density dependence, as well as the fits for each impactor type individually.

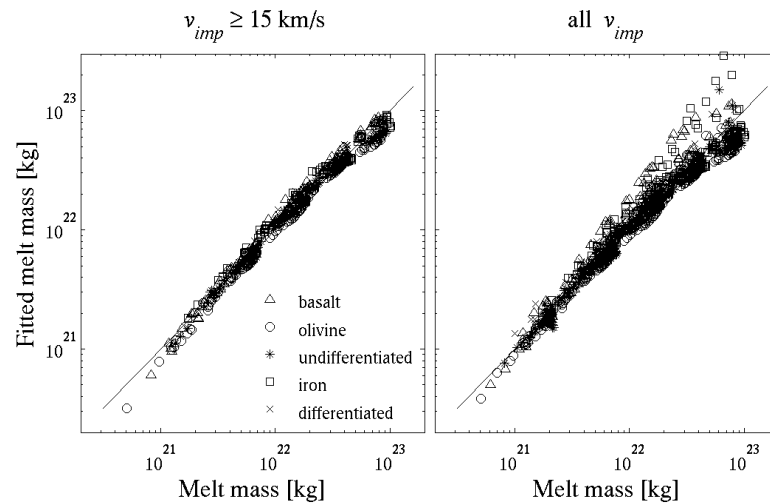


Figure 4-15 Quality of fit for melt production as a function of impactor density and crater size. The 1:1 line is also shown. For all impactor types, slow impacts deviate from the trend.

When fitting each of the impactor types separately, the exponent on the crater diameter, ξ , is similar (2.33–2.64), but not identical for all impactor types. There does not appear to be a general trend with the bulk density of the impactor, the material's sound speed, or other equation of state properties. The melt production is difficult to calculate from first principles, due to the unknown partitioning between thermal and kinetic energy. As suggested by the results, the partitioning of the energy appears to be different between the impactor types. This is not surprising given the apparent differences in the impact process and the range of melt and ejecta produced for a given set of impact conditions.

4.5.6 Melt distribution

The geographic distribution of melt on the planetary surface is a key for determining whether the impact crater cavity will be preserved or whether the planet will be resurfaced by the melt. The melt distribution can be affected by the total melt amount produced, the details of the excavation flow, and the depth of penetration of the impactor and the resulting rebound of the planet. We find that the properties of the impactor affect the distribution of melt on the surface, and thereby change the range of impact conditions for which we expect the impact crater to be preserved (Figure 4-16, Figure 4-17). This is expected due to the changes in melt production, depth of penetration, and the qualitative appearance of the impact process for each of the impactor types, as described above. No consistent and general trend of melt cover versus impactor density is present, as impact velocity and angle play an important role (e.g., Figure 4-16). Some specific trends are as follows. For basalt impactors, significant melt cover is present for slow, head-on, and energetic impacts. With increasing impact angle, downrange deposition of melt is generally only observed for slow (6 km/s), intermediate angle impacts. For olivine impactors, the surface melt cover is usually more than that for basalt impactors, and significantly more melt is deposited downrange of the impact. Undifferentiated and differentiated impactors generally produce a melt distribution similar to that for olivine impactors; however, for some impact conditions they produce a larger surface melt cover fraction (e.g., Figure 4-17 (a): $v_{imp} = 6$ km/s, $\gamma = 0^\circ$ versus (b): $v_{imp} = 15$ km/s, $\gamma = 0-15^\circ$; $E_k = 5.9 \times 10^{29}$ J in both cases). For iron impactors, head-on impacts produce little or no surface melt outside of the crater cavity. For oblique iron impacts, more melt is deposited downrange of the crater than for all other impactor types.

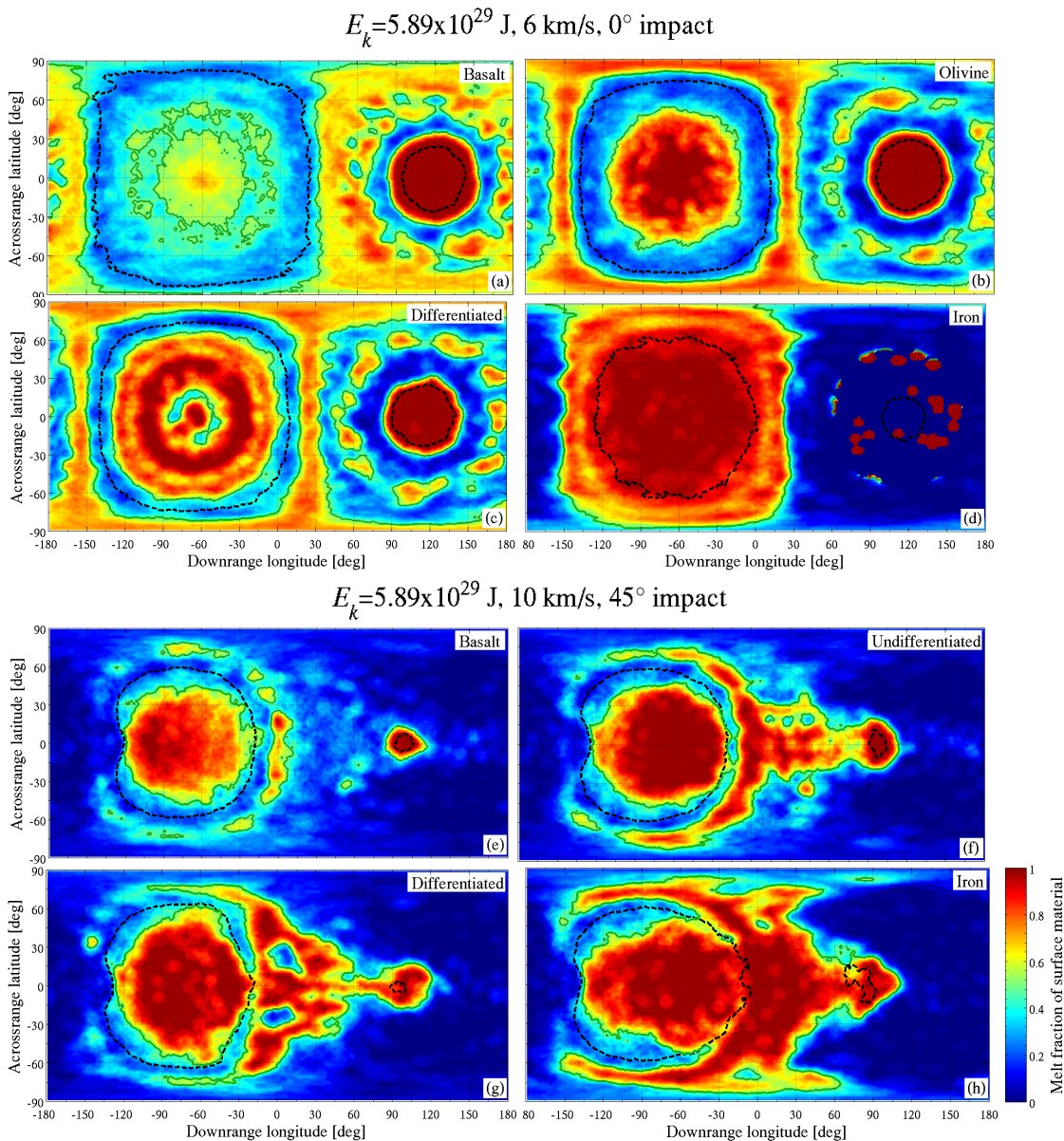


Figure 4-16 Surface melt cover maps. Surface melt distribution as a function of impactor types, velocity, and angle for an impact energy of 5.9×10^{29} J: (a–d) $v_{imp} = 6$ km/s, $\gamma = 0^\circ$ and (e–h) $v_{imp} = 10$ km/s, $\gamma = 45^\circ$. Melt pools (more than 50% surface melt fraction) are outlined in dark green; crater cavities (less than 50% surface crust fraction) are outlined with a dashed, black line. In the case of slow, head-on impacts (a–d), the melt distribution is similar for olivine and undifferentiated impactors. For the higher impact velocity and oblique impacts, the olivine, undifferentiated, and differentiated impactors all produce very similar surface melt distributions.

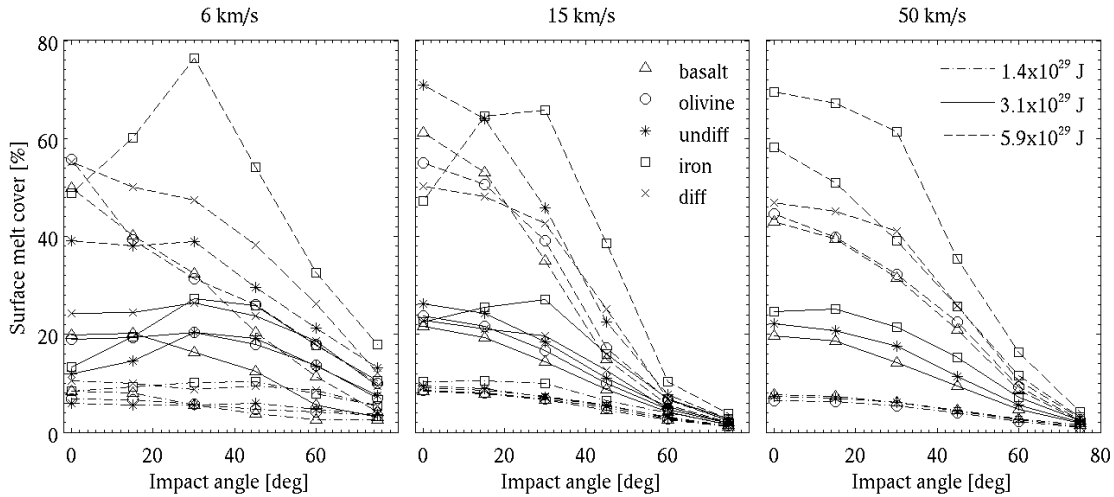


Figure 4-17 Surface melt cover fraction resulting from impacts by the five impactor types (symbol types) and for a range of impact energies ($E_k = 0.5\text{--}5.9 \times 10^{29}$ J, line types), as a function of impact velocity (6, 15, 50 km/s) and angle.

Marinova et al. (submitted) showed that for planetary-scale impacts by basalt impactors, the surface melt cover is related to the total melt amount. We find that this relationship holds for all impactor types simulated here, and particularly that the results from all impactor types can be fitted simultaneously without taking into account the difference in density of the impactors. While they used a power law dependence, here we use a sigmoid function $\left(\frac{1}{1+e^{-x}}\right)$ to capture the boundary condition of surface melt fraction going to 1 as the melt mass goes to infinity. We use the fit

$$f_{melt} = \frac{-1}{e^{-\Psi}} + \frac{1+e^{-\Psi}}{e^{-\Psi}(1+e^{-\Gamma M_{melt}''-\Psi})}$$

where f_{melt} is the fraction of the planet covered by melt, M_{melt}'' is the mass of melt normalized by the mass of the surface layer ($M_{surf} = 7.09 \times 10^{22}$ kg), and Ψ and Γ are fitting constants. The sigmoid function has the appropriate shape, and the pre-factors in the above equation are used to ensure that the resulting surface melt fraction ranges from 0 to 1. The shape of the function is determined by the last component, where Γ sets how

steeply the function rises, and Ψ sets at what melt mass the inflection point occurs. Fitting all simulations for all impactor types, the best fit (and 95% confidence intervals) is given by $\Psi = -1.56 \pm 0.12$ and $\Gamma = 1.84 \pm 0.11$; the mean absolute errors are 11, 12, 15, 10, and 9% for the basalt, olivine, undifferentiated, iron, and differentiated impactor results, respectively (Figure 4-18). For all impactor types, the largest errors are associated with impacts that produce the most melt, in which case the fit generally underestimates the surface melt cover fraction. When looking at each impactor type separately, the factor Γ , which controls how steeply the surface melt fraction increases as a function melt mass, appears to vary with the density of the impactor: Γ is smallest for basalt, largest for iron, with values for olivine, differentiated, and undifferentiated impactors in between. It is difficult to further interpret the variation in the Γ parameters, as it does not seem that these quantities can be derived from fundamental principles, and no previous work is available to be used as a benchmark. It should also be noted that while the Γ and Ψ parameters are not the same for all impactor types, the resulting net relations are quite similar.

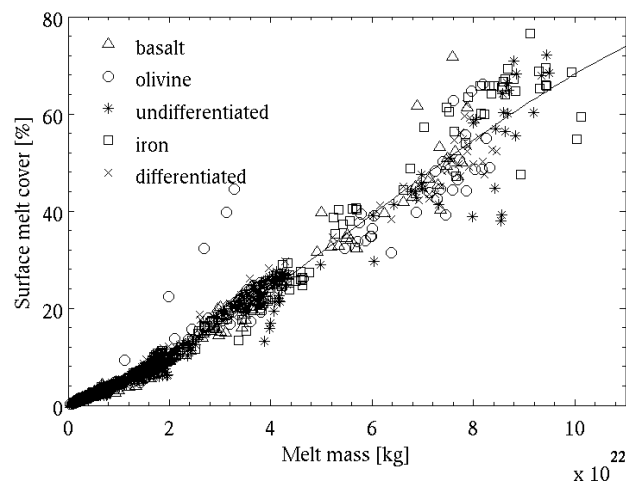


Figure 4-18 Quality of the fit of surface melt cover as a function of total melt mass.

The above relationship shows that the likelihood that a planetary surface will be resurfaced by an impact is directly proportional to the amount of melt produced. The amount of melt produced is in turn a function of impact conditions, but interestingly the surface melt fraction is a direct function of the melt mass, rather than the impactor characteristics. As such, for the most energetic, slow (6 km/s), and head-on impacts, differentiated, basalt and olivine impactors cover significantly more of the surface with melt than does an iron impactor. For oblique impacts ($> 30^\circ$), the melt (and thus surface melt cover) is generally inversely proportional to the size of the impactor. This is due to larger impacts ejecting more mass to space. As such, dense impactors (such as the iron impactor) produce more surface melt cover than less dense and geometrically bigger impactors (such as basalt and olivine impactors), for a given impact energy and velocity. At intermediate velocities (15–30 km/s), for head-on impacts, less dense impactors produce more surface melt cover than denser (e.g., iron) impactors. At intermediate impact angles the trend becomes similar to that for slow impacts, with denser impacts resulting in more surface melt, while for highly oblique impacts the surface melt cover is very similar for all impactor types, as is the melt amount.

We track the partitioning of the produced melt between three reservoirs: the planetary surface, in the mantle, and ejected to space as orbiting or escaping material (Figure 4-19). This provides further information on the preservation potential of the impact structure. Significant mantle melt may promote the formation of a thick crust, similar in thickness to the crust that was excavated by the impact, and wide-spread surface melt may result in complete resurfacing, as discussed above. Determining the thermal state of orbiting material may contribute to understanding the in-situ accretion of

moons and the geochemical mixing between moons and planets (e.g., Pahlevan and Stevenson, 2007). The trends discussed here pertain to the fraction of the total melt mass placed in each of the given reservoirs and not total melt amounts. For slow (6 km/s) head-on impacts, for impact energies of $0.1\text{--}3.1 \times 10^{29}$ J, basalt impactors place a significantly larger fraction of the melt on the surface and significantly less in the mantle than all other impactor types. This result is consistent with the relationship found between the surface melt cover and the total melt amount due to the power law dependence between the two and the different total melt produced by each impactor type. Both for a higher impact energy ($E_k = 5.9 \times 10^{29}$ J) and with increasing impact angle, the difference in fractional surface and mantle melt between the impactor types decreases, but basalt impactors continue to place the highest fraction of their melt on the surface and the smallest fraction in the mantle. This trend is consistent with the lower penetration depth of basalt impactors and their positive buoyancy with respect to the mantle, which results in the molten impactor material rising to the surface and decreasing the mantle melt fraction. With increasing velocity, the distribution of melt between the reservoirs becomes increasingly similar for the range of impactor types. For almost all impact conditions, the iron impactors place the most melt in the mantle. In most cases the iron impactors also place the smallest melt fraction on the planetary surface. The maximum ejected melt fraction for any impact condition is less than 25% of the total melt mass; basalt impactors eject the highest melt mass fraction, while iron impactors eject the lowest fraction. Overall, we find that the trends generally follow average impactor density. As such, basalt impactors generally produce the highest surface melt fraction, with olivine, differentiated, and iron impactors producing increasingly smaller surface melt fractions;

undifferentiated impactors appear to deviate from this trend. For mantle melt, iron impactors produce the highest mantle melt fraction, with undifferentiated, differentiated, olivine, and basalt impactors producing increasingly lower fractions. Because of the consistent trend with average impactor density, the simulated impactor types show the range of plausible melt partitioning for planetary-scale impacts.

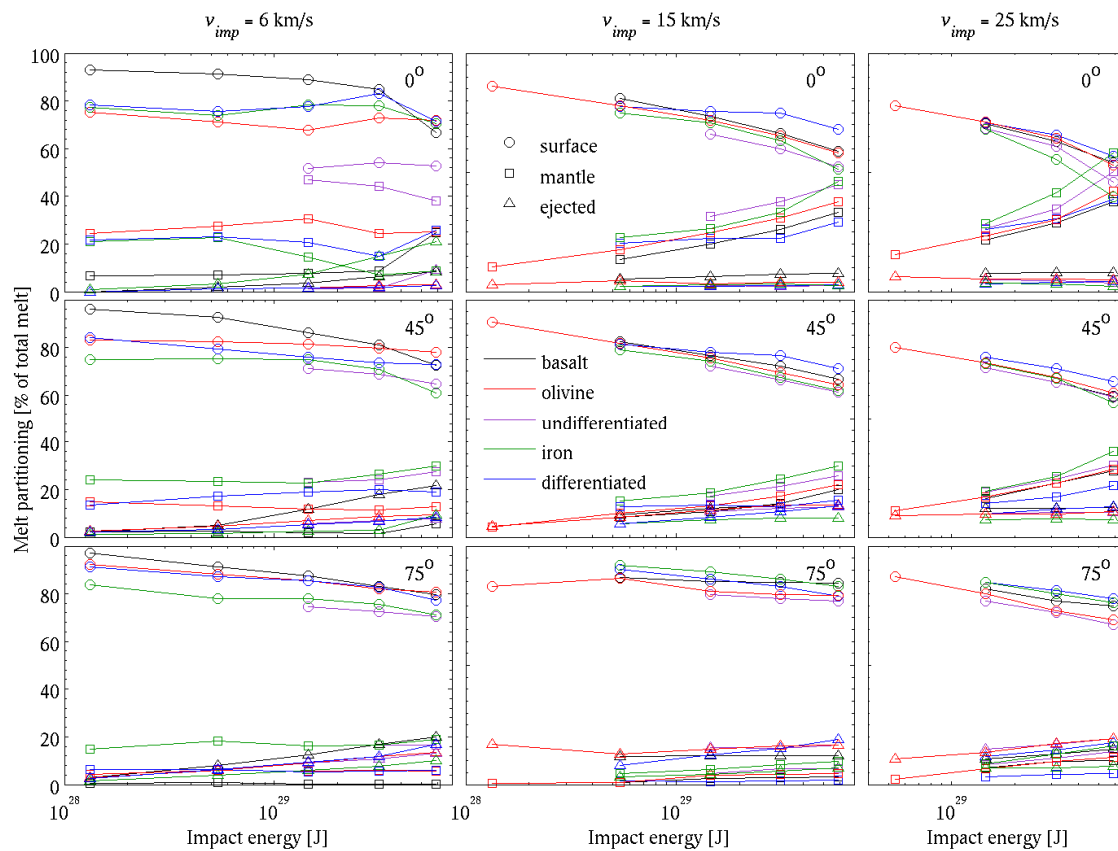


Figure 4-19 Partitioning of melt mass between three reservoirs: on the planetary surface, in the mantle, and ejected to space as orbiting or escaping material. The fraction of the produced melt mass placed in each reservoir is shown. For each reservoir the trend generally follows an ordering based on the average density of the impactor: basalt (least dense), olivine, differentiated, undifferentiated, and iron (most dense).

4.5.7 Comparison of scaling relations

The scaling relations reported here were chosen based on their development by previous studies, their usability for understanding planetary-scale craters seen on the

planets, and the apparent relations exhibited by the results. While all of these aspects were considered, a focus was placed on usability of the relations, particularly providing the simplest possible relations that provide summaries that are accurate to ~10% and using parameters that are measurable or that can be estimated. For example, being able to estimate the amount of melt produced by an impact simply based on the crater size is useful in understanding the early history of the planets, as it does not require extensive understanding of the impactor type, size, and energy.

We compare the fits obtained for each impactor type individually in an attempt to understand whether the fits provide insight into the fundamental scalings that govern planetary-scale impacts (Table 4-3). We recognize that while the relations contain some of the key influential parameters, they do not necessarily contain all of pertinent parameters and as such may be more empirical rather than providing fundamental information on impact processes. Since the relations were chosen based on usability and simplicity, and not based on a principal component or pi-scaling analysis, the fitted coefficients are correlated in all cases and for some fits they are highly correlated, $\text{corr}(A, B) > 0.7$. Due to the correlation of the fitting coefficients, we compare the “envelope” of fitting results given by the range of fits rather than compare the coefficients individually. We examine the “fit envelope” that is formed by the range of solutions obtained from the bootstrap Monte Carlo method performed on the data.

In fitting crater diameter as a function of the impact energy, velocity, and angle, we find that the fitted coefficients for the olivine and differentiated impactors are each within their 95% confidence intervals; their fit envelopes are also largely overlapping. In addition the energy and angle exponents for undifferentiated impactors are also within the

error bars. This suggests that for similar impactor material equation of state properties, the crater diameter behaves very similarly. When comparing the fit envelopes for the five impactor types for the range of simulated impact angles for a given energy and velocity, in all cases the envelopes overlap over at least half of the impact angle range; however, the basalt impactors produce a steeper-sloping envelope while the iron impactors produce a shallower envelope. This suggests that while the fits are similar when their fit envelopes are compared, the power law dependence of energy and angle are affected by the density of the impactor.

For the crater diameter as a function of impact energy and penetration depth, the relationship between the fits for the five impactor types is similar to that found for the main crater size scaling relation: the slopes of the fit envelopes, when projected for a given impact energy and a range of penetration depths, differ slightly between impactor types; however, the envelopes overlap over much of the penetration depth range. This is also the case for the relation of the penetration depth as a function of impactor mass and angle, when corrected for the fitted density dependence. Thus in both of those cases the fits are generally compatible with each other, but the power law dependence on penetration depth and impactor mass, respectively for the two fits, appears to change as a function of impactor density.

Relating the produced melt to the crater diameter produces the interesting result that, after correcting for the density dependence, the fit envelopes for the olivine, undifferentiated, iron, and differentiated impactors overlap; however, the envelope for the basalt impactor is separate. This is also apparent in plotting the correlation clusters for the pre-factor (ε) versus the crater size exponent (ζ) as obtained from the bootstrap Monte

Carlo: for the basalt impactor the cluster of fitted values is separate from the cluster for the other impactor types and no overlap for the range of either fitted parameter is present. It is peculiar that the basalt impactor results would be separate while the iron results are consistent with the intermediate-density impactors. A possible separation between these two sets of impactors is that only the basalt impactor is positively buoyant with respect to the planet.

For the surface melt cover as a function of the total melt produced, while the exponent values are slightly different between the impactors, the fit envelopes of all impactor types overlap significantly.

Table 4-3 Summary of scaling relations. Summary of all scaling relations and fits from the simulation results. The form of the scaling relations is similar to that used by Marinova et al. (submitted). Note that the normalization constants do not affect the values of the exponents, but rather only the magnitude of the multiplier constant. When including a density-dependence in the scaling, we fit only the single-material impactors. Note that here we fit a smaller range of impact energies than presented in Marinova et al. (submitted). All reported confidence intervals are 95% and are determined using the bootstrap Monte Carlo method (10^4 iterations). We report the mean absolute errors; when fitting the individual impactor types we report the error for each energy in order of increasing energy. Unless noted otherwise, we fit the simulation results of impact energies of $0.13\text{--}5.89 \times 10^{29}$ J, all angles, and all velocities.

Basalt impactor	Olivine impactor	Undifferentiated impactor	Iron impactor	Differentiated impactor
Crater size: $D' = q(E'_k)^r (v'_{imp})^s \cos^t \gamma$				
$q = 8.68 \pm 0.53$ $r = 0.391 \pm 0.014$ $s = -0.186 \pm 0.025$ $t = 0.673 \pm 0.061$ err: 13, 8, 7, 7, 10%	$q = 6.45^{+0.29}_{-0.25}$ $r = 0.362 \pm 0.010$ $s = -0.134 \pm 0.017$ $t = 0.535 \pm 0.041$ err: 14, 7, 4, 5, 8%	$q = 6.27^{+0.94}_{-0.67}$ $r = 0.360^{+0.033}_{-0.029}$ $s = -0.108^{+0.030}_{-0.036}$ $t = 0.492^{+0.046}_{-0.048}$ err: 4, 5, 9%	$q = 7.91^{+1.74}_{-1.24}$ $r = 0.421^{+0.043}_{-0.036}$ $s = -0.149^{+0.061}_{-0.066}$ $t = 0.306 \pm 0.080$ err: 12, 10, 10, 13, 17%	$q = 6.69^{+0.61}_{-0.51}$ $r = 0.364 \pm 0.020$ $s = -0.133^{+0.027}_{-0.030}$ $t = 0.514^{+0.048}_{-0.051}$ err: 17, 10, 6, 7, 10%
Fitting all simulations: $q = 7.01^{+0.60}_{-0.35}$, $r = 0.379^{+0.019}_{-0.010}$, $s = -0.133^{+0.022}_{-0.024}$, $t = 0.489^{+0.029}_{-0.043}$; err: 11, 8, 7, 13, 9% for basalt, olivine, undifferentiated, iron, and differentiated impactors, respectively; 11% overall. The fit is not improved by including a density dependence, and the fitted exponent on the density is compatible with zero.				
Depth of penetration: $h' = c(M'_{imp})^d \cos \gamma$				
$c = 0.968^{+0.084}_{-0.062}$ $d = 0.167^{+0.013}_{-0.010}$ err: 9, 9, 6, 21% for $0\text{--}45^\circ$	$c = 1.01^{+0.06}_{-0.05}$ $d = 0.155^{+0.012}_{-0.011}$ err: 12, 11, 8, 21% for $0\text{--}45^\circ$	$c = 1.02^{+0.08}_{-0.06}$ $d = 0.147^{+0.015}_{-0.014}$ err: 13, 11, 7, 21% for $0\text{--}45^\circ$	$c = 1.04^{+0.13}_{-0.11}$ $d = 0.104^{+0.015}_{-0.014}$ err: 5, 4, 5, 18% for $0\text{--}45^\circ$	$c = 1.05^{+0.07}_{-0.06}$ $d = 0.126^{+0.014}_{-0.013}$ err: 9, 8, 5, 30% for $0\text{--}45^\circ$
Fitting all impactors simultaneously: $c = 1.09 \pm 0.05$, $d = 0.148 \pm 0.009$; err: 32, 14, 19, 13, 18% for basalt, olivine, undifferentiated, iron, differentiated, respectively; 19% overall error; fitted $0\text{--}45^\circ$				
Including a density dependence: $h' = c(\rho')^w (M'_{imp})^d \cos \gamma$ $c = 0.981^{+0.031}_{-0.028}$, $w = 0.376 \pm 0.021$, $d = 0.138 \pm 0.006$, err: 13, 14, 13, 9, 14% for basalt, olivine, undifferentiated, iron, and differentiated impactors, respectively; fitted $\gamma = 0\text{--}45^\circ$				
Melt production: $M'_{melt} = \varepsilon (D')^\xi$				
$v_{imp} \geq 15$ km/s $\varepsilon = (0.937 \pm 0.018) \times 10^{-2}$ $\xi = 2.33 \pm 0.04$ err: 1, 3, 5, 5, 6%	$v_{imp} \geq 15$ km/s $\varepsilon = (1.14 \pm 0.03) \times 10^{-2}$ $\xi = 2.48 \pm 0.06$ err: 3, 3, 5, 7, 12%	$v_{imp} \geq 15$ km/s $\varepsilon = (1.11 \pm 0.03) \times 10^{-2}$ $\xi = 2.56 \pm 0.06$ err: 6, 5, 6, 13% ($0.5\text{--}5.9 \times 10^{29}$ J) [†]	$v_{imp} \geq 15$ km/s $\varepsilon = (1.06 \pm 0.04) \times 10^{-2}$ $\xi = 2.64 \pm 0.06$ err: 4, 5, 11, 13% ($0.5\text{--}5.9 \times 10^{29}$ J) [†]	$v_{imp} \geq 15$ km/s $\varepsilon = (1.03 \pm 0.04) \times 10^{-2}$ $\xi = 2.59 \pm 0.08$ err: 2, 3, 7, 16% ($0.5\text{--}5.9 \times 10^{29}$ J) [†]
Fitting all impactors simultaneously, $v_{imp} \geq 15$ km/s: $\varepsilon = (1.06 \pm 0.01) \times 10^{-2}$, $\xi = 2.52 \pm 0.03$; err: 13% overall; 21, 9, 9, 12, 11% for basalt, olivine, undifferentiated, iron, and differentiated impactors, respectively.				

Including density dependence: $M'_{melt} = \varepsilon(\rho')^\kappa (D')^\xi$: $\varepsilon = (1.07 \pm 0.02) \times 10^{-2}$, $\kappa = 0.180 \pm 0.036$, $\xi = 2.48 \pm 0.04$; err: 11% overall; 12, 10, 9, 14, 11% for basalt, olivine, undifferentiated, iron and differentiated impactors, respectively.				
Fitting all impactors simultaneously, all v_{imp}: $\varepsilon = (1.03 \pm 0.01) \times 10^{-2}$, $\xi = 2.33 \pm 0.04$; err: 20% overall; 31, 15, 14, 25, and 15% for basalt, olivine, undifferentiated, iron, and differentiated impactors, respectively.				
Including density dependence: $M'_{melt} = \varepsilon(\rho')^\kappa (D')^\xi$: $\varepsilon = (1.04 \pm 0.01) \times 10^{-2}$, $\kappa = 0.217 \pm 0.052$, $\xi = 2.28 \pm 0.04$; err: 19% overall; 22, 15, 14, 27, and 16% for basalt, olivine, undifferentiated, iron and differentiated impactors, respectively.				
Melt cover: $f_{melt} = \frac{-1}{e^{-\Psi}} + \frac{1 + e^{-\Psi}}{e^{-\Psi}(1 + e^{-\Gamma M'_{melt} - \Psi})}$				
$\Psi = -1.74 \pm 0.29$ $\Gamma = 2.00^{+0.34}_{-0.29}$ err: 18, 10, 8, 9, 10%	$\Psi = -1.18^{+0.40}_{-0.33}$ $\Gamma = 1.52 \pm 0.26$ err: 11, 13, 22, 14, 14%	$\Psi = -1.69^{+0.28}_{-0.22}$ $\Gamma = 1.88^{+0.23}_{-0.26}$ err: 10, 15, 14, 11, 10%	$\Psi = -1.78^{+0.23}_{-0.20}$ $\Gamma = 2.09 \pm 0.23$ err: 15, 11, 10, 9, 7%	$\Psi = -1.19 \pm 0.18$ $\Gamma = 1.55 \pm 0.14$ err: 14, 4, 11, 8, 10%
Fitting all impactors simultaneously: $\Psi = -1.56 \pm 0.12$, $\Gamma = 1.84 \pm 0.11$, err: 12% overall; 11, 12, 15, 10, 9% for basalt, olivine, undifferentiated, iron, and differentiated impactors, respectively.				

†A reduced range of impact energies was fitted since no low-energy impacts could be simulated for the specified impact characteristics (see Table 4-1).

4.5.8 Planetary deformation

Planetary-scale impacts generate strong shocks within the planet, which can produce strong oscillations and deformation of the planet. For low energy impacts, the energy in the initiated shock is relatively small, and the energy may be dissipated before it can traverse the diameter of the planet. However, for the higher energy impacts simulated here, the energy in the shock is sufficient to cross the planet, eject material at the antipode from the impact, and further reverberate through the planet. Significant deformation of the planet can produce deep fracturing of the crust, which could promote volcanism (Williams and Greeley, 1994), and the crust may further be weakened or melted through frictional heating caused by the oscillations. Impact-induced oscillations are particularly forceful due to the short timescale over which they occur: the planet oscillates a few times in under 8 hrs, with the most extreme deformation occurring during the initial 4 hrs. While SPH modeling cannot directly capture any frictional melting or

crustal fracturing caused by the oscillations, we examine the maximum deformation of the planet as a first-order approximation of the process, as well as to compare whether the impactor type affects the magnitude of the deformation. The deformation is defined here as the maximum radial size of the planet (R_{max}), as measured from the geometric center of the planetary core material to the greatest extent of the bound planetary material; the stationary target has $R = 3,310$ km. The extent of deformation, compared to the surface melt cover is investigated (Figure 4-20). A correlation between the two parameters would suggest that the melt cover can be used as a proxy for the surface conditions. Conversely, if significant planetary deformation occurs for low surface melt cover, than the melt fraction cannot be used as an indicator of the preservation potential of the planetary surface.

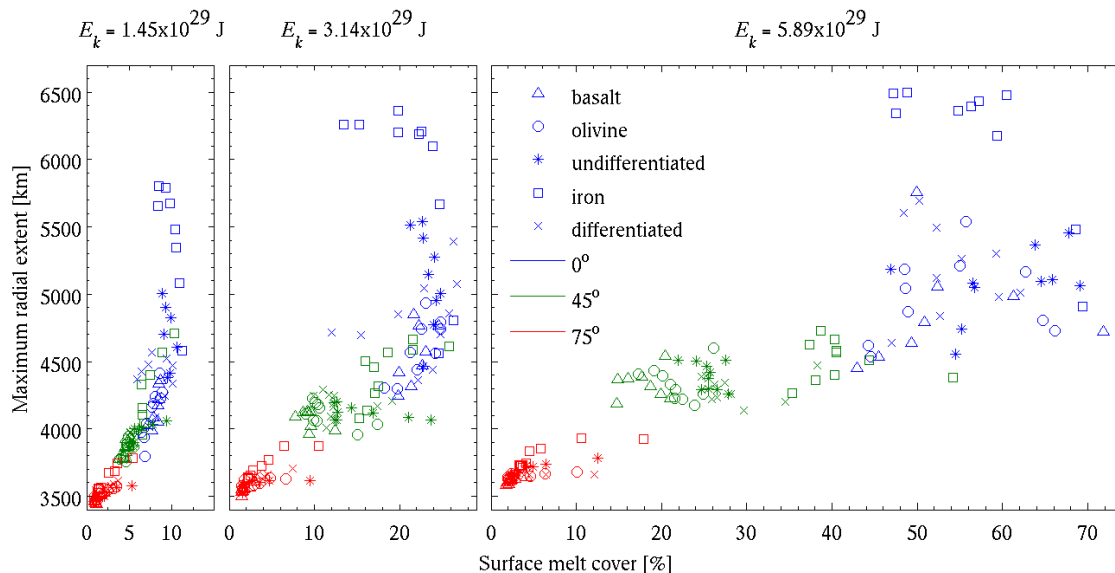


Figure 4-20 Planetary deformation versus surface melt cover. Surface deformation versus the surface melt cover for the range of simulated impactor compositions and impact angles. The legend applies to all panels. All simulated impact velocities are shown for each case; in each case, the fastest impacts produce the least deformation. The relative scale of the x-axis is the same for all panels.

We find that the magnitude of the planetary deformation is affected by the bulk density of the impactor, as is the surface melt cover: both the largest deformation and highest melt cover are seen for the densest impactors. For head-on impacts, the greatest deformation is found at lower velocities ($v_{imp} < 15$ km/s). Basalt and olivine impactors produce similar deformation (e.g., $R_{max} \approx 4,900$ km for $E_k = 3.1 \times 10^{29}$ J), with increasingly larger deformation for undifferentiated and differentiated impactors ($\sim 10\%$ larger, $R_{max} = 5,050$ km) and for iron impactors ($\sim 25\%$ larger, $R_{max} = 6,200$ km). For iron impactors, the exceedingly large warping results from the strong rebound at the site of the impact (Figure 4-A2). This type of rebound is significantly different from the whole-planet deformation that is more common for other impactor types and oblique iron impacts. For oblique impacts, the magnitude of deformation is similar for the basalt, olivine, undifferentiated, and differentiated impactors, while the iron impactors continue to produce larger deformations.

The maximum deformation is similar for the three highest energies we simulated, even though the surface melt cover varies from $\sim 12\%$ to $\sim 70\%$ for the range of energies (Figure 4-20). Thus for low impact energies, even though the surface melt cover may be quite small, the significant planetary deformation may promote additional surface resetting. For higher impact energies, the surface melt cover is likely a better predictor of the surface preservation, as large planetary deformation ($R_{max} > 5,000$ km) is correlated with surface melt cover greater than 50%. An exception to this is for slow iron impactors, due to the restoring force causing a high-velocity rebound at the impact site.

In cases where the planet undergoes extreme deformation, resurfacing is likely irrespective of the surface melt cover fraction. Thus a low predicted melt cover prediction

is not a sufficient condition to determine the preservation potential of a planetary-scale impact crater.

4.5.9 *Mantle melt*

We find that in addition to changes in the amount of mantle melt by the five simulated impactor types, the distribution of melt within the mantle also changes (Figure 4-21). The distribution of mantle melt can be overall explained by the changes in penetration depth and resulting downrange penetration. Comparing basalt and olivine impactors, olivine impactors penetrate deeper, deposit more of their energy at depth, and thus produce more mantle melt. Since both impactors have similar styles of penetration and do not accrete onto the planetary core, the distribution of the melt is generally similar, and the total amount of mantle melt is the most significant difference. In the case of undifferentiated impactors, slow, head-on impacts deposit a significantly higher fraction of their melt at depth than all other impactor types (Figure 4-19, Figure 4-21c). As the impacts become more oblique, the distribution of the melt becomes more similar to that of differentiated impactors; however, the maximum melt fraction of the mantle is higher than for all other impactor types. This could be related to the sinking of the impactor to the core-mantle boundary, while still leaving a “plume” of material through the mantle and reaching to the surface of the planet. For iron impactors, the consistent penetration of the impactor to the planetary core results in significantly more mantle melt than all other impactors, as well as a change in the shape of the mantle melt (Figure 4-21g). However, note that we do not consider iron melt at high pressures. Differentiated impactors result in mantle melt that is qualitatively a hybrid of the melt distribution of olivine and iron impactors. As such, differentiated impactors produce significant melt

near the sub-impact point, an elongation of the mantle melt distribution similar to that for iron impactors, and an additional elongated downrange melt similar to that of olivine impactors. This results from the impactor's olivine being slowed down and depositing its energy during the initial stages of impactor penetration, while the impactor core is slowed down – and deposits its energy – later and thus deeper in the mantle. For higher velocity impacts ($v_{imp} \geq 15\text{km/s}$), the mantle melt distribution is similar for all impactor types. This is consistent with the observations for all other impact features, where fast impacts are all similar and generally approximate a point source explosion. That is, the impactors are much smaller than their slower counterparts, for a given impact energy, and are slowed down quickly, thus depositing their energy near the surface and initiating a strong shockwave due to the high impact velocity.

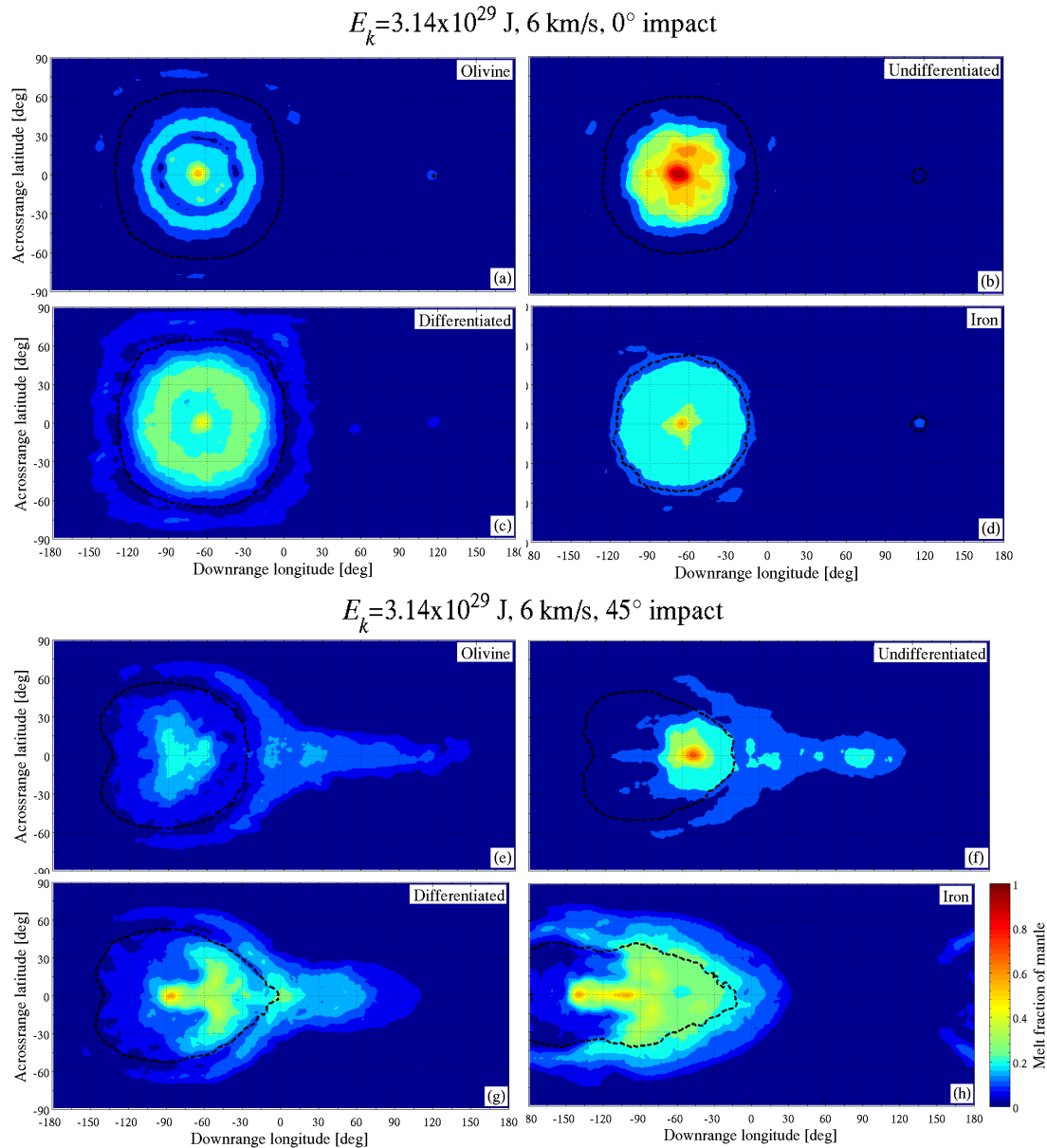


Figure 4-21 Fraction of the mantle and crust that are molten for a range of impactor types; $E_k = 3.14 \times 10^{29}$ J; $v_{imp} = 6$ km/s; (a–d): $\gamma = 0^\circ$, and (e–h): $\gamma = 45^\circ$. The crustal excavation boundary is overlaid (dashed line). The distribution of mantle melt follows the depth and style of penetration of the impactors, which corresponds to where the impact energy is deposited.

4.5.10 Material mixing

We examine the mixing of planetary material due to the impact, in an effort to understand whether processing by large impacts results in extensive mixing of the planet or the possible formation of geochemically-distinct reservoirs. The impact may cause

mixing both due to the redistribution of material and the non-uniform transfer of angular momentum; both aspects vary with impact conditions and impactor type. For head-on impacts, the rebounding material results in mantle material from depth being excavated to the surface of the planet (Figure 4-22c, d); material from around the planet moves towards the point of impact to fill in the excavated mantle material. At the antipode from the impact, as the impact shock travels through the planet, deep mantle material is accelerated toward the planetary surface and the surface layers may be ejected. The features are similar for all impactor types. For oblique impacts, the transfer of angular momentum to the planetary mantle results in circumferential mixing of mantle material; this mixing is most pronounced near the surface of the planet. For intermediate impact angles (Figure 4-22g-l: $\gamma = 45^\circ$), the radial mixing of material shows the uprange rebound that produces a folding over of the impactor and planetary mantle material, thus placing deep mantle material near the planetary surface and shallow mantle in the interior of the planet (Figure 4-2, 4-A4 through 4-A6). It is interesting to note that the impactor olivine material, as well as undifferentiated impactors, remain as spatially coherent masses, thus possibly resulting in persistent and geochemically-distinct reservoirs in the planet. For differentiated and iron impactors, the iron sinks to the planetary core, also remaining as a spatially coherent mass. The most mantle mixing occurs for iron-containing impactors and undifferentiated impactors, likely due to their deeper penetration and larger transient cavity. The planetary material mixing for highly oblique impacts shows the downrange deposition of surface material by the impact, and the lack of major disturbance of the planet (Figure 4-22e, f). Note that most of the impactor iron material does not accrete on the planet for these highly oblique impacts.

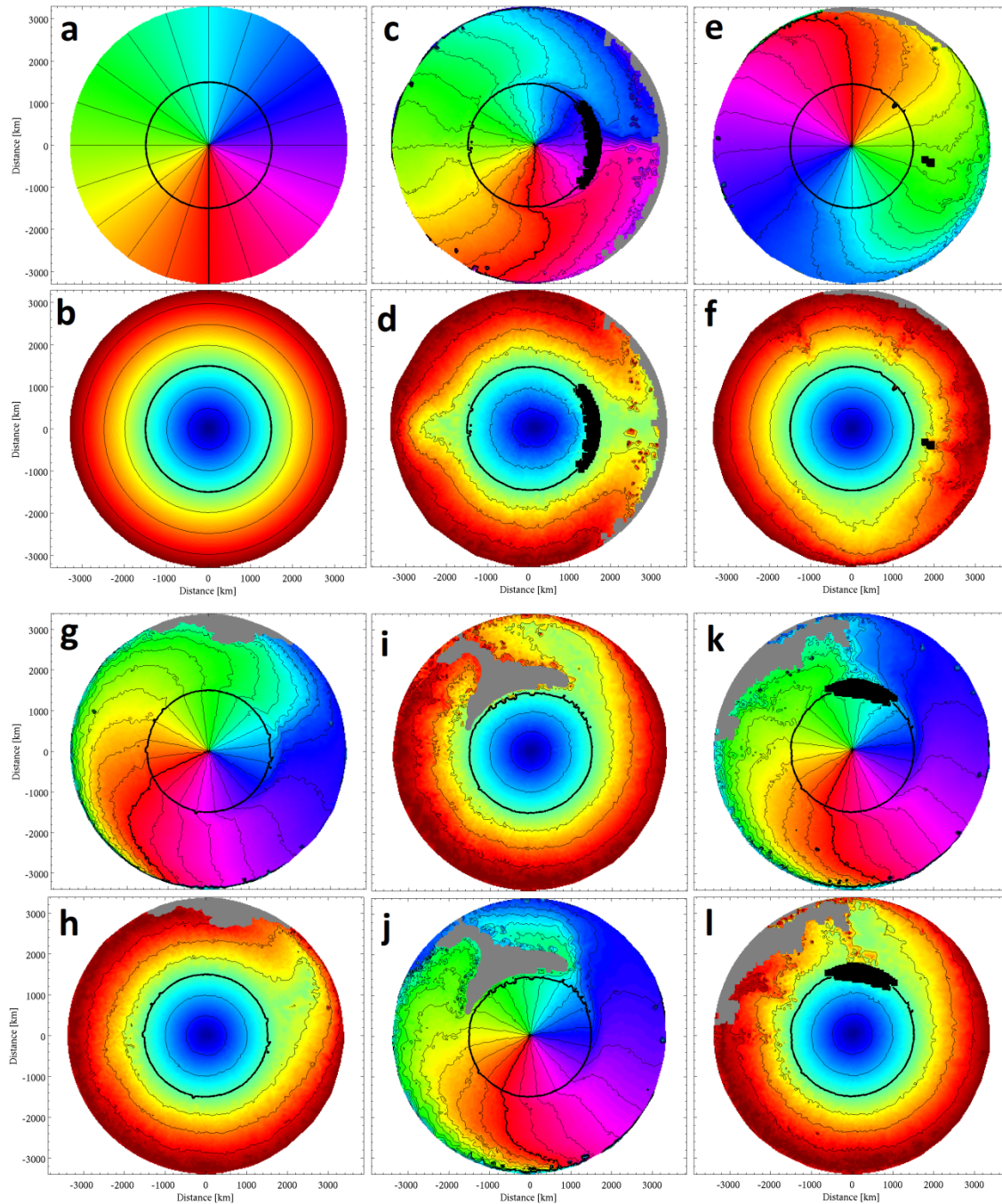


Figure 4-22 Circumferential and radial mixing of planetary and impactor material. $E_k = 3.14 \times 10^{29}$ J, $v_{imp} = 6$ km/s. Panels (a, b) show the initial location of materials in the planet; subsequent panels show how the planetary material changes location and mixes after the impact. Gray and black denote impactor rocky materials (basalt, olivine, and undifferentiated) and iron materials, respectively. Rotation of the planet is present for all oblique impacts. Shown is a slice in the plane of the impactor velocity vector; $t = 25.8$ hrs. Shown are the results for differentiated impactors for: head-on (c, d), 45° (e, f), and 75° (k, l) impacts; as well as 45° impacts by olivine (g, h) and undifferentiated (i, j) impactors.

4.5.11 Escaping and orbiting material

During the impact event, the impact energy is partitioned into thermal, kinetic, and potential energy. The partitioning of impact energy between thermal and kinetic is a key factor in understanding the trade-off between melt production (Figure 4-13) and material ejection (Figure 4-23, Figure 4-25). The two main reservoirs of kinetic energy after the impact are the increased spin rate of the planet and material ejected from the planet. Understanding the amount of orbiting mass is also important for studying the possibility of in-situ accretion of moons following a large impact.

The relative amount of escaping material between the five different impactor types does not appear to follow a general trend (Figure 4-23). This is likely due to differences in the impact process for the five impactor types, as described in *Mechanics of the impact process* and *Appendix 4-A*. Some limited trends that are present are as follows. For oblique and slower ($v_{imp} < 15$ km/s) impacts, the relative variation in escaping mass generally follows the depth of penetration of the impactor: deeper impactor penetration results in less escaping material. As the impactor penetrates deeper, escaping material will encounter an increasingly larger mass as it tries to escape. In addition, as the impactor penetrates deeper, it becomes more difficult for the impactor itself to escape. Thus for this range of impact parameters, the amount of escaping material is inversely proportional to the average density of the impactor (Figure 4-23). For the slow and highly oblique impacts, the size of the impactor also plays a role, as part of a large impactor may not encounter the target due to geometric effects, and directly escapes to space. As an example, for a given impact energy and velocity, a basalt-composition impactor has a 43% larger diameter than an iron-composition impactor. As

the impact velocity increases for a given impact energy, the impactor size decreases such that the impactor mass that does not interact with the planet due to geometric effects becomes less important.

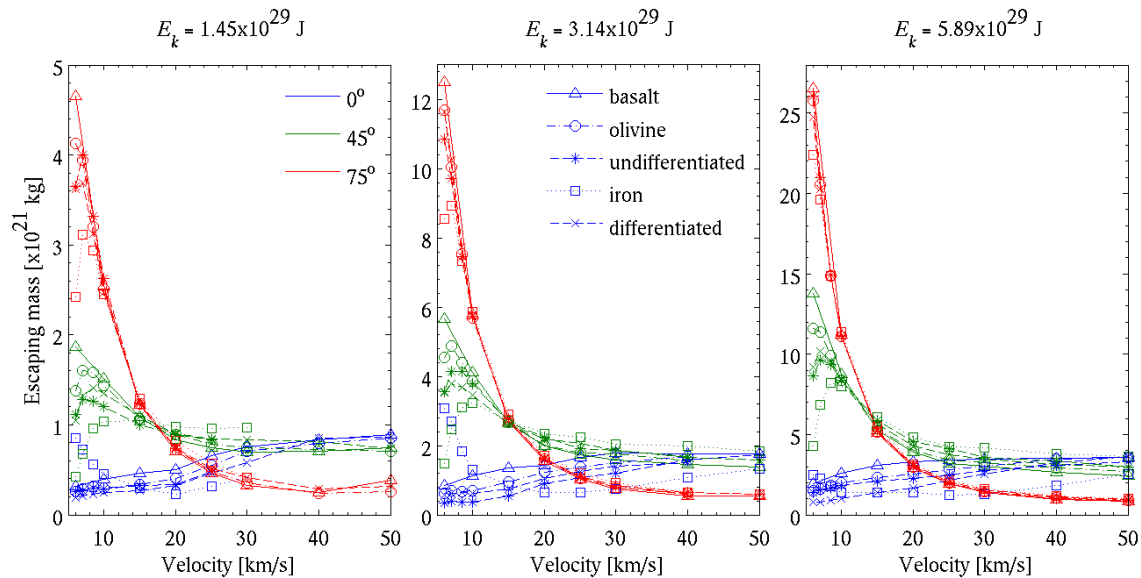


Figure 4-23 Escaping mass for all impactor types as a function of impact velocity and angle, for $E_k = 1.4\text{--}5.9 \times 10^{29}$ J. The legends apply to all panels. The trends of escaping material as a function of impactor type change as a function of slower ($v_{imp} < 15$ km/s) versus faster impacts, head-on versus oblique impacts, and whether the impactor contains iron. However, the trends are similar for all impact energies.

For head-on, iron impactors, the trend of greater penetration depth resulting in less escaping material reverses. This is due to the very strong rebound present for these impact cases, which results in a significant amount of ejected material (Figure 4-A2). The orbiting mass for this case remains similar to that for other impactor types, likely due to the difficulty of placing material in orbit by the radially outward trajectory of the ejected material.

For faster ($v_{imp} > 15$ km/s) and head-on impacts, the relative variation in amount of ejected mass is inversely proportional to the depth of penetration of the impactor, with iron impactors producing the least ejected material and basalt impactors producing the

most, and differentiated and undifferentiated impactors produce similar ejecta masses. This is similar to slower and oblique impacts. However, for faster, oblique impacts the trend is reversed, with iron impactors producing the most ejected material.

The increased amount of ejected material for iron impactors at higher impact velocities and intermediate angles may appear peculiar due to the congruent increase in melt production at these conditions, as noted in section *Melt production*. The increase in both parameters can be sustained due to the decrease in the maximum ejection velocity of the material (Figure 4-24). The decrease in maximum ejection velocity is most pronounced for 45° impacts, where the largest congruent increase in melt production and ejected mass also occurs. The greater decrease in kinetic energy and the larger gain in thermal energy for iron impactors with respect to other impactor types also support this observation. In addition, generally iron impactors result in the lowest potential energy at the end of the simulations as the impactor accretes onto the planetary core. The released potential energy provides an additional energy input to increase the melted mass of iron impactors.

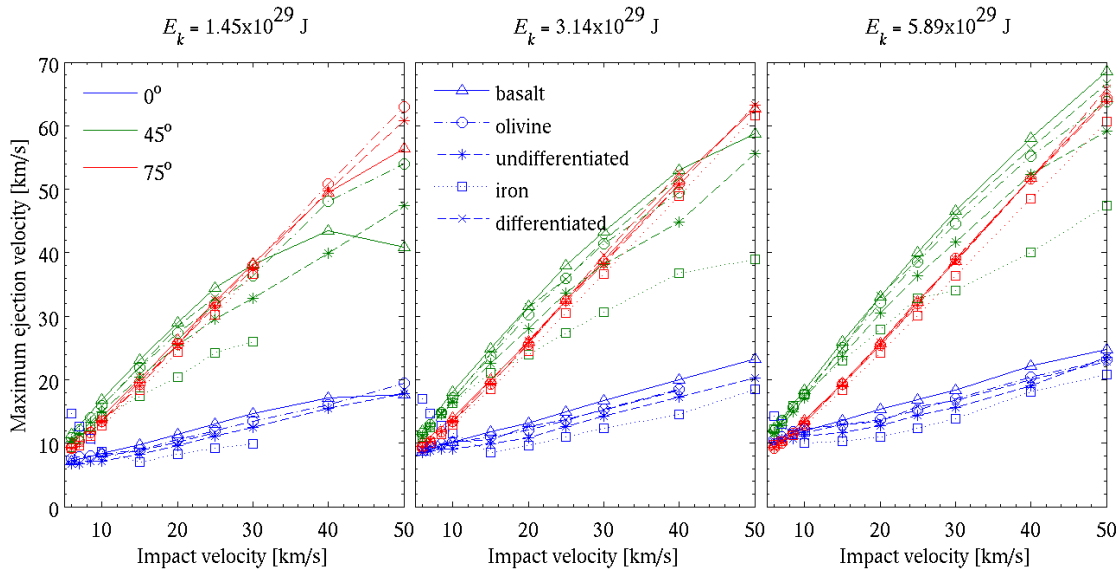


Figure 4-24 Maximum ejection velocity for the three highest impact energies, and the range of simulated impact angles (line color) and velocities (symbol and line type). The legends apply to all panels. For head-on, slow impacts, iron impactors have a significantly higher ejection velocity than all other impactor types. However, at higher impact velocities and head-on to intermediate impact angles, iron impactors have a significantly lower ejection velocity. For the most oblique impacts, the ejection velocities for all impactor types are very similar.

Trends in the amount of orbiting material with impactor type and impact conditions are difficult to interpret due to the apparent variability in the results (Figure 4-25). The variability is likely due to the small orbiting masses. These small masses are represented by a small number of SPH particles, and thus the associated uncertainty in the results causes significant variability with respect to the absolute values. Overall, the most material is placed in orbit by slow (large) and oblique impacts.

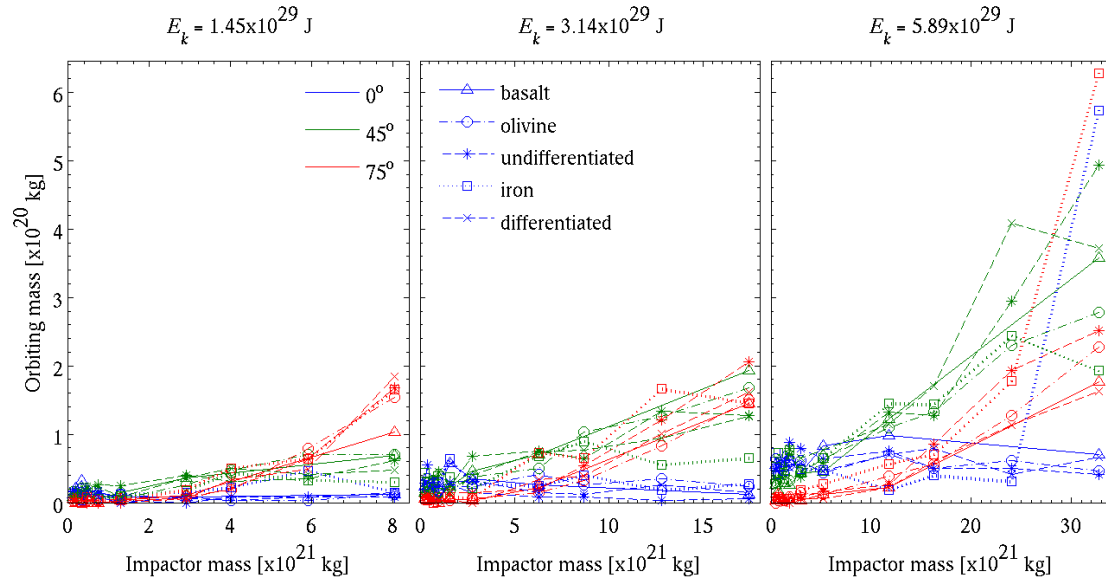


Figure 4-25 Orbiting mass as a function of impactor mass and angle, where decreasing mass represents increasing impact velocity; $E_k = 1.4\text{--}5.9 \times 10^{29}$ J. The legends apply to all panels. The amount of orbiting mass is significant only for high mass (low velocity) and oblique impacts. Note that 0.5×10^{20} kg is 6–16 particles (depending on composition), and therefore results of that magnitude should be interpreted with caution.

We find that the ejecta composition varies with impact angle and velocity, and while the relative proportions of impactor and target material in the ejecta are impactor-type specific, the trend of variation is similar for all impactor types (Figure 4-26, Figure 4-27). In all cases, mostly target material is ejected for fast and low angle impacts. This impact parameter space is also where impacts are most erosive, with up to eight times the impactor mass ejected (Figure 4-28), and therefore the impactor mass fraction of the ejected material is necessarily small. The fraction of impactor material in the ejecta increases both with decreasing velocity and with increasing impact angle; the dependence on impact angle is much stronger over the simulated range. The impactor mass fraction at low impact angles is highest for basalt, and decreases with denser impactors. Olivine and differentiated impactors have similar impactor mass fractions. In the case of differentiated impactors, the amount of impactor iron that escapes, as a fraction of the

impactor mass that escapes, is only a function of impact angle. Below impact angles of $\sim 30^\circ$, negligible amounts of impactor iron are ejected (Figure 4-26). At a 45° impact angle, 50% of the impactor core escapes, while for 60° impacts more than 90% of the impactor core is ejected.

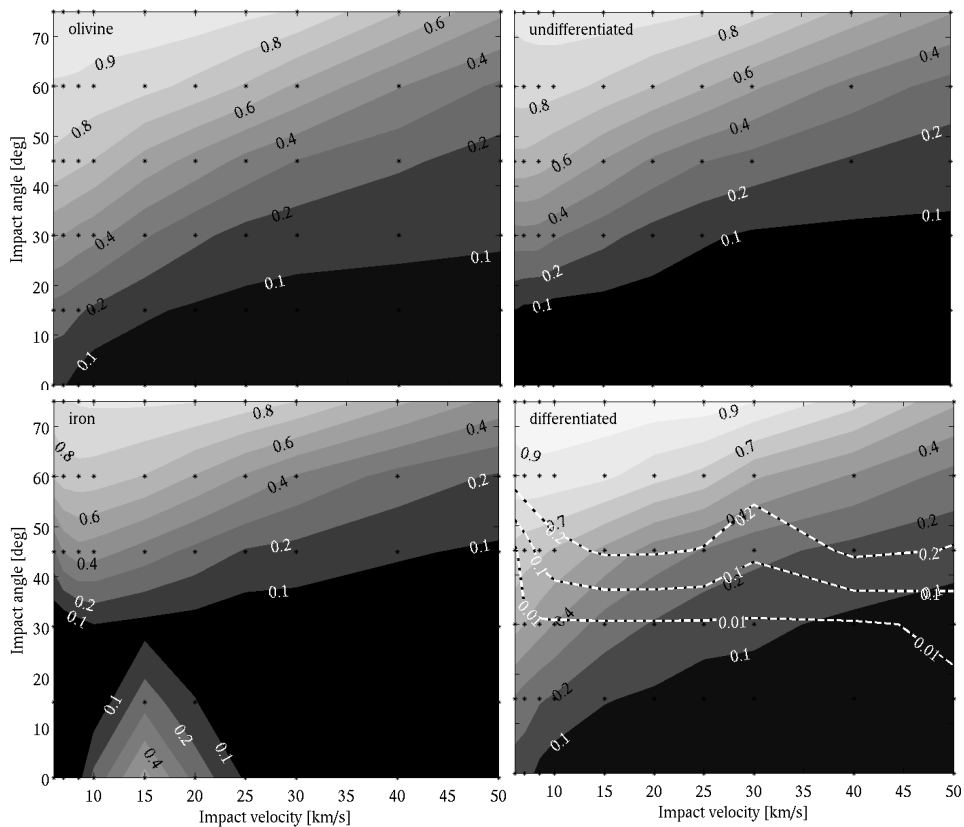


Figure 4-26 Escaping material composition for different impactor types; $E_k = 5.89 \times 10^{29}$ J. The contours and contour labels represent the fraction of impactor in the escaping material. For the differentiated impactor, the dashed white contours show the fraction of the escaping impactor material that is composed of impactor core; the relative amount of impactor core to mantle varies with impact conditions. The trend for the composition of the escaping material is similar for all impactor types; however, the absolute values are shifted with respect to each other.

The composition of orbiting material appears to be chiefly a function of the impact velocity (Figure 4-27). However, these results should be interpreted with caution, due to the small orbiting masses and associated larger resolution effects and relative uncertainties. Generally, for fast impacts ($v_{imp} > 25$ km/s), the orbiting material is

primarily composed of planetary material. For slower impact velocities, the impactor fraction in the orbiting material increases to comprise up to half of the orbiting mass. For the differentiated impactor, the fraction of the orbiting impactor mass that is composed of impactor core material is overlaid (Figure 4-27). This shows that the most impactor core material is placed in orbit for ~ 10 km/s impacts at oblique angles ($\gamma \sim 50^\circ$). These results can be used to provide insight into the impactors involved in moon-forming collisions based on a moon's composition.

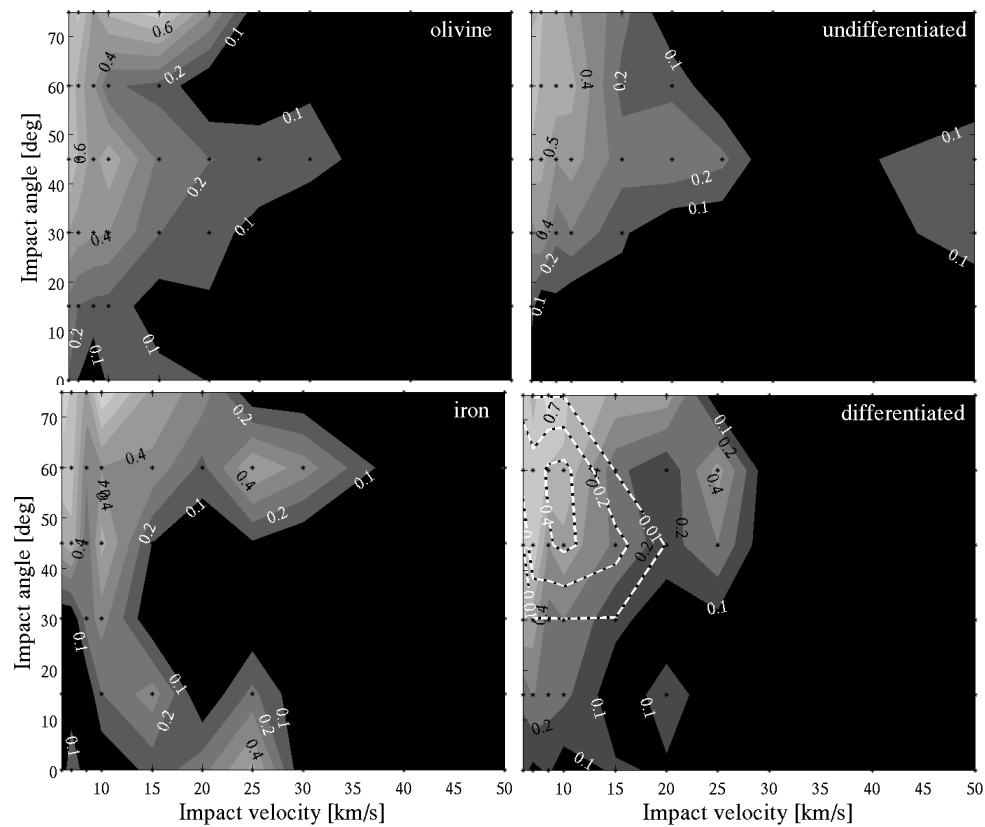


Figure 4-27 Composition of the orbiting material for different impactor types; $E_k = 5.9 \times 10^{29}$ J. The fraction of impactor material in the orbiting material is shown by the contours and contour labels. For the differentiated impactor, the dashed white contours show the fraction of the orbiting impactor material that is composed of impactor core. The compositional trend for orbiting material is similar for all impactor types.

As the amount of ejected material changes with impactor type, so do the impact conditions for which an impact produces net accretion or erosion (Figure 4-28). Net

accretion – and planetary growth – occur when the impactor mass is greater than the total ejected mass – escaping plus orbiting material. Conversely, net erosion occurs when the ejected mass is greater than the impactor mass. Escaping mass comprises 90–99% of the ejected material. An important feature in examining the net erosion and accretion is that while the largest ejected masses are for slow impacts, these masses comprise a small fraction of the impactor mass. Note that since for a given impact condition the impactor mass is the same for all impactor types, the absolute ejected masses between impactor types are proportional to their relative erosive potential.

At low velocities, the relative amount of ejected material increases with impact angle, and the most material is ejected by basalt impactors, with decreasing amounts ejected by the olivine, undifferentiated, differentiated, and iron impactors. This trend correlates with the relative size of the impactor, where the larger the impactor, the more of its material effectively misses the target and escapes. For low impact angles, the normalized escaping material amount increases as the impact velocity increases. This increase in escaping mass is fastest for basalt impactors. As such, basalt and olivine impactors produce the most ejected mass for low-angle, fast impacts and are therefore also more erosive for a given set of impact conditions than the undifferentiated, differentiated, and iron impactors. As described earlier in *Escaping material*, the ejection of material at low angles follows trends in the depth of penetration of the impactor: deeper penetration depths result in less ejected mass as the highly compressed material is effectively overlaid by a larger mass that it must accelerate outwards before escaping to space. For highly oblique impacts, as the impact velocity increases, the amount of ejected mass decreases, as the impactor size also decreases and the entire impactor encounters the

target. For velocities above ~ 15 km/s, all impactor types eject similar masses. The key trend in erosive versus accretionary impacts is that for mostly head-on impacts the velocity at which the impact becomes erosive is highest for the densest impactors, while for more oblique impacts ($> 45^\circ$) the trend reverses and the densest impactors become erosive at significantly lower velocities than less dense impactors. Thus while the impact angle probability is symmetric about 45° (Gilbert, 1893; Shoemaker, 1962), the accretion efficiency is not.

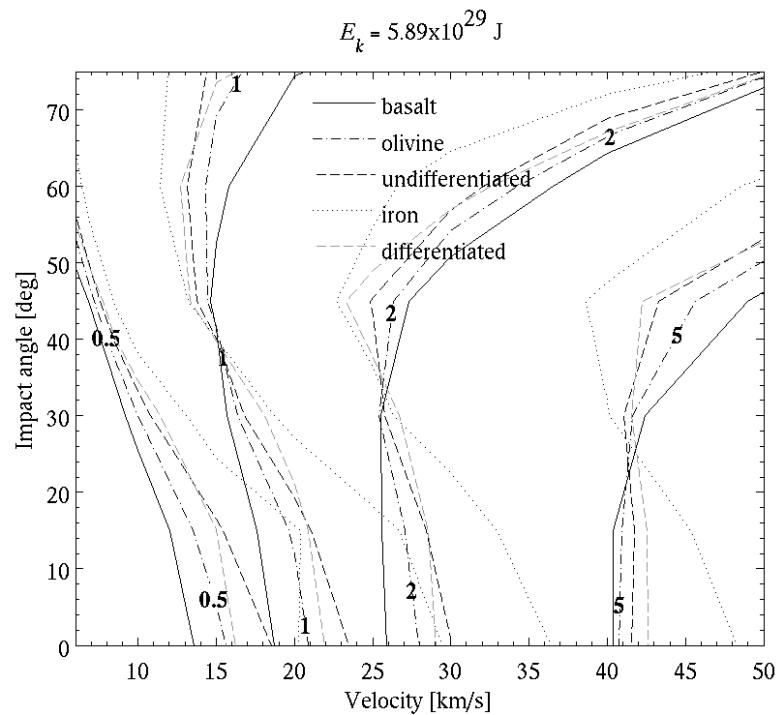


Figure 4-28 Accretional and erosional regimes. Net erosion or accretion for the range of simulated conditions. Shown is the sum of escaping and orbiting masses normalized by the impactor mass for $E_k = 5.9 \times 10^{29}$ J. The results for all other simulated impact energies are similar. The contours show the results for all simulated impactor types; the contour labels apply to their local set of contours. A value of 1 means no net mass change for the target; a value of < 1 implies net accretion of material, while a value greater than one implies net erosion. The net erosion and accretion results are congruent with the trends for changes in escaping mass with impactor type. Note that while the net erosion is greatest for head-on, fast impacts, the largest absolute ejected masses are for slow and oblique impacts (Figure 4-23, Figure 4-25).

4.5.12 Antipodal disruption

Planetary-scale impacts initiate shockwaves that are sufficiently strong to traverse the diameter of the planet and eject material at the antipode from the impact location. We find that the five simulated impactors produce similarly-sized antipodal cavities for a given set of impact conditions (Figure 4-29). The similarity in the antipodal cavity sizes is overall expected as a given set of impact conditions would initiate a shock of similar strength in the target.

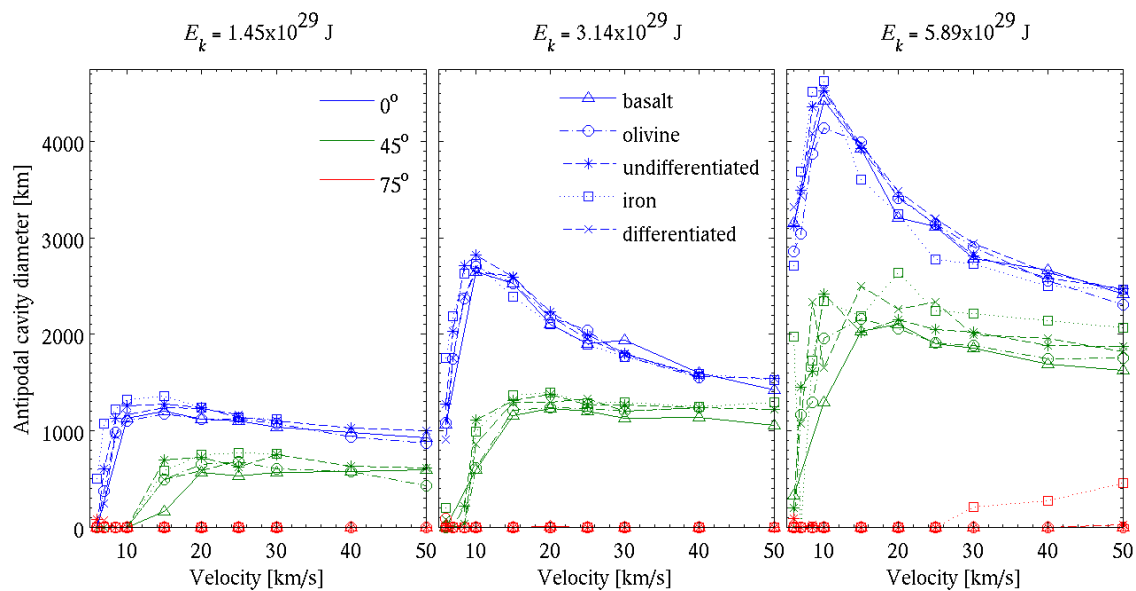


Figure 4-29 Size of the antipodal crustal cavity produced by each of the impactor types (symbols and line types), as a function of impact angle (line color) and velocity. The legends apply to all panels.

4.5.13 Post-impact rotational period

The impactor's angular momentum is partitioned between the target and the ejected material. In the former case the planetary spin rate increases, while in the latter case both the amount and velocity of the ejected material must be considered. Combining these two parameters, we find that overall, iron impactors result in up to 40% higher transfer efficiency than basalt impactors, with undifferentiated, differentiated and olivine

impactors having up to 25, 20 and 10% higher transfer efficiencies, respectively. For low-angle impacts ($\gamma \sim 15^\circ$) at slow velocities, the momentum transfer efficiency is similar for all impactor types. However, with increasing impact velocity, iron impactors become increasingly effective in transferring their angular momentum to the planet. This is consistent with the lower ejection velocity and ejected mass for this range of impact conditions. For increasing impact angle, the transfer efficiencies for the different impactor types become similar. Consistent with the angular momentum transfer efficiency, for a given set of impact parameters, iron impactors result in the fastest spin rates, while basalt impactors result in the slowest spin rates. The fastest rotation rates are produced by slow and intermediate angle impacts, for a given impact energy. A differentiated impactor with impact energies of 3.14 and 5.89×10^{29} J can produce rotation periods as short as 1 and 0.6 days (equivalent to 1 and 0.6 Martian sols), respectively. The last large impacts are likely to have been similar to the undifferentiated and differentiated impactors. These higher-density impactors also result in more efficient angular momentum transfer, further supporting the idea that the last few large impacts at the end of accretion significantly affect, and may set, the spin rate of a planet.

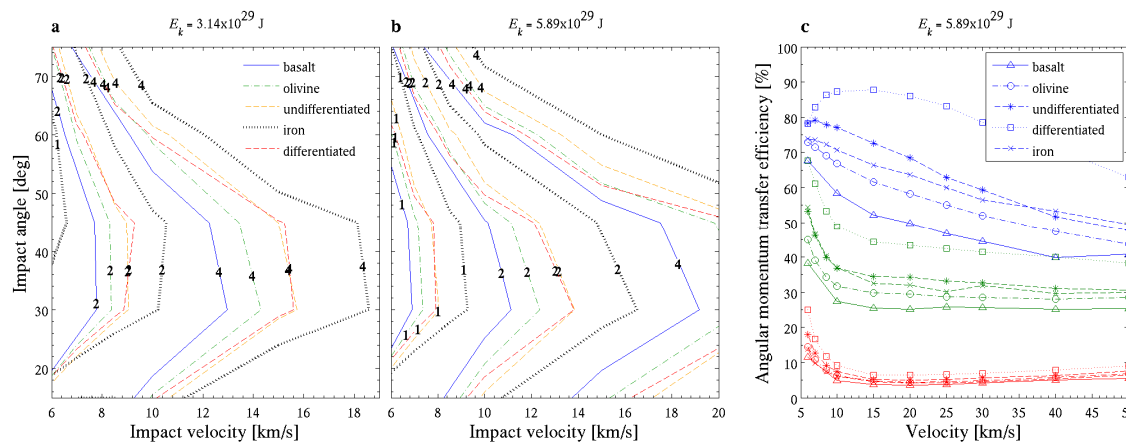


Figure 4-30 Rotation period (a–b) and angular momentum transfer efficiency (c) resulting from impacts by the five types of impactors. The legend in (a) applies to both (a–b). In (c) line color denotes the impact angle: 15° (blue), 45° (green), 75° (red). Iron impactors generally have higher angular momentum transfer efficiencies, and basalt impactors have the lowest transfer efficiencies. Therefore, iron impactors also produce the fastest planetary spin rate for a given set of impact conditions.

4.6 Resolution effects

To understand the precision of our simulation results, we examine the variation in results with changing particle size. Marinova et al. (submitted) examined the resolution effects associated with basalt impactors. Similar errors are expected to be applicable for other single-material impactors, such as the olivine, undifferentiated, and iron impactors simulated. Here we examine the resolution effects associated with differentiated impactors. Since in SPH particles are represented by a kernel-weighted function and they overlap, the properties of a particle are affected by its neighbors. As such, objects composed of multiple materials must contain a sufficient number of particles from each material to ensure accurate material interactions. In our simulations, differentiated impactors are composed of a minimum of 100 particles, thus easily satisfying the nominal SPH requirement for each particle to interact with about 40 neighbors (Canup, 2004). Shown are the variation in results between differentiated impactor simulations with 118

km (nominal), 150 km, and 180 km particle smoothing lengths, for impact energies of $1.4\text{--}5.9 \times 10^{29}$ J (Table 4-4, Figure 4-31). The mean absolute errors, when comparing each of the lower resolutions with the nominal resolution, are less than 10% for all examined parameters, and are less than 5% for most features. These errors are similar to those found for basalt impactors (Marinova et al., submitted).

In most cases the behavior of the impactor iron appears physically realistic, as the iron accretes onto the planetary core. In a small number of cases, where a few iron particles are mixed with the mantle, the iron does not descend to the planetary core on the timescale of the simulation (~ 26 hrs). This condition is only present for small and highly oblique (75°) impacts where only a few (< 10) impactor iron particles accrete onto the planet, and for small head-on impacts where the impactor core descends to the planetary core but remains mixed with some olivine particles at the core-mantle boundary. Thus while small volumes of isolated material may not act physically, the movement and interaction between larger volumes is realistic and the key features of the impact are represented.

Table 4-4 Summary of resolution comparisons. Shown are the mean absolute differences for $E_k = 1.4\text{--}5.9 \times 10^{29}$ J, with respect to the nominal (118 km) resolution ($N = 200,000$ particles). Excavated and antipodal cavity size: normalized by the circumference of the planet; maximum penetration depth: normalized by the radius of the planet (3,310 km); ellipticity and rotation period: normalized by the nominal simulation results; melt cover: normalized by the planetary surface area (1.45×10^{14} m²); melt mass: normalized by the mantle mass (4.9×10^{23} kg); and escaping mass: normalized by the impactor mass.

Resolution	Crater size	Antipode size	Max. depth	Ellipticity	Rotation period	Melt cover	Melted mass	Escaping mass
150 vs. 118 km	1.8%	1.6%	2.0%	1.7%	5.5%	4.5%	0.4%	6.3%
180 vs. 118 km	3.1%	2.8%	2.5%	3.0%	9.3%	6.4%	0.7%	7.2%

To investigate whether any systematic bias is present, the distribution of the differences between the resolutions is examined (Figure 4-31). We find that for most parameters the variation is normally distributed, and thus no systematic bias is present. However, in the case of the crater size, the lower resolutions consistently produce smaller crater cavities than the nominal resolution (Figure 4-31a). This is expected due to the finite size of the particles, which average the energy and velocity gradients set by the passing shockwave over their smoothing length. Compared to large particles, smaller particles effectively sample more points along the gradient to determine whether the material at that point meets the excavation or melting criterion. This effect is apparent in many of the studied features, including the small increase in crater and antipodal cavity size with decreasing particle size (Figure 4-31a, b). In the case of escaping material (Figure 4-31h), low masses are represented by a small number of particles, and thus a change of just a few particles results in a large relative difference. The variations in rotation frequency are correlated with the variations in escaping mass, as angular momentum is carried away by escaping material.

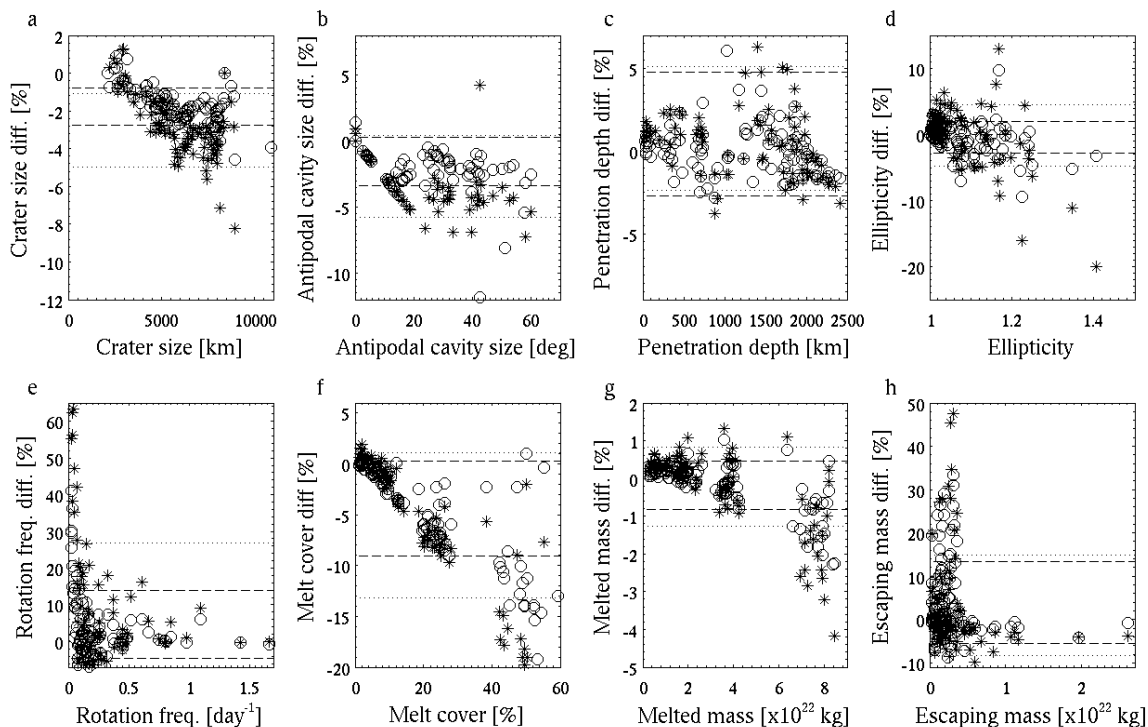


Figure 4-31 Resolution effects summary. The difference in results between the nominal (118 km) resolution and the 150 km (circles) and 180 km (stars) resolutions for $E_k = 1.4\text{--}5.9 \times 10^{29}$ J. The standard deviations associated with each resolution comparison are overlaid (dashed for 150 km and dotted for 180 km particles). In calculating the percent error, the parameters are normalized as in Table 4-4: crater and antipode size: normalized by the planet circumference; maximum penetration depth: by the radius of the planet (3,310 km); ellipticity and rotation frequency: by the 118 km resolution results; melt cover: by the planetary surface area; melt mass: by the mantle mass; and escaping mass: by the impactor mass. The linear feature in (b) is composed of data points where an antipode was present at the nominal resolution, but not at the lower resolution simulations.

4.7 Conclusions

The presented simulations show the effect of impactor composition on the surface expression and geophysical consequences of planetary-scale impacts. We compare the results from five impactor types: basalt, olivine, undifferentiated, iron, and differentiated (50% core diameter). Planetary-scale impacts are expected to be differentiated objects, due to their large size; however, we also simulate undifferentiated impactors. While a purely basalt, olivine, or iron impactor is unlikely, this range of simulated impactor

compositions encompasses the likely range of densities for planetary-scale impactors in the inner Solar System at the end of accretion.

We find that the crater size is largely independent of the impactor composition and structure, though exceptions are present, especially at low impact velocities and for head-on impacts. The crater size is expected to be largely insensitive to the impactor type due to the importance of the strength of the shockwave in excavating material, which is a function of the impact conditions and less so the impactor composition. However, the impactor type greatly affects the shape of the crater cavity, due the significant difference in the penetration depth for the different impactor types. Denser, and thus smaller, impactors penetrate deeper, and iron-containing impactors commonly penetrate and then accrete onto the planetary core. In the case of oblique impacts, the large penetration depth results in significant downrange penetration. In the case of iron and differentiated impactors, this results in significant elongation of the crater cavity for slow, intermediate angle impacts. As the denser impactors produce higher-ellipticity cavities, the prevalence of elongated craters in the planets is more readily explained.

The melt production, escaping mass, and ejection velocity are also affected by the impactor type. These features are intimately connected, as they represent the partitioning of energy between thermal and kinetic. For slow impacts, impactors with a higher density are more likely to accrete onto the planet, thus ejecting less mass and producing more melt. In the case of head-on, iron impacts, however, a strong rebound is initiated that ejects a significant amount of mass; an associated decrease in melt production is present. With higher impact velocity the trend of higher melt production for higher-density impacts remains; however, an additional effect is present: the melt production and ejected

mass for iron impactors both increase due to a significant decrease in the maximum ejection velocity.

While the melt production is affected by the impactor type, the surface melt cover fraction as a function of the total melt production follows the same proportionality for all impactor types. Accordingly, the partitioning of melt between the surface, mantle, and ejecta reservoirs is a function of impactor type. The deeper-penetrating impactors deposit more of their energy at depth, and as such more of their melt remains in the mantle. This is also compatible with the correlation of depth of penetration with less energy going into escaping material.

In understanding the mixing of material during the impact event, as well as the final placement of the impactor material, the depth of penetration plays an important role. Basalt impactors penetrate the least, and cause little mixing of the planetary mantle. Due to their low density, and positive buoyancy with respect to the planetary mantle, basalt impactors remain at the surface of the planet at the end of the simulation. Olivine impactors penetrated deeper, and thus cause more mixing of the planetary mantle, especially for oblique impacts where circumferential mixing is initiated. The most mantle and impactor mixing occurs for undifferentiated impactors. For oblique impacts, the strong and asymmetrical rebound brings deep planetary mantle material to the surface while surface mantle material becomes buried. In the case of differentiated and iron impactors, the effects are even more pronounced, as the impactor iron material sweeps through the planetary mantle and then accretes onto the planetary core.

Both a well-mixed, undifferentiated impactor or the core of a differentiated impactor sweeping through a planetary mantle would allow for the interaction of iron

with mantle material over a large volume. These results have implications for the suggestion by Davies (2008) that Venus may have lost its water through the reaction of iron and mantle material in a giant impact between similarly-sized bodies. Davies (2008) proposed that a head-on impact would be needed since Venus has no moons, and oblique impacts place material in orbit around the target. However, our simulations show that $\sim 45^\circ$ impacts, which are also most likely to occur, produce a much more significant sweeping effect through the planetary mantle, allowing for a much larger reaction volume, and thus may be more effective in dehydrating Venus' mantle. While an off-axis impact would alter Venus' rotational period, the planet would then be de-spun by solar tides in $\sim 10^8$ yrs and together with atmospheric tides could produce the planet's currently observed rotational rate (Ingersoll and Dobrovolskis, 1978). Further simulations, using the appropriate impactor and target sizes and compositions, as well as chemical analyses, would be needed to gain more insight into the process.

The conditions for which the impact results in net erosion or accretion are also dependent on the impactor type, proportional to the variation in ejected mass. As such, for head-on and low angle impacts, basalt impactors produce a net erosional effect for velocities above about 18 km/s while for iron impactors this is above a velocity of about 27 km/s. For more oblique impacts, the trend is reversed, and iron impactors become erosive for impact velocities above ~ 12 km/s while basalt impactors are erosive for velocities greater than ~ 18 km/s.

The planetary rotation rate resulting from mega-impacts, given no rotation in the pre-impact planet, is a combination of the angular momentum that is carried by the impactor and how much of this angular momentum is ejected to space. While more

oblique impacts carry more angular momentum, they also eject more material. Thus the fastest rotation rates result from intermediate and slow impacts. The low ejected masses seen for iron impacts also result in the fastest rotation rates for these denser impactors; basalt impactors produce the slowest rotation rates for a given set of impact parameters. For the two highest impact energies simulated here, the differentiated impactor produced planetary rotation rates of 1 and 0.6 days (or Martian sols).

Using the results from the new simulations, we re-examine the possibility that the Mars dichotomy is the remnant of a single, large impact (Marinova et al., 2008; Wilhelms and Squyres, 1984). The apparent decrease in crater size with increasing impactor density (Figure 4-6), for a set of impact conditions suggests that a more energetic undifferentiated or differentiated impact would be required to form the dichotomy, compared to the basalt impactors used by Marinova et al. (2008). However, a key feature of the Mars dichotomy is its elliptical shape. Both differentiated and undifferentiated impactors produce significantly elliptical craters at increasingly lower impact angles (Figure 4-9), thus increasing the probability that an impact could produce a crater with the required shape. The surface melt cover is ~50% for craters of the required size, similar to that for the basalt impactors. The newly-examined parameter space shows that the Mars dichotomy can be formed for a wide range of impact energies, velocities, angles, and impactor compositions. Thus forming the dichotomy is likely: the preservation of such a crystal asymmetry through geologic time remains an open question.

4.8 Appendix A. Details of the impact events

Visualizing the evolution of the transient cavity and the fate of the impactor and target material provides insight into the impact process and the variation in impact results that can be expected from the range of simulated impact conditions and impactor types. The figures below show the progression of the impact, and the associated captions describe the details of the impact event. The reported time, t , represents the time since the start of the simulation. The impact event occurs within 10 min of the simulation start.

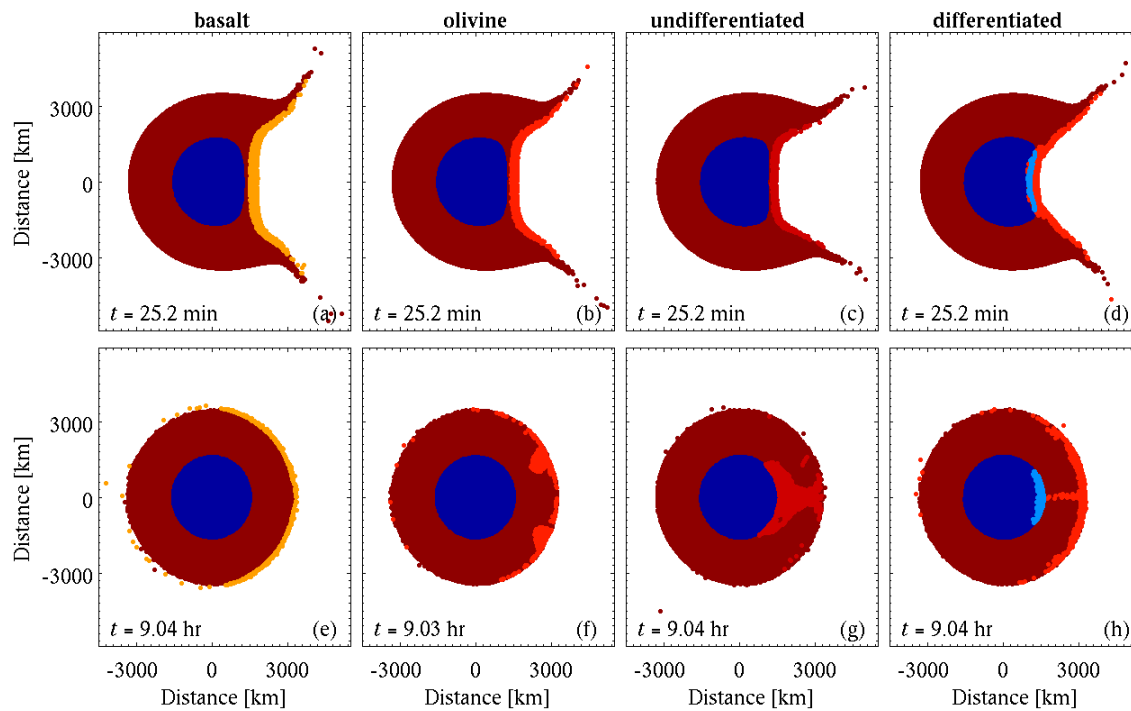


Figure 4-A1. $E_k = 3.14 \times 10^{29}$ J (nominal 10,000 km), $v_{imp} = 6$ km/s, $\gamma = 0^\circ$ (head-on); (a, e) basalt (orange), (b, f) olivine (light red), (c, g) undifferentiated (rusty red), (d, h) differentiated (light red and light blue for olivine and iron, respectively). Dark red and blue represent olivine and iron in the planet, respectively. For olivine and undifferentiated impactors, the shapes of the transient cavity are similar (b, c), however, the rebound is larger for undifferentiated impactors. The most pronounced difference is the final location of the impactor material. In the case of the basalt impactor, the impactor material covers the planet surface and none is entrained in the planetary mantle. For olivine impactors, some impactor material does remain in the planetary mantle, forming a ring around the impact point, to a depth of about 500 km (d). For undifferentiated impactors, the impactor material sinks to the planetary core after the impact event. For the rocky impactors material is ejected at $\sim 45^\circ$ angle, similar to that for small impacts.

Differentiated impactors produce an angular and wedge-shaped transient cavity (c). During the impact, the core of the impactor is absorbed into the core of the planet. The planet

rebounds in a manner similar to the basalt and olivine impactors. However, for the differentiated impactors, during the impact process impactor olivine material becomes entrained in the planet at the sub-impact point; as the event progresses most of this material rises to the planetary surface through the simulation time (f).

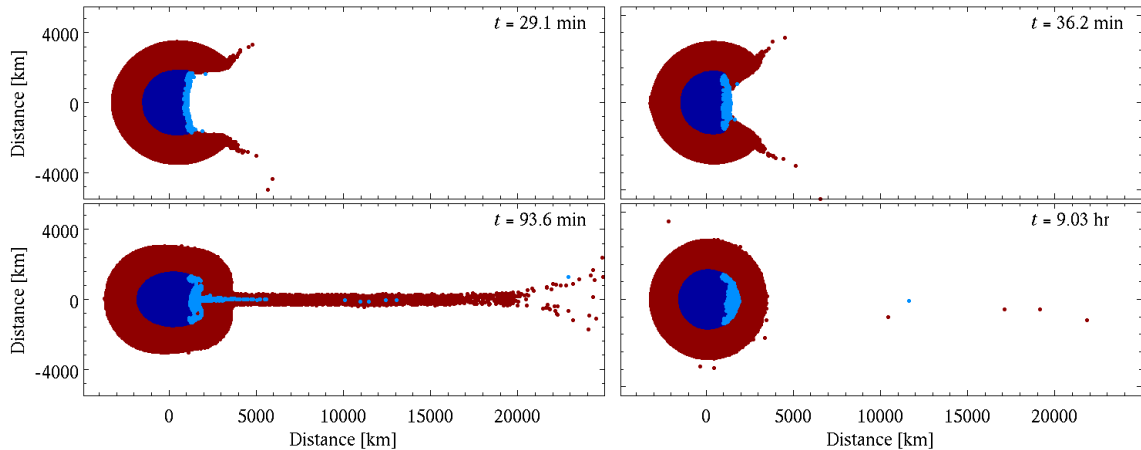


Figure 4-A2. $E_k = 3.14 \times 10^{29}$ J, $v_{imp} = 6$ km/s, $\gamma = 0^\circ$, iron impactor. The impact event is quite different for iron impactors: the impactor penetrates through the planetary mantle and accretes onto the planetary core with an apparent minimal interaction with the surrounding mantle. The transient crater cavity is U-shaped (a). The planetary mantle then appears to flow back into the cavity (b) while the core of the planet begins to rebound (c). The rebound is significantly more powerful than for all other impactor types, likely due to the effective deposition of the impact energy at a much greater depth and thus a stronger reflected shock causing the rebound. Significant amounts of material are ejected by the rebound (Figure 4-23). At the end of the simulation all impactor iron material on the planet has accreted onto the planetary core (d). Red and blue represent olivine and iron, respectively, where light blue is impactor iron.

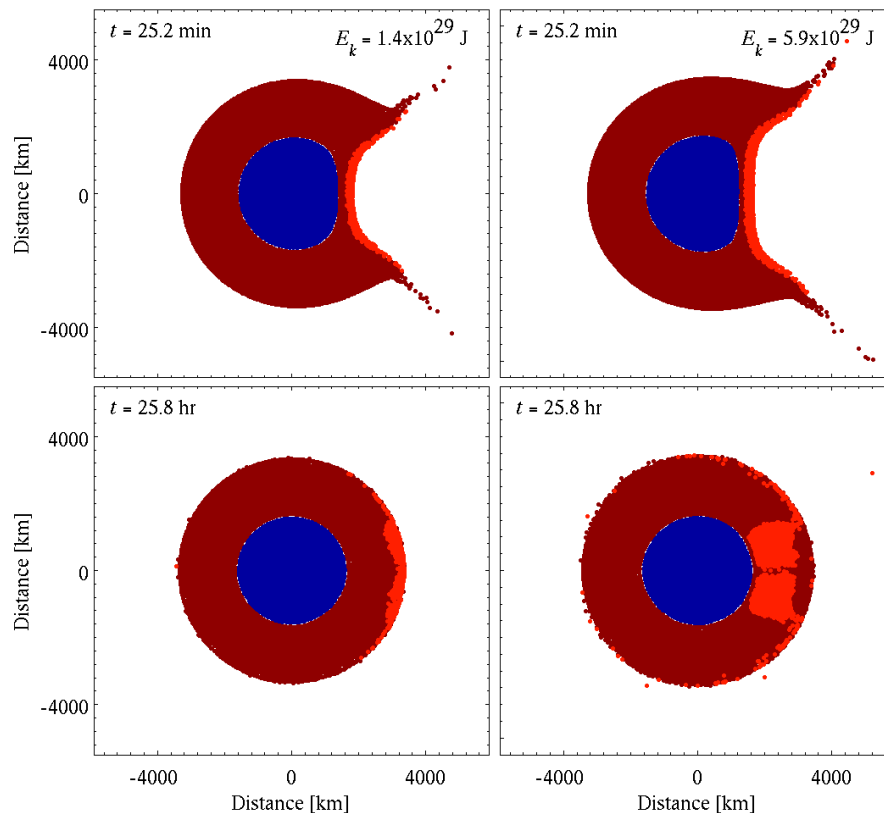


Figure 4-A3. $E_k = 1.45 \times 10^{29}$ J (a, c) and 5.89×10^{29} J (b, d), $v_{imp} = 6$ km/s, $\gamma = 0^\circ$, olivine impactor. For a lower impact energy and the same impact velocity and angle (a, c), the impact event proceeds similarly for all impactor types, taking into account the lower energy availability. In the case of olivine impactors, however, no ring of impactor material around the impact point forms in the mantle but instead the impactor material forms ~ 400 km thick surface layer at the impact site. At higher impact energy ($E_k = 5.89 \times 10^{29}$ J), the basalt, iron, and differentiated impactors behave similarly, scaling for the increased available energy. For the olivine impactor (b, d), significantly more of the impactor material is entrained in the planetary mantle, spanning the entire thickness (d). For the differentiated impactor, the thickness of the layer of impactor material at the planetary surface increases significantly, rather than in its lateral expanse.

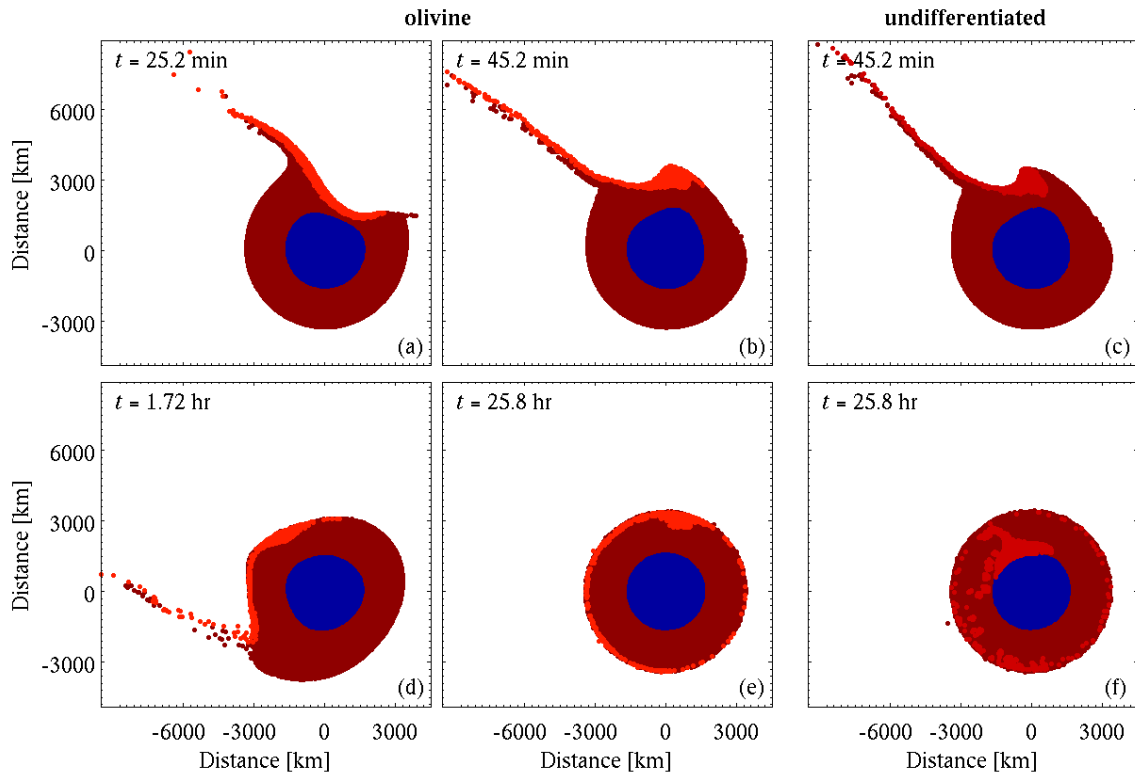


Figure 4-A4. $E_k = 3.14 \times 10^{29}$ J, $v_{imp} = 6$ km/s, $\gamma = 45^\circ$, olivine (a, b, d, e) and undifferentiated (c, f) impactors. For oblique impacts, the impactor penetrates downrange into the planet and produces an asymmetrical redistribution of material. For olivine and basalt impactors, the impact process and final distribution of material is very similar. Due to the obliqueness of the impact, a “tail” of material is ejected (b, c) and the uprange material rebounds (b, c) in the direction of impact (i.e., in the downrange direction) as the impactor continues to excavate the cavity (Figure 4-2). The impact process is very similar for a basalt impactor.

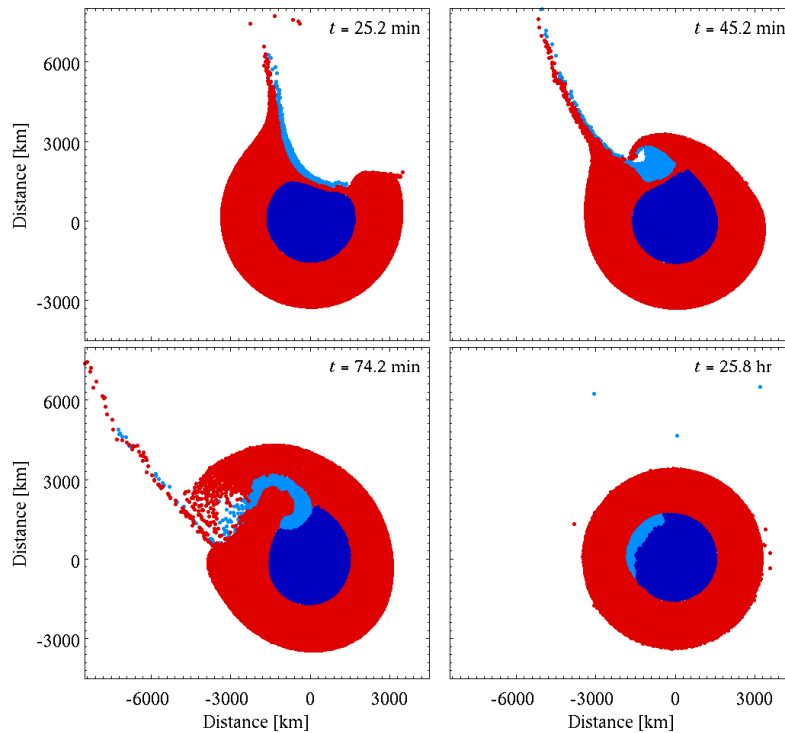


Figure 4-A5. $E_k = 3.14 \times 10^{29}$ J, $v_{imp} = 6$ km/s, $\gamma = 45^\circ$, iron impactor. For an iron impactor, however, the impact event proceeds differently due to the much deeper penetration of the impactor: for basalt and olivine the depth of penetration is about 1,300 and 1,500 km, while for the iron impactor it is $> 1,800$ km (the impactor penetrates the planetary core). Oblique iron impactors penetrate a significant distance downrange into the planet, this effectively sweeping through the planetary mantle (a). The uprange material in the transient cavity rebounds, which results in an effective folding over of the impactor material (b, c). The majority of the impactor is accreted onto the planetary core during the first few hours after the impact; some impactor material is entrained in the planetary mantle and surface and is expected to descend through the mantle with time.

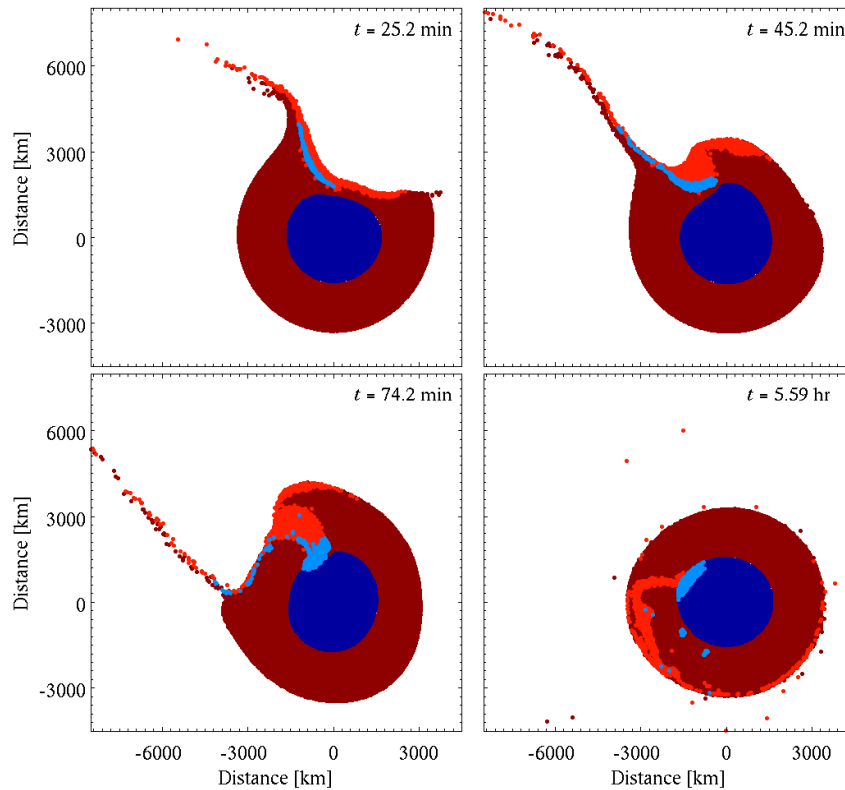


Figure 4-A6. $E_k = 3.14 \times 10^{29}$ J, $v_{imp} = 6$ km/s, $\gamma = 45^\circ$, differentiated impactor. The impact event for differentiated impactors combines the main features of the impacts by olivine and iron impactors. As such, the impactor core penetrates deeply into the planet, sweeps through much of the planetary mantle, and largely accretes onto the planetary core. The impactor mantle material remains shallower than the impactor core material, both mixing with the planetary mantle and spreading over the surface. As the uprange material rebounds, planetary and impactor mantle material fold over each other; the impactor core generally does not participate as it has already accreted onto the planetary core (c). As the planetary oscillations subside, the impactor mantle is both mixed in with the planetary mantle and covers much of the planetary surface (d).

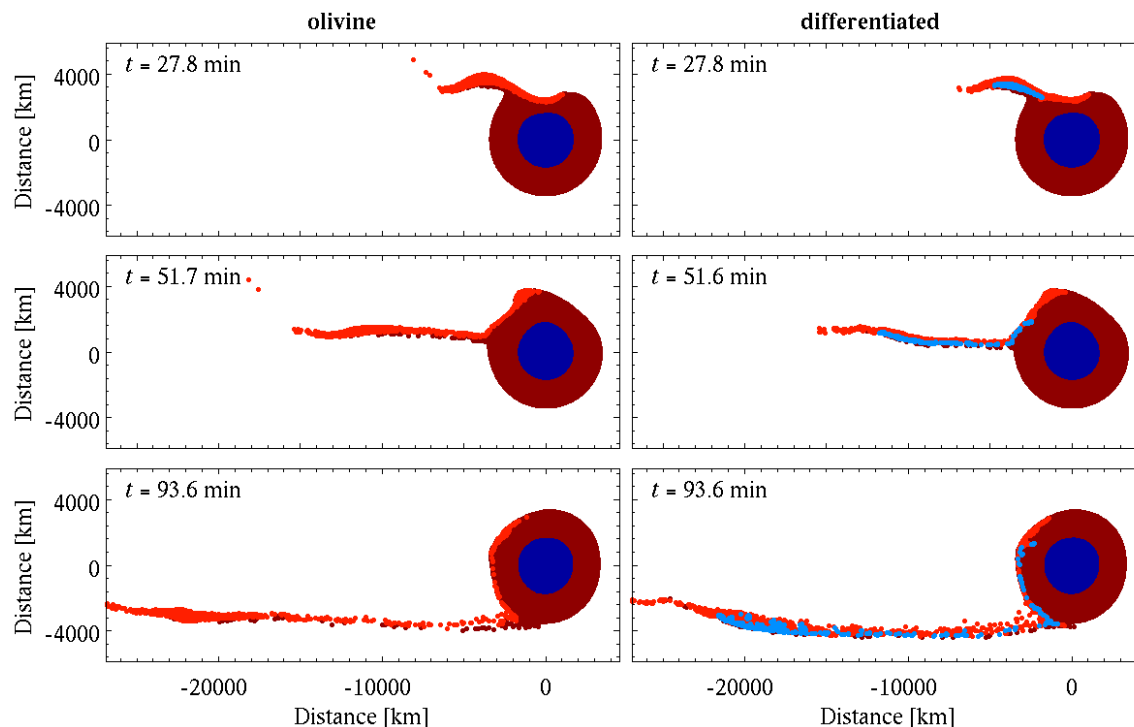


Figure 4-A7. $E_k = 3.14 \times 10^{29}$ J, $v_{imp} = 6$ km/s, $\gamma = 75^\circ$, olivine (a, c, e) and differentiated (b, d, f) impactors. For these highly oblique impacts, the impact process for the basalt and olivine impactors is quite similar. In both cases the impactor grazes the planet (a), its trajectory is modified, and is then mostly ejected. The impactor penetrates through about half of the planetary mantle. No mixing of the impactor and planetary mantle occurs. Some of the impactor material is deposited onto the planet surface (e). A “tail” of ejected material is present, part of which re-impacts the planet thus covering the surface with impactor material, while the rest escapes. Oblique impacts by a differentiated impactor proceed similarly to those by olivine and basalt impactors. Since for these highly oblique impacts a large fraction of the impactor misses the planet, for a differentiated impactor it is mostly its olivine exterior that interacts with the planet. The impactor core is sheared during the impact (b), and over 90% is ejected to space (f).

The iron impactor penetrates deeper into the planet during the initial encounter, thus causing a rebound of the uprange material and folding over on the transient cavity similar to the 45° impact (Figure 4-A5). During this process the iron sweeps through part of the mantle. As the impact progresses, part of the impactor sinks towards the planetary core; some material continues to descend through the mantle for the duration of the simulation. About 90% of the impactor escapes to space. The escaping material is less spatially coherent than ejecta from basalt and olivine impactors.

The impact event proceeds similarly for both lower and higher impact energies, with an apparent increase in the spatial coherence of the ejected material.

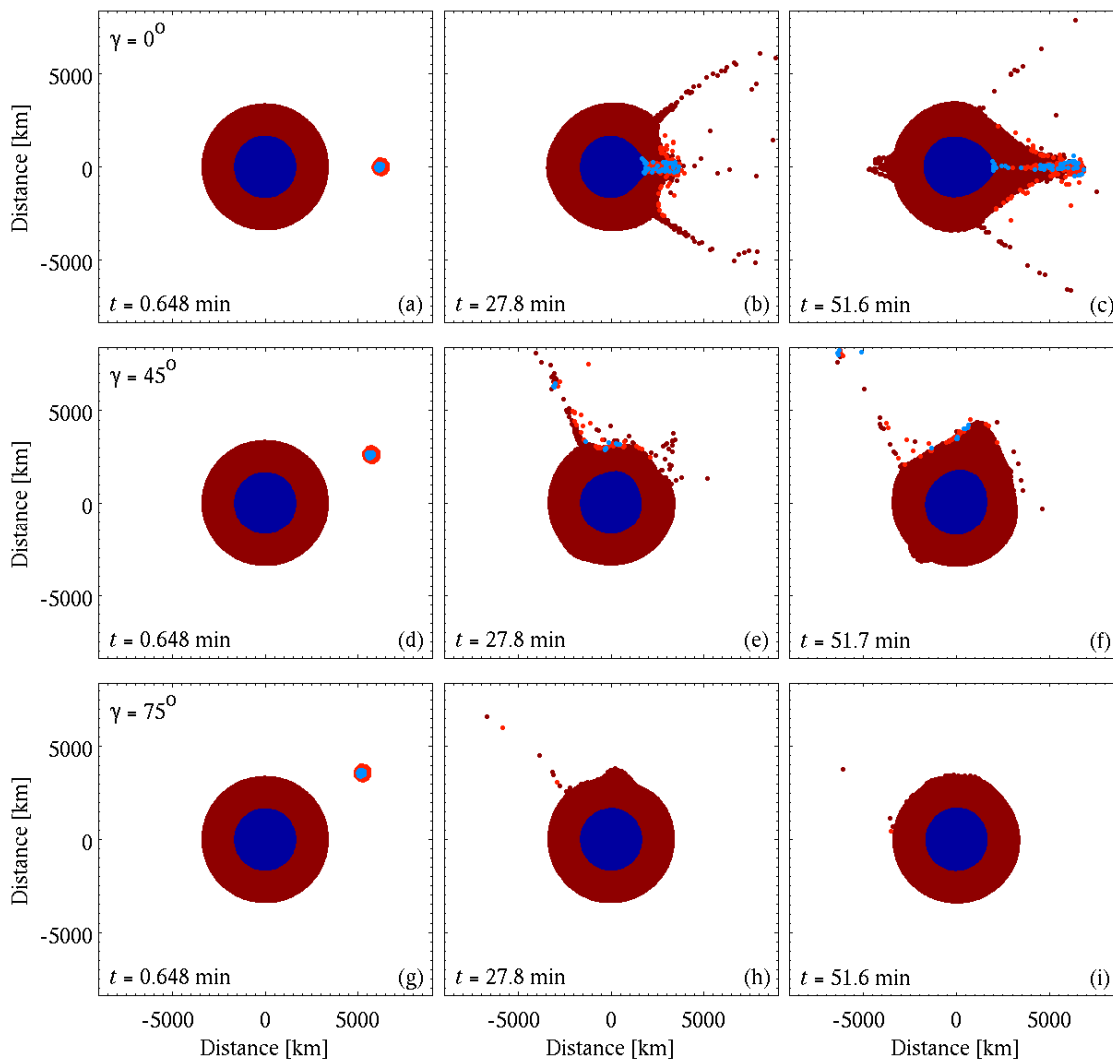


Figure 4-A8. $E_k = 3.14 \times 10^{29}$ J, $v_{imp} = 20$ km/s, $\gamma = 0^\circ$, 45° , and 75° , differentiated impactor. In the case of head-on, fast impacts, the process proceeds similarly to their lower-velocity counterparts. A notable difference is the smaller transient impact cavity due to the smaller impactor; the shallower depth of penetration also results in shallower deposition of the impact energy. Interestingly, the rebound and maximum deformation are similar for the slow and faster impact velocities. Due to the smaller penetration depth the rebound is initiated earlier.

For the iron impactor, the majority of the impactor still accretes onto the planetary core; however, since the rebound process initiates earlier, part of the impactor is rebounded. While much of this material re-accretes, about 30% of the impactor is ejected to space. This effect is seen as an increase in the total escaping mass (Figure 4-23).

For the differentiated impactor, the impactor core does not fully accrete onto the planetary core before a rebound is initiated, and thus some of this material is rebounded into space, similar to the iron impactor event. Little impactor olivine remains in the planetary mantle due to the smaller impactor mass and the efficiency of the rebound in excavating material, compared to the slower impacts. The rebounded material reaccretes onto the surface of the planet.

For intermediate angle impacts ($\gamma = 45^\circ$; d–f), the basalt and olivine impactors behave similarly to slower oblique impacts, with the expected modification of less surface cover by the impactor material due to the smaller impactor mass. For iron and differentiated impactors, due to

the smaller impactor mass and therefore the shallower depth of penetration, the impactor iron does not directly accrete onto the planetary core but is instead deposited on the surface of the planet during the simulated ~25 hrs. It is expected that this material will descend through the planetary mantle on a timeframe longer than the simulated time.

The lower and higher energy impacts proceed very similarly, taking into account expected changes in depth of penetration and ejected mass due to the smaller and larger impactor masses, respectively.

For highly oblique impacts ($\gamma = 75^\circ$; g-i), the basalt and olivine impactors are significantly sheared and predominantly ejected, similar to the process during the slower impacts. The ejecta tail and surface impactor cover are scaled to the smaller impactor mass. The iron and differentiated impactors also behave similarly to their slower impact counterparts, with about 90% of the impactor ejected in both cases, including the majority of the impactor core for differentiated impactors.

For both lower and higher energy impacts, the impacts qualitatively proceed similarly, taking into account the expected changes based on the decrease or increase in available energy and the impactor mass.

4.9 References

- Andrews-Hanna, J. C. et al., 2008. The Borealis Basin and the Martian crustal dichotomy. *Nature*. 453, 1212–1215.
- Asimow, P. D., 2007. Magmatism and the evolution of the Earth's interior. *Goldschmidt Conference Abstracts*.
- Asphaug, E. et al., 2006. Hit-and-run planetary collisions. *Nature*. 439, 155–160.
- Benz, W. Numerical modeling of non-radial stellar pulsation: Problems and prospects. *NATO ASI series C*. Kluwer, Dordrecht, 1990, 269.
- Bertka, C. M., Fei, Y. W., 1998. Density profile of an SNC model Martian interior and the moment-of-inertia factor of Mars. *Earth and Planetary Science Letters*. 157, 79–88.
- Borg, L. E. et al., 2002. Constraints on the petrogenesis of Martian meteorites from the Rb-Sr and Sm-Nd isotopic systematics of the Iherzolitic shergottites ALH77005 and LEW88516. *Geochimica et Cosmochimica Acta*. 66, 2037–2053.
- Canup, R. M., 2004. Simulations of a late lunar-forming impact. *Icarus*. 168, 433–456.

- Canup, R. M., 2008. Lunar-forming collisions with pre-impact rotation. *Icarus*. 196, 518–538.
- Canup, R. M., Agnor, C. B., Accretion of the terrestrial planets and the Earth-Moon system. In: R. M. Canup, K. Righter (Eds.), *Origin of the Earth and Moon*. University of Arizona Press, Tucson, AZ, 2000, 113–129.
- Cintala, M. J., Grieve, R. A., 1998. Scaling impact melting and crater dimensions: Implications for the lunar cratering record. *Meteoritics & Planetary Science*. 33, 889–912.
- Davies, J. H., 2008. Did a mega-collision dry Venus' interior? *Earth and Planetary Science Letters*. 268, 376–383.
- Dence, M. R., 1965. The extraterrestrial origin of Canadian craters. *Annals of the New York Academy of Sciences*. 123, 941–969.
- Fassett, C. I. et al., 2009. Caloris impact basin: Exterior geomorphology, stratigraphy, morphometry, radial sculpture, and smooth plains deposits. *Earth and Planetary Science Letters*. 285, 297–308.
- Gault, D. E., Impact cratering. In: R. Greeley, P. H. Schultz (Eds.), *A primer in lunar geology*. NASA Ames, Moffett Field, 1974, 137–175.
- Gault, D. E., Wedekind, J. A., 1978. Experimental impact craters formed in water – gravity scaling realized. *Transactions – American Geophysical Union*. 59, 1121.
- Gilbert, G. K., 1893. The Moon's face, a study of the origin of its features. *Bull. Philos. Soc. Wash. (D.C.)*. 12, 241–292.
- Grieve, R. A. F., Cintala, M. J., 1992. An analysis of differential impact melt-crater scaling and implications for the terrestrial impact record. *Meteoritics*. 27, 526–538.

- Hartmann, W. K., Davis, D. R., 1975. Satellite-sized planetesimals and lunar origin. *Icarus*. 24, 504–515.
- Hauck, S. A., Phillips, R. J., 2002. Thermal and crustal evolution of Mars. *Journal of Geophysical Research – Planets*. 107, 5052.
- Herd, C. D. K., 2003. The oxygen fugacity of olivine-phyric martian basalts and the components within the mantle and crust of Mars. *Meteoritics & Planetary Science*. 38, 1793–1805.
- Holsapple, K. A., 1993. The scaling of impact processes in planetary sciences. *Annual Reviews of Earth and Planetary Science*. 21, 333–373.
- Holsapple, K. A., Schmidt, R. M., 1982. On the Scaling of Crater Dimensions: 2. Impact Processes. *Journal of Geophysical Research*. 87, 1849–1870.
- Holsapple, K. A., Schmidt, R. M., 1987. Point source solutions and coupling parameters in cratering mechanics. *Journal of Geophysical Research*. 92, 6350–6376.
- Housen, K. R. et al., 1979. Asteroidal regoliths. *Icarus*. 39, 317–351.
- Ingersoll, A., Dobrovolskis, A., 1978. Venus' rotation and atmospheric tides. *Nature*. 275, 37–38.
- Lee, D.-C., Halliday, A. N., 1996. Hf-W isotopic evidence for rapid accretion and differentiation in the early Solar System. *Science*. 274, 1876–1879.
- Marinova, M. M. et al., 2008. Mega-impact formation of the Mars hemispheric dichotomy. *Nature*. 453, 1216–1219.
- Marinova, M. M. et al., submitted. Geophysical consequences of planetary-scale impacts into a Mars-like planet. *Icarus*.

- McCord, T. B. et al., 1970. Asteroid Vesta: Spectral reflectivity and compositional implications. *Science*. 168, 1445–1447.
- O'Keefe, J. D., Ahrens, T. J., 1993. Planetary cratering mechanics. *Journal of Geophysical Research*. 98, 17011–17028.
- Pahlevan, K., Stevenson, D. J., 2007. Equilibration in the aftermath of the lunar-forming giant impact. *Earth and Planetary Science Letters*. 262, 438–449.
- Sanloup, C. et al., 1999. A simple chondritic model of Mars. *Physics of the Earth and Planetary Interiors*. 112, 43–54.
- Shoemaker, E. M., Interpretation of Lunar Craters. In: Z. Kopal, (Ed.), *Physics and Astronomy of the Moon*. Academic Press, New York, 1962, 283–359.
- Tackley, P. J., 2000. Mantle convection and plate tectonics: toward an integrated physical and chemical theory. *Science*. 288, 2002–2007.
- Thomas, P. C. et al., 1997. Vesta: spin pole, size, and shape from HST images. *Icarus*. 128, 88–94.
- Thomas, P. C. et al., 2005. Differentiation of the asteroid Ceres as revealed by its shape. *Nature*. 437, 224–226.
- Tillotson, J. H., *Metallic equations of state for hypervelocity impact*. GA-3216, General Atomics, San Diego, California, 1962.
- Wilhelms, D. E., Squyres, S. W., 1984. The Martian hemispheric dichotomy may be due to a giant impact. *Nature*. 309, 138–140.
- Williams, D. A., Greeley, R., 1994. Assessment of antipodal-impact terrains on Mars. *Icarus*. 110, 196–202.

CHAPTER 5
HOLOCENE CARBONATE REEF STRUCTURES IN THE
HYPER-ARID GEBEL UWEINAT REGION OF THE SAHARA
DESERT (SOUTHWESTERN EGYPT)



© M. Marinova

5.1 Abstract

In 1933 the Hungarian explorer László Almásy discovered rock art depicting swimmers in a cave in the driest region of the Sahara Desert. Almásy speculated that the rock art indicated very different environmental conditions at the time the art was produced. There is now considerable evidence of a wetter climate 10,500 to 5,000 years BP, possibly supporting grasslands. Here we report evidence that newly-discovered, morphologically-distinct carbonate structures, which line the walls of two valleys in Gebel Uweinat, were formed in standing water. Gebel Uweinat is in currently the driest core of the Sahara desert and is in the vicinity of the Cave of the Swimmers. The carbonate structures comprise what appear to be shoreline carbonate formations, and date back to 8,100 and 9,400 years BP. The chemical and morphological similarity of these formations to carbonate structures from modern lakes suggests that these lakes, and likely the swimmer's lake, contained fresh, standing water suitable for human and animal use.

5.2 Introduction

The mountainous Gebel Uweinat region of the Sahara Desert is located in southwest Egypt, near the triple border with Sudan and Libya (N22°, E25°). This area, including the studied sites, receive negligible rain at the present time (Haynes, 2001), as shown in Figure 5-1. Extensive rock art in the area depicts scenes of abundant animals, as well as putative images of swimmers, and studies of the rock art have assumed that the animals and scenes depicted on the walls represent real activities in the lives of the painters (Haynes, 1980). Thus the images suggest that there was a significantly different climate in this region during the time humans created the rock art, though precipitation

rates and the extent of vegetation cover are uncertain. Previous exploration of the Egyptian desert has found supporting evidence of a wetter climate 10,500 to 5,000 years ago, concurrent with the expected timeframe for the creation of the rock art (e.g. Haynes, 2001; Hoelzmann et al., 1998; Kuper and Kröpelin, 2006; Navarro-González et al., 2007; Nicoll, 2001).

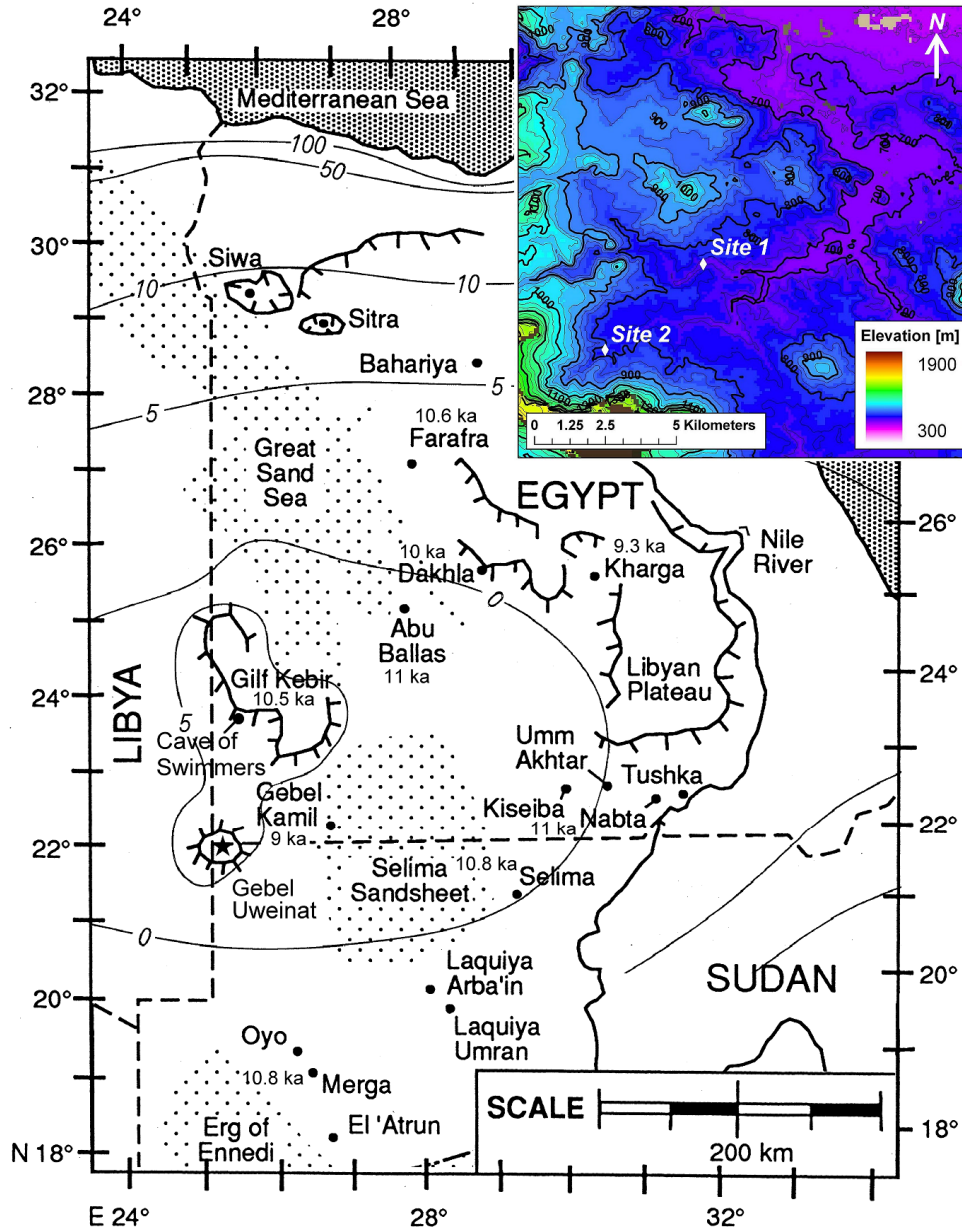


Figure 5-1. Contextual map of the eastern part of the Sahara and the studied sites. Map is modified from Nicoll (2001). The study area, Gebel Uweinat, is indicated (star; N 22°, E 25°). The Cave of the Swimmers (north of the study sites) and the timing of onset of the most recent wet period for select sites in the eastern Sahara are labeled (Kuper and Kröpelin 2006; Nicoll 2001). Ages are reported in calibrated years BP. The modern annual precipitation amounts in millimeters (isohyet contours) are overlaid (Haynes, 2001). The inset shows the topography of the northeast part of Gebel Uweinat (Shuttle Radar Topography Mission), where the study sites are found: Site 1 (N 21°58', E 25°06') and Site 2 (N 21°56', E 25°04').

The Gebel Uweinat area, located deep in Egypt's Western Desert, has not been fully explored with respect to understanding the climatic history of the area. Dateable artifacts of past humid periods there are limited to an ostrich egg-shell, with a radiocarbon age of $7,280 \pm 90$ yrs BP ($\sim 9,200$ calibrated yrs BP; Wendorf and expedition, 1977). While some parts of southwest Egypt have been largely explored, such as Gilf Kebir (200 km NE from the study sites), the Selima Sand Sheet (300 km to the east), and other more distant sites (Figure 5-1), deposits from these sites generally suggest intermittent rainfall producing ephemeral watering holes and ponds (Kröpelin, 1987; Lindstädter and Kröpelin, 2004) and questions remain about the extent of vegetation cover. In addition, the location of Gebel Uweinat in the currently driest core of the Western Desert provides an important constraint on the range of past climatic conditions.

While exploring the Gebel Uweinat area, we discovered reef-like and morphologically-distinct carbonate structures in two narrow valleys. Here we examine the composition and morphology of these reef-like structures to determine their likely mode and timing of formation. These results provide constraints on the environmental conditions in the Eastern Sahara during the carbonates' formation period.

5.2.1 Site description

Gebel Uweinat is a mountainous range in the southwest of Egypt, with a maximum elevation of 1,934 m. The basement rock is Precambrian granites, granite gneisses, and diorites, which are exposed at elevations above $\sim 1,000$ m (Issawi, 1980). The last significant deformation and plutonism occurred during the Precambrian. At lower elevations and at the study sites, the Precambrian basement is overlaid by a

Cambro-Ordovician unit of hard quartzitic sandstone beds interbedded with highly consolidated conglomerate and syenite porphyry sheets (Burolet, 1963; Issawi, 1980).

During our preliminary exploration of the Gebel Uweinat region, two valleys were discovered that contained morphologically-distinct carbonate structures forming reef-like benches along the valley walls. Both of these valleys are located in likely ancient valley network channels, as apparent from aerial photographs, and from the area's topography. At Site 1, the carbonate structures form a distinct bench along the sandstone valley wall; the bench is continuous for over 50 m and is about 1 m thick vertically (Site 1, N 21°58', E 25°06', elevation 715 m; Figures 5-1, 5-2a, b). The carbonate bench is "pasted" onto the valley wall and is not part of the stratigraphic sequence. At this location the valley is about 20 m deep. No apparent shorelines were observed. We also found similar carbonate structures in a neighboring valley ~5 km away, and at a slightly higher elevation than the first site (Site 2, N 21°56', E 25°04', elevation 775 m; Figures 5-1, 5-2c). The height of the surrounding, broader valley is about 10 m. The two sites have similar geological characteristics and are tributaries that combine downrange.

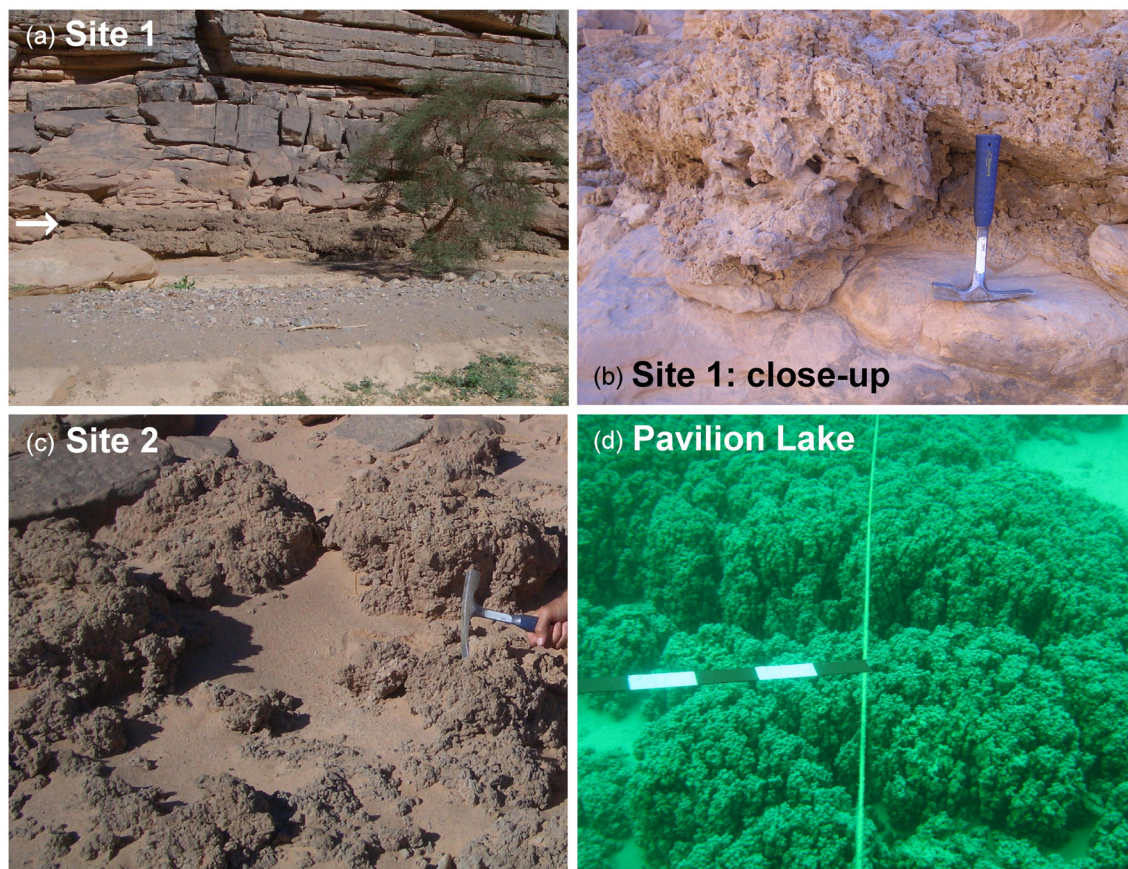


Figure 5-2. Calcite structures at the study sites: (a) carbonate bench (arrow) lining the side of the valley at Site 1, (b) close-up of carbonates at Site 1, and (c) the structures at Site 2. Calcite structures that are morphologically and chemically similar to those at Gebel Uweinat are found in Pavilion Lake, British Columbia, Canada (d) at a depth of 10–15 m (Laval et al., 2000; Lim et al., 2009); each segment on the scalebar is 10 cm.

5.3 Methods

We collected a single large sample (~20 cm across) from each of the two explored locations in Gebel Uweinat, Site 1 and Site 2, during November 2005. Each sample was subsampled into three pieces from different parts of the rock. Information on the orientation of the collected samples was not preserved.

The samples were examined for composition, micro-scale morphology, and radiocarbon dated. Total carbonate content was determined by acid digestion with acetic acid (0.5 M). The mineralogical composition was studied using X-ray powder diffraction

(XRD) on a Phillips X-Pert Pro diffractometer with Cu K- α radiation. Measurements were taken in the range of $5^\circ \leq 2\theta \leq 75^\circ$ at 45 kV and 40 mA. Step size was 0.008° , with a scan step time of 100 ms. The mineralogical composition was determined using X'Pert High Score software. The internal morphology of the samples was analyzed with scanning electron microscopy, using the LEO 1550 VS FESEM system. X-ray energy dispersive spectrometer (EDS) analysis was conducted with the Oxford INCA Energy 300 system.

Radiocarbon ages were determined using accelerator mass spectrometry (AMS) by Beta Analytic, Inc; the lab accession numbers for the samples were 260177, 260178, and 262282. The samples were not pre-treated, and were only washed with de-ionized water before analysis. The modern reference standard was 95% the ^{14}C activity of the National Institute of Standards and Technology (NIST) oxalic acid (SRM 4990C); the Libby ^{14}C half-life (5,568 yr) was used. Measured $^{13}\text{C}/^{12}\text{C}$ ratios were calculated relative to the PDB-1 standard. The reported results are corrected for isotopic fractionation using the measured $\delta^{13}\text{C}$ ratio. Calibrations are calculated using the INTCAL04 Radiocarbon Age Calibration (2004).

5.4 Results

Samples from both sites were analyzed for bulk mineralogy and total carbonate content using XRD and acid digestion, respectively. Bulk XRD mineralogical analysis of the samples showed carbonates and quartz as the main minerals, with other minor constituents (less than a few percent total weight fraction). The carbonate is in the form of calcite, with up to 5% magnesium. The average total calcite weight fraction is 46% for

Site 1, with the three subsamples giving 42.5%, 49.0%, and 46.8% by weight. For Site 2, the average total calcite content was 28% by weight, with the three subsamples giving 29.2%, 28.2%, and 26.0% by weight. The quartz component is likely contributed by the ubiquitous sand sheets and dunes in the region. Energy dispersive spectrometer (EDS) analyses showed some of the minor mineralogical components to be calcium sulphate, magnetite, ilmenite, (Na, Al) pyroxenes, and orthoclase (Figure 5-3). The composition at both sites is similar, consistent with their close proximity.

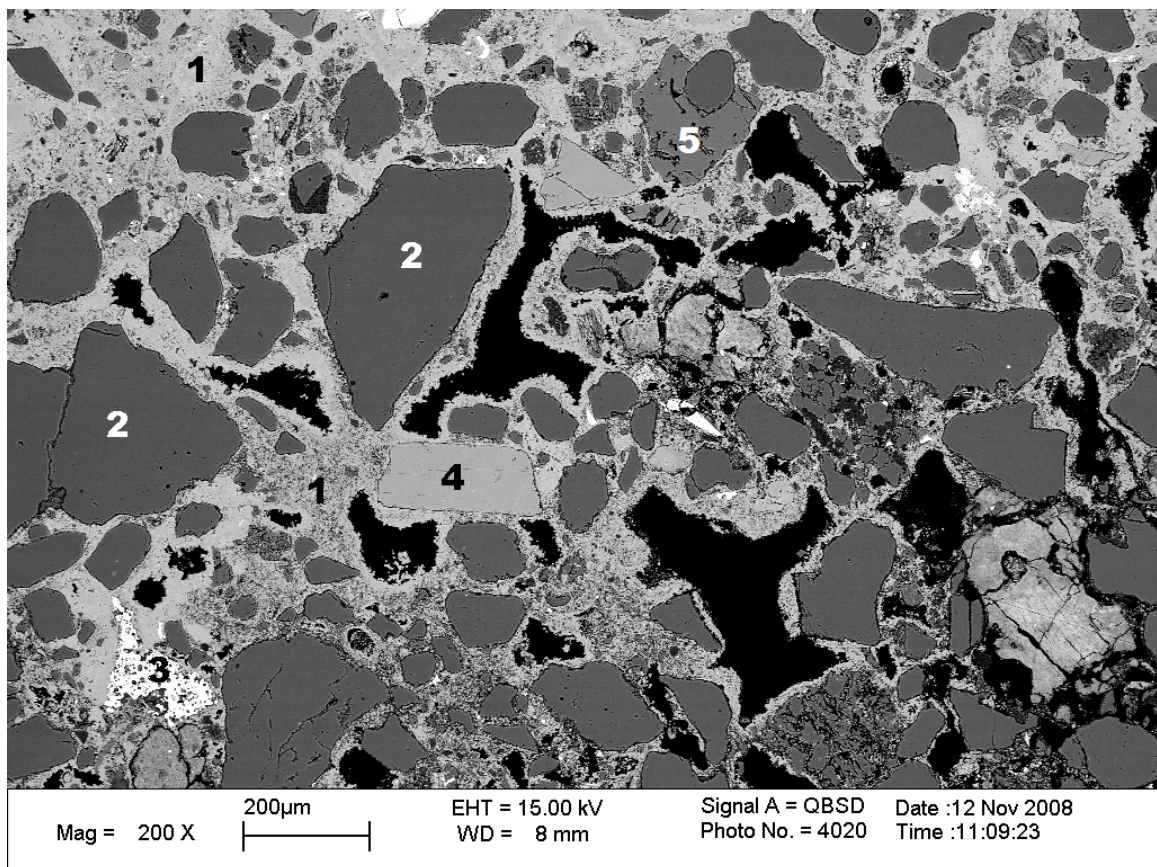


Figure5- 3. Calcite matrix and composition. SEM image of a thin-section of the calcite structures at Site 1. The matrix is calcite (1), the most ubiquitous incorporated mineral is quartz (2); iron oxides/ilmenite (3, bottom left), pyroxenes (Na, Al pyroxenes in this image; 4), and orthoclase (5) are also present. The lack of significant rounding of the grains suggests short transport distances. The morphology and composition at Site 2 is similar.

Microscopic examination of the samples from both sites shows a calcite matrix primarily embedded with quartz, with other mineral grains as a minor component (Figure 5-3). The quartz grains are angular with little rounding, similar to the angular nature of the quartz grains in the surrounding sandstone rocks (Issawi, 1980). The persistent angular grains suggest short transport distances. No fossils or pollen were observed.

The calcite structures were dated using radiocarbon dating of the bulk sample. Two subsamples from Site 1 were dated, giving similar dates: 7,970 calibrated years BP and 8,190 cal yrs BP. For Site 2, the carbonate age is 9,440 cal years BP. The measured radiocarbon ages – corrected for carbon isotopic fractionation – were $7,150 \pm 50$ ^{14}C yrs BP and $7,400 \pm 60$ ^{14}C yrs BP for Site 1, and $8,380 \pm 50$ ^{14}C yrs BP for Site 2. The $\delta^{13}\text{C}_{\text{PDB}}$ values for samples from Sites 1 and 2 are -6.0% (both subsamples) and -6.1% , respectively, and are consistent with an atmospheric source for the carbon (about -7% ; Smith et al., 2004). In addition, carbonate-bearing rocks are not present upstream of the study sites, based on geological mapping surveys (Issawi, 1980) as well as our own exploration. While no springs were found upstream, carbon input from groundwater cannot be ruled out. The similarity in $\delta^{13}\text{C}$ between the two sites indicates that the relative ages are precise. The organic carbon content of the samples is below the detection limit of the measurement: less than 0.3 weight percent.

5.5 Discussion

The calcite structures discovered at Gebel Uweinat indicate a wetter climate in the area about 8,100 and 9,400 years BP. These measurements provide a new and unique data point for the Gebel Uweinat area. The results are consistent with previous studies of

Egypt's Western Desert, which show the last humid period in the area to have been 10,500 to 5,000 years BP. These data are based on stratigraphy and radiocarbon dating (Haynes 2001; Hoelzmann et al. 1998; Kuper and Kröpelin, 2006; Nicoll 2001), thermoluminescence dating (Navarro-Gonzalez et al. 2007), and reconstruction of lake levels through shoreline and geochemical analyses (Damnati, 2000). The ages also correlate with the time of the creation of the local rock art. The range of measured ages between the two sites is likely due to an extended period of carbonate precipitation and the limited number of samples collected at each site. The timing of carbonate formation may also have been influenced by minor differences between the sites, such as erosion or dune movement. We also cannot rule out slight differences in water chemistry affecting the rate of calcite precipitation through time.

The distinct morphology of the calcite structures, which is similar both on the exterior and the interior of the formations (Figure 5-3), and the constant elevation, "bath-tub ring" appearance of the reef at site 1 (Figure 5-2a), imply that the morphology is authigenic and not the result of weathering; weathering is expected to modify the flat top surface of the bench and result in a difference between the morphology of the outer and inner fabric. Features of re-precipitation or texture change are not visible within the collected samples (Figure 5-3). Due to the exploratory nature of the expedition, we were not able to conduct extensive sampling of the sites or a systematic search of the area to map out any broader distribution of carbonates.

The constant elevation, bench-like reef is consistent with formation in the shallows of a lake, implying long-term standing water. Both sites are currently in

enclosed topographic lows in their respective channel beds. The basin for Site 1, which has a more fully developed reef structure, is deeper and better defined.

Samples from both sites have very similar chemical compositions, consistent with their close proximity and the similarity of their geological settings. This includes their predominantly calcite and quartz composition. The low molar Mg/Ca ratio (< 0.05) in the calcite suggests that the structures formed in a freshwater lake (e.g. Eugster and Hardie, 1978; Gasse and Fontes, 1992; Pachur and Hoelzmann, 2000). In addition, carbonates formed in saline environments commonly contain evaporates that further point to the saline local environment at the time of precipitation (Lisker et al., 2009).

The presence of quartz in the samples is expected due to the ubiquitous quartz sand dunes throughout the region. However, the quantity of the quartz and the relation of the quartz grains to the calcite provide information on the local conditions at the time of carbonate precipitation. Exposed sand dunes can persist through wetter climates, until the rain precipitation is sufficient to support extensive vegetative cover. The high levels of quartz in the calcite matrix suggest that while standing water was present, as required for the formation of the carbonate structures, blowing sand was common and the vegetation cover was minimal. This conclusion is in contrast to previous work suggesting that grassy vegetative cover stabilized aeolian sands in southwestern Egypt during the Early Holocene (Nicoll, 2004). A decrease in the deposition of terrigenous, aeolian sediment off the coast of Mauritania between 14,800 and 5,500 calendar yrs BP has been interpreted as a nearly complete vegetative cover of the Sahara during this time (Adkins et al., 2006; deMenocal et al., 2000). However, the high quartz content in our samples

suggests that the off-shore sedimentation rates may not be representative of the vegetation cover in eastern Sahara.

The discovered Saharan carbonate reefs have a very similar morphology and carbonate composition to calcite reefs reported from modern, fresh-water lakes such as Pavilion Lake in British Columbia, Canada (Figure 5-2d; Laval et al., 2000; Lim et al., 2009). At Pavilion Lake, the microbialites seen at 10–15 m represent similar macro and micro morphologies, including overall size of the structures. Their composition is also calcite with up to 5% Mg. A particular difference between the reefs at the two sites is the minimal presence of quartz in the carbonate structures in Pavilion Lake, due to the extensive vegetative cover at the site and therefore limited availability of windblown sand.

Of closer geographic proximity and of similar morphology are the Pleistocene “coralloid” stromatolites found at the Dead Sea Fault Escarpment (Lisker et al., 2009). While these structures bear a general morphological resemblance, the carbonate is in the form of aragonite and evaporates such as halite, gypsum, and anhydrites form the main and/or secondary minerals.

At Pavilion Lake, the carbonate morphology that is similar to the Saharan sites is found to have a growth rate of 2.5–5 cm/1,000 year (Brady et al., 2009; Laval et al., 2000). If the growth rates at the Gebel Uweinat sites were similar, this would suggest long-term, of order thousands of years, standing water in the vicinity of the Cave of the Swimmers and other numerous rock art sites.

5.6 Conclusions

The discovered reef-like, calcite benches in narrow valleys in Gebel Uweinat in southwest Egypt indicate the presence of long-term standing water, but sparse vegetation cover, about 8,100 and 9,400 years BP. Our results are in contrast to previous suggestions that any lakes in the area were ephemeral (Kröpelin, 1987; Lindstädter and Kröpelin, 2004). Consideration of the time required to form extensive carbonate structures suggests that the onset of increased rainfall, presence of standing water, and likely human habitation were earlier than these dates. The age of the reefs suggests standing water at a time that is in agreement with the plausible ages for rock art in the area, as well as for the images in the Cave of the Swimmers (Almásy, 1934).

5.7 Acknowledgements

We thank George Rossman, Jess Adkins, Fliegel Jezerniczky Expeditions, the members of the field party, and the field leader and guide Andras Zboray. Funding was provided by the NASA Astrobiology program, an NSERC postgraduate fellowship, a Canadian Space Agency supplement, and a research scholarship from the German Research Foundation.

5.8 References

- Adkins, J. et al., 2006. The "African humid period" and the record of marine upwelling from excess ^{230}Th in Ocean Drilling Program Hole 658C. *Paleoceanography*. 21, PA4203.
- Almásy, L., 1934. *The Unknown Sahara (Az Ismeretlen Szahara)*. Franklin Press, Budapest.
- Brady, A. L. et al., 2009. Constraining carbon sources and growth rates of freshwater microbialites in Pavilion Lake using ^{14}C analysis. *Geobiology*. 7, 544–555.
- Burollet, P. F., 1963. Reconnaissance géologique dans le sud-est du bassin de Kufra. *Inst. Francais Pétrole*. 18, 1537–1545.
- Damnati, B., 2000. Holocene lake records in the Northern Hemisphere of Africa. *Journal of African Earth Sciences*. 31, 253–262.
- deMenocal, P. et al., 2000. Abrupt onset and termination of the African Humid Period: rapid climate responses to gradual insolation forcing. *Quaternary Science Reviews*. 19, 347–361.
- Eugster, H. P., Hardie, L. A., Saline Lakes. In: A. Lerman (Ed.), *Lakes – chemistry, geology, physics*. Springer-Verlag, Berlin, 1978, 237–293.
- Gasse, F., Fontes, J. C., Climatic changes in northwest Africa during the last deglaciation (16–7 ka BP). In: E. Bard, W. S. Broecker (Eds.), *The last deglaciation: Absolute and radiocarbon chronologies*. NATO ASI Series, 1992, 297–325.
- Haynes, C. V., Jr, 2001. Geochronology and climate change of the Pleistocene – Holocene transition in the Darb el Arba'in Desert, Eastern Sahara. *Geoarchaeology: An International Journal*. 16, 119–141.

- Haynes, V., 1980. Quaternary geology and archaeological observations. *Geographical Journal: Journey to the Gilf Kebir and Uweinat*. 146, 59–63.
- Hoelzmann, P. et al., 1998. Mid-Holocene land-surface conditions in northern Africa and the Arabian Peninsula: A data set for the analysis of biogeophysical feedbacks in the climate system. *Global biogeochemical cycles*. 12, 35–52.
- Issawi, B., 1980. Geology, stratigraphy and structure of Southwest Egypt. *Geographical Journal: Journey to the Gilf Kebir and Uweinat*. 146, 72–75.
- Kröpelin, S., Palaeoclimatic evidence from early to mid-holocene playas in the Gilf Kebir (Southwest Egypt). In: J. A. Coetzee (Ed.), *Palaeoecology of Africa*. A.A. Balkema, Rotterdam, Brookfield, 1987.
- Kuper, R., Kröpelin, S., 2006. Climate-controlled Holocene occupation in the Sahara: motor of Africa's evolution. *Science*. 313, 803–807.
- Laval, B. et al., 2000. Modern freshwater microbialite analogues for ancient dendritic reef structures. *Nature*. 407, 626–629.
- Lim, D. S. S. et al., 2009. Limnology of Pavilion Lake B.C. – Characterization of a microbialite forming environment. *Fundamental and Applied Limnology*. 173, 329–351.
- Lindstädter, J., Kröpelin, S., 2004. Wadi Bakht revisited: Holocene climate change and prehistoric occupation in the Gilf Kebir region of the Eastern Sahara, SW Egypt. *Geoarchaeology: An International Journal*. 19, 753–778.
- Lisker, S. et al., 2009. Stromatolites in caves of the Dead Sea Fault Escarpment: implications to latest Pleistocene lake levels and tectonic subsidence. *Quaternary Science Reviews*. 28, 80–92.

- Navarro-González, R. et al., 2007. Paleoeecology reconstruction from trapped gases in a fulgurite from the late Pleistocene of the Libyan Desert. *Geology*. 35, 171–174.
- Nicoll, K., 2001. Radiocarbon chronologies of prehistoric human occupation and hydroclimatic change in Egypt and Northern Sudan. *Geoarchaeology: An International Journal*. 16, 47–64.
- Nicoll, K., 2004. Recent environmental change and prehistoric human activity in Egypt and Northern Sudan. *Quaternary Science Reviews*. 23, 561–580.
- Pachur, H.-J., Hoelzmann, P., 2000. Late Quaternary palaeoecology and palaeoclimates of the eastern Sahara. *Journal of African Earth Sciences*. 30, 929–939.
- Smith, J. R. et al., 2004. Constraints on Pleistocene pluvial climates through stable-isotope analysis of fossil-spring tufas and associated gastropods, Kharga Oasis, Egypt. *Palaeogeography, Palaeoclimatology, Palaeoecology*. 206, 157–175.
- Wendorf, F., Members of the combined prehistoric expedition, 1977. Late Pleistocene and recent climatic changes in the Egyptian Sahara. *Geographical Journal*. 143, 211–234.